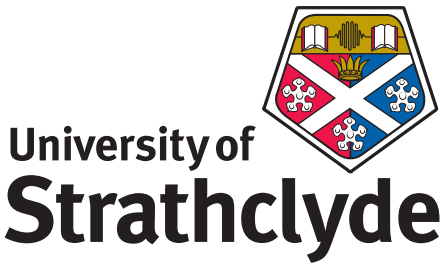

Cancer Therapy: Origin and Application

Fiona L. Roberts

Department of Mathematics & Statistics

University of Strathclyde

Glasgow, UK

April 2012

This thesis is submitted to the University of Strathclyde for the degree of Doctor of Philosophy in the Faculty of Science.

This thesis is the result of the author's original research. It has been composed by the author and has not been previously submitted for examination which has led to the award of a degree.

Signed: Date:

Acknowledgements

I would like to thank my supervisors Dr Gabriel Barrenechea and Dr Steven Webb for all their help and support throughout the course of this PhD. I would also like to thank the University of Strathclyde for funding my studies.

I am so grateful to my family and friends for all their support. I would especially like to thank my Mum and sister for always being there for me, without them this wouldn't have been possible!

Abstract

In this thesis we use mathematical techniques to model two biological systems. First, we examine the growth dynamics of the antibiotic producing bacteria *Streptomyces coelicolor* and present a system of PDEs. We study the system both numerically and analytically. Due to oscillations in the numerical solution when solved using NAG, which uses a finite difference discretization, we change to a finite element discretization which corrects the oscillations.

S. coelicolor also produces anticancer drugs, these can be encapsulated during the self-assembly of nanometre-sized vesicles, BPVs (biomimetic polymer vesicles) which are used as a novel targeted cancer therapy. We present a system of ODEs that focuses on the binding kinetics between cell-surface receptors and targeting molecules (ligands) on the BPV. We solve the system numerically, showing there is an optimal number of ligands per BPV for optimal uptake by tumour cells. We extend the model to allow for the infiltration of BPVs into tumour spheroids. Numerical solutions show that the growth of the spheroid is linear if the therapeutic BPVs are absent, and slows in the other case (for some parameter values). Using large time asymptotics we explore regions of parameter space where either steady states or travelling waves will occur.

Contents

1 Introduction **1**

1.1 Origin of Anti-Cancer Drugs 1

1.2 Targeted Cancer Therapy 9

1.3 Thesis Outline 20

2 Antibiotic Production in *Streptomyces coelicolor* **22**

2.1 Introduction 22

2.2 Model Derivation 23

2.2.1 Initial and Boundary Conditions 26

2.2.2 Parameter Values and Rescalings 27

2.3 Numerical Results 32

2.3.1 Parameter Sensitivity 36

2.4 Analytical Results of Radial Symmetric Growth 43

2.5 Travelling Wave Analysis 49

2.6 Discussion 56

3 Finite Element Solutions of the Reduced *Streptomyces* Model 58

3.1 Introduction 58

3.2 A Simplified Problem 59

3.2.1 Time Discretization 60

3.2.2 Space Discretization using FEM 61

3.2.3 A Quasi-Newton Algorithm 65

3.2.4 Numerical Results 66

3.2.5 A Critical Evaluation of θ 69

3.3 Reduced *Streptomyces* Model 74

3.3.1 Assessment of the FEM Method 77

3.4 Discussion 80

3.A Appendix 81

3.A.1 Comparing Numerical Solutions: Heaviside Function vs Continuous Function 84

4 Novel Targeted Cancer Therapy **92**

4.1 Introduction 92

4.2 Model Derivation 93

4.2.1 Parameterization and Non-dimensionalization 100

4.3 Numerical Results 104

4.3.1 Parameter Sensitivity 108

4.4 Singular Perturbation Analysis 116

4.5 Discussion 129

5 BPV Infiltration into Tumour Spheroids **131**

5.1 Introduction 131

5.2 Model Derivation 134

5.2.1 Initial and Boundary Conditions 137

5.2.2 Non-Dimensionalization 139

5.3 Numerical Results 141

5.3.1 Large Time Behaviour 145

5.4 Extension to Multiple Binding 157

5.5 Numerical Results 163

5.5.1 Large Time Behaviour 169

5.6 Discussion 182

6 Conclusions and Future work **185**

6.1 *S. coelicolor* Growth and Metabolite Production 185

6.2 Targeted Cancer Therapy 188

Bibliography **192**

Chapter 1

Introduction

1.1 Origin of Anti-Cancer Drugs

Streptomycetes are soil-dwelling multicellular filamentous bacteria, from the actinobacteria phylum [5], with a complex life cycle of morphological differention and metabolite production. An important feature of streptomycetes is their metabolite production, the common antibiotic streptomycin is produced by *Streptomyces griseus* and was the first drug to cure tuberculous meningitis [81, 93]. About 60% of the world's naturally derived antibiotics are produced by streptomycetes [9]. This family of bacteria can not only produce antibiotics but also anti-cancer agents [10] and tumour suppressors, hence there are extensive studies on the growth and metabolite production of streptomycetes. The species we focus on is *Streptomyces coelicolor*. The genome of strain A3(2) (which was sequenced in 2002) gave a wealth of information which has aided the genetic engineering of new compounds for medical use [9], for example the metabolite undecylprodigiosin has anti-cancer properties [45, 63].

As mentioned previously *S. coelicolor* has a complex life cycle. On a solid surface, a bacterial colony starts with the germination of a single spore in a nutrient rich environment. The hyphae emerge as a few germ tubes which grow in length by apical tip extension and branching [34]. The hyphae grow linearly behind the tip, with the hyphal extension being a result of new cell wall material forming at the tip [39]. This growing network of filaments are referred to as the substrate (vegetative) mycelium and extends into the nutrient rich environment.

S. coelicolor is a saprophyte, meaning that they degrade and utilise dead organic matter as a nutrient source. As the colony grows localised nutrient deprivation occurs, resulting in lysis (or breakdown) of substrate hyphae in these regions. In responce to this *S. coelicolor* undergoes morphological differentiation and the growth of aerial hyphae starts after a transient period of no growth. Aerial hyphae are coated in a hydrophobic sheath allowing them to break the surface tension and extend vertically above the solid media [34, 99]. Their morphological structure is different to that of substrate mycelium, while in the substrate the hyphae are linear and branched the aerial hyphae are helical and are the precursors to the reproductive cycle. The aerial hyphae extend and septate into around 50 compartments. Each containing a copy of the linear chromosome, each compartment then matures into a hydrophobic spore [31]. The spores are dispersed into new environments, if these new environments are nutrient rich then the life cycle continues, see Figure 1.1 for a sketch of the life cycle described above.

The initiation of the secondary metabolite occurs as the aerial hyphae begin to grow [10]. In *S. coelicolor*, there are four antibiotics produced; actinorhodin (Act), undecylprodigiosin (Red), calcium-dependent antibiotic (CDA) [9] and methylenomycin A [100]. There is no consensus as to why secondary metabolites are produced. There is the theory of competition where the host species can inhibit growth of other bacteria in nutrient deprived areas. A recent paper by

Luti *et al* [63] shows an increased production in Red when grown together with live or dead cultures of the bacteria *Bacillus subtilis*. However, in laboratory conditions, where there is no inter-species competition for resources, metabolite production is observed [64]. Hodgson [46] hypothesised that the origin of the secondary metabolite was to keep the primary metabolite pathways running when a specific nutrient was low until such time that the nutrient was restored.

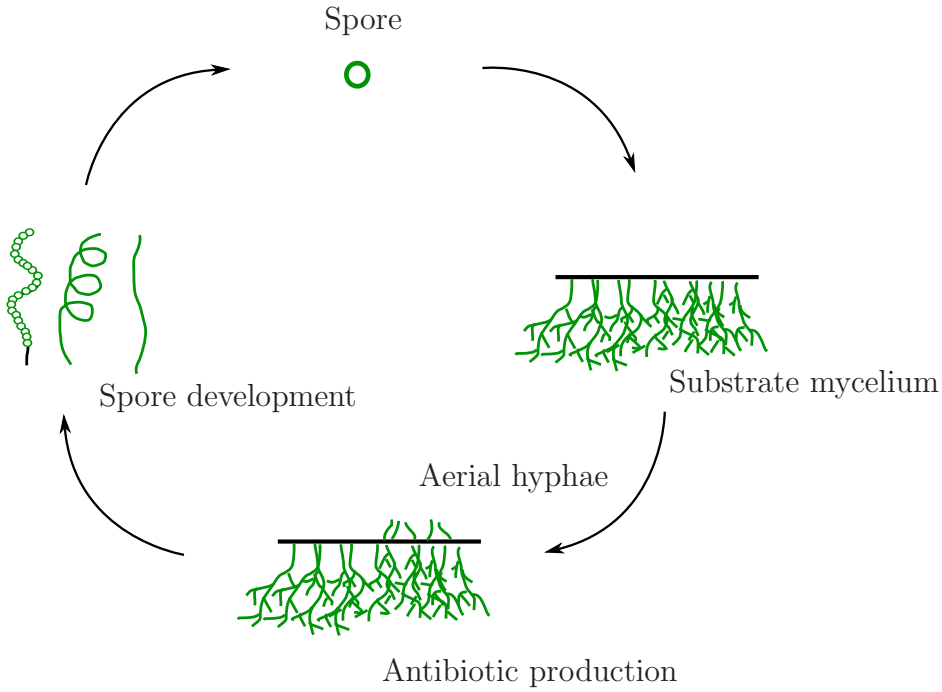

Figure 1.1: A sketch of streptomycetes life cycle in soil. The germination of a spore results in a network of filaments referred to as the substrate mycelium. As nutrient deprivation occurs, the aerial hyphae growth is initiated along with the biosynthesis of secondary metabolites such as antibiotics. The aerial hyphae become helical and septate into compartments which mature into spores. The release of the spores completes the life cycle. For a review of this complex life cycle see [34].

The growth of *S. coelicolor* changes when grown on different medium. We have

described the growth on solid medium but for commercial production of secondary metabolites it is not appropriate to cultivate streptomycetes in this way. Instead they are grown in liquid media. In this media, the morphology of the colony changes to clumps or spherical pellets with maximum diameter of roughly 900μm, for example see Figure 1.2. It turns out that it is this cell aggregation that is important for secondary metabolite production [64].

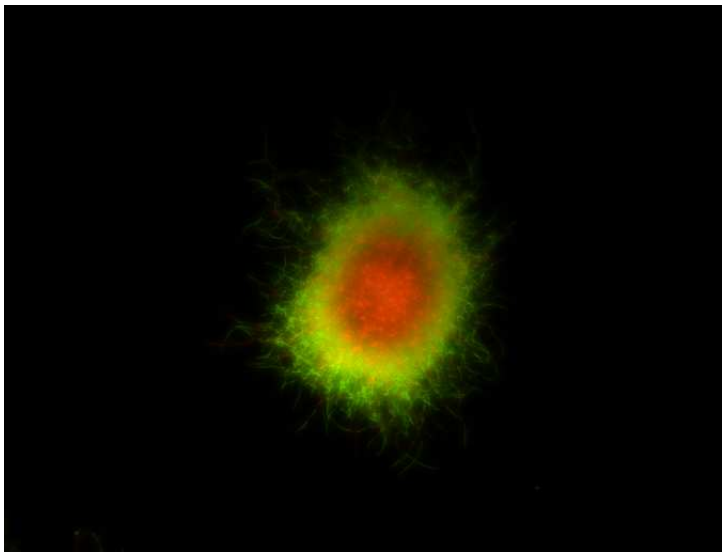

Figure 1.2: *S. coelicolor* pellet after 24 hours (diameter $\sim 260\mu$m) of growth in liquid media, viewed under fluorescent microscopy, the dead cells fluoresce red and the living fluoresce green. This image was taken during a growth experiment, see Chapter 2 for more details.

The differences in morphology of the colony changes the differentiation processes that occur during the streptomycetes life cycle [25, 64]. It has been seen that apoptosis (programmed cell death) plays an important role in the developing pellets, with the pellets growing radially until an arrest which is caused by cell death at the centre of the pellet. After a period of time, the viable mycelium initiates growth (now referred to as the secondary mycelium) and the pellet

radius increases again. The time of growth/arrest and final pellet density is dependent on the initial density of the inoculum (spores).

Due to the lack of aerial hyphae differentiation in liquid cultures it is assumed that nutrient limitation experienced by the pellets affects the antibiotic production by the mycelium [50, 64, 91]. Nutrient depletion occurs in the centre of the pellet, therefore nutrients must diffuse from the media into the centre of the pellet if there is to be a resupply to that region. It is thought that the lack of nutrient at the centre of the pellet causes lysis of cells [91] and it has been shown by Manteca *et al* (2008), [64], that antibiotic production has a strong correlation with the secondary mycelium with biosynthetic genes being activated during the arrest phase.

The growth of this filamentous bacteria along with the production of important metabolites is a very complex process which is still not completely understood. Mathematical modelling the system may shed some light on the driving mechanisms of growth and help in the optimization of metabolite production within an industrial setting.

Mathematical Modelling Background

There are a limited number of previous mathematical models that specifically look at the growth of *Streptomyces coelicolor* but there is a large number of models that look at other species in the genus which have similar growth properties. We shall give a review of previous mathematical models that have been applied to the growth of bacterial pellets and also those of fungal growth despite the size difference, nutrient translocation and filament fusion, the filamentous growth behaviour is very similar to that of filamentous bacteria.

Yang *et al* [102] presented a model for tip growth and branching for *Streptomyces tendae*. The model was extended from work in [101] and focused on the relationship between branching and septation. The model includes deterministic and stochastic parts; the kinetics of septation and apical extension are governed by the deterministic whereas branching is taken to be random. Typical results show a 2-D developing pellet that initiates growth from a single germ tube. This produces realistic looking pellets although the authors neglect the possibility of having nutrient deficiencies, which could only be realistic at early stages of development where no nutrient deficits occur.

Using the Yang *et al* model framework [101, 102], Meyerhoff *at el* [66] presented a general model for the pellet development of microorganisms, focusing on the growth of single hyphal elements. Here the authors addressed the issues of shear stress on the pellet and nutrient limitation that occurs within a pellet due to limited substrate diffusion, with the death of mycelium as a consequence. The tip extension is controlled by a diffusable limiting factor present within the cell. The model presented assumes that the spherical pellets are divided into spherical layers, each layer having an averaged cell density, cell mass concentration and substrate consumption rates. The authors extended the work in [65] in an attempt to move from the microscopic to macroscopic scale, with the aim of reducing the simulation time of the very detailed model presented in [66]. Again they assume the division of pellets into rings, and hold cell density, growth and substrate concentration constant in each layer instead of a single hypha within each ring.

Fungal growth is very similar to that of filamentous bacteria if size is neglected, hence we also look to previous mathematical models that describe fungal growth. Davidson [22] presents a system of reaction-diffusion equations that have three variables; biomass density, internal and external substrate concentrations. The

external substrate is the energy source for the whole system. The author allows for influx and efflux of substrate over the mycelium wall which is taken to be proportional to the biomass density. A capped biomass growth is assumed due to space restrictions. The hyphae movement is limited depending on the availability of internal substrate, with the internal substrate actively moving toward high densities of biomass. Initially the system is examined in radially symmetric space using the NAG routine D03PCF to solve the system numerically. They found that a travelling front appeared, following a wave of biomass density decrease. This behaviour is reflected in the internal substrate concentration, with the external substrate being used in regions where biomass is present (external substrate is initially taken to be uniform in the domain). The author then goes on to examine the growth in 2-D in a heterogeneous medium, where tiles are used to represent the distribution of external substrate and no diffusion is allowed between tiles.

Using work from Davidson [22], Boswell *et al* [13] remodelled aspects of the fungal growth. The model assumes that hyphae growth is a result of a trail left behind as the hyphal tip extends. The authors take into account the translocation of internal nutrients within the hyphae, allowing for passive diffusion of nutrients through the network as well as active motion toward the hyphal tip. Anastomosis is also included and is described by a loss of hyphal tips. The resulting model is a system of mixed hyperbolic-parabolic equations in two spatial dimensions. To solve it, the system is discretized using a finite difference scheme. After spatial discretization, the resulting ODEs are split into stiff (diffusion) and nonstiff (convection) parts, with the convection terms being discretized using flux limiters to retain positivity. This splitting method allowed the two parts to be solved separately.

This same splitting method was presented in Boswell *et al* [14] for a similar

model, in 1-D with less complex hyphal tip flux term. The system is solved on a heterogeneous domain, determined by the initial condition assigned for the external substrate, with glucose only present in droplets at the edge of the domain and not at the centre where inoculation occurs. The diffusion of external substrate is set to zero indicating no diffusion of nutrients between neighbouring agar plates. The results show that the highest concentration of biomass would be present in glucose rich areas, but due to reverse translocation there is biomass present in the regions of no glucose and it is concluded that this was solely due to diffusion.

In our work, we derived a model for *S. coelicolor* growth using a similar frame work to that in Boswell *et al* [13]. However, due to differences between the biological systems, we neglect the processes of translocation of nutrients and anastomosis which do not occur in *S. coelicolor* growth. The flux of hyphal tips in our system is taken to be a combination of random diffusion and directed movement up a substrate gradient. We look at metabolite production which is not present in [13, 14], we also assume that oxygen and substrate are limiting factors, and within designated concentrations of these factors hyphal and tip decay is modulated and antibiotics are produced.

As mentioned previously, *S. coelicolor* produces metabolites, some are classed as anticancer drugs, for example undecylprodigiosin [45, 63]. Traditional cancer therapies are not cell-specific and so side-effects are observed by patients. New targeted cancer therapies are in development in which anticancer drugs are targeted to specific tumour cells via appropriate vectors, which should reduce side-effects. In the next section, we shall discuss the development of these cancer therapies.

1.2 Targeted Cancer Therapy

A tumour initially starts as a single mutated cell. This single cell will divide continuously, obtaining necessary nutrients from the existing surrounding tissue vascular system. The resulting cells grow at an exponential rate into a small mass of cells. As the mass grows, nutrients cannot diffuse adequately to the centre of the cellular mass which results in the tumour having 3 distinct regions; an inner necrotic core (composed of dead cells), a hypoxic (an area of low oxygen concentration critical in tumour progression) region where the cells are quiescent (non-proliferating) and an outer proliferating edge. After a few weeks, the growth rate will eventually decrease and the avascular tumour will reach a saturated size (roughly 2 mm in diameter). *In vivo* the tumour cells typically then express tumour angiogenesis factors (TAFs) such as vascular endothelial growth factor (VEGF) [38, 53]. Here, angiogenesis is the growth of new blood vessels from parent vessels. If the tumour can be vascularized, the blood supply can be re-established giving the tumour nutrients to continue to grow. Another consequence of the tumour obtaining a blood supply is the formation of metastatic growths, as cells from the original tumour can then migrate to neighbouring tissues through the blood stream forming secondary (or metastatic) tumours [44]. The most common tissues for secondary tumours are the brain, bones, adrenal and liver. For an in-depth review of these processes see [4].

It is proposed that the accumulation of mutations in a single cell in the tumour suppressor genes and proto-oncogenes (once mutated they become oncogenes) that allows for cancers to develop [83]. These genes are responsible for the regulation of cell growth and apoptosis (programmed cell death). Mutations of these genes can cause a cell to respond differently or ignore signals received from surrounding normal cells. There are specific pathways to ensure the genomic

integrity of the cell, for example DNA damage repair pathways which, if switched off, can allow the cell to progress through the cell cycle passing the mutation to successive cell generations. There are many mutagenic and carcinogenic agents in our environment: for example, UV light, x-rays and tobacco smoke. Some genetic conditions can also increase a persons chance of developing cancer, for example Li-Fraumeni syndrome is an autosomal-dominant hereditary disorder of whom over 75% have a mutation in the *TP53* gene [33]. This gene encodes the tumour suppressor protein p53, a vital protein in regulating the cell cycle, DNA repair and apoptosis [83] . For full details of DNA repair processes see [4].

Head and neck squamous cell carcinoma (HNSCC)

Cancer is one of the leading cause of death in the UK. Head and neck squamous cell carcinoma (HNSCC), in particular, account for more than 500,000 new cancer cases worldwide each year [43]. Squamous cell carcinoma are tumours of the epithelial cells (cells covering the surface of all tissues) these include tumours of the nasal and oral cavities, larynx, pharynx and paranasal sinuses. There have been great advances in cancer treatments and survival rates in general; for example the survival rate of a woman with breast cancer is 82% after 5 years which is a large increase to that of 30 years ago when it was only 52%, figures taken from Cancer Research UK [1]. This is not the case however for HNSCC, over the past 30 years the survival rate after 5 years has not increased from 50% [49]. As with many cancers early detection is vital. Patients presenting at stage I can have a 90% survival rate after 5 years, but if presented at stage IV the patients have survival rates less than 40% [23]. The majority of presentations occuring in the latter stages of the disease with noticable symptoms such as a mass, pain or obstruction in the airways [23]. The location of the HNSCC tumour can be life changing, with typical changes being to the facial appearance,

speech impairment and problems with swallowing after surgery. The typical risk factors for HNSCC include having a history of tabacco use and heavy alcohol consumption. Patients with HNSCC are normally male over the age of 40 [26].

With histological examination of tumours from the head and neck it has been proven that the human papilloma virus (HPV) subtype 16 has an etiological role, i.e. the origin or causation, in tumour development. HPV-16 accounts for 20-25% of HNSCC tumours [24, 94] and its role is similar to that of HPV-positive cervical cancer. This is a growing concern as the typical risk factors don't apply to HPV-positive HNSCC as it presents in younger patients with lower alcohol and tabacco consumption, and is also thought to be sexually transmitted [43, 89, 94]. Although, a HPV-positive tumour has a better prognosis than the HPV-negative tumour [24], possibly due to the positive tumour having less p53 mutations which can initiate apoptosis pathways when treatment such as ionizing radiation and chemotherapy are used [55].

Treatment of cancer varies depending on the individual patient, the type of tumour and what stage the tumour has progressed to. With HNSCC in the early stages, the traditional method of treatment is to obtain control of the tumours environment by surgically removing the tumour and then radiation therapy (radiotherapy) either before or after surgery [15]. Radiotherapy uses ionizing radiation to introduce free radicals which damage the DNA by introducing double stranded breaks. The cells will either apoptose after the mutation has been inherited by daughter cells or it will slow their growth. Although radiotherapy does has disadvantages, it uses free radicals which causes problems for treating low oxygen regions of the tumour [67, 69]. The tumour will be more resistant to the therapy as it is oxygen that makes the breaks in the DNA permanent. So, when oxygen is low, damage to the DNA tend not to be permanent [16]. There is also the problem that this therapy is non-specific to tumour cells. So normal

cells, as well as tumour cells, are damaged with the radiation. This means that continuous radiation cannot be administered. The damage uncured by the normal cells may result in the patient having side-effects which may include; dry mouth and eyes, fibrosis, soreness and ulcers in the mouth and throat, and also additional cancerous growths (a long term side-effect) may emerge [54].

If the tumour is at a later stage chemotherapy is also introduced [86]. This treatment uses cytoxic drugs which target cells that have a high proliferation rate. Their aim is to affect mitosis or to induce apoptosis, so more aggressive tumours are normally more sensitive to these drugs [80]. The treatment has better results when treating a more differentiated tumour, as regulation of apoptotic pathways may still be intact. The drugs are delivered through the blood stream and so normal cells, for example epithelium, that have a high proliferation rate are also affected by the treatment, which can result in side-effects such as nausea, hair loss and toxicity of organs [92]. The unfortunate outcome with chemotherapy, much like an infection with antibiotics, is that the tumour can become resistant to the drugs. Additionally, on the cell surface, pumps have been found that actively remove the drugs from the cytosol [4].

Advancements in treatment

There have been advancements over these traditional cancer treatments, including for example promising molecular targeting therapies such as monoclonal antibodies. For a full review of the use of monoclonal antibodies see [38], it has been shown that in solid tumours, such as colorectal and HNSCC, the epidermal growth factor receptor (EGF-R) is overexpressed. EGF-R is a receptor which activates a cascade of intracellular signalling when bound by a ligand. Cetuximab is an anti-EGF-R monoclonal antibody, which interferes with the

ligand-binding domain thereby influencing the intracellular signalling. This enhances the tumour cells apoptosis, prevents DNA repair mechanisms (damage from radiation or chemotherapy is then permanent) and it also reduces normal cell toxicity. This discovery is described as significant is found to have a limited effect. Other targets for similar therapies have been identified, such as VEGF.

Macrophages are fully differentiated white blood cells. They play a major component in the human immune system and have two main roles: the first is a non-specific defence, where the macrophage will phagocytose cell debris in an inflammatory response; the second role is antigen presentation, they phagocytose a pathogen and present the antigen (normally a protein on the pathogen surface) to an immune T-cell, which will then invoke an appropriate immune response to the pathogen. For a general overview of macrophages and their role in the immune system see [4].

Within the tumour microenvironment, it is common to find tumour-associated macrophages (TAMs) which have an important role in tumour progression and survival of the patient. It has been shown that there is a correlation between high numbers of TAMs and poor prognosis for specific cancer types such as breast cancer and squamous cell carcinoma [58]. The accumulation of TAMs offers an opportunity for a targeted cancer therapy, although TAMs are not usually tumouricidal but can be if they become activated by an antibody or a particular signalling molecule [11]. Sometimes, when TAMs are in the hypoxic regions of the tumour microenvironment, they can actually aid the tumour cells by producing angiogenesis factors and factors to promote growth [58]. It has been attempted by Griffiths *et al* [41] to use genetically modified macrophages as targeted cancer agents that will exploit changes in gene expression in hypoxic regions of tumours to express cytochrome P450, an enzyme that will activate a chemotherapeutic agent to an active form. Their results are promising but

transferring this treatment to *in vivo* is proving difficult.

Recently, biologists have been developing drug and gene delivery devices using synthetic biomimetic polymer vesicles (BPVs) or sometimes referred to in the literature as polymersomes. Their work follows from liposomal targeting [20, 78]. Liposomes are biological structures that are found within cells that have a lipid bilayer morphology. They have been used as a delivery device but have recently proven unsuccessful due to the following factors: the liposomes being leaky and removed quickly from circulation, by the reticuloendothelial system (RES) [48]. This problem was overcome somewhat by the addition of polyethylene glycol (PEG) to the liposomes surface, which greatly increases the circulation time [48]. Liposomes loaded with anti-cancer drugs have been modified to target cancer cells by adding folic acid to their surface. Folate receptors are overly expressed in cancer cells [76] and appears to be an ideal initial target [56]. Although the expression is not exclusive to cancer cells which may lead to cytotoxicity to normal tissue.

Liposomes are internalized by receptor-mediated endocytosis (and not by fusing with the cell membrane) [62]. Unfortunately when loaded with DNA, the integrity of the genetic information is compromised [79] which results in liposomes not being ideally suitable as a gene delivery vector. BPVs on the other hand are synthetic and so can be produced with desirable characteristics which should overcome these shortcomings of liposomal targeting.

BPVs are synthetic copolymer amphiphiles (also referred to as polymersomes in literature) that mimic the self-assembly capabilities of phospholipids that are found naturally in all cells (for example the cell membrane, liposomes) [27]. A complete BPVs is composed of diblock copolymers and contain hydrophobic and hydrophilic elements. At pH$<$7 the diblock copolymers exist as monomers,

when the pH is raised to a more physiological (pH $\sim$ 7) level the copolymers polymerise in a similar mannor to that of lipids in cell membranes, with the hydrophobic regions at the core and hydrophilic regions on the surface, resulting in a stable (5-50 times tougher than liposomes [37]) nanometre-sized spheroid with an aqueous core [59, 60]. During polymerisation it has been shown that encapsulation of molecules, including hydrophilic components in the aqueous core [8] and hydrophobic drugs within the membrane, are possible. Specifically, the encapsulation of anticancer drugs has been observed such as doxorubicin (DOX) or paclitaxel (TAX) [2], and a finding of great importance is that the encapsulation ability of the BPV is ideal for it to be used as a vector for gene therapy [59, 61].

As with the liposomes it is important to add molecules that can disguise the BPV from the immune system. This is done by combining the hydrophilic copolymer with biomimetic poly(2-methacryloxyethyl phosphorylcholine) or
PMPC, (PEG can also be used) [68]. By adding these "stealth" molecules the circulation time of the BPV is increased greatly [59], and found to be more advantageous than using liposomes as a drug delivery system [57]. The hydrophobic copolymer used is poly(2-diisopropylaminoethyl methacrylate) or PDPA and is pH sensitive, which is important for the release of the encapsulated payload within targeted cells [68].

BPV up-take by cells

Tumour cells endocytose the BPVs (the process by which the BPVs are internalized by the cells). There are many endocytic pathways including pinocytosis (ingestion of fluid and small particles) and phagocytosis (ingesting large particles), often referred to as cell drinking and cell eating respectively. Pinocytosis

can be divided into 4 different pathways; macropinocytosis, clathrin-dependent, caveolin-dependent and clathrin/caveolin independent, we shall focus our attention on macropinocytosis and clathrin-dependent (also known as receptor-mediated) pathways, as the process of BPV internalization, as discussed in [3], is most likely due to one of these.

Macropinocytosis is the process in which relatively large volumes of non-specific solute is internalized by the cell [88]. The process of macropinocytosis requires 2 cell surface ruffles to extend into the extracellular environment. The ruffles subsequently join at the furthermost point, creating a vesicle and encapsulating solutes/molecules present. The vesicle is then entered into the endosomal pathway.

Receptor-mediated endocytosis requires that a ligand binds to a specific receptor on the cell surface. Underneath the cell membrane there are clathrin coated pits. The cell membrane invaginates and then pinches off from the cell membrane, creating a clathrin coated vesicle. The clathrin detaches from the vesicle within seconds, and the resulting uncoated vesicle will enter into the endosomal pathway. For specificity to HNSCC cells (and not normal cells) it has been proposed that the targeting ligand HN-1 peptide is used [47]. For a full review of the various endocytosis pathways see [4, 21].

Whether the BPV is internalized by macropinocytosis or receptor mediated endocytosis the internal process remains the same. Once internalized the BPV enters an endosome, which naturally has a lower pH ($\sim 5-6$) [4]. A consequence of entering a region of lower pH is the dissociation of the BPV which results in the release of the BPV contents into the endosome. It has been shown that the DNA remains viable in this lower pH as it forms a complex with the PMPC-PDPA copolymer [59]. The sudden increase in particle number changes

the osmotic pressure within the endosome causing it to rupture, releasing the contents of the dissociated BPV. The pH of the cytosol is 7.2, this change in environment results in the PMPC-PDPA losing its affinity for the DNA, which is then becomes free within the cytosol [61]. See Figure 1.3 for a sketch of DNA encapsulation by BPV self-assembly.

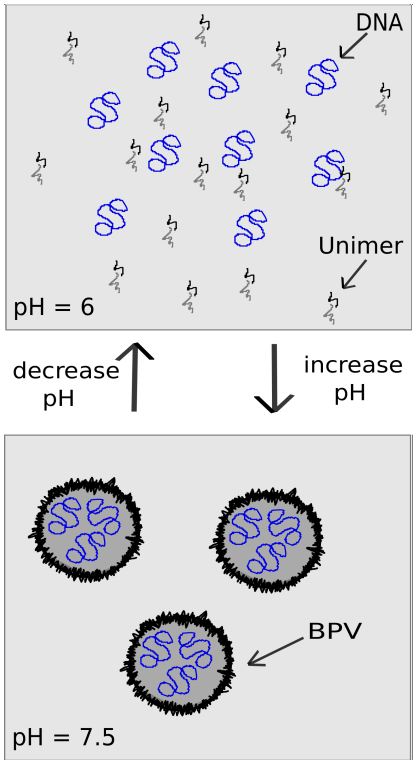

Figure 1.3: A sketch of DNA encapsulation during BPV self-assembly. Components of the BPV exist as unimers at a low pH. When the pH rises, the unimers combine to produce the BPV and while doing so the DNA is encapsulated.

Lomas *et al* [59, 60] have shown promising results using BPVs as a gene vectors, using both Chinese hamster ovary cells and human dermal fibroblast cells, as GFP (green fluorescent protein) was shown to be expressed in the cytosol of the cells after internalization of BPVs containing a GFP-encoding DNA plasmid. BPVs are very promising, not only in the targeted treatment of cancer but

can be applied to other diseases. The research into the treatment of cancer is ongoing, aiming to improve life expectancy and reduce the side-effects.

Mathematical Modelling Background

There is a long history of applying mathematics to the study of cancer. Specific aspects of tumour development are generally focused on, including avascular tumour growth, angiogenesis (the process by which a tumour becomes vascularized), and cancer therapy (traditional and novel). In this section we give a short review of some of the mathematical models in these fields.

The study of avascular tumour growth was first proposed by Thomlinson and Gray [90] in 1955 to study the structure of lung cancer, with the avascular tumours having a necrotic core due to lack of oxygen diffusion. This model has been extended by Greenspan [40] to include a chemical inhibitor produced by the necrosis of cells that slows the growth of the tumour, resulting in a spheroid containing 3 distint regions; necrotic core, quiescent (non-diving cells) and a proliferating edge. Apoptosis is an important factor in tumour development, which is addressed by Byrne and Chaplain [17] who introduced an externally sourced growth inhibitor, for example an anti-cancer drug or signal from neighbouring cells. Ward and King [95] introduce a model that does not present cells in different classes, rather they allow for volume fractions of living or dead cells contained in a fixed volume. The cells reproduce or die dependent on a concentration of external nutrient. Typical model solutions show a travelling wave profile or growth retardation due to nutrient-deficient conditions within the spheroid or due to necrosis. Ward and King follow up this work in [96] to show that the passing of cellular material across the boundary of the tumour

surface is necessary for growth saturation.

Angiogenesis is the process of vascularization which is extremely important in the development and spread of cancer. In general, models of angiogenesis have incorporated the release of TAFs (tumour-angiogenesis factors) from tumour cells, resulting in vascularization of the tumour from a nearby parent vessel. The methods commonly used to model angiogenesis are split between continuum and discrete. In [19] Chaplain and Stuart use a system of two non-linear reaction-diffusion equations focused on the migration of endothelial cells from a parent vessel to a specific TAF profile. Another approach that has been used by Orme and Chaplain [71] is to model the interaction between the tumour cells and the vasculature, showing migration of tumour cells, regression of blood vessels and the formation of a necrotic core. These authors continued their work to look at the initial stages of angiogenesis [72], by modelling the formation of capillary buds and initial branching from the parent vessel. Discrete models appear to be better equipped to follow the individual progression of migrating vessels, with the use of cellular atomator models being advantageous. Anderson *et al* [6] discretize their continuum model which then enables them to follow of individual sprout tips, resulting in a network of capillaries, including anastomosis (or loops).

The treatment of cancer is an important issue, and as a result there are many models with varying treatment types. For example, there are models which include the administration of traditional therapies such as chemotherapy drugs or radiotherapy. Panovska *et al* [75] present a system of nonlinear partial differential equations that model continuous infusion of a vascular tumour and varying different types of chemotherapy. The results include growth arrest or slowing, or when using an anti-angiogenesis drug reverting the tumour to an avascular state. Due to the side effects of chemotherapy, there have been novel treatments

developed and modelled; for example, the use of tumour associated macrophages (TAMs) [73, 98]. In these studies, the authors present systems of nonlinear partial differential equations which describe infiltration of the macrophages into a tumour spheroid. In Chapter 5, we adapt these model frameworks to include BPV infiltration.

We mentioned previously the targeting of liposomes to cancer cells. A deterministic mathematical model was presented by Ghaghada *et al* [36] who used a system of ordinary differential equations to model a carrier (liposome) with folate ligands incorporated to attach to folate receptors on the cell surface. The model takes into account the tether length of the ligands and receptor spatial distributions. Their results show a reasonable agreement between model simulations and experimental data, and found an interesting result that when a very large number of ligands per liposome are used, less liposomes are internalized. We build our modelling framework from aspects of this model, and extend it to include tumour cells, an internalized class of carrier (BPVs) and the release of drug.

1.3 Thesis Outline

In this thesis, we aim to model two biological systems. Chapters 2 and 3 will focus on the mathematical modelling of *Streptomyces coelicolor* growth and metabolite production. Then, in Chapters 4 and 5 we move on to the modelling of a novel cancer treatment, targeting BPVs to specific tumour cells.

In Chapter 2, we derive the equations that model *S. coelicolor* growth and metabolite production. We first conduct a parameter sensitivity analysis. Further numerical results indicate the presence of a travelling wave, which we anal-

yse using travelling wave analysis.

In Chapter 3, we address numerical problems that appear in Chapter 2 by solving a reduced growth model. We use the θ-method to discretize time, finite elements for spatial discretization, and a quasi-Newton algorithm to solve the system in Matlab. Initially, we test the algorithm on a simpler system that contains the important aspects of the reduced growth model, and carry out an investigation into the θ value and the time step, δ_t.

In Chapter 4, we derive a model for targeted cancer therapy, where we focus on the binding kinetics between cancer cell receptors and ligands on the BPV surface. We parameterize the model using values from the literature and carry out a parameter sensitivity analysis around these base values. The numerical simulations show a sharp transition close to $t = 0$, hence we conduct a singular perturbation analysis which allows us to find analytical solutions for the inner solution that match with these numerical observations.

In Chapter 5, we extend the model for targeted cancer therapy to include the spatial effects within a tumour spheroid and focus on the infiltration of BPVs into the spheroid. We implicitly introduce the concept of membrane deformation during internalization of the BPV by varying the internalization function from a constant rate to a Heaviside function, whereby a prescribed number of bonds must be made between receptor and ligand before internalization can occur. We then look at the large time behaviour of the system and conduct a bifurcation analysis using AUTO to find travelling wave and steady state bifurcation curves in various regions of parameter space.

We then finish (in Chapter 6) with a discussion of the work and present possible future directions.

Chapter 2

Antibiotic Production in *Streptomyces coelicolor*

2.1 Introduction

In this chapter we present a "tip and trail" type model to describe the growth of a *Streptomyces coelicolor* pellet. *S. coelicolor* is a multicellular organism forming filamentous colonies which develop from a single spore. In solid culture, hyphae grow through apical tip extension and branching forms a network of filaments (referred to as mycelium) [34]. When nutrients become limited the growth of aerial hyphae is induced, which grow above the substrate mycelium which then initiates the production of antibiotics [32]. Two different antibiotics are released, one is released from the living mycelium (actinorhodin, Act) and the other is released when the cells lyse (undecylprodigiosin, Red) [9]. The initiation of aerial hyphae growth also signals the reproductive cycle. The aerial hyphae undergo septation, these compartments mature into spores which will be dispersed into

a new nutrient rich area.

In an industrial setting, *S. coelicolor* is cultured in flasks of medium (containing nutrients for growth and development), and form spherical pellets. The process of antibiotic production is slightly different in liquid culture as sporulation generally doesn't occur [25, 64]. It has been shown that there are two growth phases, separated by an arrest phase. The first phase is the growth of the substrate mycelia described above, forming an early pellet. After some time, the hyphae start to die (through apoptosis) at the centre which causes the arrest phase. The second growth phase produces a new substrate from the viable mycelium, which can then go on to produce antibiotics [64]. It has also been reported that lack of nutrient at the centre of the pellet causes lysis and initiates the release of metabolite activators and subsequently antibiotics [91].

2.2 Model Derivation

A short time after germination of a spore, tip cells extend outward (from the germinated spore) with hyphae forming behind the tips. The tip cells extend and branch creating a network of filaments. The tip cells and hyphae both consume oxygen and substrate (the medium in which the Streptomyces is grown and contains all the nutrients required for growth) due to movement and general maintenance of the cells. Unlike filamentous fungi, there is no translocation of nutrients, i.e. there is no transfer of nutrients from one area of the growing colony to another that may be deprived, hence we assume that tip cells will actively move to a higher concentration of oxygen/substrate. We also assume a general random motion of hyphal tips and hyphae extension is then proportional to the tip flux (a system referred to as tip and trail). The antibiotic is produced from

the living mycelium (hyphae). It is not continuously produced but is dependent on the concentration of oxygen and substrate.

The system we derive is defined by five partial differential equations for tip cell density (number of tips per mm^2), $p(r,t)$, hyphae density (mm hyphae per mm^2), $m(r,t)$, substrate concentration (g glucose per mm^2), $s(r,t)$, oxygen concentration (g oxygen per mm^2), $c(r,t)$, and antibiotic concentration (g antibiotic per mm^2), $a(r,t)$, where $r \in \mathbb{R}^3$, we use 1-D radially symmetric space, for simplicity.

The equation describing the rate of change of tips cells is given by

$$\frac{\partial p}{\partial t} = -\frac{1}{r^2}\frac{\partial}{\partial r}\left(r^2 J_p\right) + bH(c-\hat{c})H(s-\hat{s})p - d_p^{back}p - d_p^{max}H(\hat{c}-c)p, \quad (2.1)$$

where J_p is the flux of the tips and $H(\cdot)$ are Heaviside functions. The network of filaments produced during pellet development is due to tip cell branching, which we assume is given by the constant rate b. If the concentration of substrate or oxygen falls below a threshold ($\hat{s}$ or $\hat{c}$, for substrate and oxygen, respectively) we assume that the tips stop branching. The tip cells have a limited life span, with the background death rate given by d_p^{back}. Also, during times of stress, i.e. when the oxygen concentration falls below a critical level, $\hat{c}$, the death rate of the tips is increased and the additional death rate is given by d_p^{max}. The units of all parameters can be found in Table 2.1.

The equation that governs the rate of change of hyphae reads

$$\frac{\partial m}{\partial t} = \gamma\left|J_p\right| - d_m^{back}m + d_m^{max}H(\hat{c}-c)m, \quad (2.2)$$

where hyphal extension is given by a proportion, γ, of the absolute value of the flux of the tips, J_p. Similarly to the tip equation, hyphae die at a constant rate d_m^{back} which is increased by d_m^{max} when oxygen falls below a critical level.

The rate of change of substrate is given by

$$\frac{\partial s}{\partial t} = D_s \frac{1}{r^2}\frac{\partial}{\partial r}\left(r^2 \frac{\partial s}{\partial r}\right) - d_s^p |J_p| \gamma - d_s^b b H(c-\hat{c}) H(s-\hat{s}) p - (d_s^{cp} p + d_s^{cm} m)\, s, \quad (2.3)$$

where D_s is the diffusion coefficient of substrate and d_s^p is the rate of consumption associated with tip flux on substrate. The substrate is also utilised for tip branching, which is represented by the rate of consumption d_s^b. General maintenance of the tips and hyphae consume substrate, which are represented by the consumption rates d_s^{cp}, d_s^{cm}, respectively. The equation for oxygen is very similar to that of substrate.

$$\frac{\partial c}{\partial t} = D_c \frac{1}{r^2}\frac{\partial}{\partial r}\left(r^2 \frac{\partial c}{\partial r}\right) - d_c^p |J_p| \gamma - d_c^b b H(c-\hat{c}) H(s-\hat{s}) p - \left(d_c^{cp} p + d_c^{cm} m\right) c, \quad (2.4)$$

where D_c is the diffusion coefficient of oxygen, and the costs associated with tip movement, tip branching and general maintenance usage by tips and hyphae are given by d_c^p, d_c^b, d_c^{cp} and d_c^{cm} respectively. The final equation describes the rate of change of the antibiotic concentration and is given by

$$\frac{\partial a}{\partial t} = D_a \frac{1}{r^2}\frac{\partial}{\partial r}\left(r^2 \frac{\partial a}{\partial r}\right) + r_a H\left(c - \hat{c}\right) H\left((\hat{s} - s)(s - \bar{s})\right) m. \quad (2.5)$$

We assume that the antibiotic production is of actinorhodin, a diffusible antibiotic, from living hyphae during growth cessation. We assume that it is produced at a constant rate r_a by the hyphae but only during specific nutrient regions; the substrate has to be limited for antibiotic production to be initiated but the production will be switched off when the substrate is too low and oxygen must be above the critical value for the cells to be viable, i.e. $\bar{s} < s(r,t) < \hat{s}$ where $\hat{s} > \bar{s}$, and $c(r,t) > \hat{c}$ for antibiotic production. An example of the Heaviside function used, $H\left((\hat{s} - s)(s - \bar{s})\right)$, is depicted in Figure 2.1.

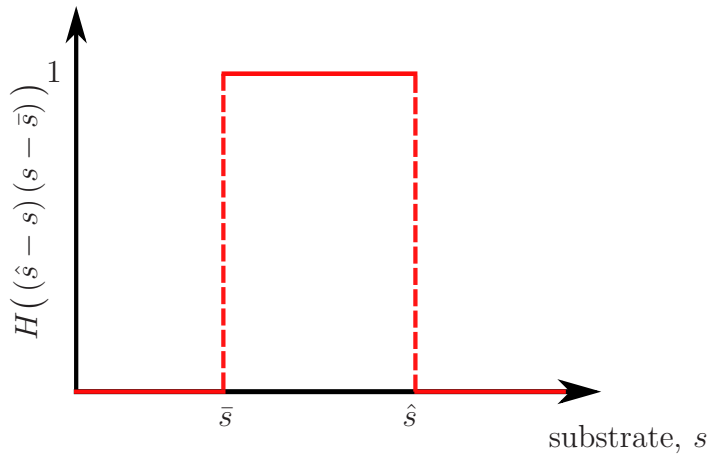

Figure 2.1: Shown is a graph of $H\big((\hat{s}-s)(s-\bar{s})\big)$ as a function of s. $H\big((\hat{s}-s)(s-\bar{s})\big) = 1$ when $\bar{s} < s(r,t) < \hat{s}$ and zero elsewhere.

In equations (2.1)-(2.4) there is a term to describe tip flux. We assume that the tips move randomly via Fickian diffusion. We also assume that the tips migrate up the concentration gradient of the substrate, which is given by a taxis term. Hence, the tip flux in radially symmetric space is given by

$$J_p = \left(-D_p \frac{\partial p}{\partial r} + \chi p \frac{\partial s}{\partial r}\right) H(c-\hat{c}) H(s-\hat{s}),$$

where D_p and χ are positive constants. We include Heaviside functions, $H(\cdot)$, to restrict the movement of the tips at low concentrations of the growth limiting factors, substrate and oxygen.

2.2.1 Initial and Boundary Conditions

The system given by the equations (2.1)-(2.5) is solved on the radially symmetric 1-D spatial domain $[0, L]$ for $t \geq 0$, and is subject to the following initial

conditions

$$p(r,0) = p_0(r), \quad m(r,0) = m_0(r), \quad s(r,0) = s_0, \quad c(r,0) = c_0, \quad a(r,0) = 0. \tag{2.6}$$

We use zero flux boundary conditions at the origin and a mixture of zero flux and Dirichlet at $r = L$, they are as follows

$$\text{at } r = 0, \quad J_p = \frac{\partial s}{\partial r} = \frac{\partial c}{\partial r} = \frac{\partial a}{\partial r} = 0, \tag{2.7a}$$

$$\text{at } r = L, \quad J_p = \frac{\partial a}{\partial r} = 0, \quad \text{and} \quad s = s_0, \quad c = c_0. \tag{2.7b}$$

We use Dirichlet boundary conditions for substrate and oxygen at $r = L$ as we assume that the pellet is grown in nutrient rich conditions, hence surrounding the pellet there will be the constant levels of substrate and oxygen, s_0 and c_0, respectively, with the domain we prescribe large enough that the hyphae and tips do not extend to the edge of the boundary.

2.2.2 Parameter Values and Rescalings

To aid the parameter search we conducted an experiment with the aim of finding the overall growth rate of a *S. coelicolor* pellet. With guidance from Dr P. Hoskisson (SIPBS, University of Strathclyde), three, 50ml flasks of yeast extract-malt extract (YEME) media were made. To these, at staggered times of 4 hours, each flask was inoculated with $50\mu l$ of *S. coelicolor* spore culture and incubated at 30^oC on a shake platform.

After 24 hours, $5\mu l$ of culture was pipetted onto a microscope slide. To which $5\mu l$ of *Bac*Light™ was pipetted onto the slide, mixed together with the culture with the tip of the pipette and a coverslide was placed over the sample, with care to remove any bubbles. This was repeated for the 20 and 16 hour samples.

*Bac*Light™ is a fluorescent stain that contains two nucleic acid stains, propidium iodide (red) and SYTO9 (green) [85]. The staining can be viewed under fluorescent microscopy, SYTO9 stains both living and dead cells, propidium iodide can only stain dead cells due to cell membrane degeneracy, hence living cells will fluoresce green and the dead cells will fluoresce red when viewed.

We observed the samples using fluorescent microscopy, 20x objective lens. In Figure 2.2 we show the progression of the pellet over 16-24 hours, during this period of time we observe what appears to be linear growth of the pellet.

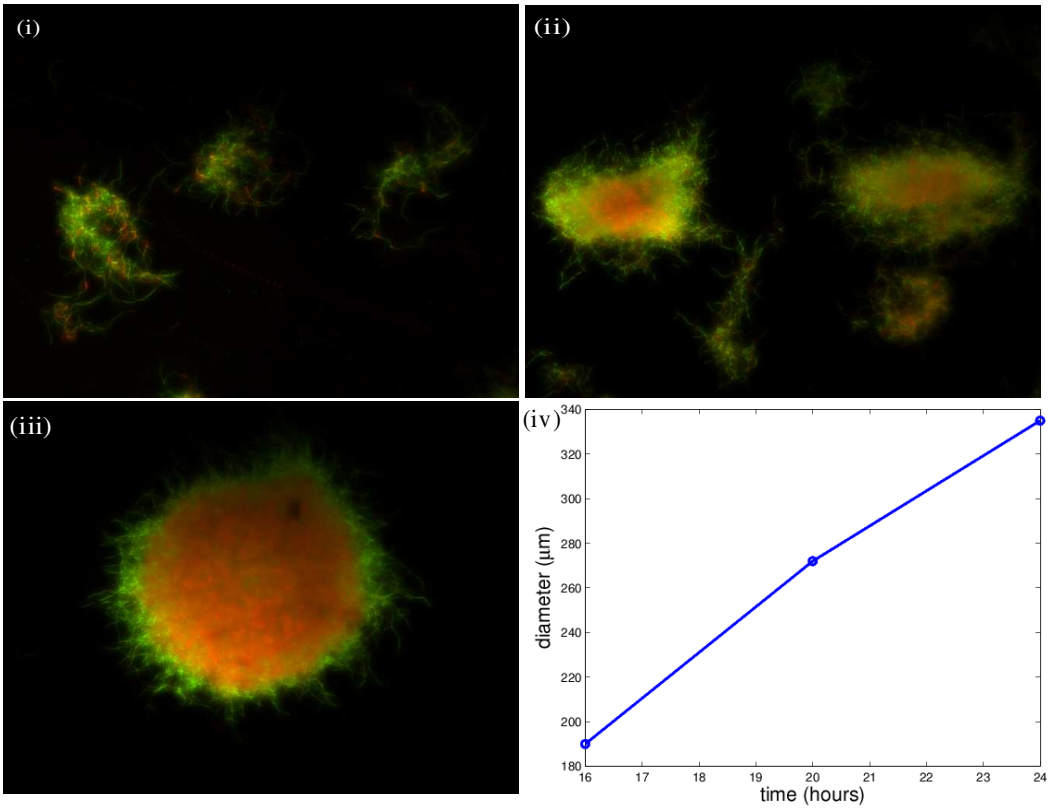

Figure 2.2: *S. coelicolor* pellets at (i) 16 hours, (ii) 20 hours and (iii) 24 hours after staining with *Bac*Light. The living mycelia fluoresces green while the dead regions fluoresce red. Progressing from 16-24 hours we observe the change in pellet diameter and size of the necrotic core. (iv) shows the change in diameter over the 8 hour window.

With data provided by Dr P. Hoskisson (including the hyphal extension rate and distances from tip to branches), we deduce that

$$\text{branching rate} = \frac{\text{hyphal extension rate}}{\text{distance from tip to branch}} = \frac{20\mu\text{m h}^{-1}}{11\mu\text{m}} = 1.818\text{h}^{-1}.$$

This provides us with an initial estimate to the branching rate parameter, which will examine later in the parameter sensitivity analysis. Unfortunately, other parameter values could not be derived from the data provided so we looked to literature to find appropriate values.

First, for the random motion coefficient of the tip cells, D_p, we use $D_p = 3.5 \times 10^{-6}$ cm^2 s^{-1}, which has been taken from Barton *et al* [7], which describes the penetration of E. coli RP48 through sand-packed cores with a galactose and peptone nutrient source, see Table I of [7]. The diffusion coefficient of oxygen was obtained from Oostra *et al* [70] who presented a mathematical model to describe oxygen limitation in (fungal) solid-state fermentation and calculated the diffusion of oxygen coefficient from their biological experiments. We assume our diffusion coefficient of oxygen to be comparable, $D_c = 3 \times 10^{-9}$ m^2 s^{-1}, see Table II [70].

We now look the growth of fungal mycelia which is very similar to that of *S. coelicolor*, albeit on a different scale. There have been multiple mathematical models presented that describe the growth of fungal mycelia by Boswell *et al* [12, 13] from which we've taken the diffusion coefficient for external substrate (glucose), D_s. From [13] (Table 1), we assume a value $D_s = 0.3456$ cm^2 day^{-1}. We assume the initial condition for substrate, s_0, is given by $s_0 = 3 \times 10^{-5}$ mol glucose cm^{-2} and we assume the decay of tips and hyphae to be given by $d_p^{back} = d_m^{back} = 0.5$ day^{-1}, see [12].

In the *S. coelicolor* model we include an increased rate of the decay of tips and hyphae when oxygen becomes limited. We take this value to be $d_p^{max} = d_m^{max} =$

20 h^{-1} which was presented in Meyerhoff *et al* (1995) in a model describing the development of a microbial pellet [66].

Elibol and Mavituna (1999) presented a kinetic model for actinorhodin (ACT) production by *S. coelicolor* and deduced their rate of ACT production at the stationary phase of growth. Therefore we take, r_a, the production of ACT from this study to be $r_a = 0.137$ mg ACT (g cells-h)$^{-1}$ [30]. We assume that the diffusion coefficient for ACT is the same as for the substrate, therefore $D_a = 0.3456$ cm^2 day^{-1} and that ACT has a half life of 10 hours (Dr Hoskisson, personal communication), hence we take $d_a = \dfrac{\ln 2}{10} = 0.0693$ h^{-1}.

Finding the individual consumption rates of substrate and oxygen due to tip branching and tip movement has proved difficult. Therefore, inspection of the model, we see that the rates for substrate and oxygen consumption due to tip branching are $d_s^b = O\left(\dfrac{s_0}{p_0}\right)$ and $d_c^b = O\left(\dfrac{c_0}{p_0}\right)$, respectively. The rates for substrate and oxygen consumption due to the flux of the tips are $d_s^p = O\left(\dfrac{s_0}{m_0}\right)$ and $d_c^p = O\left(\dfrac{c_0}{m_0}\right)$, respectively. Hyphal extension is proportional to the movement of the tips and we vary γ as no conclusive value could be found.

Other parameters such as the consumption rates of substrate or oxygen by hyphae or tips have been very difficult to estimate. Therefore later we will vary these in the appropriate numerical simulations.

We introduce the following rescalings

$$m = \tilde{m} m_s, \quad p = \tilde{p} p_s, \quad s = \tilde{s} s_s, \quad c = \tilde{c} c_s$$

where $m_s = p_s = 10^{-2}, s_s = 10^{-4}$ and $c_s = 10^{-8}$. Using these rescalings, the resulting system will be of $O(1)$ with $L = 1$. The rescaled parameter values are given in Table 2.1.

Parameter	Value and units	Rescaled	Reference
m_0	10^{-3} (mm hyphae) mm^{-2}	0.1	estimate
p_0	10^{-3} (no. tips) mm^{-2}	0.1	estimate
s_0	5.4×10^{-5} (g glucose) mm^{-2}	0.54	[14]
c_0	9.1872×10^{-9} (g O_2) mm^{-3}	0.91872	[74]
a_0	0 (g act) mm^{-3}	0	estimate
D_p	1.2786 mm^2 h^{-1}	-	[7]
D_s	1.44 mm^2 h^{-1}	-	[13]
D_c	8.1 mm^2 h^{-1}	-	[70]
D_a	1.44 mm^2 h^{-1}	-	estimate
χ	0.279 (g glucose mm^{-2})$^{-1}$ mm^2 h^{-1}	2.79×10^{-5}	[22]
b	1.818 h^{-1}	-	Hpc
d_p^{max}	20 h^{-1}	-	[66]
d_m^{max}	20 h^{-1}	-	[66]
d_p^{back}	0.0208 h^{-1}	-	[12]
d_m^{back}	0.0208 h^{-1}	-	[12]
d_s^p	$\approx$ 0.054 g glucose (mm hyphae)$^{-1}$	5.4	estimate
d_c^p	$\approx 9.1872 \times 10^{-6}$ g O_2 (mm hyphae)$^{-1}$	9.1872	estimate
γ	$\left(\frac{\text{no. tips}}{\text{hyphae}}\right)^{-1}$	-	estimate
d_s^b	$\approx$ 0.054 g glucose (no. tips)$^{-1}$	5.4	estimate
d_c^b	$\approx 9.1872 \times 10^{-6}$ g O_2 (no. tips)$^{-1}$	9.1872	estimate
d_s^{cp}	(no. tips mm^{-2})$^{-1}$ h^{-1}	-	estimate
d_s^{cm}	(mm hyphae mm^{-2})$^{-1}$ h^{-1}	-	estimate
d_c^{cp}	(no. tips mm^{-2})$^{-1}$ h^{-1}	-	estimate
d_c^{cm}	(mm hyphae mm^{-2})$^{-1}$ h^{-1}	-	estimate
r_a	0.137×10^{-4} g act (g hyphae)$^{-1}$ h^{-1}	-	[30]
d_a	0.0693 h^{-1}	-	Hpc
$\hat{c}$	-	1/3	Hpc
$\hat{s}$	-	2/3	Hpc
$\bar{s}$	-	1/3	Hpc

Table 2.1: The initial and parmeter values with their rescaled values for the *S. coelicolor* model with a reference for their origins. Hpc = Dr Hoskisson, personal communication.

Although we have good approximations for the diffusion coefficients from the literature, when it came to running simulations they had to be scaled down to reproduce the growth of the pellet that we observed experimentally. This also included the fine tuning of the consumption parameters d_s^b, d_c^b, d_s^p and d_c^p. Unfortunately there were some parameters we could not find experimentally or in the literature, so we estimated these to give a good fit with the experiments.

Due to the uncertainty regarding these parameters, later, we shall carry out a parameter sensitivity analysis which will highlight the parameters that are key in affecting metabolite production and pellet growth.

2.3 Numerical Results

To solve the system we use NAG routine D03PHF, which solves parabolic PDEs using finite differences to discretize space and then the method of lines to convert the system of PDEs into a system of ODEs. The system of ODEs is then solved using the backward differentiation formula or θ-scheme.

In Figure 2.3, we show the typical solution when solved using the rescaled parameter values. In (i) we show the total biomass (i.e. hyphae plus the tips). We notice that, as time increases, the biomass moves outward from the centre toward the substrate source. The substrate and oxygen diffuse into the pellet, and hence a concentration gradient occurs. The growth and maintenance of the biomass causes the substrate and oxygen to decay in the regions where biomass is present, this reduction in nutrients results in the decay of biomass, shown in (ii) and (iv). Hence the resulting pellet has an inner necrotic core with no living biomass, a region of biomass which grows slowly and the outer rim where most growth occurs due to there being the highest concentration of nutrients

there. The antibiotic is produced by the living hyphae during nutrient depletion conditions, hence we see antibiotic production out of phase behind the biomass, in (iii). We set $\hat{s} = \frac{2}{3}$, $\bar{s} = \frac{1}{3}$ and $\hat{c} = \frac{1}{3}$ as we know from biological experiments that the hyphae will produce antibiotic when there is roughly 2/3 of the glucose left in the media and will stop producing it when the glucose level decreases below 1/3 (Dr Hoskisson, personal communication).

We notice in Figure 2.3 (i) and (iii) there are oscillations present at the origin which result in the solutions becoming negative in this region, which is not representative of the biological system but a numerical artifact. We explore an alternative method of solving this system in Chapter 3 to see if the oscillations can be removed from the numerical solution.

Figure 2.4 shows the same solutions as in Figure 2.3 but depicted in a different way. By presenting the solutions in this way we can see that the growth of the pellet is approximately linear, which indicates the possibility of a travelling wave, which we explore later in this chapter.

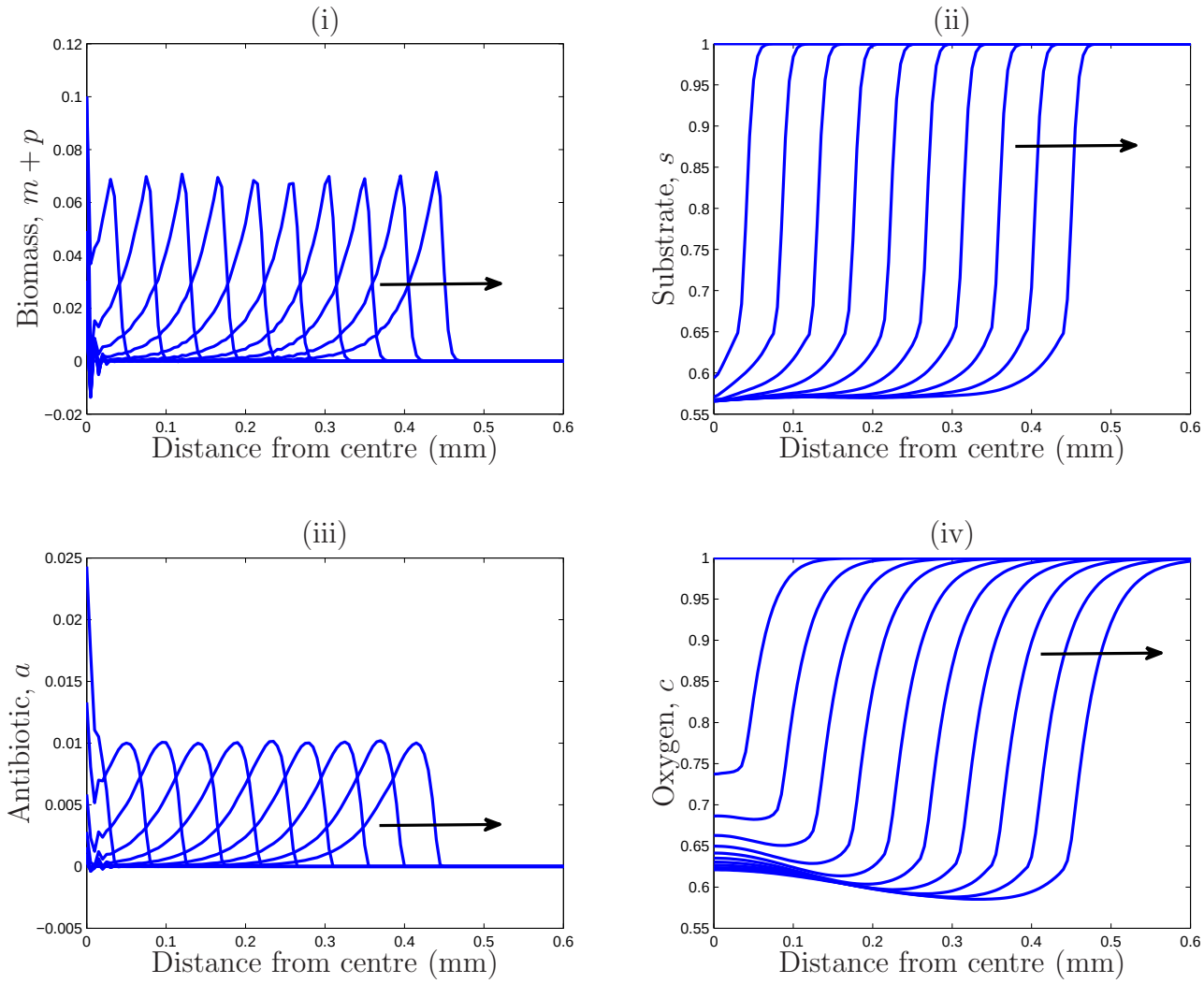

Figure 2.3: Numerical solutions of the system (2.1)-(2.5) when solved using NAG routine D03PHF with $N = 201$ grid points on $[0, 1]$. (i) shows the total biomass (tips and hyphae), (ii) shows the substrate, (iii) shows the antibiotic concentration and (iv) shows the oxygen concentration. Each line represents the solution at successive times, the arrow indicates the direction of movement with increasing time. Solved with the following parameter values $d_p^{back} = d_m^{back} = 0.5, d_p^{max} = d_m^{max} = 20, b = 3, d_s^p = d_c^p = 10, d_s^b = d_c^b = 1, d_s^{cp} = d_s^{cm} = d_c^{cp} = d_c^{cm} = 1, \gamma = 400, D_p = 6.25\times10^{-6}, D_s = 6.25\times10^{-5}, D_c = 6.25\times10^{-4}, D_a = 6.25\times10^{-6}$ and $\chi = 1.25 \times 10^{-4}$.

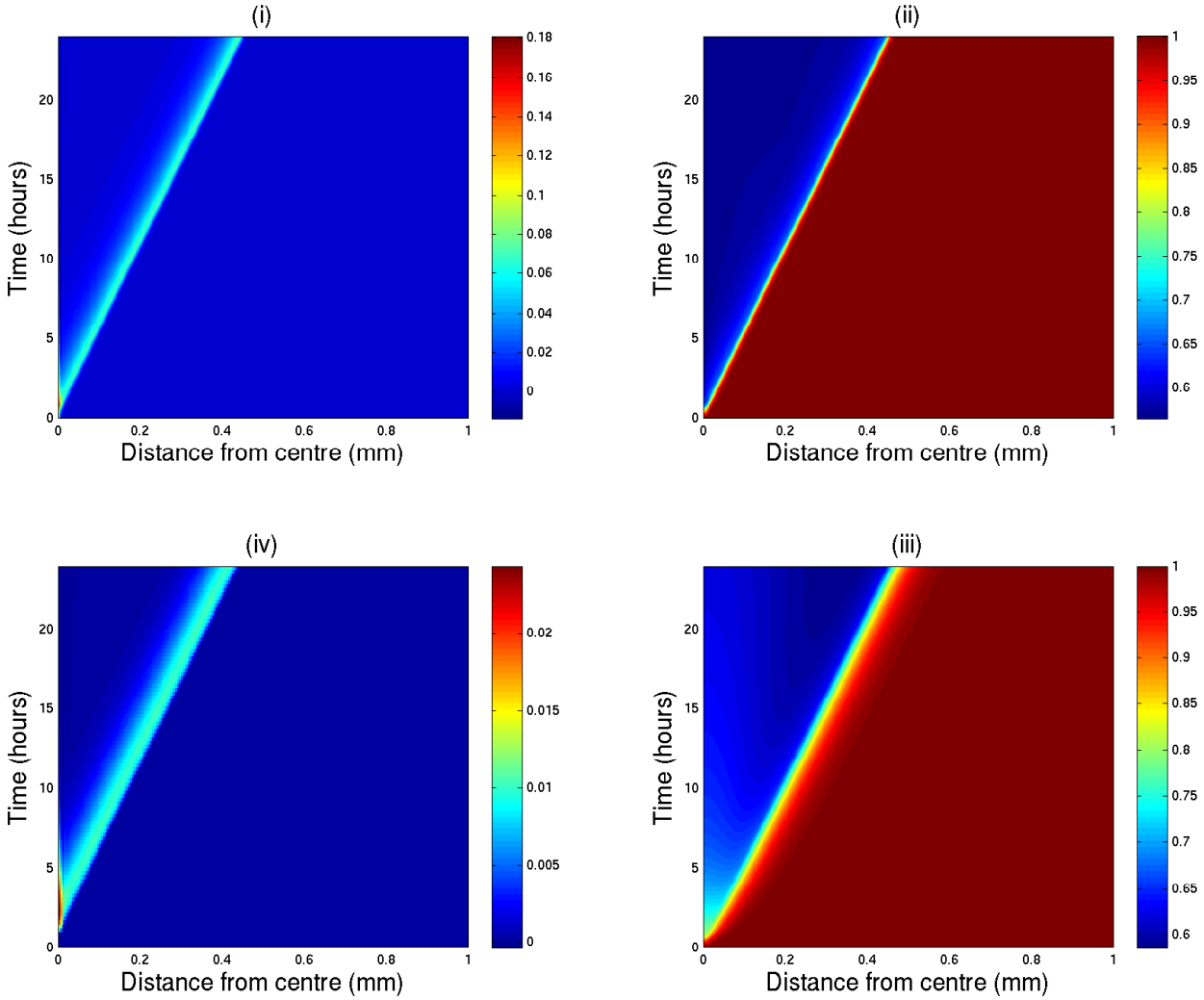

Figure 2.4: Shows how the densities of (i) total biomass, i.e. tips and hyphae, (ii) substrate, (iii) oxygen and (iv) antibiotic change over time when the system (2.1)-(2.5) was solved using NAG routine D03PHF with $N = 201$ grid points on $[0, 1]$. Solved with the following parameter values $d_p^{back} = d_m^{back} = 0.5, d_p^{max} = d_m^{max} = 20, b = 3, d_s^p = d_c^p = 10, d_s^b = d_c^b = 1, d_s^{cp} = d_s^{cm} = d_c^{cp} = d_c^{cm} = 1, \gamma = 400, D_p = 6.25 \times 10^{-6}, D_s = 6.25 \times 10^{-5}, D_c = 6.25 \times 10^{-4}, D_a = 6.25 \times 10^{-6}$ and $\chi = 1.25 \times 10^{-4}$.

2.3.1 Parameter Sensitivity

Obtaining all of the parameter values proved to be difficult. Of those that we were unable to estimate, while running simulations we found the solutions were sensitive to some paramaters. A parameter sensitivity analysis has been carried out to give us insight into how these parameters affect pellet growth and final hyphal and antibiotic densities.

In Figure 2.5, we vary the parameter b which represents the branching rate of the tips. Shown in (i), (iii), (v) and (vi) are the solution profiles at the final time, when b is varied between 1.2 and 4.8. The pellet grows through tip extension and branching, hence when b is increased we expect that the final solution profile will have a larger radius with a greater density, which is shown in (ii) and (iv) respectively.

The next parameter we vary is d_s^p, shown in Figure 2.6, which represents the cost of the tip flux on substrate. As we increase d_s^p, the tips consume more substrate for the purpose of movement. We notice that the pellet radius varies slightly but there is a much larger change in biomass density as d_s^p varies. As we increase d_s^p the density of tips and hyphae decreases. The decrease in biomass density due to the increased cost results in less living cells consuming the substrate, which leads to less substrate being consumed which is observed in Figure 2.6 (iii). The decrease in biomass density also affects antibiotic production and oxygen consumption which are also decreased when d_s^p is increased.

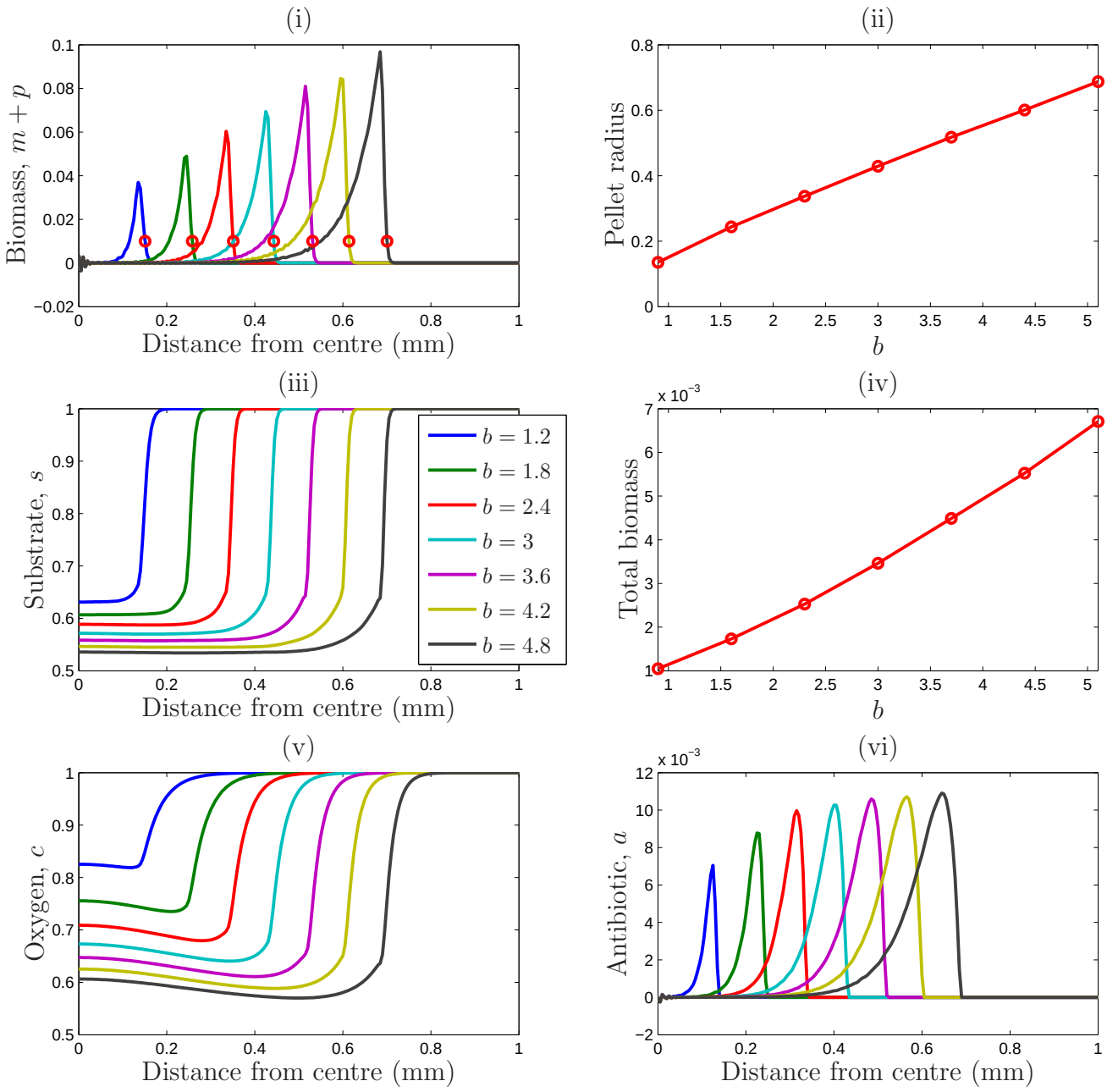

Figure 2.5: Shown in (i), (iii), (v) and (vi) are the final time, $T = 24$ hours, solution profiles for biomass, substrate, oxygen and antibiotic, respectively, for varying values of b (shown) the branching rate of the tips. The red circles in (i) indicates the approximate point of the leading part of the pellet, when $m + p = 0.01$. In (ii) we show the pellet radius and (iv) shows the total biomass (at the final time) at each value of b. The remaining parameters are as in Figure 2.4.

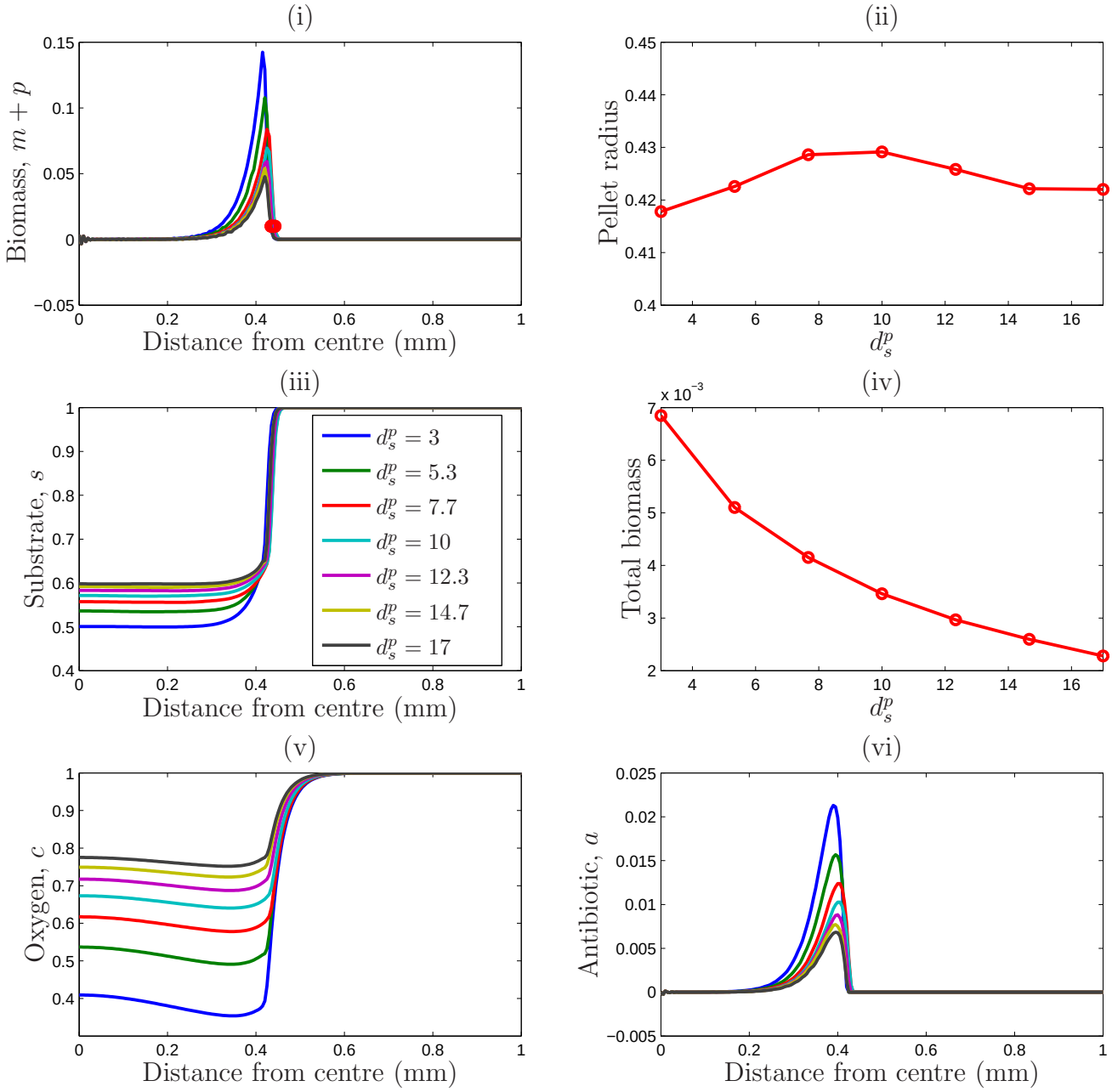

Figure 2.6: Shown in (i), (iii), (v) and (vi) are the final time ($T = 24$ hours) solution profiles for biomass, substrate, oxygen and antibiotic, respectively, for varying values of d_s^p, cost on substrate of tip movement. In (ii) we show the pellet radius and (iv) shows the total biomass (at the final time) at each value of d_s^p. The remaining parameters are as in Figure 2.4.

Figure 2.7 shows the final solution profiles when we vary γ, the parameter that represents hyphal growth due to tip extension. We would assume that by increasing the rate of hyphal extension there would be an increase in biomass, but as shown in Figure 2.7 (i) we see the opposite. There is however an increase in hyphae density (not shown) but the density of tips is reduced hence there is an overall decrease in pellet biomass. The decrease in biomass is due to the increased cost of tip flux on oxygen and substrate when increasing γ, the greater cost results in a less dense pellet. However, due to the individual increase in hyphae, we do see an increase in antibiotic production.

We now examine the effect of varying d_p^{back}, the parameter that represents the background death rate of tips, shown in Figure 2.8. The background death of tips is independent of substrate or oxygen, hence when the death rate is low we see a higher density of biomass. Unlike previous simulations, the biomass is present in the centre of the pellet, which results in a lower concentration of both substrate and oxygen in the centre of the pellet due to living biomass consuming more nutrients. As the death rate is increased, the final pellet radius and density decrease, hence less oxygen and substrate are consumed. Due to the biomass decrease there is also a slight reduction in antibiotic production.

The final parameter we look at is d_c^b, the cost of tips branching on oxygen, see Figure 2.9. Instantly, we notice that varying this parameter has a minimal affect on both final biomass density and pellet radius, and no effect on antibiotic production. There is an increase of oxygen consumption with increased cost of branching but it is not enough to reach the threshold $\hat{c}$ to switch off the tip flux or antibiotic production.

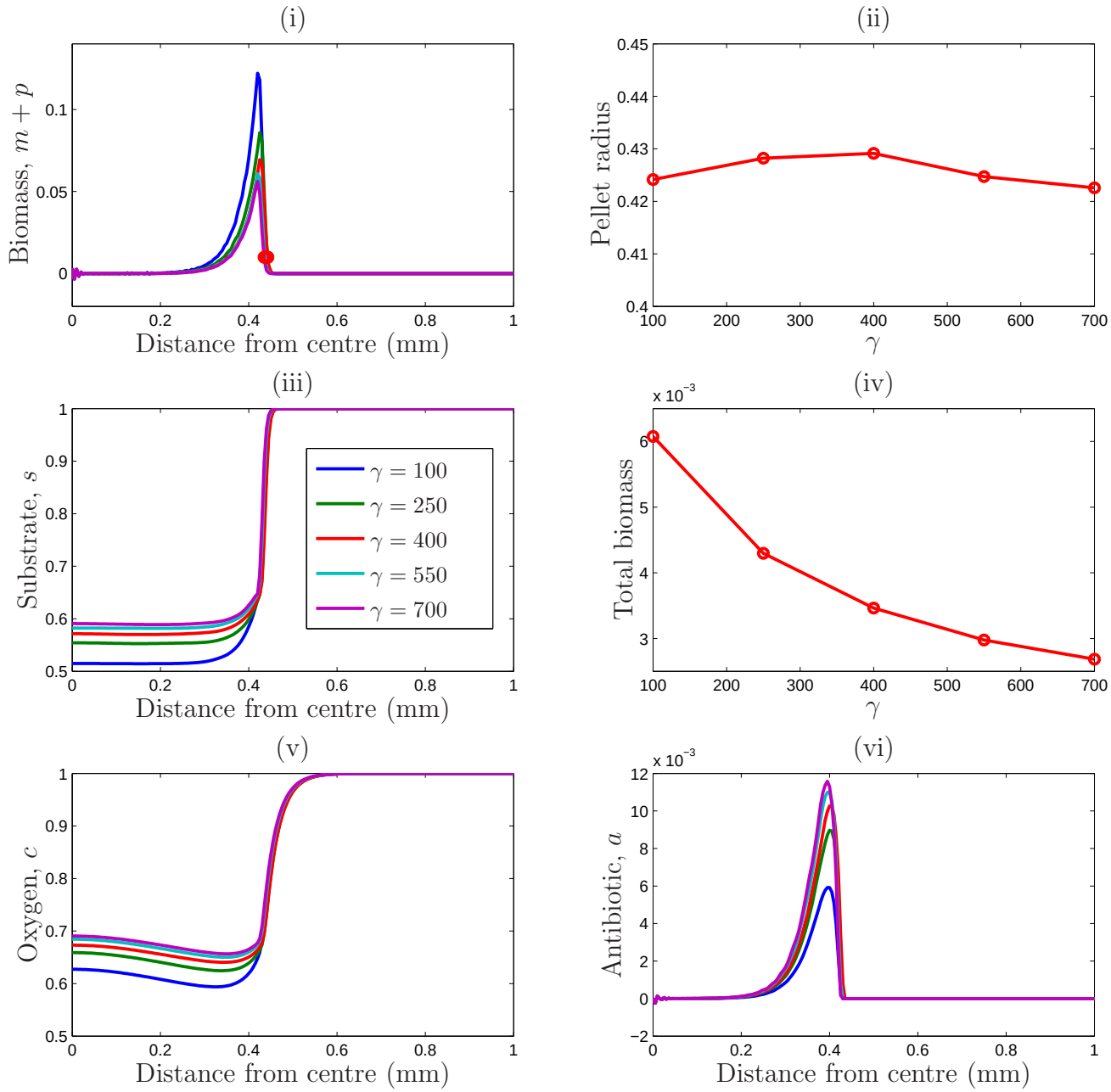

Figure 2.7: Shown in (i), (iii), (v) and (vi) are the final time solution profiles for biomass, substrate, oxygen and antibiotic, respectively, for varying values of γ, hyphal growth on due to tip extension. In (ii) we show the pellet radius and (iv) shows the total biomass (at the final time) at each value of γ. The remaining parameters are as in Figure 2.4.

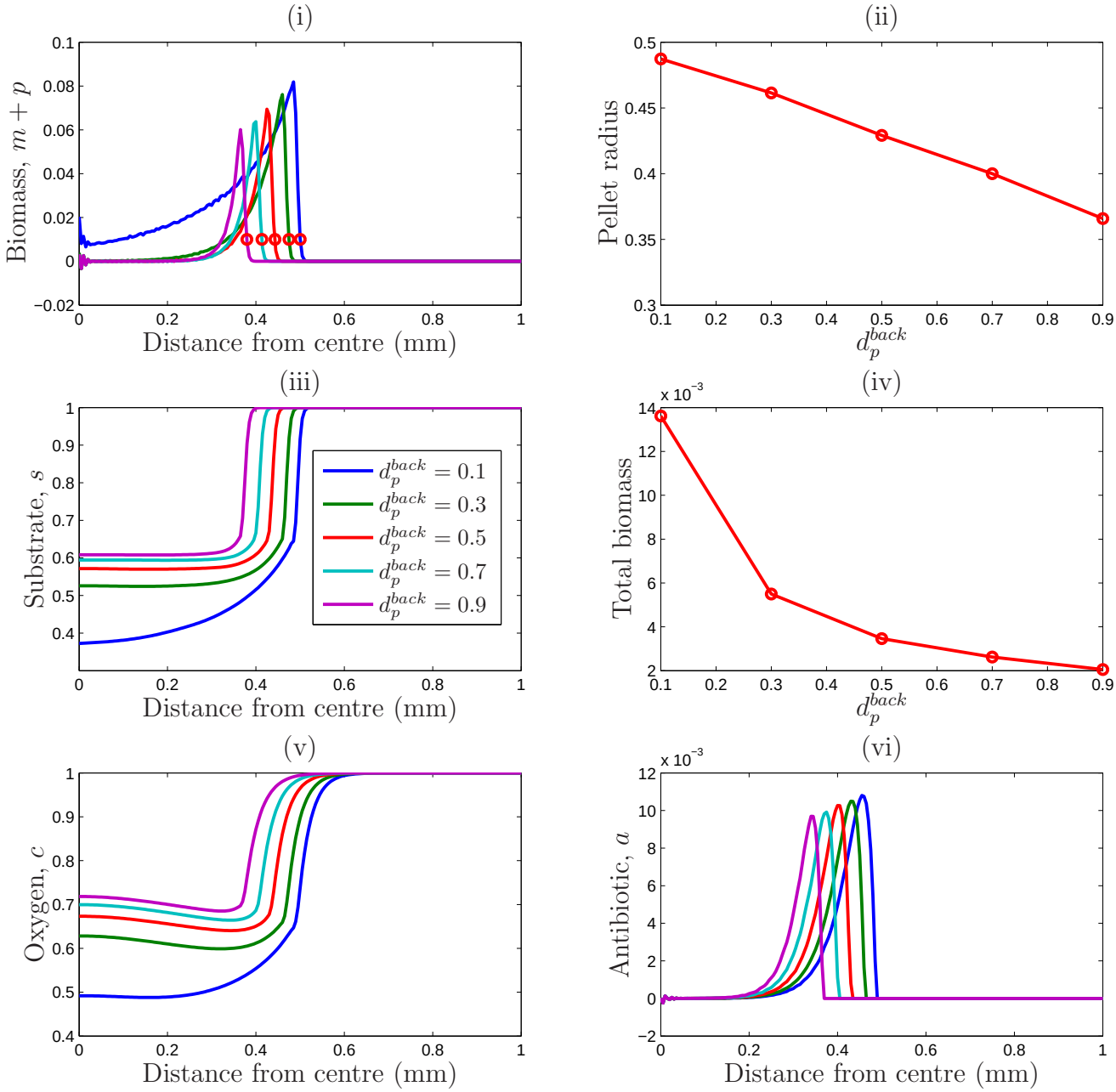

Figure 2.8: Shown in (i), (iii), (v) and (vi) are the final time solution profiles for biomass, substrate, oxygen and antibiotic, respectively, for varying values of d_p^{back}, constant rate of the background death of tips. In (ii) we show the pellet radius and (iv) shows the total biomass (at the final time) at each value of d_p^{back}. The remaining parameters are as in Figure 2.4.

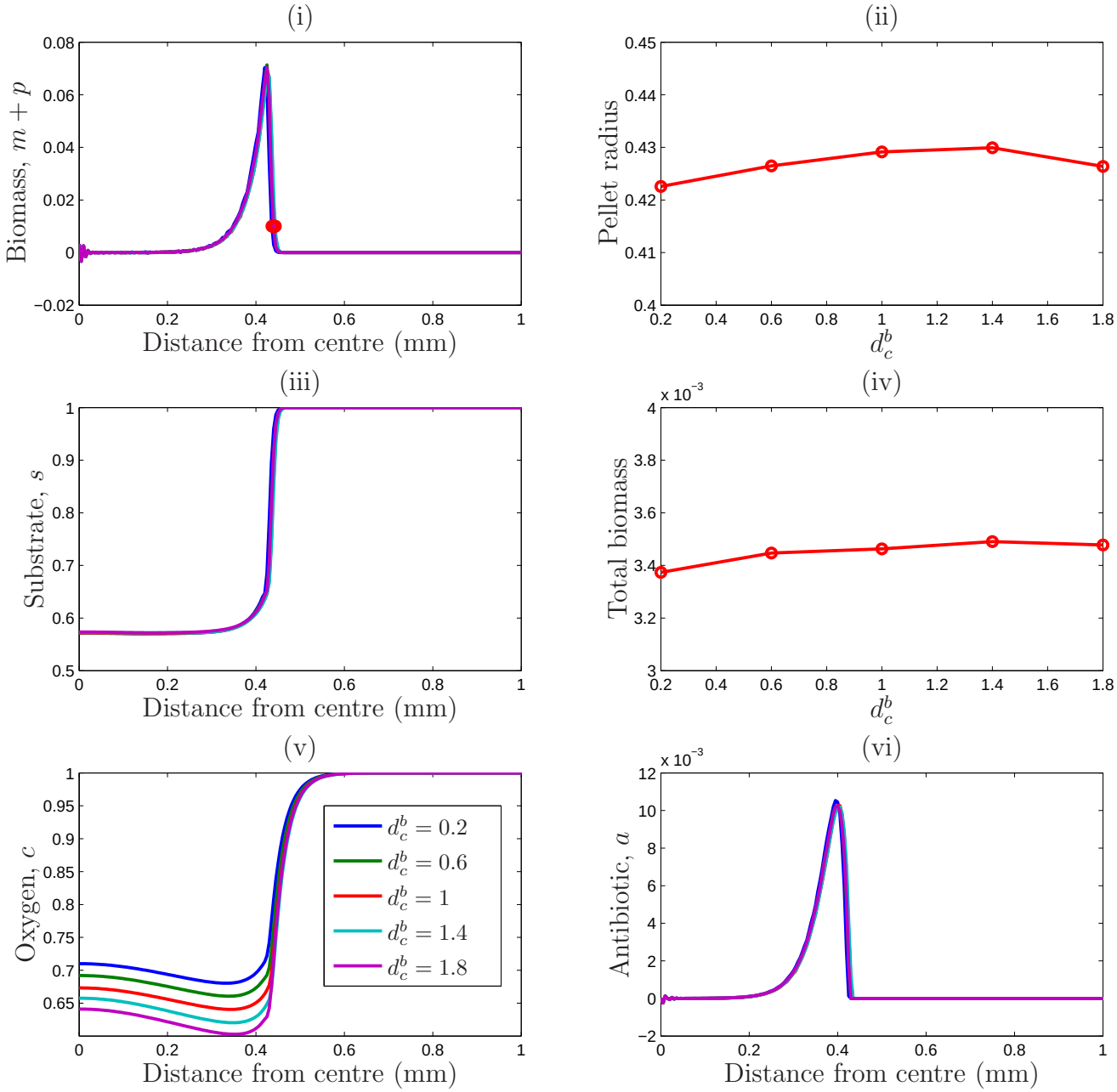

Figure 2.9: Shown in (i), (iii), (v) and (vi) are the final time solution profiles for biomass, substrate, oxygen and antibiotic, respectively, for varying values of d_c^b, constant rate of the cost of tips branching on oxygen. In (ii) we show the pellet radius and (iv) shows the total biomass (at the final time) at each value of d_c^b. The remaining parameters are as in Figure 2.4.

We have shown that by varying these parameters we can change the growth rate and antibiotic production of the *Streptomyces* pellet. As expected, increasing the branching rate b produces a larger, more dense pellet. When we increase the cost of tip flux on the substrate, d_s^p, the pellet does not decrease in size, but becomes less dense and hence produces less antibiotic. We observe an interesting result when varying γ, the parameter that represents hyphal growth due to tip extension. When increasing γ the pellet remains the same size with a decreasing density but the antibiotic production is increased. When increasing the background death rate of tips the pellet radii and density decreases, indicating that the tips are the driving force of pellet growth. The final parameter we examined was d_c^b, the cost of tip branching on oxygen. By increasing d_c^b we observe very little change in biomass density and overall pellet size, although it is clear that more oxygen is being consumed within the pellet.

2.4 Analytical Results of Radial Symmetric Growth

The purpose of this section is to find analytical solutions of the system (2.1)-(2.4) so that we can get insight into the growth dynamics of the *Streptomyces* pellet.

In an attempt to find analytical solutions and compare them to the numerical results of the system (2.1)-(2.4), we use the properties of the Heaviside function to separate the analytical solution into four different regions which are dependant on substrate and oxygen concentrations. Note that we now neglect the antibiotic equation, (2.5), since it is uncoupled from the system.

The four regions we consider correspond to:

1. $s(r,t) \simeq s_0 > \hat{s}$ and $c(r,t) \simeq c_0 > \hat{c}$, i.e. substrate and oxygen rich
2. $s(r,t) \simeq s_0 > \hat{s}$ and $0 < c(r,t) < \hat{c}$, i.e. substrate rich and oxygen deprived
3. $s(r,t) < \hat{s}$ and $c(r,t) > \hat{c}$, i.e. substrate deprived and oxygen rich
4. $s(r,t) < \hat{s}$ and $c(r,t) < \hat{c}$, i.e. substrate and oxygen deprived

Region 1: $s(r,t) \simeq s_0 > \hat{s}$ and $c(r,t) \simeq c_0 > \hat{c}$

In this scenario, we assume that the pellet is very small with the nutrients, substrate and oxygen, unlimiting to pellet growth. Using the assumption that substrate and oxygen is constant withing the pellet, i.e. $s(r,t) \simeq s_0 > \hat{s}$ and $c \simeq c_0 > \hat{c}(r,t)$, the system (2.1)-(2.4) reduces to

$$\begin{aligned} \frac{\partial p}{\partial t} &= -\frac{1}{r^2}\frac{\partial}{\partial r}\left(r^2 J_p\right) + \left(b - d_p^{back}\right) p, \\ \frac{\partial m}{\partial t} &= \gamma |J_p| - d_m^{back} m. \end{aligned}$$

Note that the flux of the tips is now described by $J_p = -D_p \dfrac{\partial p}{\partial r}$.

The tip equation is then

$$\frac{\partial p}{\partial t} = \frac{D_p}{r^2}\frac{\partial}{\partial r}\left(r^2 \frac{\partial p}{\partial r}\right) + (b - d_p^{back})p, \tag{2.8}$$

which is decoupled from the rest of the system and we can solve this using separation of variables. Specifically, we let $p(r,t) = T(t)R(r)$ to give the following:

$$T' - Tc = 0 \qquad \text{where } c \text{ is the separation constant,} \tag{2.9}$$

and

$$r^2 R'' + 2rR' + r^2 R\left(\frac{c-\lambda}{D_p}\right) = 0, \qquad \text{where} \qquad \lambda = d_p - b. \tag{2.10}$$

Equation (2.9) has the solution,

$$T(t) = A\exp(-ct), \tag{2.11}$$

where A is the constant of integration. Equation (2.10) is of the form of the spherical Bessel differential equation which has a solution of the form,

$$R(r) = \frac{BJ_{\frac{1}{2}}(kr)}{\sqrt{kr}} + \frac{CY_{\frac{1}{2}}(kr)}{\sqrt{kr}}, \quad \text{where} \quad k = \sqrt{\frac{c-\lambda}{D_p}}, \tag{2.12}$$

where B and C are constants, and $J_{\frac{1}{2}}(x)$ and $Y_{\frac{1}{2}}(x)$ are the half integer Bessel functions of the first and second kind, respectively:

$$J_{\frac{1}{2}}(x) = \sqrt{\frac{2}{\pi x}}\sin(x) \quad \text{and} \quad Y_{\frac{1}{2}}(x) = -\sqrt{\frac{2}{\pi x}}\cos(x).$$

Therefore,

$$R(r) = \frac{B'\sin(kr)}{kr} - \frac{C'\cos(kr)}{kr},$$

where B' and C' are constants. Since the solution for $p(r,t)$ at the origin is finite we know that C' must be zero, and using the zero flux boundary condition (at $r = L$) we obtain,

$$R(r) = \frac{B'\sin(kr)}{kr}, \tag{2.13}$$

subject to the transcendental equation $\tan(kL) - kL = 0$, which determines the separation constant c and corresponding eigenfunctions $R(r)$.

Hence the general analytical solution to equation (2.8) is given by

$$p(r,t) = E\sum_{k=1}^{\infty}\frac{\exp(-ct)\sin(kr)}{kr}, \tag{2.14}$$

where $E = AB'$ is a constant.

Note that although $\sin(kr)$ is periodic around zero we anticipate that the linear sum of the eigenfunctions (2.14) will approximate to give a positive function that matches $p(r,t)$.

We now consider what happens as oxygen becomes limiting, i.e. $c(r,t) < \hat{c}$.

Region 2: $s(r,t) \simeq s_0 > \hat{s}$ and $c(r,t) < \hat{c}$

Here, we assume that the pellet has unlimited substrate but is growing under anaerobic conditions, i.e. $c(r,t) < \hat{c}$. Using the assumption that $s(r,t) \simeq s_0 > \hat{s}$ and $0 < c(r,t) < \hat{c}$, the system (2.1)-(2.4) reduces to

$$\frac{\partial p}{\partial t} = -(d_p^{max} + d_p^{back})p, \tag{2.15}$$

$$\frac{\partial m}{\partial t} = -(d_m^{max} + d_m^{back})m, \tag{2.16}$$

$$\frac{\partial c}{\partial t} = D_c \frac{1}{r^2}\frac{\partial}{\partial r}\left(r^2 \frac{\partial c}{\partial r}\right) - d_c^b bp - c\left(d_c^{cp}p + d_c^{cm}m\right), \tag{2.17}$$

which leads to the following solutions for tips and hyphae, respectively,

$$p(r,t) = A\exp\Big(-t\left(d_p^{max} + d_p^{back}\right)\Big),$$
$$m(r,t) = B\exp\Big(-t\left(d_m^{max} + d_m^{back}\right)\Big),$$

where A and B are constants. Thus, in an anaerobic state we expect tips and hyphae to exponentially decline at an exponential rate given by the sum of the background and maximum death rates, i.e. $d_p^{max} + d_p^{back}$.

Region 3: $s(r,t) < \hat{s}$ and $c(r,t) > \hat{c}$

In this situation, the pellet is growing in glucose restricted media under aerobic conditions. This pellet is at an intermediate size with glucose deprivation occurring within the pellet core. Using the assumption that $0 < s(r,t) < \hat{s}$ and

$c(r,t) > \hat{c}$, the system (2.1)-(2.4) reduces to

$$\begin{aligned}
\frac{\partial p}{\partial t} &= -d_p^{back} p, \\
\frac{\partial m}{\partial t} &= -d_m^{back} m, \\
\frac{\partial s}{\partial t} &= D_s \frac{1}{r^2}\frac{\partial}{\partial r}\left(r^2 \frac{\partial s}{\partial r}\right) - s\left(d_s^{cp} p + d_s^{cm} m\right), \\
\frac{\partial c}{\partial t} &= D_c \frac{1}{r^2}\frac{\partial}{\partial r}\left(r^2 \frac{\partial c}{\partial r}\right) - c\left(d_c^{cp} p + d_c^{cm} m\right).
\end{aligned}$$

This reduced system decouples the tips, p, and hyphae, m, equations and can be solved easily with the solutions given by

$$p(r,t) = A \exp\left(-t d_p^{back}\right), \tag{2.18}$$

$$m(r,t) = B \exp\left(-t d_m^{back}\right), \tag{2.19}$$

where A and B are constants.

The expressions (2.18)-(2.19) are of the exponential decay of tips and hyphae under the conditions of limited glucose but plentiful oxygen. Figure 2.10 shows the decay of tips and hyphae at a fixed point in the domain. We see that the solutions are exponentially decreasing. The fit between the analytical and numerical solutions are very good for early times corresponding to glucose restricted, aerobic media conditions.

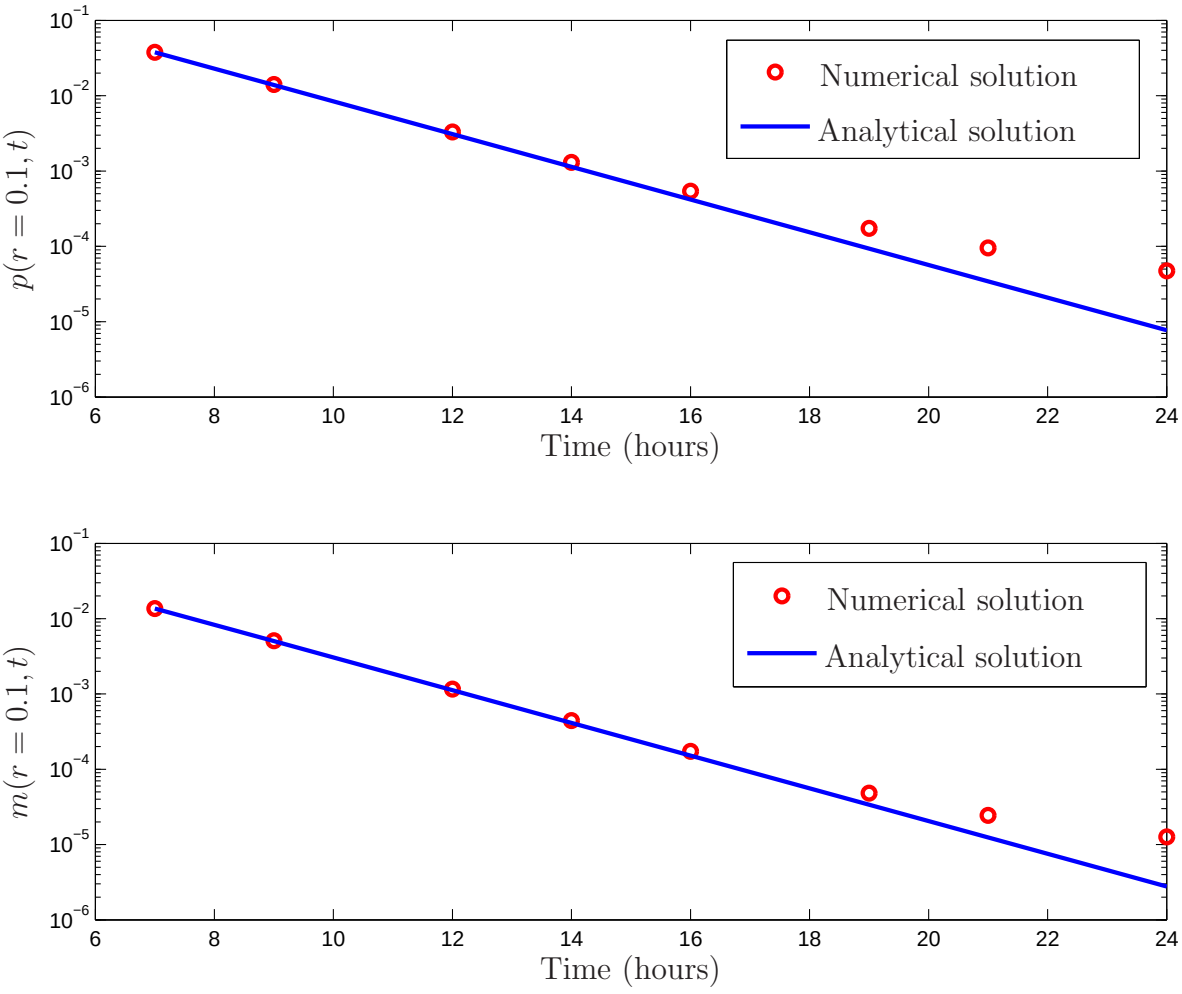

Figure 2.10: Log plot of the analytical solution of the tip equation (top) and hyphae equation (bottom), for fixed space versus time, matched to the corresponding numerical solution, with $d_p^{back} = 0.5$. We choose A and B to best fit the numerical data, the values are $A = B = 0.45$ and in the region where $0 < s < \hat{s}$ and $c > \hat{c}$.

Region 4: $s(r,t) < \hat{s}$ and $c(r,t) < \hat{c}$

Here, we are assuming that the pellet grows in glucose and oxygen deprived conditions. The pellet is fully developed with glucose and oxygen deprivation at the core. Using the assumption that $0 < s(r,t) < \hat{s}$ and $0 < c(r,t) < \hat{c}$, the system (2.1)-(2.4) reduces to

$$\begin{aligned}\frac{\partial s}{\partial t} &= D_s \frac{1}{r^2}\frac{\partial}{\partial r}\left(r^2 \frac{\partial s}{\partial r}\right) - s\left(d_s^{cp} p + d_s^{cm} m\right), \\ \frac{\partial c}{\partial t} &= D_c \frac{1}{r^2}\frac{\partial}{\partial r}\left(r^2 \frac{\partial c}{\partial r}\right) - c\left(d_c^{cp} p + d_c^{cm} m\right),\end{aligned}$$

with the equations for tips and hyphae given by (2.15) and (2.16), respectively. We solve these cases, and in particular we wish to have the solution for the tips, $p(r,t)$, as it is the tips that determine the growth rate and overall size of the pellet. We have

$$\frac{\partial p}{\partial t} = -p\left(d_p^{max} + d_p^{back}\right), \qquad \frac{\partial m}{\partial t} = -m\left(d_m^{max} + d_m^{back}\right),$$

the solutions of which are given by

$$\begin{aligned}p(r,t) &= A\exp\left(-t(d_p^{max} + d_p^{back})\right), \\ m(r,t) &= B\exp\left(-t(d_m^{max} + d_m^{back})\right),\end{aligned}$$

where A and B are constants. Again, we see that in glucose and oxygen depleted areas, tips and hyphae decay exponentially with the exponent $d_p^{max} + d_p^{back}$.

2.5 Travelling Wave Analysis

When looking at the numerical results in Figure 2.3 we notice that there is a wave-like advancement through the domain, hence in this section we carry out a travelling wave analysis. For simplicity we explore a reduced system of

partial differential equations derived from the *S. coelicolor* model, (2.1)-(2.5). A travelling wave is described as a wave of constant shape propagating with constant speed. First, we compare the reduced system (derived from (2.1)-(2.4), at this stage we neglect the antibiotic as it is decoupled from the system) to the *S. coelicolor* growth model. We then carry out the analytical travelling wave analysis on the reduced system.

The system (2.1)-(2.4) is solved using NAG routine D03PHF in Fortran, with an initial seeding of biomas (hyphae and tips) at the origin in an oxygen and substrate enriched media with boundary conditions described by (2.7). For the corresponding solution profiles see Figure 2.3.

From numerical simulations such as that shown in Figure 2.3 (and the parameter sensitivity analysis) we see that substrate is the key limiting growth factor. Typically, we observe that $c > \hat{c}$. Hence, setting $c > \hat{c}$ and assuming that the consumption rate of substrate by hyphae, d_s^{cm}, is small we can reduce the model to two partial differential equations by decoupling the equations for hyphae and oxygen, (2.2) and (2.4) respectively, to give

$$\frac{\partial p}{\partial t} = -\frac{\partial}{\partial x}\big(J_p\big) + bpH(s-\hat{s}) - d_p^{back}p, \tag{2.20}$$

$$\frac{\partial s}{\partial t} = D_s\frac{\partial^2 s}{\partial x^2} - d_s^p|J_p|\gamma - d_s^b bpH(s-\hat{s}) - d_s^{cp}sp, \tag{2.21}$$

subject to the initial conditions

$$p(x,0) = p_0(x) \quad \text{and} \quad s(x,0) = 1,$$

with the following boundary conditions

$$J_p = 0, \quad \frac{\partial s}{\partial x} = 0, \quad \text{at} \quad x = 0,$$

$$J_p = 0, \quad s = 1, \quad \text{at} \quad x = 1.$$

We should note that by changing the coordinate system we do not resolve the

numerical problem of oscillations close to the origin in the tip solution, this is examined later in Chapter 3.

To facilitate the travelling wave analysis, we regularise the Heaviside functions replacing them with a continuous Hill function to overcome difficulties with the Heaviside discontinuity. We write

$$H(s-\hat{s}) \simeq f(s) = \frac{s^\alpha}{\hat{s}^\alpha + s^\alpha} \qquad \text{with} \qquad \alpha > 1. \tag{2.22}$$

The system (2.20)-(2.21) is solved again using NAG routine D03PHF in Fortran. We compare these numerical results to the full system results when we let $d_s^{cm} = 0$ (decoupling the hyphae, oxygen and antibiotic equations). The comparison is shown in Figure 2.11. The comparison between the full *S. coelicolor* growth model and the reduced model is very good when α is large, hence we now carry out the travelling wave analysis using this reduced system.

We find the spatially homogeneous steady states by setting $\dfrac{\partial}{\partial t} = 0$ and $\dfrac{\partial}{\partial x} = 0$ resulting in

$$\begin{aligned} 0 &= bpf(s) - d_p^{back} p, \\ 0 &= d_s^b bpf(s) + d_s^{cp} sp. \end{aligned}$$

The solutions of which are, $p = 0$ and $s = s^*$, $p \neq 0$ and $s = \left(\dfrac{d_p^{back} \hat{s}^\alpha}{b - d_p^{back}} \right)^{\frac{1}{\alpha}}$. Additionally, we can deduce that the state ahead of the advancing wave is $(p, s) = (0, 1)$.

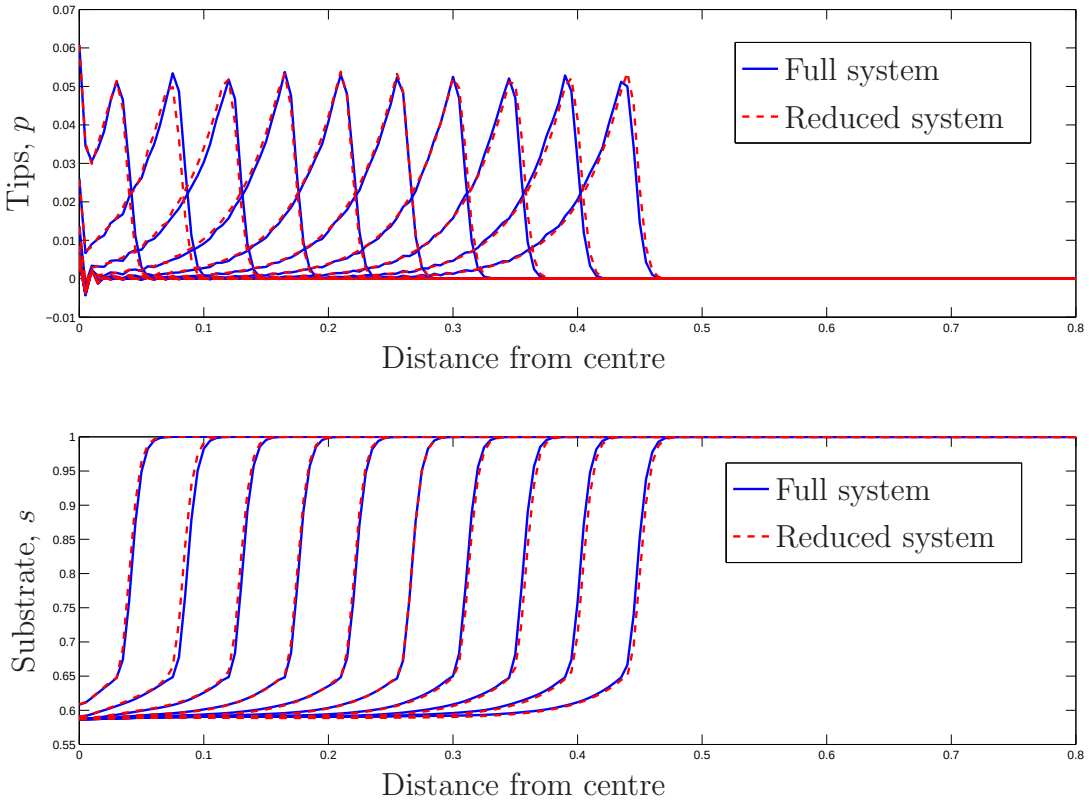

Figure 2.11: Shows the comparison of of the full *S. coelicolor* growth model (when $d_s^{cm} = 0$), (2.1)-(2.4), to the reduced model, (2.20)-(2.21), when using $f(s)$ instead of $H(s - \hat{s})$, see equation (2.22), we take $\alpha = 300$.

In the usual way, we seek travelling wave solutions of the form $p(x,t) = P(z)$, where $z = x - vt$ and v is the constant wave speed. Substituting the travelling wave variable into the system (2.20)-(2.21), we get

$$P'' + \frac{v}{D_p f(S)} P' - \frac{\chi}{D_p}\Big(PS'\Big)' + \frac{f'(S)}{f(S)}\Big(P' + \frac{\chi PS'}{D_p}\Big) + \frac{bf(S) - d_p^{back}}{D_p f(S)} P = 0,$$

$$S'' + \Big(vS' - d_s^p\big| - D_p P' + \chi PS'\big|\gamma - d_s^b bPf(S) - d_s^{cp} PS\Big)\frac{1}{D_s} = 0,$$

with

$$f(S) = \frac{S^\alpha}{\hat{S}^\alpha + S^\alpha} \quad \text{and} \quad f'(S) = \frac{S^{\alpha-1}\hat{S}^\alpha \alpha}{(\hat{S}^\alpha + S^\alpha)^2} S',$$

where the prime denotes the derivative with respect to z. The boundary conditions in terms of z are given below:

$$\begin{aligned} &P(\pm\infty) = 0, \qquad S(-\infty) = s^*, \qquad S(+\infty) = 1, \\ &P'(\pm\infty) = 0 \qquad \text{and} \qquad S'(\pm\infty) = 0. \end{aligned}$$

By letting $Q = S'$ and $W = P'$ we get a system of four first-order ordinary differential equations, given by

$$P' = W, \tag{2.23}$$

$$S' = Q, \tag{2.24}$$

$$\begin{aligned} W' = &-\frac{v}{D_p f(S)} W + \frac{\chi}{D_p}\Big(WQ + PQ'\Big) - \frac{f'(S)}{f(S)}\Big(W + \frac{\chi PQ}{D_p}\Big) \\ &-\frac{bf(S) - d_p^{back}}{D_p f(S)} P, \end{aligned} \tag{2.25}$$

$$Q' = -\Big(vQ - d_s^p\big| - D_p W + \chi PQ\big|\gamma - d_s^b bPf(S) - d_s^{cp} PS\Big)\frac{1}{D_s}, \tag{2.26}$$

with

$$f'(S) = \frac{S^{\alpha-1}\hat{S}^\alpha \alpha}{(\hat{S}^\alpha + S^\alpha)^2} Q.$$

We linearised about the steady state $(P, S, W, Q) = (0, 1, 0, 0)$ to get a system of the form,

$$\frac{dU}{dz} = AU, \qquad \text{where} \qquad U = (P, S, W, Q)^T$$

and A is the Jacobian matrix, with the eigenvalues given by $\det(A - \lambda I) = 0$. Solving this characteristic equation, we obtain

$$\lambda_1 = 0, \qquad \lambda_2 = -\frac{v}{D_s} < 0,$$

and

$$\lambda_{3,4} = -\frac{1}{2D_p}\Big(v(\hat{s}^\alpha + 1) \pm \sqrt{(v + v\hat{s}^\alpha)^2 - 4D_p(d_p^{back} - b)(\hat{s}^\alpha + 1)}\Big).$$

For $(0, 1, 0, 0)$ to be a stable node we require,

$$v \geq v_{min} = \frac{2\sqrt{(\hat{s}^{\alpha}+1)(b-d_p^{back})D_p}}{(\hat{s}^{\alpha}+1)} = 0.0079.$$

This places a constraint on the branching rate and decay rate of the tips, we require $b \geq d_p^{back}$ for the wavespeed to be real and biologically relevant. We notice that

$$\lim_{\alpha\to\infty} v_{min} = 2\sqrt{(b-d_p^{back})D_p} = 0.0079,$$

v_{min} is therefore an increasing function of the branching rate and the diffusion rate of the hyphal tips (given by b and D_p, respectively), and a decreasing function of the decay rate of the tips, d_p^{back}.

We expect the travelling wave solutions to travel at some speed greater than or equal to the minimum wavespeed, v_{min}. We can calculate the corresponding numerical wavespeed using simulation data produced when solving the system (2.20)-(2.21) and it is given by $v_n = 0.0105$ which is indeed greater than the predicted minimum wavespeed.

In Figure 2.12 we observe the effect on the minimum and numerical wavespeeds when we vary key parameters, b, d_p^{back} and D_p which represent the branching rate, background decay rate, and random movement of the hyphal tips, respectively. In (i) we vary the branching rate, b, as we have previously seen in Figure 2.5 increasing b results in a larger pellet. In this case increasing b increases both the numerical and minimum wavespeeds, although there is an overall greater increase in numerical speed. In (ii) we vary the background death rate of the tips, d_p^{back}, and we find that by increasing this the analytical and numerical wavespeeds decrease, although it is more pronounced in the numerically obtained values. In (iii) we vary the random movement coefficient of the tips, D_p. We would expect an increase in wavespeed when increasing the random movement of tips and we do see an increase in both analytical and numerical wavespeeds when we increase

D_p, but unlike (i) and (ii) the greatest increase occurs in the analytical speed. In all cases the analytical wavespeed (v_{min}) is always below the numerical speed (v_n) as we would expect.

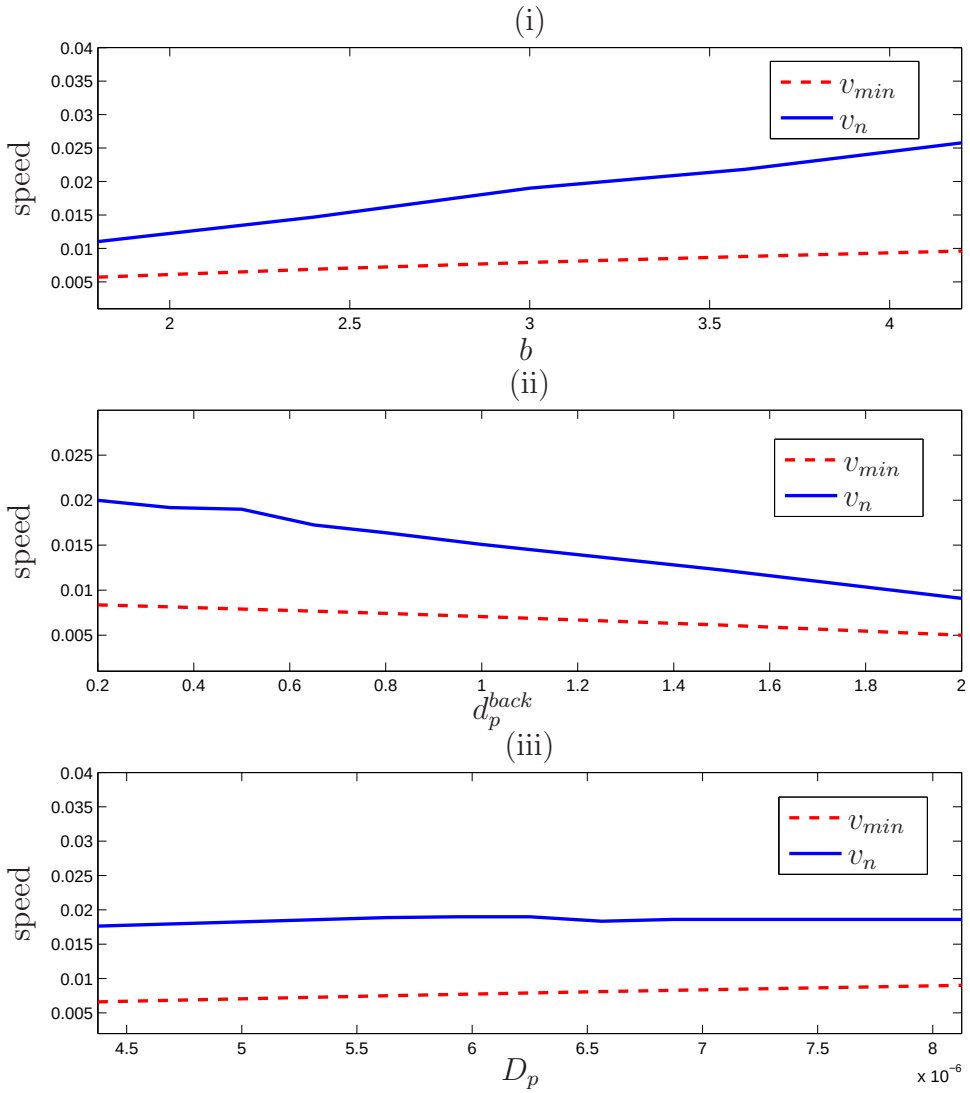

Figure 2.12: Shows the minimum wavespeed, v_{min}, and numerical wavespeed, v_n, when we vary three key parameters that occur in the expression for the minimum wavespeed. The parameters we vary are (i) b, (ii) d_p^{back} and (iii) D_p. The remaining parameters are as in Figure 2.4.

2.6 Discussion

In this chapter we present a tip and trail model that describes the growth of a *Streptomyces coelicolor* pellet and the associated antibiotic production. The *Streptomyces* family are of great importance for their production of secondary metabolites, such as anti-cancer drugs and antibiotics, and by modelling the biological system we get key information that can enhance growth and optimize metabolite production.

The model we present is a typical tip and trail model, hence hyphal extension arises from the movement of the tip cells which move randomly and towards a high concentration of glucose. A network of filaments is produced through tip branching, these process are all energetic therefore the substrate (glucose) is consumed for branching, movement and also the general maintenance of the cells. These process are not anaerobic hence we have included usage of the oxygen as well. We do neglect the aerial hyphae which is a precursor to metabolite production, but it has been shown that in submerged cultures of *S. coelicolor* they do not form.

To parameterize the model we carried out a biological experiment and produced a growth curve, this could not give all the parameters required so we looked to literature for the remaining values. Due to the sensitivity of the system the model parameters had to be fine tuned, with the unknown parameters estimated to fit the observed experimental data. With uncertainty surrounding some of the the values, we carried out a parameter sensitivity analysis which gave insight into which parameters affected the pellet growth the most. Interestingly, we found that when increasing γ, the hyphal extension proportionality parameter, there was an increase in antibiotic production but an overall decrease in pellet density.

To find analytical solutions to the model we used the properties of the Heaviside function to examine four cases which are determined by the concentrations of substrate and oxygen. The case where the pellet is very small with very high concentrations of substrate and oxygen we were able to find an analytical solution for the tips for a very early time frame, this results in a good match. We also found another analytical solution for the tips when the pellet is of intermediate size, where the mycelia have utilised the substrate in the centre of the pellet causing glucose deprivation but the pellet is still small enough that the oxygen concentration does not affect cell viability. We found this to be an exponentially decaying solution.

The typical dynamics of the system shows a wave-like propagation into the domain, see Figure 2.3, hence we conducted a travelling wave analysis. We found an expression for the minimum wavespeed, v_{min}. The numerical wavespeed, v_n, was calculated and found to be indeed always greater than the minimum. We can see from the v_{min} expression that the wave speed is an increasing function of branching rate and tip diffusion and a decreasing function of tip decay rate, which is to be expected.

Chapter 3

Finite Element Solutions of the Reduced *Streptomyces* Model

3.1 Introduction

As discussed in Chapter 2 we continue to model the growth of *Streptomyces coelicolor*, a multicellular bacterium very important in the world's production of antibiotics, [52], and anticancer drugs [18]. The bacterium are found naturally in soil, but when grown for antibiotic production *S. coelicolor* are grown within flasks of liquid media which contain all the nutrients required for growth. As a result of growing the bacterium in this way, spherical pellets of biomass form, which is not seen in soil colonies.

In Chapter 2 we described a radially symmetric reduced growth model (2.20)-(2.21), which we solved using the NAG routine D03PHF. The typical numerical solutions were not ideal with oscillations present, namely in the solution for the tips, $p(r,t)$, see Figure 2.3. As an attempt to reduce these oscillations we now

turn to the use of the Finite-Element Method (FEM).

FEM involves using a "weak" formulation to approximate the PDE, where the second derivatives are converted into first derivatives. Finite elements are most commonly used when solving problems on complex domains due to the advantageous nature of the spatial discretization. In 2-D the domain is commonly discretized into triangles which can be refined in areas of interest.

In this chapter we first attempt to solve a simplified problem in 1-D, that contains the main aspects of the reduced *S. coelicolor* growth model, including its nonlinearity. This problem will play the role of a test for our numerical method (using a quasi-Newton algorithm).

Using the numerical method formulated, with the inclusion of adaptive timestepping, we solve the reduced *S. coelicolor* growth model and present the results.

3.2 A Simplified Problem

As a starting point and to test the numerical strategy we begin by solving the following simplified system, with coupled variables $a(x,t)$ and $m(x,t)$:

$$\frac{\partial a}{\partial t} + \xi(m) D_2 m \frac{\partial a}{\partial x} - D_1 \frac{\partial^2 a}{\partial x^2} = 0, \tag{3.1}$$

$$\frac{\partial m}{\partial t} + (1+a)m + \gamma D_1 \left| \frac{\partial a}{\partial x} + m \right| = 0, \tag{3.2}$$

where

$$\xi(m) = H(m - m^*) H(\hat{m} - m), \tag{3.3}$$

with $m^*, \hat{m} > 0$, and H is the Heaviside function defined by,

$$H(m) = \begin{cases} 0 & \text{if} \quad m < 0, \\ 1 & \text{if} \quad m \geq 0. \end{cases}$$

The system is solved in $[0, L] \times (0, T)$ with initial conditions given by,

$$\begin{aligned} a(x,0) &= \begin{cases} 1 & \text{if} \quad x \leq 0.1, \\ 0 & \text{elsewhere}, \end{cases} \\ m(x,0) &= 1, \end{aligned}$$

and boundary conditions,

$$\frac{\partial a}{\partial x} = 0 \quad \text{at} \quad x = 0, x = L. \tag{3.4}$$

We choose the parameter values such that transport in the problem will dominate over diffusion, and are given by

$$\begin{aligned} D_1 &= 0.01, \qquad D_2 = 3, \qquad \gamma = 0.1, \\ \hat{m} &= 0.7, \qquad m^* = 0.3. \end{aligned}$$

This system includes all the interesting aspects of the reduced *Streptomyces* model, such as the inclusion of a Heaviside function that controls the convection of $a(x,t)$ depending on the value of $m(x,t)$. The system has been developed to include the non-linear aspects seen in the reduced *Streptomyces* model, with the inclusion of the absolute values which are required in the reduced growth model (2.20)-(2.21) to account for the direction of the tip flux.

3.2.1 Time Discretization

We use as time discretization a fully implicit θ-scheme. Let us divide $(0, T)$ into M time steps, with $\delta_t = \dfrac{T}{M}$, and let us denote $a^n = a(x, t^n)$ where $t^n = n\delta_t$. Then, the method reads

$$\mathbf{U}^{n+1} + \delta_t \theta A \mathbf{U}^{n+1} + \delta_t (1-\theta) A \mathbf{U}^n - \mathbf{U}^n = 0, \tag{3.5}$$

where $\mathbf{U} = (a, m)^T$, and

$$A\mathbf{U} = \begin{pmatrix} -D_1 \dfrac{\partial^2 a}{\partial x^2} + \xi(m) D_2 m \dfrac{\partial a}{\partial x} \\ (1+a)m + \gamma D_1 \left| \dfrac{\partial a}{\partial x} + m \right| \end{pmatrix}.$$

Note that the initial conditions are given by

$$\begin{aligned} a^0 &= \begin{cases} 1 & \text{if} \quad x \leq 0.1, \\ 0 & \text{elsewhere,} \end{cases} \\ m^0 &= 1. \end{aligned}$$

When $\theta = 1$ the discretization is called implicit Euler (1st order), and Crank-Nicolson when $\theta = \dfrac{1}{2}$ (2nd order [77]). In component form, (3.5) reads as follows

$$\begin{aligned} & a^{n+1} + \delta_t \theta \xi(m^{n+1}) D_2 m^{n+1} \frac{\partial a^{n+1}}{\partial x} - \delta_t \theta D_1 \frac{\partial^2 a^{n+1}}{\partial x^2} \\ & + \delta_t (1-\theta) \xi(m^n) D_2 m^n \frac{\partial a^n}{\partial x} - \delta_t (1-\theta) D_1 \frac{\partial^2 a^n}{\partial x^2} - a^n = 0, \end{aligned} \tag{3.6}$$

$$\begin{aligned} & m^{n+1} + \delta_t \theta (1 + a^{n+1}) m^{n+1} + \delta_t \theta \gamma D_1 \left| \frac{\partial a^{n+1}}{\partial x} + m^{n+1} \right| \\ & + \delta_t (1-\theta)(1+a^n) m^n + \delta_t (1-\theta) \gamma D_1 \left| \frac{\partial a^n}{\partial x} + m^n \right| - m^n = 0, \end{aligned} \tag{3.7}$$

where a^n, a^{n+1} satisfy the boundary conditions (3.4).

The choice of an implicit scheme is due to stability reasons. Explicit schemes were also explored but did not produce satisfactory results due to the lack of stability.

3.2.2 Space Discretization using FEM

We now turn to the space discretization of the system (3.6)-(3.7). Let

$$L^2(I) := \{q : I \to \mathbb{R} : \int_I |q|^2 < \infty\},$$

and

$$V := \{q \in L^2(I) : q' \in L^2(I)\} \subseteq C^0(I).$$

Then, we multiply (3.6) by a test function q, where $q \in V$, integrate (3.6) by parts, and apply the boundary condition given by (3.4), which results in the following weak form

$$\begin{aligned}
&\int_0^L a^{n+1}q + \delta_t\theta D_2 \int_0^L \xi(m^{n+1})m^{n+1}\frac{\partial a^{n+1}}{\partial x}q \\
&+ \delta_t\theta D_1 \int_0^L \frac{\partial a^{n+1}}{\partial x}\frac{\partial q}{\partial x} + \delta_t(1-\theta)D_2 \int_0^L \xi(m^n)m^n\frac{\partial a^n}{\partial x}q \\
&+ \delta_t(1-\theta)D_1 \int_0^L \frac{\partial a^n}{\partial x}\frac{\partial q}{\partial x} - \int_0^L a^n q = 0.
\end{aligned} \tag{3.8}$$

Analogously, we multiply (3.7) by a test function v (where $v \in L^2(I)$) and integrate resulting in the weak form given by

$$\begin{aligned}
&\int_0^L m^{n+1}v + \delta_t\theta \int_0^L (1+a^{n+1})m^{n+1}v + \delta_t\theta\gamma D_1 \int_0^L \left|\frac{\partial a^{n+1}}{\partial x} + m^{n+1}\right| v \\
&+ \delta_t(1-\theta)\int_0^L (1+a^n)m^n v + \delta_t(1-\theta)\gamma D_1 \int_0^L \left|\frac{\partial a^n}{\partial x} + m^n\right| v \\
&- \int_0^L m^n v = 0.
\end{aligned} \tag{3.9}$$

To solve this system (3.8)-(3.9) numerically we discretize $[0, L]$ in N intervals, introducing the nodes

$$x_0 = 0, \quad x_{i+1} = x_i + h, \quad \text{for} \quad i = 0, ..., N-1,$$

where $h = \dfrac{L}{N}$.

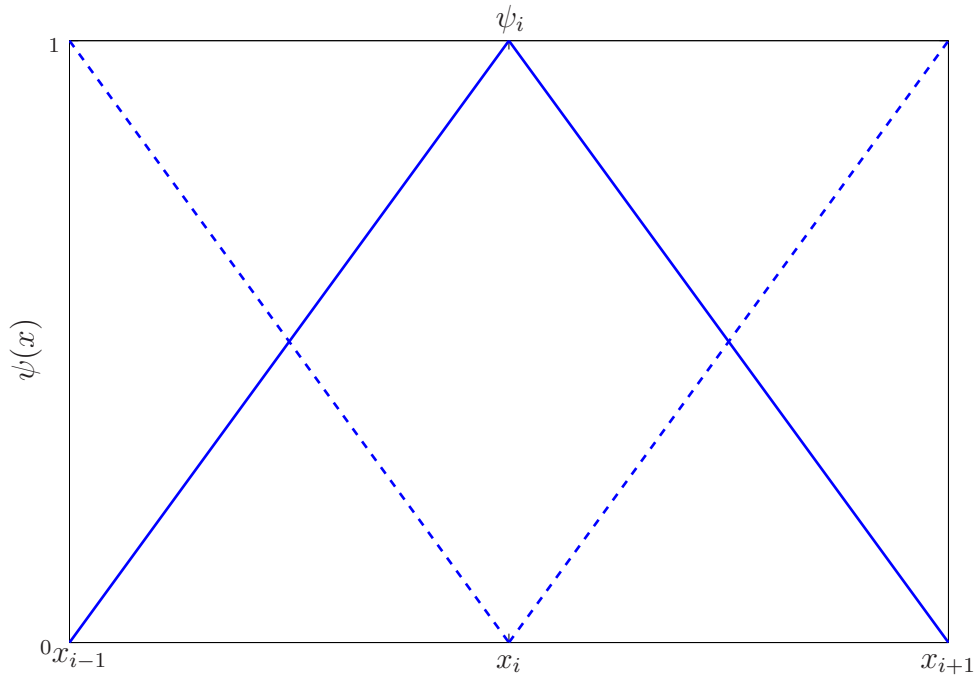

Figure 3.1: Spatial discretization is carried out using the basis functions which satisfy $\psi_i(x_j) = \delta_{ij}$.

Let $\{\psi_0, \psi_1, ..., \psi_N\}$ be the basis for q, v which is given by the typical "hat" function (see Figure 3.1 for a graphical representation)

$$\psi_i(x) = \begin{cases} \dfrac{x - x_{i-1}}{x_i - x_{i-1}} & \text{if} \quad x \in [x_{i-1}, x_i], \\ \dfrac{x_{i+1} - x}{x_{i+1} - x_i} & \text{if} \quad x \in [x_i, x_{i+1}], \\ 0 & \text{elsewhere}, \end{cases}$$

for every $i = 1, .., N-1$, with

$$\psi_0(x) = \frac{x_1 - x}{x_1 - x_0} \quad \text{and} \quad \psi_N(x) = \frac{x - x_{N-1}}{x_N - x_{N-1}},$$

at the boundaries. These functions satisfy $\psi_i(x_j) = \delta_{ij}$. We then let

$$q(x) = \sum_{i=0}^{N} q_i \psi_i(x), \qquad v(x) = \sum_{l=0}^{N} v_l \psi_l(x),$$

and we approximate $a^{n+1} \simeq a_h^{n+1}$ and $m^{n+1} \simeq m_h^{n+1}$, where

$$a_h^{n+1} = \sum_{j=0}^{N} a_j^{n+1}\psi_j \quad \text{and} \quad m_h^{n+1} = \sum_{k=0}^{N} m_k^{n+1}\psi_k.$$

Equations (3.8)-(3.9) are then discretized as follows:

$$\begin{aligned}
&\sum_{j=0}^{N} a_j^{n+1} \int_0^L \psi_j\psi_i + \delta_t\theta D_2 \sum_{j=0}^{N}\sum_{k=0}^{N} a_j^{n+1}m_k^{n+1} \int_0^L \xi(m^{n+1})\psi_k \frac{\partial\psi_j}{\partial x}\psi_i \\
&+ \delta_t\theta D_1 \sum_{j=0}^{N} a_j^{n+1} \int_0^L \frac{\partial\psi_j}{\partial x}\frac{\partial\psi_i}{\partial x} + \delta_t(1-\theta)D_1 \sum_{j=0}^{N} a_j^{n} \int_0^L \frac{\partial\psi_j}{\partial x}\frac{\partial\psi_i}{\partial x} \\
&+ \delta_t(1-\theta)D_2 \sum_{j=0}^{N}\sum_{k=0}^{N} a_j^{n}m_k^{n} \int_0^L \xi(m^{n})\psi_k \frac{\partial\psi_j}{\partial x}\psi_i \\
&- \sum_{j=0}^{N} a_j^{n} \int_0^L \psi_j\psi_i = 0,
\end{aligned} \tag{3.10}$$

$$\begin{aligned}
&(1+\delta_t\theta) \sum_{j=0}^{N} m_j^{n+1} \int_0^L \psi_j\psi_l \\
&+ \delta_t\theta \sum_{j=0}^{N}\sum_{k=0}^{N} a_j^{n+1}m_k^{n+1} \int_0^L \psi_j\psi_k\psi_l + \delta_t\theta\gamma D_1 \int_0^L \left|\frac{\partial a^{n+1}}{\partial x} + m^{n+1}\right| \psi_l \\
&+ \delta_t(1-\theta) \sum_{j=0}^{N}\sum_{k=0}^{N} a_j^{n}m_k^{n} \int_0^L \psi_j\psi_k\psi_l + \delta_t(1-\theta)\gamma D_1 \int_0^L \left|\frac{\partial a^{n}}{\partial x} + m^{n}\right| \psi_l \\
&- (1-\delta_t(1-\theta)) \sum_{j=0}^{N} m_j^{n} \int_0^L \psi_j\psi_l = 0,
\end{aligned} \tag{3.11}$$

for every $i, l = 0, ..., N$. We write this nonlinear system in the following compact form,

$$\mathbf{G}(\mathbf{a}^{n+1}, \mathbf{m}^{n+1}) = \mathbf{0}. \tag{3.12}$$

The components of $\mathbf{G}$ are denoted by G_i. Every integral appearing in the definition of G_i is approximated using Simpson's Rule.

3.2.3 A Quasi-Newton Algorithm

To compute the Jacobian for this system analytically may be very difficult and time consuming. We therefore describe a quasi-Newton algorithm which approximates it using a finite difference method, see [51] for a full description. To initialize the algorithm we let $\mathbf{V} = \mathbf{U^0}$, and

$$\sigma_i = \max(|V_i|, 1)\eta_i,$$

with η_i given by

$$\eta_i = \begin{cases} 1 & \text{if} \quad V_i = 0, \\ \dfrac{V_i}{|V_i|} & \text{otherwise.} \end{cases}$$

We make the approximation

$$D\mathbf{G}(\mathbf{V}) \simeq \mathbf{J}, \quad \text{where} \quad \mathbf{J} = J_{ij}, \tag{3.13}$$

where each J_{ij} is defined as follows

$$J_{ij}(\mathbf{V}) = \begin{cases} \dfrac{G_i(\epsilon e_i) - G_i(\mathbf{V})}{\epsilon}, & \text{if} \quad V_i = 0, \\ \dfrac{G_i(\mathbf{V} + \epsilon e_i \sigma_j) - G_i(\mathbf{V})}{\epsilon \sigma_j} & \text{otherwise,} \end{cases}$$

where $\epsilon = 10^{-4}$, and e_i is the unit vector in the ith direction. Note that the Jacobian is a sparse matrix and as a time saving process we did not compute all entries. If the code returned an entry of the Jacobian whose absolute value is less than 1×10^{-15} we set that entry to zero. Then, the quasi-Newton algorithm is initialized by: $\mathbf{V}_0 = \mathbf{U}^n$, and we iterate

$$\mathbf{V}_{k+1} = \mathbf{V}_k - \mathbf{J}^{-1}\mathbf{G}(\mathbf{V}_k), \tag{3.14}$$

where k is the iteration, for $k = 0, 1, ...$ until convergence, i.e. when the error is satisfies $\left|\left|\mathbf{J}^{-1}\mathbf{G}(\mathbf{V}_k)\right|\right| \leq 10^{-5}$. At convergence we let,

$$\mathbf{U}^{n+1} = \mathbf{V}_{k+1}.$$

3.2.4 Numerical Results

Using the algorithm described in the previous section, we solve the simplified problem (3.1)-(3.2), obtaining typical solutions depicted by Figure 3.2.

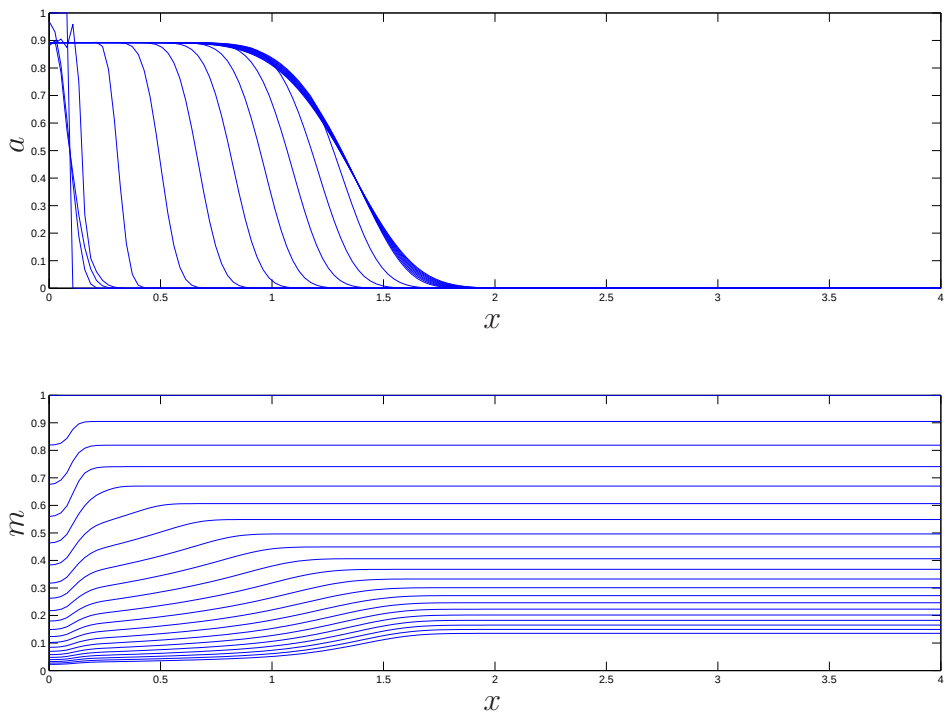

Figure 3.2: The simplified system (3.12) was solved in $[0, 4]$ with $h = 0.0267$ and $\delta_t = 0.0005$. The θ-scheme used is implicit Euler ($\theta = 1$), each line represents a time $t = 0, 0.1, 0.2, ..., 2$.

We observe the general dynamics of the system in Figure 3.2, $a(x,t)$ travels across the domain with time, until $m(x,t) < m^*$, which switches $\xi(m)$ from 1 to zero resulting in the transport of $a(x,t)$ stopping and the dynamics change to diffusion-driven. For a closer inspection of the solutions we look to Figure 3.3. In this Figure we split the solution into four main sections, (i) when $\xi(m) = 0$, (ii) and (iii) when $\xi(m) = 1$ for part or all of the domain, and finally (iv) when $\xi(m) = 0$.

In the first column of Figure 3.3, $\xi(m) = 0$ resulting in the diffusive behaviour of $a(x,t)$, with increasing time $m(x,t)$ decreases at different rates depending on $a(x,t)$. In the second column, we see that close to the origin $m(x,t) \leq \hat{m}$ resulting in $\xi(m) = 1$. This initiates growth and transport of $a(x,t)$. In the third column, transport dominates the behaviour of $a(x,t)$ with $m^* \leq m(x,t) \leq \hat{m}$. In the final column, $m(x,t) \leq m^*$ resulting in $\xi(m) = 0$ which switches off transport of $a(x,t)$ and so the behaviour is again driven by diffusion.

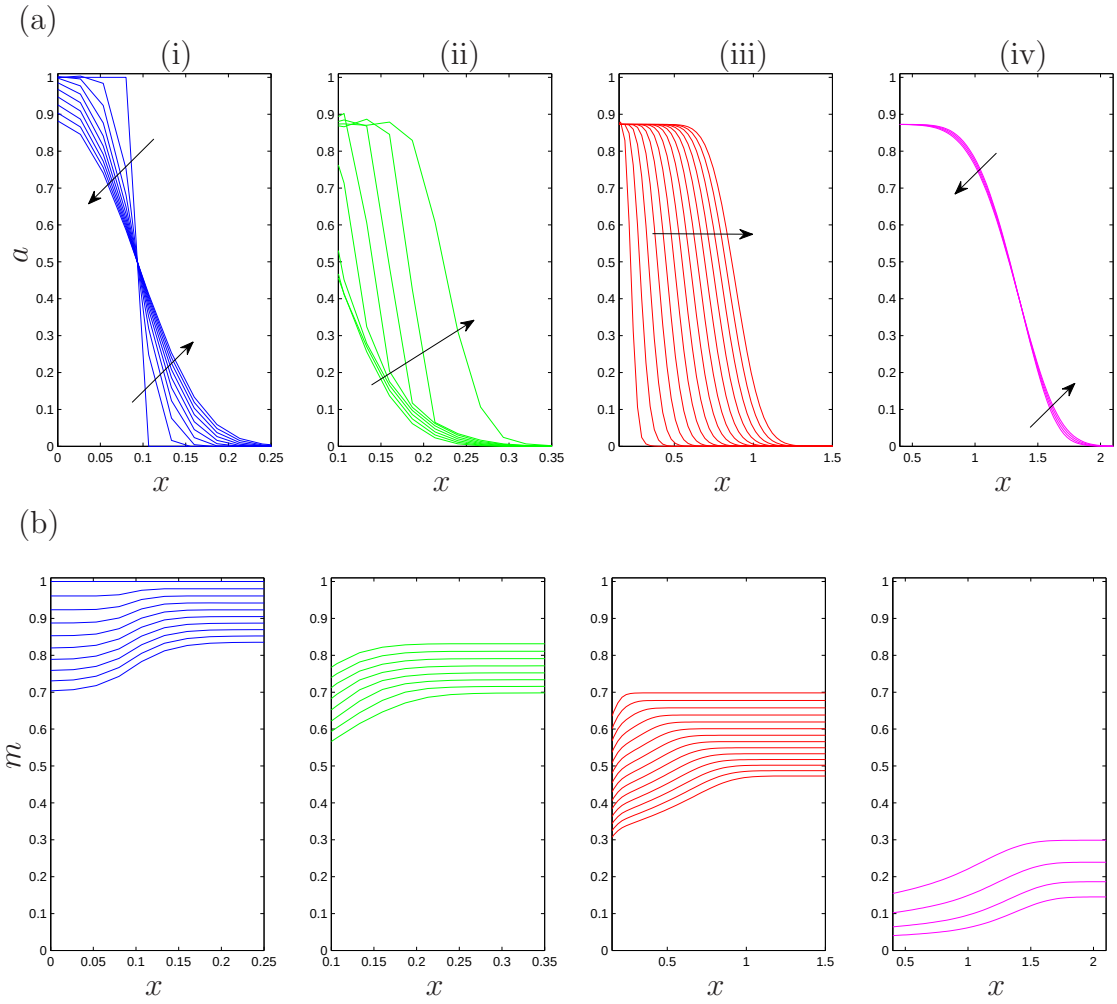

Figure 3.3: The system (3.12) was solved in $[0, 4]$ with $N = 251$ and $\delta_t = 0.005$, with $\theta = 1$. (a) The solution for $a(x, t)$, (i) $m > \hat{m}$, hence diffusion-driven dynamics. (ii) The solution starts to propagate as $m \leq \hat{m}$, and transport can be clearly seen in (iii) as $m^* < m < \hat{m}$. (iv) $m < m^*$ hence diffusion-driven movement. The arrows indicate the direction of movement with increasing time. (b) The solution for $m(x, t)$ at different times. With $\hat{m} = 0.7, m^* = 0.3$.

3.2.5 A Critical Evaluation of θ

In this section we perform an evaluation of the time discretization in our problem by varying θ. Figures 3.4-3.5 show the solution of (3.12) at time $t = 0.5$ and $t = 2$, respectively, for varying values of θ, ranging between $\frac{1}{2} \leq \theta \leq 1$. The fully implicit θ-scheme is first order accurate when $\theta = 1$, second order accurate when $\theta = \frac{1}{2}$, see [77].

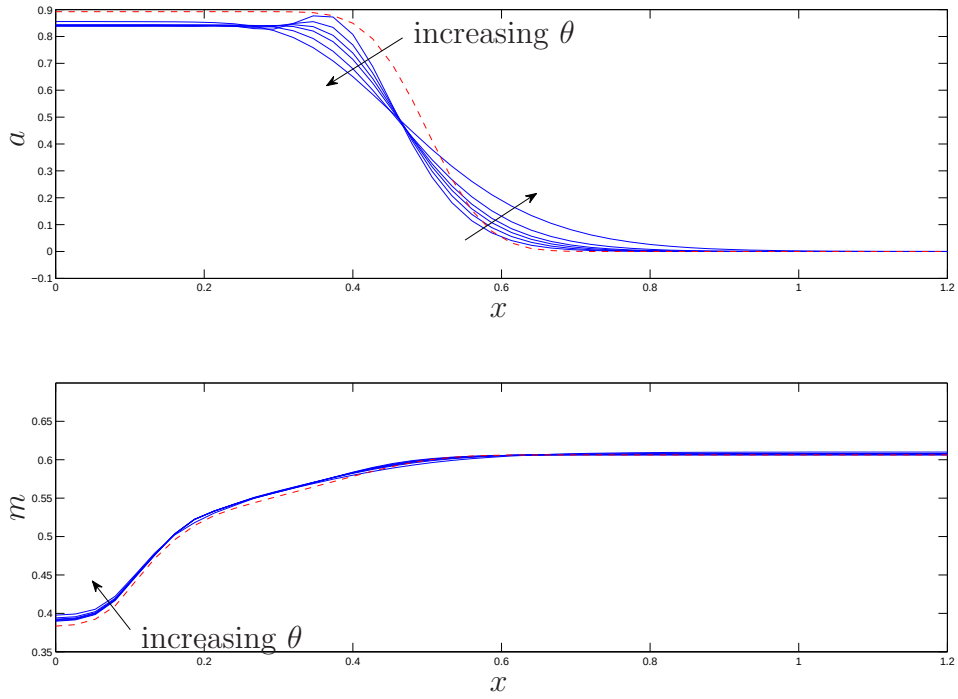

Figure 3.4: The simplified system (3.12) was solved in $[0, 4]$ with $h = 0.0267$ and $\delta_t = 0.025$. The solid lines represent the test system solved with varying values of θ. The arrow represents the increasing value of θ. The dashed red line is the system solved with $\delta_t = 0.0005$ and $\theta = 1$ as a reference solution. The solution presented is at $t = 0.5$.

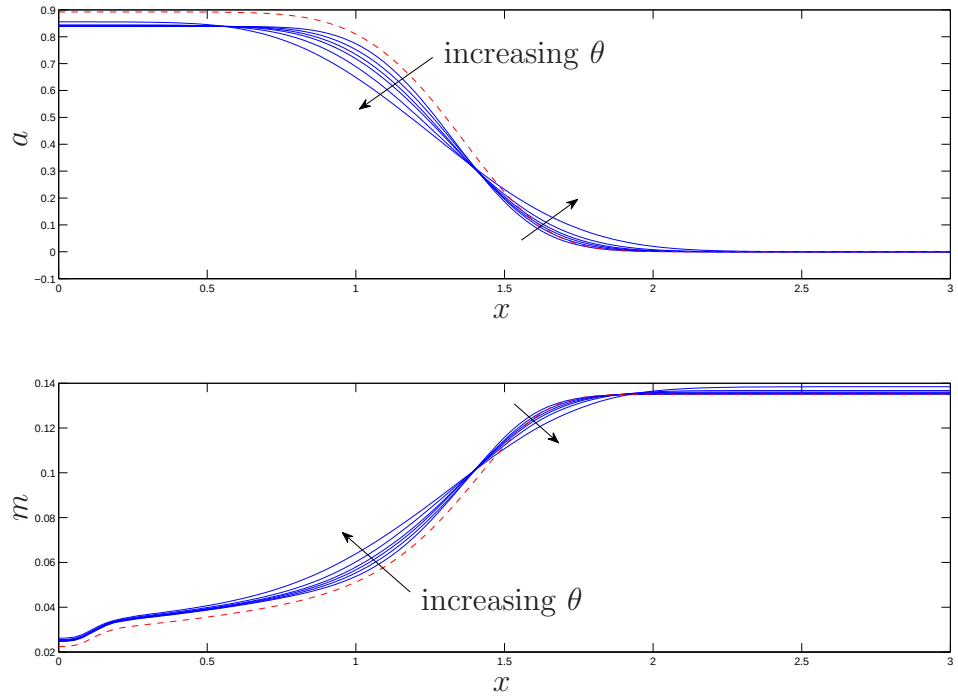

Figure 3.5: The simplified system (3.12) was solved on $[0, 4]$ with $h = 0.0267$ and $\delta_t = 0.025$. The solid lines represent the test system solved with varying values of θ. The arrow represents the increasing value of θ. The dashed red line is the system solved with $\delta_t = 0.0005$ and $\theta = 1$ as a reference solution. The solution presented is at $t = 2$.

To "test" the θ-scheme, we solved the system (3.12) with varying values of θ, each with the same grid refinement h and time step δ_t. Clearly, from Figures 3.4-3.5 there is a diffusive effect with different θ values. We know that when using implicit Euler the solutions look stable, Crank-Nicolson is on the edge of the stability region and so the solutions occasionally look less stable (see [77]) which can be seen in Figure 3.4 when $\theta = \frac{1}{2}$.

We now explore varying the time-step when solving the system (3.12) using

Crank-Nicolson method. In Figure 3.6 we decrease the time step to gauge accuracy. We see that the solution for $\delta_t = 0.005$ is not really different from the one using $\delta_t = 0.0025$; the solutions appear to converge when $\delta_t \leq 0.005$. We use this information later when directly compairing Crank-Nicolson with implicit Euler.

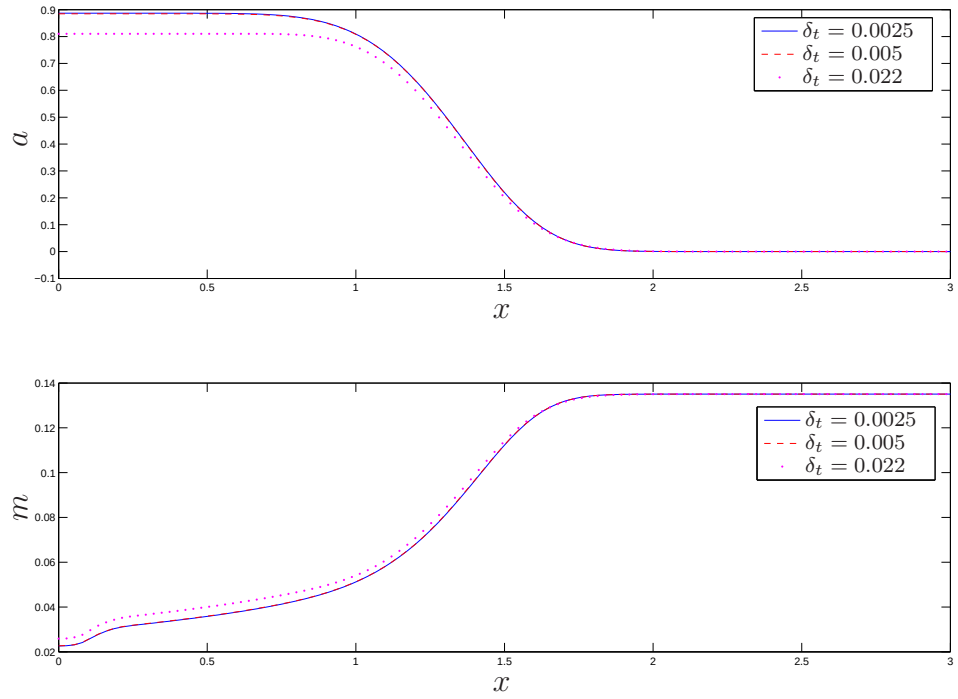

Figure 3.6: The simplified system (3.12) was solved in $[0, 4]$ with $h = 0.0267$ and $\theta = 0.5$. To gauge accuracy of the time discretization δ_t was varied, the chosen values are $\delta_t = 0.022, 0.005, 0.0025$.

As a check, we solve the system (3.12) with implicit Euler and varying time-steps. We have already used a reference solution, when $\theta = 1$, in Figures 3.4-3.5 where $\delta_t = 0.0005$. In Figure 3.7 we decrease the time-step further to check this reference line is acceptable. We notice that there is no distinct difference between

the solutions when solved with $\delta_t = 0.00033$ or $\delta_t = 0.0005$; the solutions appear to converge when $\delta_t \leq 0.0005$. If $\delta_t = 0.0005$ is used, we have an accurate solution for this problem.

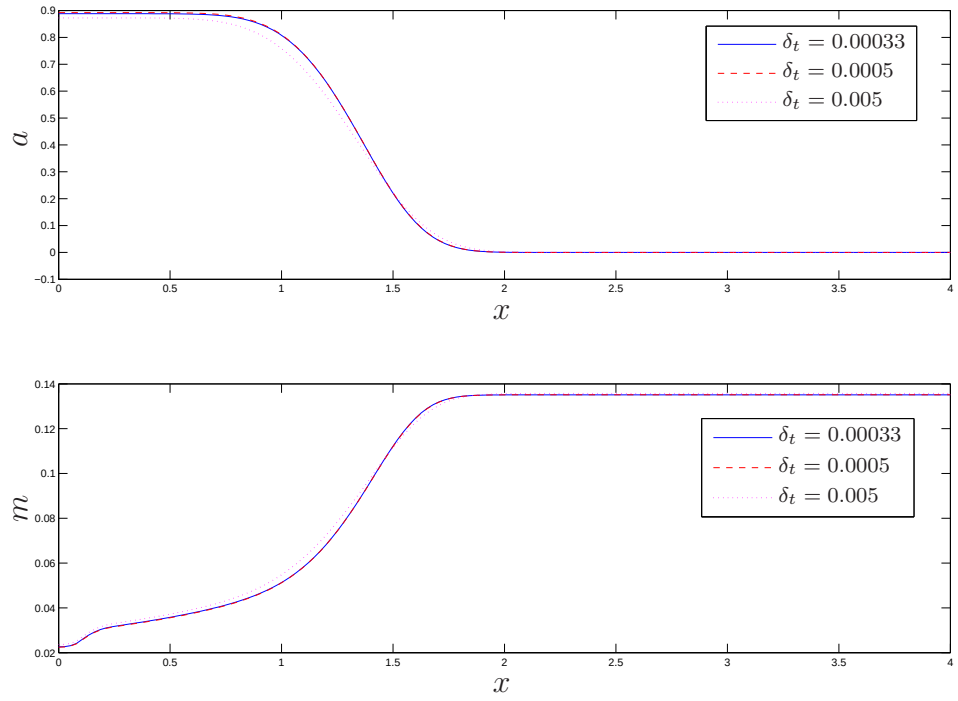

Figure 3.7: The simplified system (3.12) was solved in $[0, 4]$ with $h = 0.0267$ and $\theta = 1$. To gauge accuracy of the time discretization δ_t was varied, the chosen values are $\delta_t = 0.005, 0.0005, 0.00033$.

We now perform a direct comparison between implicit Euler and Crank-Nicolson. When solving with Crank-Nicolson we use $\delta_t = 0.005$, as we have seen in Figure 3.6 that it is accurate, with implicit Euler we use the reference solution, when solved with $\delta_t = 0.0005$. In Figure 3.8 there is no noticeable difference between the two solutions. We can say that we have accurate solutions for both Crank-Nicolson and implicit Euler.

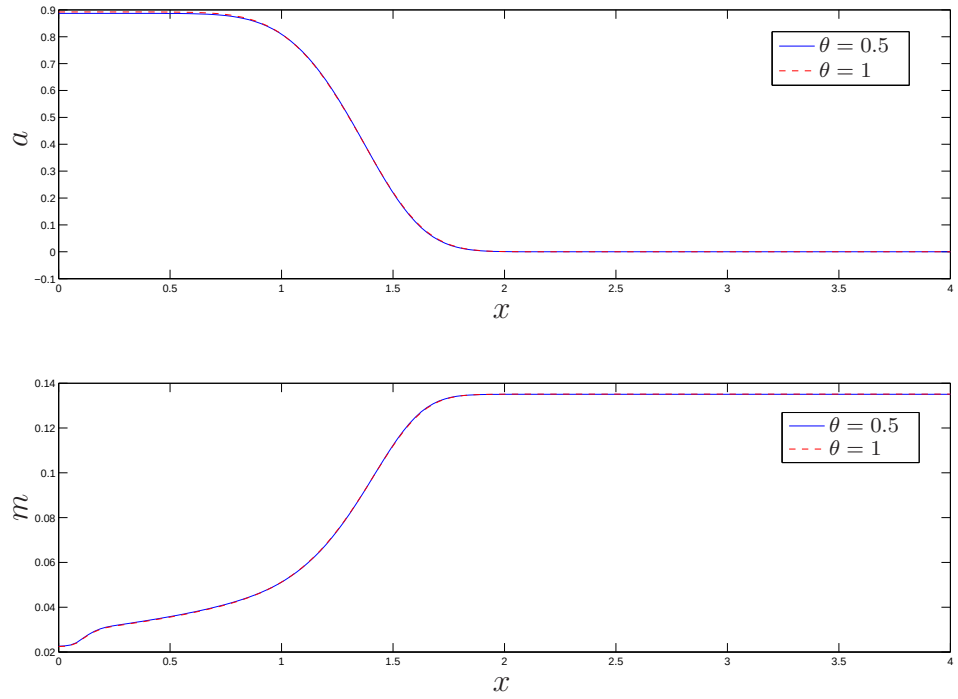

Figure 3.8: For a comparison between implicit Euler and Crank-Nicolson the simplified system (3.12) was solved in $[0, 4]$ with $h = 0.0267$, when solved with implicit Euler and Crank-Nicolson, we set $\delta_t = 0.0005$ and $\delta_t = 0.005$ respectively.

In conclusion, with the testing of θ and δ_t, when $h = 0.0267$, we choose Crank-Nicolson due to the method being second order with the acceptable stability and the fact that we observe less diffusivity. We also examined the computational cost of running implicit Euler and Crank-Nicolson, due to the very small time step required when solving with implicit Euler is costly, Crank-Nicolson is cheaper with less timesteps required for the same accuracy. We must include that care must be taken when deciding a time step due to the Heaviside function, if the time step is too large information from the decay of $m(x, t)$ is not

fully represented by the Heaviside function, altering the solution greatly.

With the results obtained from this simplified system we are now confident in our full numerical scheme to extend it to solve the reduced *Streptomyces* model.

3.3 Reduced *Streptomyces* Model

In this section we will extend the numerical scheme used in the previous section to solve the (rescaled) reduced model for *Streptomyces* growth we described in Chapter 2. The *Streptomyces* growth model is given by,

$$\frac{\partial p}{\partial t} + \frac{\partial}{\partial x}\left(J_p\right) - bE(s)p + d_p^{back}p = 0, \tag{3.15}$$

$$\frac{\partial s}{\partial t} - D_s\frac{\partial^2 s}{\partial x^2} + d_s^b bE(s)p + d_s^p\gamma\left|J_p\right| + d_s^{cp}sp = 0. \tag{3.16}$$

Recall, from Chapter 2, that the tip density is represented by $p(x,t)$, substrate concentration by $s(x,t)$ and the tip flux is given by,

$$J_p = \left(-D_p\frac{\partial p}{\partial x} + \chi p\frac{\partial s}{\partial x}\right)E(s),$$

where

$$E(s) = H(s - \hat{s}). \tag{3.17}$$

Recall that H is the Heaviside function defined by,

$$H(s) = \begin{cases} 0 & \text{if} \quad s < 0, \\ 1 & \text{if} \quad s \geq 0. \end{cases}$$

The system is solved in the domain $[0, L]$ with zero flux boundary conditions given by

$$J_p = 0, \quad \frac{\partial s}{\partial x} = 0 \quad \text{at } x = 0, \text{ and } x = L, \tag{3.18}$$

and the initial conditions

$$\begin{aligned} p(x,0) &= \frac{p_0}{2}\Big(1-\tanh\big((x-\lambda_1)\varepsilon^{-1}\big)\Big), \\ s(x,0) &= 1, \end{aligned}$$

where $\varepsilon = 10^{-3}$, $\lambda_1 = 1.25\times10^{-6}$ and $p_0 = 0.1$. The system (3.15)-(3.16) is solved with the parameter values (see Chapter 2 for details of parameter rescalings)

$$\begin{array}{llllll} D_p = 6.25\times10^{-6}, & \chi = 1.25\times10^{-4}, & D_s = 6.25\times10^{-5}, \\ \hat{s} = 2/3, & d_p^{back} = 0.5, & b = 3, \\ d_s^{cp} = 1, & \gamma = 400, & d_s^{b} = 1, \\ d_s^{p} = 10. \end{array}$$

In the model we have a Heaviside function which acts like a switch. This controls the regions in which the tips can grow and move depending on the concentration of the substrate (the medium in which the *Streptomyces* pellet is contained and has all the nutrients required for growth). When the substrate $s(x,t) < \hat{s}$ the tips cannot branch or migrate.

Sometimes it is appropriate to approximate functions, often to simplify the expressions as in the case of Ward and King 1997, [95], who approximated a Michaelis-Menten type function (Hill function) with a Heaviside function. We examine this further in the appendix, where we introduce regularized functions to avoid the discontinuities that arise in the Heaviside function.

We adopt the same technique of time and space discretization as in the simplified model, recall we discretize time with a θ-scheme and for spatial discretization we use first-order piecewise linear finite elements (see Section 3.1.1 and Section 3.1.2 for full a description). The fully discretized nonlinear system reads

$$\mathbf{F}(\mathbf{p}^{n+1}, \mathbf{s}^{n+1}) = \mathbf{0}. \tag{3.19}$$

We approximate $p^{n+1} \simeq p_h^{n+1}$ and $s^{n+1} \simeq s_h^{n+1}$, where

$$p_h^{n+1} = \sum_{j=0}^{N} p_j^{n+1}\psi_j, \quad \text{and} \quad s_h^{n+1} = \sum_{j=0}^{N} s_j^{n+1}\psi_j,$$

and write (3.19) in component form as follows

$$\begin{aligned}
&\sum_{j=0}^{N} p_j^{n+1} \int_0^L \psi_j\psi_i + D_p\delta_t\theta \sum_{j=0}^{N} p_j^{n+1} \int_0^L \frac{\partial\psi_j}{\partial x}\frac{\partial\psi_i}{\partial x}E(s^{n+1}) \\
&- \chi\delta_t\theta \sum_{j=0}^{N}\sum_{k=0}^{N} p_j^{n+1}s_k^{n+1} \int_0^L \psi_j \frac{\partial\psi_k}{\partial x}\frac{\partial\psi_i}{\partial x}E(s^{n+1}) - b\delta_t\theta \sum_{j=0}^{N} p_j^{n+1} \int_0^L \psi_j\psi_i E(s^{n+1}) \\
&+ d_p^{back}\delta_t\theta \sum_{j=0}^{N} p_j^{n+1} \int_0^L \psi_j\psi_i + D_p\delta_t(1-\theta) \sum_{j=0}^{N} p_j^{n} \int_0^L \frac{\partial\psi_j}{\partial x}\frac{\partial\psi_i}{\partial x}E(s^{n}) \\
&- \chi\delta_t(1-\theta) \sum_{j=0}^{N}\sum_{k=0}^{N} p_j^{n}s_k^{n} \int_0^L \psi_j \frac{\partial\psi_k}{\partial x}\frac{\partial\psi_i}{\partial x}E(s^{n}) - b\delta_t(1-\theta) \sum_{j=0}^{N} p_j^{n} \int_0^L \psi_j\psi_i E(s^{n}) \\
&+ d_p^{back}\delta_t(1-\theta) \sum_{j=0}^{N} p_j^{n} \int_0^L \psi_j\psi_i - \sum_{j=0}^{N} p_j^{n} \int_0^L \psi_j\psi_i = 0,
\end{aligned} \tag{3.20}$$

$$\begin{aligned}
&\sum_{j=0}^{N} s_j^{n+1} \int_0^L \psi_j\psi_l + D_s\delta_t\theta \sum_{j=0}^{N} s_j^{n+1} \int_0^L \frac{\partial\psi_j}{\partial x}\frac{\partial\psi_l}{\partial x} \\
&+ d_s^b b\delta_t\theta \sum_{j=0}^{N} p_j^{n+1} \int_0^L E(s^{n+1})\psi_j\psi_l + d_s^p\gamma \int_0^L \left|J_p^{n+1}\right|\psi_l \\
&+ d_s^{cp}\delta_t\theta \sum_{j=0}^{N}\sum_{k=0}^{N} s_j^{n+1}p_k^{n+1} \int_0^L \psi_j\psi_k\psi_l + D_s\delta_t(1-\theta) \sum_{j=0}^{N} s_j^{n} \int_0^L \frac{\partial\psi_j}{\partial x}\frac{\partial\psi_l}{\partial x} \\
&+ d_s^b b\delta_t(1-\theta) \sum_{j=0}^{N} p_j^{n} \int_0^L E(s^{n})\psi_j\psi_l + d_s^p\gamma \int_0^L \left|J_p^{n}\right|\psi_l \\
&+ d_s^{cp}\delta_t(1-\theta) \sum_{j=0}^{N}\sum_{k=0}^{N} s_j^{n}p_k^{n} \int_0^L \psi_j\psi_k\psi_l - \sum_{j=0}^{N} s_j^{n} \int_0^L \psi_j\psi_l = 0,
\end{aligned} \tag{3.21}$$

for all $i, l = 0, ..., N$. To evaluate the integrals we use Simpson's rule, which is exact for polynomials degree ≤ 3 and appropriate for all the integrals presented.

3.3.1 Assessment of the FEM Method

In this section we present numerical results for the nonlinear system $\mathbf{F}(\mathbf{U}) = \mathbf{0}$, (3.19). We use the algorithm described in Section 3.2.3 to solve the nonlinear system (3.19), to optimize the code we introduced an adaptive time step. The implementation is as follows:

1. At convergence, if the iteration, j, of the quasi-Newton scheme is ≤ 10, then $\mathbf{U}^{n+1} = \mathbf{V}_{j+1}$ and if

   - $j \leq 2$, let $\delta_t^n = 2\delta_t$,
   - $j > 2$, let $\delta_t^n = \dfrac{\delta_t}{2}$.

   In both cases an upper bound $\delta_t^n \leq \delta_t^{ini}$ is placed on δ_t^n, where δ_t^n is the time step that will be used in the next iteration and δ_t^{ini} is the initial time step used at initialization of the algorithm.

2. If after the 10th iteration the quasi-Newton scheme has not converged, we re-start the loop with $\delta_t = \dfrac{\delta_t}{4}$.

Using this adaptive time stepping allows the code to reduce δ_t considerably when it is required, increasing it when it's appropriate and making sure the time step doesn't get bigger than δ_t^{ini} to retain accuracy. We recall that the upper bound δ_t^{ini} was needed to avoid losing important features of the solution.

As concluded in Section 3.2.5, we discretize time with Crank-Nicolson (i.e. when $\theta = \dfrac{1}{2}$) as it was shown to be optimal for a similar type of problem. Here we take in initial look at convergence of solutions when refining the mesh. We solve the system $\mathbf{F}(\mathbf{U}) = \mathbf{0}$ on four different mesh sizes; $h = 10^{-3}, 5 \times 10^{-4}, 2.5 \times 10^{-4}, 1.25 \times 10^{-4}$, solved with the same initial timestep $\delta_t^{ini} = 0.005$. The results are shown in Figure 3.9.

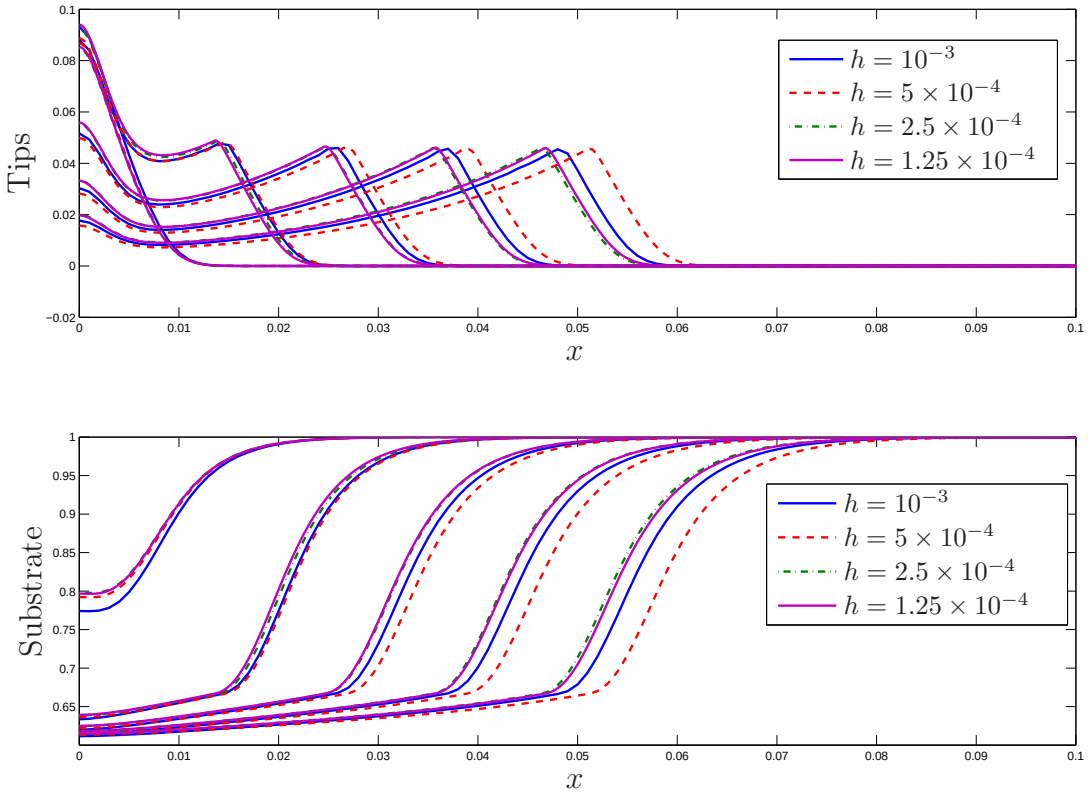

Figure 3.9: The system (2.20)-(2.21) was solved using finite elements. The system was solved with $h = 10^{-3}, 5 \times 10^{-4}, 2.5 \times 10^{-4}, 1.25 \times 10^{-4}$, $\delta_t^{ini} = 0.005$ and the solutions are presented at time, $t = 1, 2, ..., 5$.

We can see from Figure 3.9 that as the mesh is refined the numerical solutions appear to converge.

We now show the numerical solutions when solved for a longer time and to reduce the computational expense we set $h = 10^{-3}$. The solutions are shown in Figure 3.10.

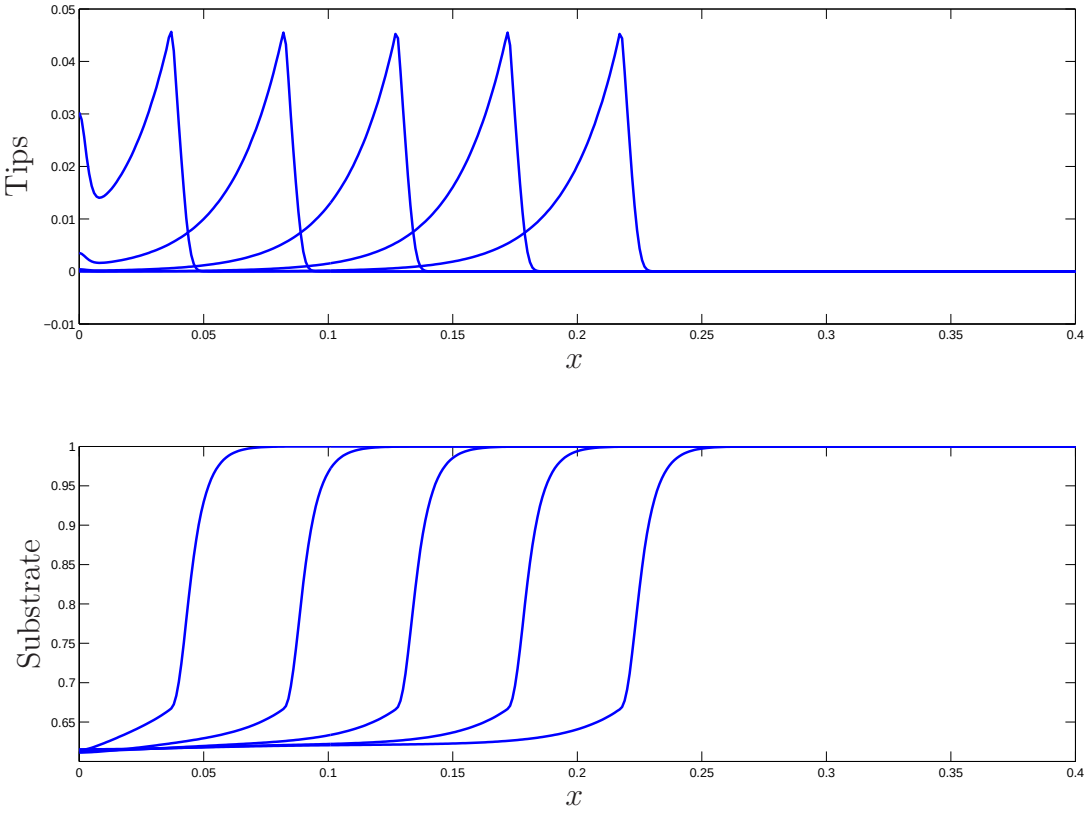

Figure 3.10: Finite element solution solved on $[0, 0.4]$ with 401 grid points ($h = 0.001$) and initial $\delta_t = 0.005$. The solution is presented at time $t = 4, 8, ..., 20$.

The tip equation (3.15) is governed by the tip flux, tip branching and tip decay, both flux and branching are controlled by a Heaviside switch which is dependent on the concentration of substrate. The tips diffuse randomly and actively migrate towards a high concentration of substrate, this can be seen in the solution. As the tips consume the substrate they make the substrate gradient region move which encourages active migration and branching of the tips, creating a wave that travels across the domain. Behind the wave there is decay of the tips, modelled by the term $d_p^{back} p$ in (3.15). If $d_p^{back} = 0$ we would have similar solutions to

our simplified system, (3.1)-(3.2) where there is no decay behind the wavefront.

In the biological pellet, the highest concentration of tips will be found at the edge of the pellet, the results represent this. We also notice that the solutions are non-oscillatory, a problem which arose when solving the system using NAG routine D03PHF in Chapter 2.

3.4 Discussion

In this chapter we developed a finite element numerical scheme for solving the reduced *Streptomyces* model by introducing a simplified problem as an initial starting point which was then extended to the reduced *Streptomyces* model framework.

When looking at the simplified problem we examined the θ-scheme. Due to the diffusivity brought to the system when using implicit Euler (i.e. when $\theta = 1$) we decided to use the less diffusive Crank-Nicolson (when $\theta = \frac{1}{2}$), which resulted in being able to use a larger time step and obtain the same accuracy. Having carried out this study we decided use Crank-Nicolson as the time discretization when solving the reduced *Streptomyces* model.

We used the quasi-Newton algorithm developed for the simplified problem to solve the reduced *Streptomyces* model. We carried out a study to test mesh convergence, which we observe at early time. Due to the refined mesh being computationally expensive we could only run the simulation over a short time-frame.

The aim of this chapter was to produce non-oscillatory solutions when solving

the reduced *Streptomyces* model, as in Chapter 2 oscillations were present when solving with NAG. We hypothesize that it is the finite difference discretization of this problem that is the cause of the observed oscillations. We previously ruled out the choice of coordinate system as the cause due to the oscillations being present when solving with Cartesian coordinates in NAG. We have reached our objective, we have non-oscillatory solutions which are essentially non-negative.

3.A Appendix

In this appendix we present some interesting exploratory results. We look at the numerical solutions when changing the substrate diffusion coefficient. By lowering the diffusion gradient of the substrate we effectively introduce a scenario where the liquid medium is of a different composition which may have an effect on the biomass growth and the resulting antibiotic production. We assume that because we see convergence of numerical solutions in Figure 3.9 that the finite element code is working correctly. Therefore we can assume that the following numerical results will also converge if the mesh was to be refined. Figure 3.11 shows the finite element solution with $D_s = 6.25 \times 10^{-6}$. For a comparison with the solution for $D_s = 6.25 \times 10^{-5}$ see Figure 3.12.

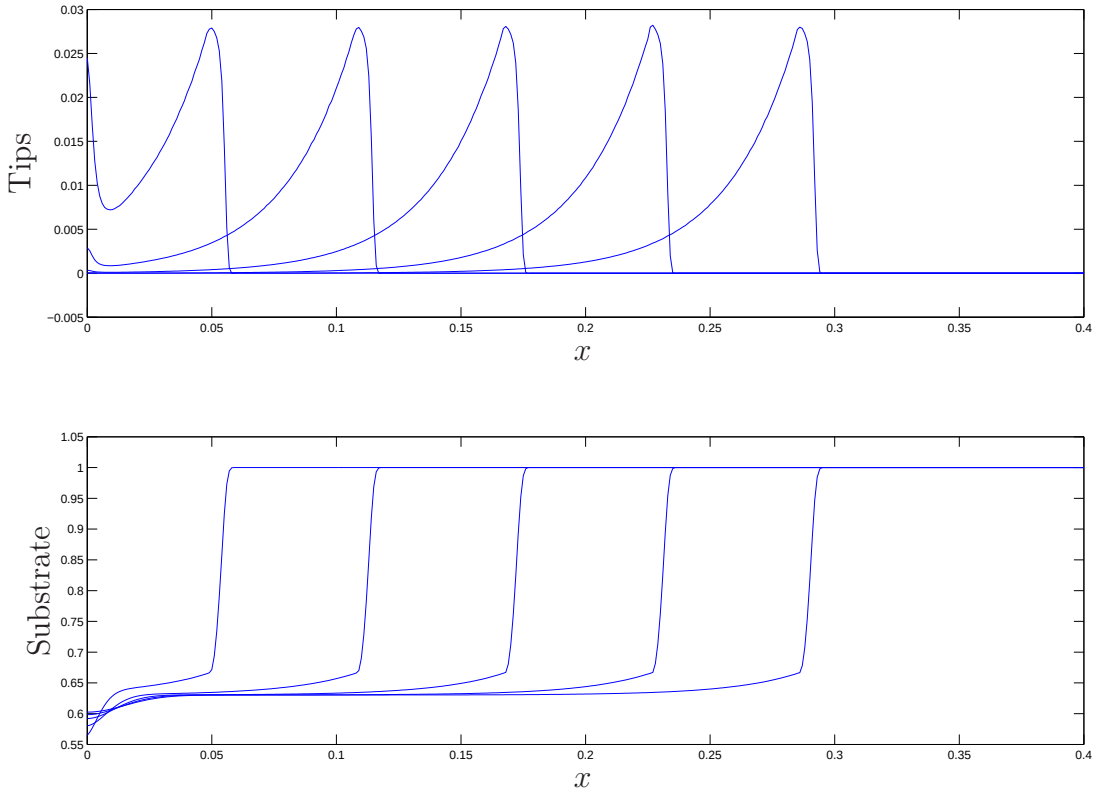

Figure 3.11: Finite element solution in $[0, 0.4]$ solved with 401 grid points ($h = 0.001$), initial $\delta_t = 0.005$, with $D_s = 6.25 \times 10^{-6}$. We show time $t = 4, 8, ..., 20$.

Figure 3.12 shows the two solutions ($D_s = 6.25 \times 10^{-5}$, $D_s = 6.25 \times 10^{-6}$) at time $t = 4, 16$. By decreasing the diffusion coefficient of the substrate, D_s, we instantly notice the increased steepness of the gradient of $s(x, t)$. The speed of transport of the tips has increased with reducing D_s, this is due to the increased gradient of $s(x, t)$. The tips movement is driven by the chemotaxis term, $\chi p \dfrac{\partial s}{\partial x}$, thereby increasing the distance travelled along the domain. We also observe a decrease (an average of 18.9%) in the tip density, where density is defined as the

integral

$$\int_0^L p\ dx = \frac{h}{2}\sum_{i=1}^{N}\big(p(x_{i-1}) + p(x_i)\big),$$

where $h = \dfrac{L}{N}$ and N is the number of intervals in $[0, L]$. Having a less substrate diffusion results in a pellet with a larger radius but its density is lower.

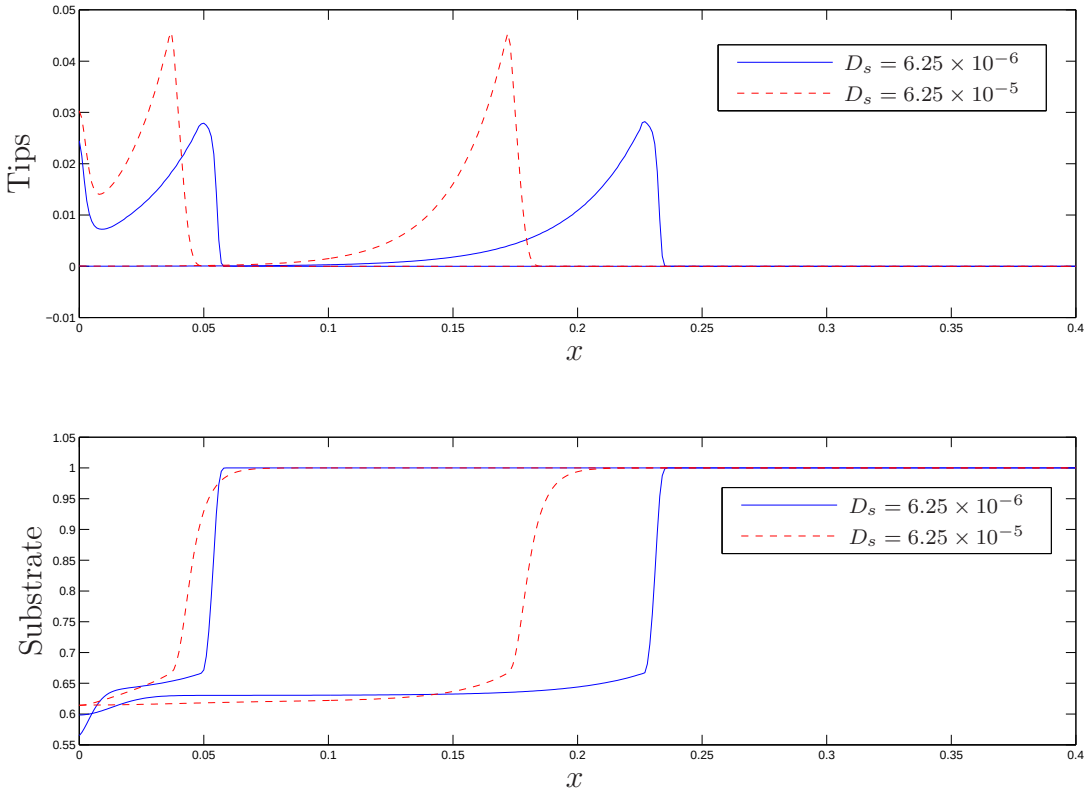

Figure 3.12: Finite element solution in $[0, 0.4]$ solved with 401 grid points ($h = 0.001$) and initial $\delta_t = 0.005$. The blue line represents the numerical solution when solved with $D_s = 6.25\times10^{-6}$. The red dahsed line represents the numerical solution when solved with $D_s = 6.25 \times 10^{-5}$, at time $t = 4, 16$.

3.A.1 Comparing Numerical Solutions: Heaviside Function vs Continuous Function

We stated in Section 3.3 that it is sometime necessary to regularize functions. Here we explore numerical results when we approximate the Heaviside function, $E(s)$, with two continuous functions, given below.

$$f(s) = \frac{s^\alpha}{\hat{s}^\alpha + s^\alpha}, \tag{3.22}$$

$$g(s) = \frac{1}{2}\Big(1 + \tanh\big(\lambda_2(s - \hat{s})\big)\Big), \tag{3.23}$$

where $\alpha = 800$ and $\lambda_2 = 50000$. If we let $\alpha \to \infty$ and $\lambda_2 \to \infty$, $f(s) \to E(s)$ and $g(s) \to E(s)$, respectively.

We have carried out a comparison of the Heaviside function $E(s)$, (3.17), and the smooth function $f(s)$, (3.22), to see if the discontinuity of $E(s)$ has an effect on the solution, see Figure 3.13.

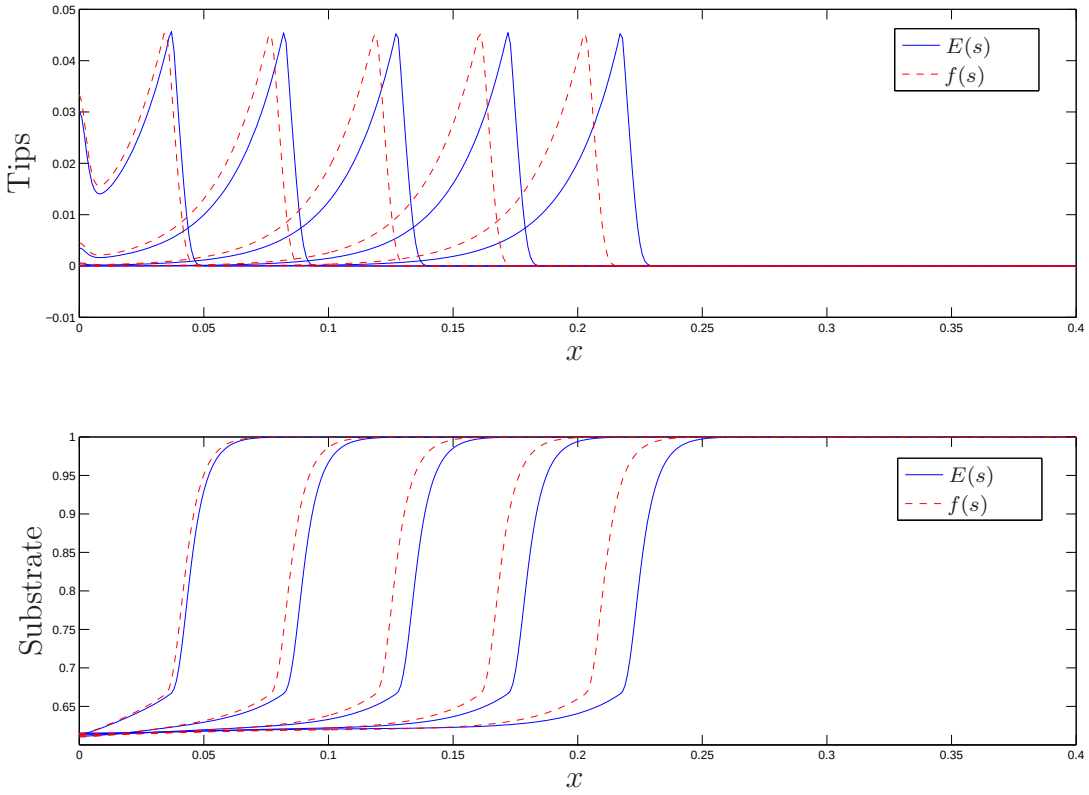

Figure 3.13: Finite element solution in $[0, 0.4]$ solved with 401 grid points ($h = 0.001$) and initial $\delta_t = 0.005$. The blue line represents the numerical solution when solved with $E(s)$. The red dashed line represents the solution when solved with $f(s)$, at time $t = 4, 8, ..., 20$.

In Figure 3.13 we compare the solution of the *Streptomyces* growth model when solved with the Heaviside, $E(s)$ and the smooth function, $f(s)$. We can see the solutions do vary, it appears the $f(s)$ solution is out of phase with the Heaviside solution, and the difference between them is growing in magnitude as time increases. We now compare the solution when solved with the Heaviside, $E(s)$ and the second smooth function, $g(s)$, see Figure 3.14.

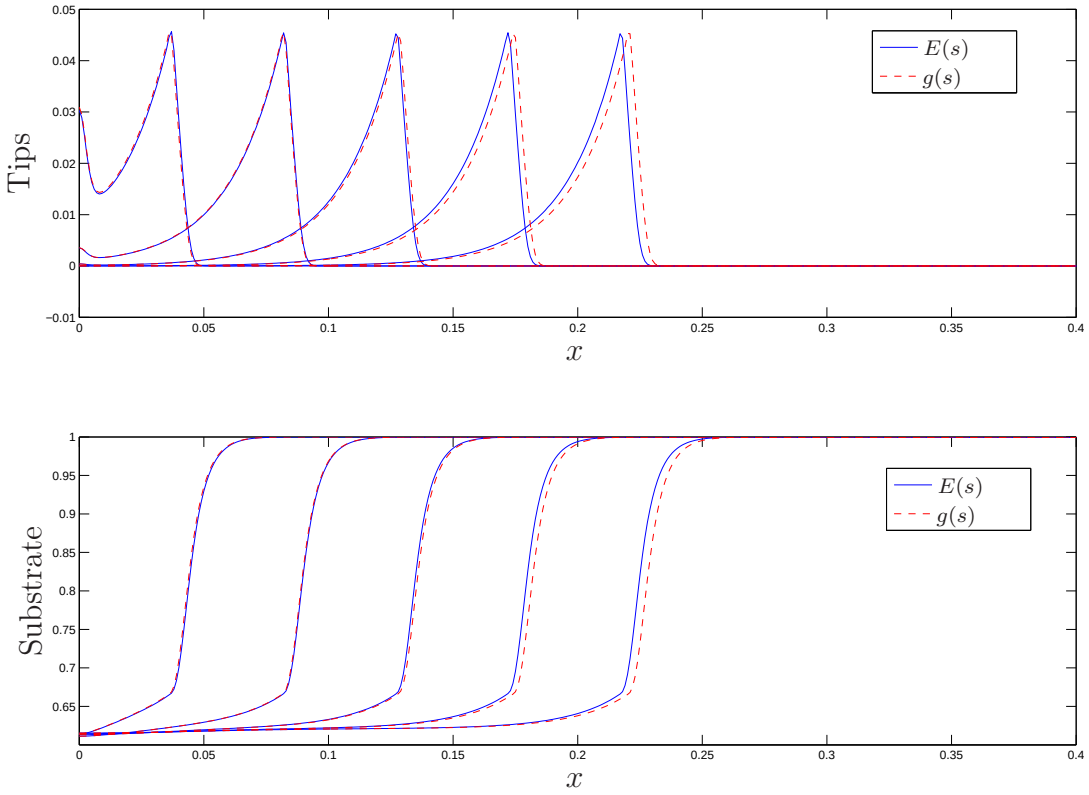

Figure 3.14: Finite element solution in $[0, 0.4]$ solved with 401 grid points ($h = 0.001$) and initial $\delta_t = 0.005$. The blue line represents the numerical solution when solved with $E(s)$. The red dashed line represents the solution when solved with $g(s)$, at time $t = 4, 8, ..., 20$.

Shown above in Figure 3.14, we compare the two solutions when solved with $E(s)$ and $g(s)$. The comparison between the solutions is difficult to see at $t = 4$, unlike Figure 3.13 where the difference is clear and grows in magnitude as time progresses. In Figure 3.15, we show all three solutions $E(s), f(s)$, and $g(s)$ at $t = 4$ and $t = 20$. This comparison lets us observe how the initial ($t = 4$) differences of the three solutions progress to the final time, $t = 20$.

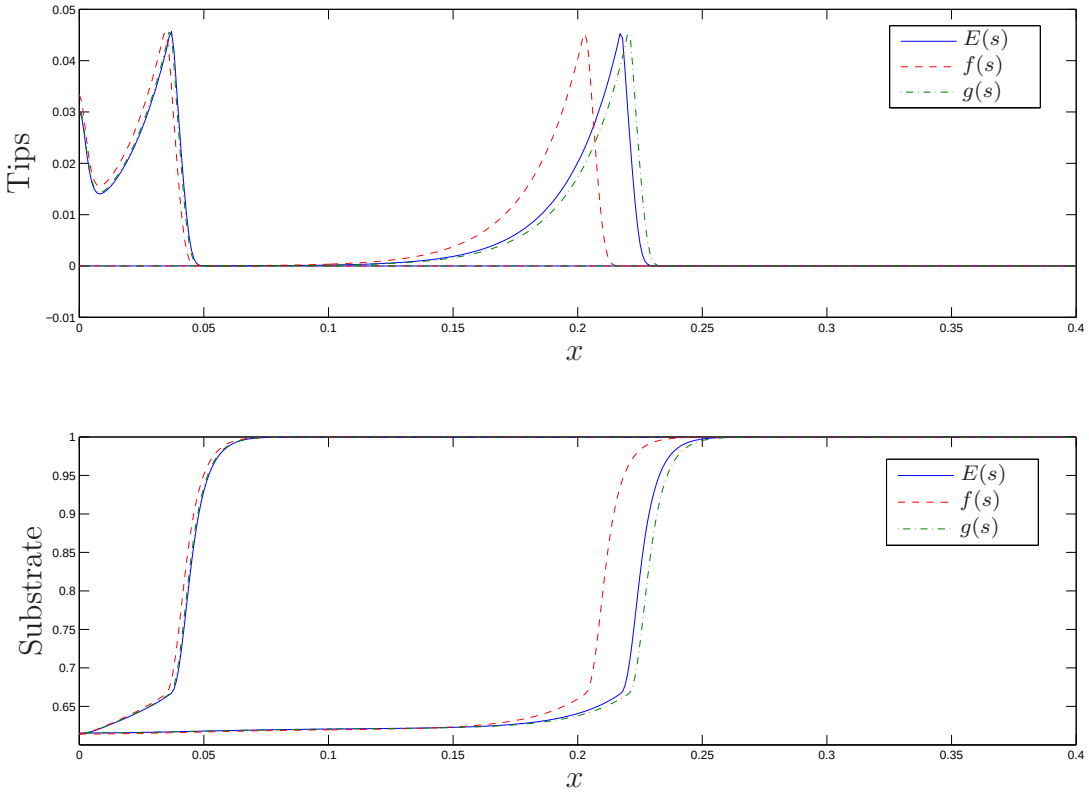

Figure 3.15: Finite element solution in $[0, 0.4]$ solved with 401 grid points ($h = 0.001$) and initial $\delta_t = 0.005$ at time, $t = 4, 20$. The blue line represents the solution when solved with $E(s)$, the red dashed line represents the solution when solved with $f(s)$, and the green dot-dashed line when $g(s)$ is used.

We should note that in Figures 3.13, 3.14 and 3.15 have all been solved with $D_s = 6.25 \times 10^{-5}$. From the results, it is clear that care must be taken when approximating a Heaviside function with a smooth function (if ever). In this case, when $D_s = 6.25 \times 10^{-5}$, we can conclude that the only approximation we should allow is

$$E(s) \simeq g(s).$$

We now look at the comparison between solutions when solving with the discontinuous function $E(s)$ and the two smooth functions $f(s)$ and $g(s)$, given by (3.17), (3.22) and (3.23), respectively, when $D_s = 6.25 \times 10^{-6}$. The first comparison, shown in Figure 3.16, is between $E(s)$ and $f(s)$.

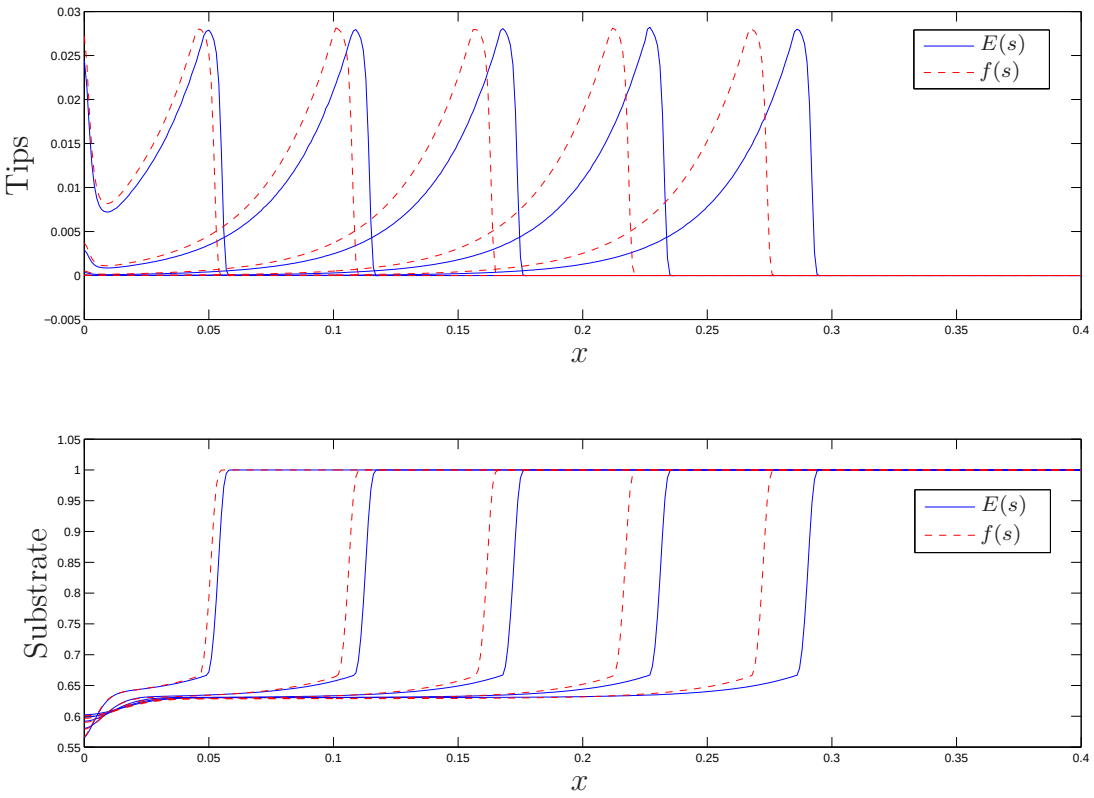

Figure 3.16: Finite element solution in $[0, 0.4]$ solved with 401 grid points ($h = 0.001$) and initial $\delta_t = 0.005$. The blue line represents the numerical solution when solved with $E(s)$. The red dashed line represents the solution when solved with $f(s)$, at time $t = 4, 8, ..., 20$.

We observe a similar outcome as in Figure 3.13, where the solutions are out of phase and the error between them increases over time.

We now examine the numerical solutions of (3.19) when solved with $E(s)$ and $g(s)$, shown in Figure (3.17).

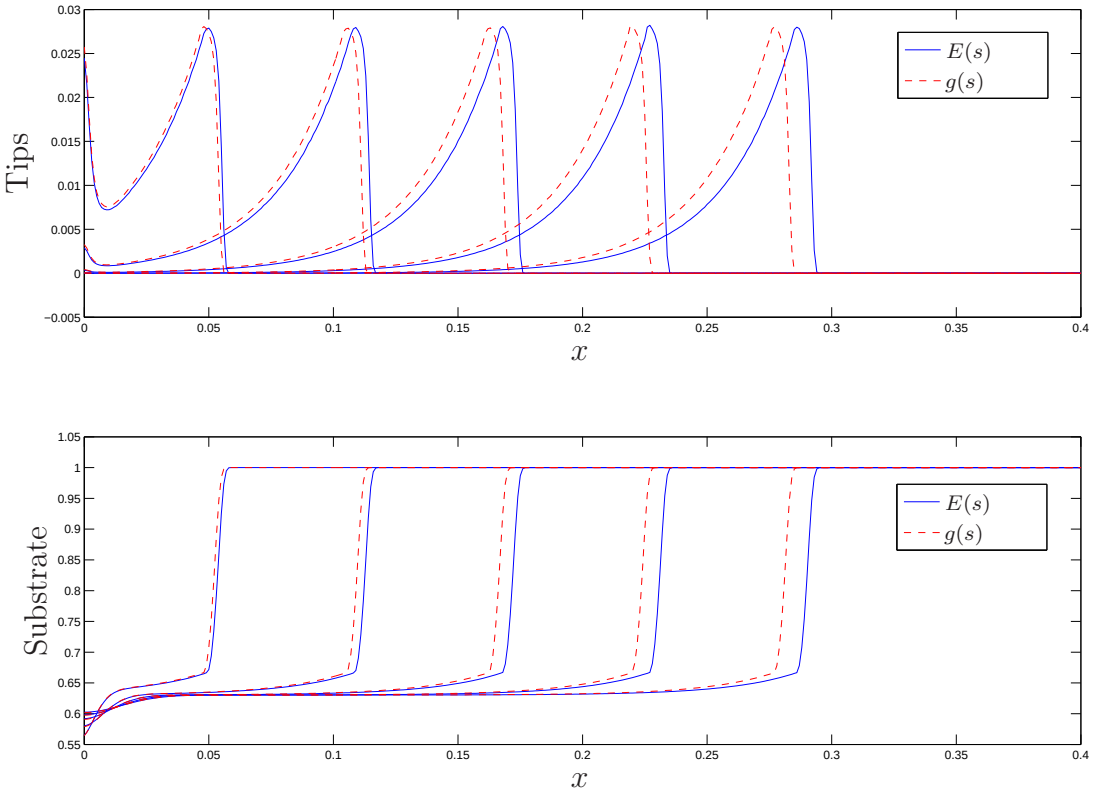

Figure 3.17: Finite element solution in $[0, 0.4]$ solved with 401 grid points ($h = 0.001$) and initial $\delta_t = 0.005$. The blue line represents the numerical solution when solved with $E(s)$. The red dashed line represents the solution when solved with $g(s)$, at time $t = 4, 8, ..., 20$.

The solutions do appear to be a good match at early time, but an error is present and it is increasing in magnitude over time. However, the error is not as large as in Figure 3.16 (when solved with $f(s)$).

In Figure 3.18 we have presented the three solutions, $E(s), f(s)$ and $g(s)$ at

$t = 4, 20$. This figure shows the initial and final errors that appear when solving the nonlinear system $\mathbf{F}(\mathbf{U}) = \mathbf{0}$, (3.19).

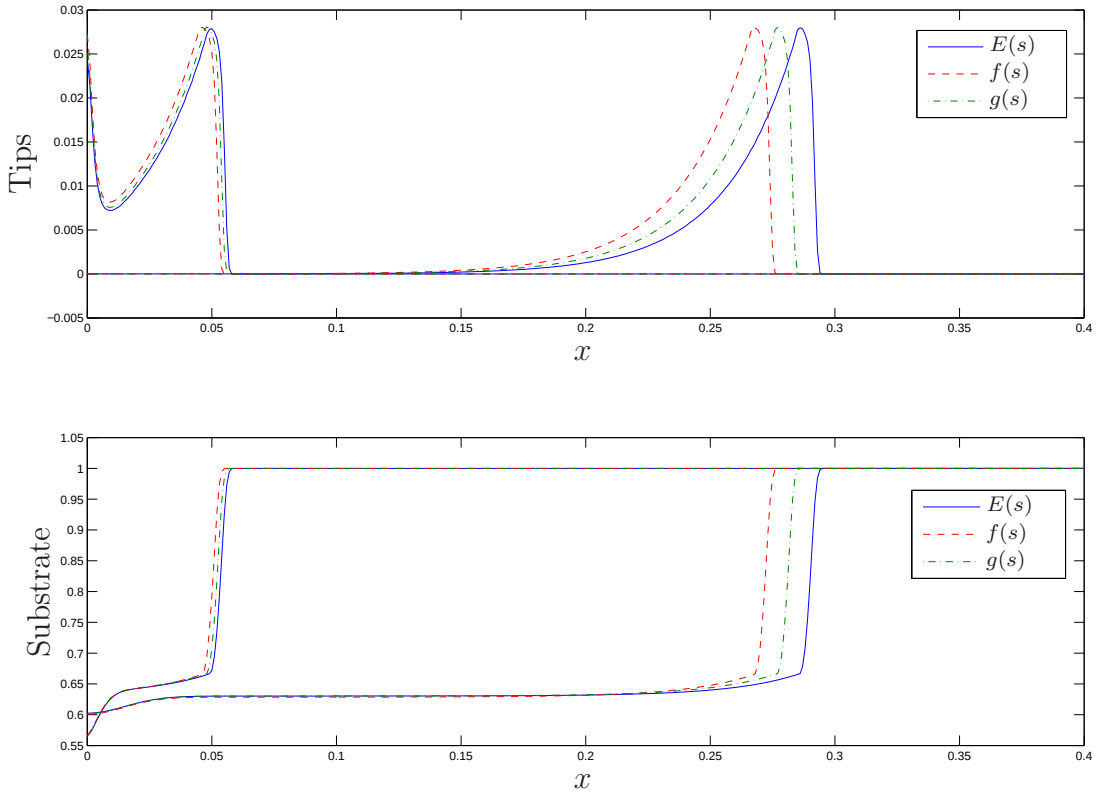

Figure 3.18: Finite element solution in $[0, 0.4]$ solved with 401 grid points ($h = 0.001$) and initial $\delta_t = 0.005$ at time, $t = 4, 20$. The blue line represents the solution when solved with $E(s)$, the red dashed line represents the solution when solved with $f(s)$, and the green dot-dashed line when $g(s)$ is used.

When solving the nonlinear system $\mathbf{F}(\mathbf{U}) = \mathbf{0}$ using FEM, if an approximation of $E(s)$ is to occur we should accept, with caution

$$E(s) \simeq g(s).$$

We conclude that when approximating a Heaviside function with a continuous function, a precautionary study should be carried out. We found that when $D_s = 6.25 \times 10^{-5}$ or $D_s = 6.25 \times 10^{-6}$, the Heaviside function $E(s)$ could be approximated by the hyperbolic tan function $g(s)$, but not with the Hill function $f(s)$. Although there is an error between solutions when using $E(s)$ and $g(s)$ when $D_s = 6.25 \times 10^{-5}$ and $D_s = 6.25 \times 10^{-6}$ but the error is not as large as when solved using $f(s)$. An approximation can be made but with caution.

Chapter 4

Novel Targeted Cancer Therapy

4.1 Introduction

Biomimetic polymer vesicles (BPVs) are synthetic diblock copolymers that self assemble into nanometre-sized vesicles that can encapsulate anti-cancer drugs during assembly [2]. A novel targeted cancer therapy has been proposed to use BPVs to specifically target HNSCC (head and neck squamous cell carcinoma) cancer cells using the HN-1 peptide, a receptor specific to HNSCC tumour cells [47].

The BPVs enter tumour cells via the cells endocytic pathway, there is no conclusive evidence for which pathway the BPVs take. We assume (based on recent evidence, see [3]) for modelling purposes that it is by receptor-mediated endocytosis. Once internalized the BPV enters an endosome which causes the BPV to rupture due to the change in pH, and subsequently the rupture of the endosome due to an increased osmotic pressure. The anti-cancer drug is then released into the cells cytosol.

Using targeted BPVs for cancer therapy is not limited to drug delivery, but is also shown effective as a gene therapy delivery agent [59]. Due to the properties of the BPVs the DNA to be delivered is protected from extracellular and intracellular proteolic enzymes which would normally degrade the genomic integrity of the DNA.

4.2 Model Derivation

The starting point for the modelling is the binding of the BPVs to the cancer cell surface. Specifically the binding kinetics between receptors on the cell surface and corresponding ligands on the BPVs. The idea is that ligands embedded on the BPV surface bind to receptors on the tumour cell surface. A ligand-receptor complex then arises through this binding event, thereby effectively attaching the BPV to the tumour cell surface. We will consider multiple binding events between BPV ligands and cell surface receptors. We also assume that any bond can be broken resulting in the BPV dissociating from the cell surface when previously attached by only one bond. Note that once a BPV is bound to a cell we assume that it cannot bind to a neighbouring cell using free ligands, i.e. any further ligand-receptor complexes that arise will be on the original cell. At some rate the BPV will be internalized (the rate of internalization may depend on the number of ligand-receptor bonds between the BPV and the cell, more details later). The drug release is accounted for by lysis of the BPV at a constant rate once internalized. See Figure 4.1 for a sketch of the processes involved in BPV uptake.

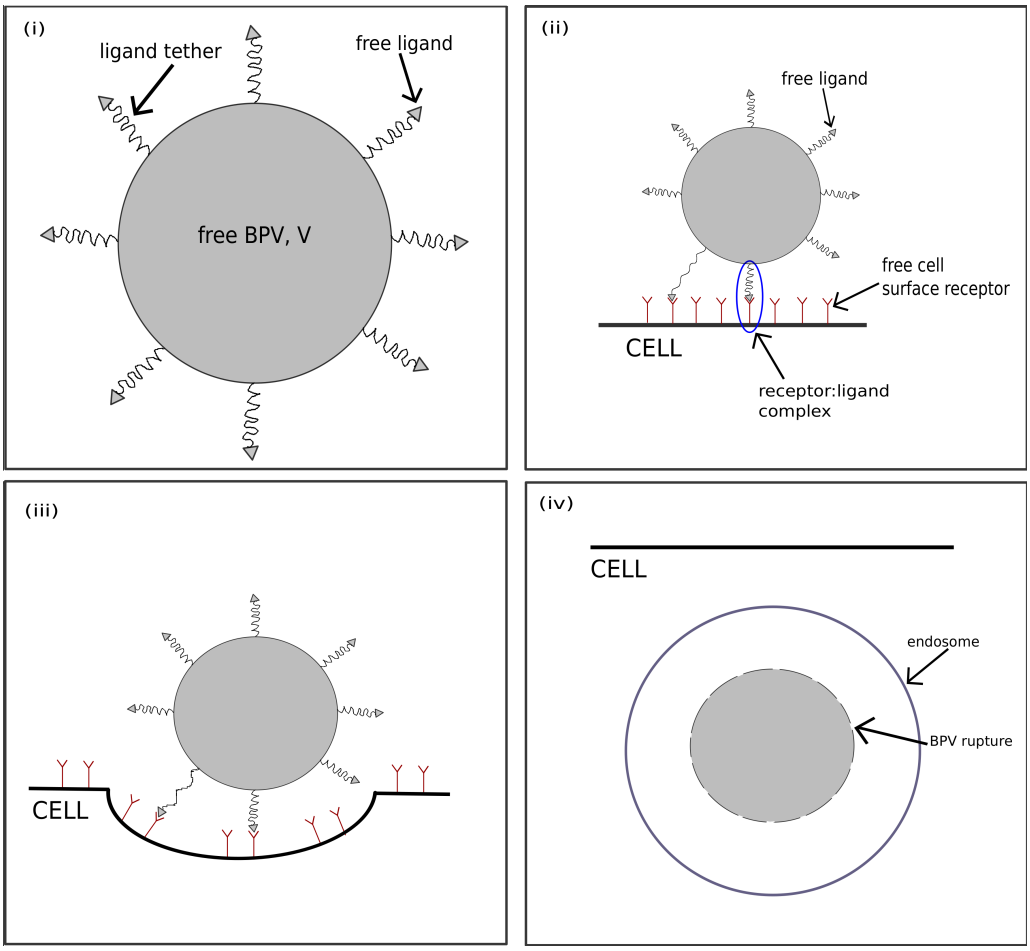

Figure 4.1: A sketch indicating the (i) structure of the free BPV, (ii) receptor:ligand binding, (iii) cell membrane deformation during receptor-mediated endocytosis of the BPV (iv) the rupture of the BPV releases its contents within the endosome due to the pH change. Changes in the osmotic pressure with the endosome causes it to rupture, releasing the BPVs contents into the cell.

We first assume that the system is well-mixed and so we ignore any spatial effects and use a system of $n + 5$ ordinary differential equations (where n is the maximum number of bound complexes) to model the system. The model variables are: tumour cells per cm^3, $m(t)$; moles of receptor-ligand complexes bound with j bonds per cm^3, $B^j(t)$ (with $j = 1, ..., n$); moles of free vesicle

ligands per cm^3, $L(t)$; moles of cell receptors per cm^3, $F(t)$; moles of internalized BPVs per cm^3, $B_{in}(t)$; and, moles of intracellular drug per cm^3, $P(t)$.

We also define the following relationships between variables,

$$V(t) = \frac{L}{l}, \quad f(t) = \frac{F}{m}, \quad b^j(t) = \frac{B^j}{lm}, \quad b_{in}(t) = \frac{B_{in}}{m} \quad \text{and} \quad \phi(t) = \frac{P}{m}, \tag{4.1}$$

where $V(t)$ is the number of free BPVs per cm^3, l is the fixed moles of free ligands per BPV, $f(t)$ is the moles of unbound receptors per cell, $b^j(t)$ describes the number of BPVs bound with j complexes per cell, $b_{in}(t)$ is the number of internalized BPVs per cell and $\phi(t)$ describes the mole of drug per cell.

We describe how the tumour cells change over time with the following ODE,

$$\frac{dm}{dt} = \overbrace{rm\left(1 - \frac{m}{K}\right)}^{\text{growth}} - \overbrace{g(\phi)m}^{\text{death}}, \tag{4.2}$$

where we assume that the cells undergo logistic growth at constant rate r, and the carrying capacity of the system is K. The cell death is described by $g(\phi)$, which we assume is constant when there is no intracellular drug present, otherwise it is an increasing saturating function of the intracellular drug concentration.

By using the expression described in (4.1), which states that

$$V(t) = \frac{L}{l} = \frac{\text{moles of free ligands per cm}^3}{\text{moles of free ligands per BPV}} = \text{number of free BPVs per cm}^3,$$

we can derive an equation that describes the rate of change of free BPVs per cm^3 by using the following equation for the rate of change of ligands:

$$\frac{dL}{dt} = - \overbrace{k_a LF}^{\substack{\text{initial receptor-} \\ \text{ligand binding}}} + \overbrace{k_d B^1}^{\substack{\text{dissociation of} \\ \text{complex}}}, \tag{4.3}$$

this equation states that, by using the law of mass action, free ligands bind to free receptors at the rate k_a, and the reverse reaction is taken at the rate k_d. Diving (4.3) by l (mole of free ligands per BPV), we get the rate of change of free BPVs per cm^3:

$$\frac{dV}{dt} = -\, k_a V F + \frac{k_d}{l} B^1. \tag{4.4}$$

Remember that l is fixed and constant.

Receptor-ligand complexes bound by 1 bond changes over time by,

$$\begin{aligned} \frac{dB^1}{dt} = & \overbrace{k_a L F}^{\substack{\text{initial receptor-}\\ \text{ligand binding}}} - \overbrace{k_d B^1}^{\substack{\text{dissociation of}\\ \text{complex}}} - \overbrace{k_a \left(\rho_l l N_A - 1\right) \rho_f F B^1}^{\substack{\text{association of}\\ 1\to 2 \text{ complexes}}} \\ & + \overbrace{2 k_d B^2}^{\substack{\text{dissociation of } 2\to 1\\ \text{complexes}}} - \overbrace{k_i B^1}^{\substack{\text{internalization of}\\ \text{complex with 1 bond}}}. \end{aligned} \tag{4.5}$$

We use the law of mass action to describe the binding kinetics. A receptor-ligand complex bound by one bond occurs by ligands and receptors binding at the constant association rate k_a. The reaction is reversible at the constant dissociation rate k_d. We allow for multiple binding events, therefore subsequent binding can occur at rate k_a to produce BPVs bound by 2 receptor-ligand complexes.

In equation (4.5) we have terms including ρ_l and ρ_f. Theses terms describe the fraction of ligands and receptors, respectively, that are available for 2-D binding. The term 2-D binding is used to describe the subsequent binding after an initial complex is formed. Due to the BPV being much smaller than the cell we assume only a proportion of ligands can reach the cell receptors due to the ligand tether length, see Figure 4.1 (ii) for an example of 2-D binding. This may result in an increased association rate compared to that if no complexes have formed due to close proximty of receptors and ligands (however, we choose to keep the association rate constant throughout). Using ρ_l and ρ_f we can make assumptions about the positioning of the receptors, for example if ρ_f is low this represents

little receptor clustering on the cell surface and therefore a small number of receptors available for 2-D binding. A low ρ_l would, for example, represent a large BPV or a small ligand tether length. The term $(\rho_l l N_A - 1)$ in the third term of (4.5) represents the available ligands on the BPV for subsequent binding after the initial binding event, where N_A is Avogadro's constant, i.e. there is one less ligand available for subsequent binding for the BPV to become bound by 2 complexes, B^2. Dissociation of a receptor-ligand complex bound by 2 bonds results in a B^1 and this happens at the rate $2k_d$, we use the factor two to represent that any one of the two bonds can dissociate. Internalization of BPVs occur at a constant rate k_i.

In general, receptor-ligand complex bound by i bonds changes over time by,

$$\begin{aligned}\frac{dB^i}{dt} &= \overbrace{k_a\left(\rho_l l N_A - (i-1)\right)\rho_f F B^{i-1}}^{\substack{\text{association of}\\ (i-1)\to i \text{ complexes}}} - \overbrace{ik_d B^i}^{\substack{\text{dissociation of } i\to(i-1)\\ \text{complexes}}} \\ &\quad - \overbrace{k_a\left(\rho_l l N_A - i\right)\rho_f F B^i}^{\substack{\text{association of}\\ i\to(i+1) \text{ complexes}}} + \overbrace{(i+1)k_d B^{i+1}}^{\substack{\text{dissociation of } (i+1)\to i\\ \text{complexes}}} \\ &\quad - \underbrace{k_i B^i}_{\substack{\text{internalization of}\\ \text{complex with } i \text{ bonds}}},\end{aligned} \tag{4.6}$$

where $2 \leq i \leq n-1$. This is the general case which describes the multiple binding kinetics; complexes with $(i-1)$ and i bonds associate at the rate k_a to produce complexes with i and $(i+1)$ respectively; complexes with i bonds dissociate at the rate ik_d to produce complexes with $(i-1)$ bonds; and complexes with $(i+1)$ dissociate at the rate $(i+1)k_d$ to produce complexes with i bonds; we assume that the complex with i bonds (and hence the BPV) can be internalized at the constant rate, k_i.

Finally, receptor-ligand complex bound by n bonds change over time by,

$$\frac{dB^n}{dt} = \overbrace{k_a\left(\rho_l l N_A - (n-1)\right)\rho_f F B^{n-1}}^{\substack{\text{association of} \\ (n-1)\to n \text{ complexes}}} - \overbrace{nk_d B^n}^{\substack{\text{dissociation of } n\to(n-1) \\ \text{complexes}}}, \\ - \underbrace{k_i B^n}_{\substack{\text{internalization of} \\ \text{complex with } n \text{ bonds}}}, \tag{4.7}$$

where n is the maximum number of complexes that can form (which is given by $\rho_l l N_A$). As in the general case, complexes with n bonds are formed when there is an association of additional bond (at rate k_a) when $(n-1)$ bonds are present, and the dissociation occurs at the rate nk_d since any one of the n bonds can break. Again we assume that a BPV with n complexes can internalized at a constant rate, k_i.

We describe the rate of change of free receptors by,

$$\frac{dF}{dt} = - \overbrace{k_a F L}^{\substack{\text{initial receptor-} \\ \text{ligand binding}}} - \overbrace{k_a \sum_j^n (\rho_l l N_A - j)\rho_f F B^j}^{\text{subsequent binding with ligands}} \\ + \overbrace{k_d \sum_j^n j B^j}^{\text{dissociation of } j \text{ bonds}} - \overbrace{d_f F}^{\text{receptor half-life}} + \overbrace{R(b_{tot})m.}^{\text{receptor production}} \tag{4.8}$$

There is a loss of receptors due to the initial and subsequent binding with BPV ligands at the association rate k_a, and a gain of receptors when dissociation occurs (at the rate k_d). We assume that receptor production occurs on the cell surface and we assume that receptors are recruited to the cell surface at a rate proportional to the number of bound receptors. We describe this receptor recycling using the function $R(b_{tot})$, which we assume is constant if there is no bound receptors, otherwise we assume an increasing saturating function dependent on the total number of bound complexes per cell, which is given by

$$b_{tot} = \frac{1}{m}\sum_j^n j B^j.$$

Hence, as an increasing number of receptors are internalized, the rate of receptors returning to the surface (which are free to bind again) increases. We also assume that receptors have a limited life on the cell surface, with the constant linear decay rate d_f.

The rate of change in internalized BPVs over time is given by,

$$\frac{dB_{in}}{dt} = \overbrace{\frac{k_i}{l}\sum_{j}^{n} B^j}^{\text{total internalized BPVs}} - \overbrace{d_b B_{in}.}^{\text{lysis of BPVs}} \tag{4.9}$$

We use the factor $\frac{1}{l}$ to convert BPVs with j bound complexes to the number of bound BPVs. Internalized BPVs are lost due to BPV rupture at an assumed constant rate d_b. When BPVs rupture within the cell they release drug, giving the rate of change of intracellular drug as,

$$\frac{dP}{dt} = \overbrace{\nu d_b B_{in}}^{\text{drug release through lysis}} - \overbrace{d_p P,}^{\text{drug half-life}} \tag{4.10}$$

where the release of the drug is proportional to the rupture of the BPV, ν, and as with most drugs, we include a decay is drug activity which we assume occurs at constant rate, d_p.

We use the following functions for $g(\phi)$ and $R(b_{tot})$:

$$g(\phi) = d_m + \frac{\mu\phi^\beta}{P_0^\beta + \phi^\beta} \qquad \text{and} \qquad R(b_{tot}) = c_1 + \frac{c_2 b_{tot}^\alpha}{c_3^\alpha + b_{tot}^\alpha}.$$

We further impose the following initial conditions to the system,

$$\begin{aligned} &m(0) = M_0 \ \frac{\text{cells}}{\text{cm}^3}, \quad V(0) = V_0 \ \frac{\text{BPVs}}{\text{cm}^3}, \quad F(0) = F_0 \ \frac{\text{mol receptors}}{\text{cm}^3}, \\ &B^j(0) = 0, \qquad\quad B_{in}(0) = 0 \quad \text{and} \quad P(0) = 0. \end{aligned}$$

where $j = 1, ..., n$.

4.2.1 Parameterization and Non-dimensionalization

The parameterization of the system proved difficult as the majority of the parameters for specific BPV binding are unknown. Hence we look to a similar system of liposomal targeting which has similar dynamics to those of BPVs targeting and is more well understood. Specifically we look to use some parameters from a liposomal modelling study by Ghaghada *et al* [36], see Table 4.1.

Due to the similar dynamics of the two biological systems we assume the same binding kinetics as [36], in which targeted liposomes bind to folate receptors of C6 glioma cells. The binding rate constant used is $k_a = 3.701 \times 10^5$ M min^{-1}, the dissociation rate constant is $k_d = 3.701 \times 10^{-5}$ min^{-1} and the internalization rate constant is $k_i = 0.6124$ min^{-1} (where M is molarity, i.e. M $= \dfrac{\text{mol}}{\text{cm}^3}$).

Without any specific data available, we assume that the decay rate of the receptors on the cell surface is $d_f = 0.03$ min^{-1}, which has been taken from Webb and Owen (2004) [97]. We derive the production of cell receptors, c_1, by assuming that, when there is no binding, production must equal decay, so that $c_1 = d_f$, i.e. $c_1 = 0.03$ mol cell^{-1} min^{-1}. The parameters c_2 and c_3 characterise the Hill function for receptor recycling. For simplicity we make $c_2 = c_1$. The parameter c_3 is value at which the half maximum of the function $R(b_{tot})$ is reached. We assume that this value is $c_3 = 0.5$ mol cell^{-1} and we choose a simple exponent value given by $\alpha = 1$.

We let the proportions ρ_f, ρ_l vary within $(0, 1]$. Using Ghaghada *et al* [36] as a guide, we further assume that there are initially 10^4 receptors per cell. We assume that there are 10^{10} BPVs per cm^3 and 5×10^7 cells per cm^3 [35], with the tumour cells being at carrying capacity at $t = 0$ of the simulations. We assume that tumour cells divide roughly once per day, therefore the growth rate, r, is

given by $r = 1$ day^{-1} which has been used widely in previous mathematical models for tumour growth (see e.g. [73]).

From Ahmed *et al* [3], we take the half-life cytotoxicity from the BPVs containing taxol to be roughly 10 hours. Therefore, we use this as our initial estimate for the death rate of tumour cells μ, i.e. $\mu = \frac{\ln 2}{10}\text{h}^{-1} = 0.0012$ min^{-1}. From data provided by Dr Craig Murdoch from the School of Clinical Dentistry in the University of Sheffield, we notice that the time-frame of tumour size reduction occurs much faster than the half-life of 10 hours, hence we increase the order of magnitude of μ to suit and let $\mu = 1.2\text{min}^{-1}$ to make the numerical solutions match the time-frame of the experiments.

It is known that the half-life of the free drug taxol is roughly 10 hours, similar to the half-life cytotoxicity of the BPVs. We assume that the drug half-life is the time it takes for half the drug to be used by the cells, and so we take the same value for the decay rate of the drug, d_p, as that for μ. From Ahmed *et al* [3], we see that the half-life for BPVs to leave endosomes is roughly 5 hours. Hence the rate of BPV rupture, d_b can be calculated by $\mu = \frac{\ln 2}{5}\text{h}^{-1} = 0.0023\text{min}^{-1}$. As with μ, however, we found this value to give unrealistic results as compared to experiments. We found a much better match when we take $d_b = 2.3\text{min}^{-1}$.

There are a few remaining unknown parameters which we estimate to match experimental observations. The parameters along with the appropriate units for this model, are shown in Table 4.1.

Parameter	Dimensional Value	Reference
M_0	5×10^7 cell cm^{-3}	[35]
V_0	10^{10} BPV cm^{-3}	estimate
F_0	10^4 mol cell^{-1}	[36]
r	6.944×10^{-4} min^{-1}	[35]
K	5×10^7 cells cm^{-3}	estimate
k_a	3.7010×10^8 mol^{-1}min^{-1}cm^3	[36]
k_d	3.7010×10^{-5} min^{-1}	[36]
k_i	0.6124 min^{-1}	[36]
N_A	6.022×10^{23} mol^{-1}	-
$l \cdot N_A$	1200 ligands BPV^{-1}	estimate
d_f	0.03 min^{-1}	[97]
ρ_f	$(0, 1]$	estimate
ρ_l	$(0, 1]$	estimate
d_b	0.05 min^{-1}	[3]
d_p	1.2 min^{-1}	-
ν	8.3×10^{-16} mol BPV^{-1}	-
μ	1.2 min^{-1}	[3]
c_1	0.03 mol cell^{-1} min^{-1}	-
c_2	0.03 mol cell^{-1} min^{-1}	-
c_3	0.5 mol cell^{-1}	-
α	1	estimate
β	1	estimate

Table 4.1: The dimensional parameter values with the appropriate units and references (where applicable).

The parameters chosen vary greatly in order of magnitude and this has caused

problems when solving the system numerically. To overcome this we rescale the system. The dimensional variables are rescaled as follows

$$m = \hat{m}K, \qquad L = \frac{\hat{L}V_0}{N_A}, \qquad F = \hat{F}f_0K, \quad B = \frac{\hat{B}V_0}{N_A},$$
$$B_{in} = \hat{B_{in}}V_0, \quad P = \hat{P}P_0K \quad l = \frac{\hat{l}}{N_A}, \qquad t = \frac{\hat{t}}{r},$$

where the non-dimensional variables are denoted by hats. On removing the hats for convenience, the rescaled system then reads

$$\begin{aligned}
\frac{dm}{dt} &= m(1-m) - \widetilde{g}(\widetilde{\phi})m, && (4.11)\\
\frac{dV}{dt} &= -\widetilde{k_a}VF + \widetilde{k_d}B^1, && (4.12)\\
\frac{dB^1}{dt} &= \widetilde{k_a}LF - \widetilde{k_d}B^1 - \frac{\widetilde{k_i}}{\widetilde{l}}B^1 \\
&\quad -\widetilde{k_a}\{\rho_l l - 1\}\rho_f F B^1 + 2\widetilde{k_d}B^2, && (4.13)\\
\frac{dB^i}{dt} &= \widetilde{k_a}\{\rho_l l - (i-1)\}\rho_f F B^{i-1} - i\widetilde{k_d}B^i - \widetilde{k_i}B^i \\
&\quad -\widetilde{k_a}\{\rho_l l - i\}\rho_f F B^i + (i+1)\widetilde{k_d}B^{i+1}, && (4.14)\\
\frac{dB^n}{dt} &= \widetilde{k_a}\{\rho_l l - (n-1)\}\rho_f F B^{n-1} - \widetilde{k_i}B^n - n\widetilde{k_d}B^n, && (4.15)\\
\frac{dF}{dt} &= -\eta\widetilde{k_a}FL - \eta\widetilde{k_a}\sum_i^n(\rho_l l - i)\rho_f F B^i + \eta\widetilde{k_d}\sum_i^n iB^i \\
&\quad -\widetilde{d_f}F + \widetilde{R}(\widetilde{b_{tot}})m, && (4.16)\\
\frac{dB_{in}}{dt} &= \frac{\widetilde{k_i}}{l}\sum_i^n B^i - \widetilde{d_b}B_{in}, && (4.17)\\
\frac{dP}{dt} &= \widetilde{\nu}\widetilde{d_b}B_{in} - \widetilde{d_p}P, && (4.18)
\end{aligned}$$

with

$$\widetilde{g}(\widetilde{\phi}) = \widetilde{d_m} + \frac{\widetilde{\mu}\phi^\beta}{1+\phi^\beta} \qquad \text{and} \qquad \widetilde{R}(\widetilde{b_{tot}}) = \widetilde{c_1} + \frac{\widetilde{c_2}\widetilde{b_{tot}}^\alpha}{\widetilde{c_3}^\alpha + \widetilde{b_{tot}}^\alpha}$$

where

$$\widetilde{b_{tot}} = \frac{1}{m}\sum_j^n jB^j.$$

The rescaled parameters denoted by tildes are defined as

$$\widetilde{k_a} = \frac{k_a f_0 K}{r}, \qquad \widetilde{k_d} = \frac{k_d}{r}, \qquad \widetilde{k_i} = \frac{k_i}{r}, \qquad \widetilde{d_m} = \frac{d_m}{r}, \qquad \widetilde{\mu} = \frac{\mu}{r},$$

$$\eta = \frac{V_0}{N_A f_0 K}, \qquad \widetilde{d_f} = \frac{d_f}{r}, \qquad \widetilde{d_b} = \frac{d_b}{r}, \qquad \widetilde{d_p} = \frac{d_p}{r}, \qquad \widetilde{\nu} = \frac{V_0 \nu}{P_0 K},$$

$$\widetilde{c_1} = \frac{c_1}{f_0 r}, \qquad \widetilde{c_2} = \frac{c_2}{f_0 r}, \qquad \widetilde{c_3} = \frac{c_3 N_A K}{V_0}.$$

The rescaled system is then subject to the following initial conditions,

$$m(0) = 1, \;\; V(0) = 1, \;\; F(0) = 1, \;\; B^j(0) = 0, \;\; B_{in}(0) = 0, \;\; P(0) = 0, \quad (4.19)$$

for $j = 1, ..., n$. For all future analyses we use the non-dimensional system (4.11)-(4.18) and initial conditions (4.19) with the hats and tilde dropped for simplicity.

4.3 Numerical Results

Using the parameters and rescaling described in Section 4.2, we now carry out numerical simulations in order to find out the basic dynamics of the system. We solve the system numerically using the ODE solver `ode45` in Matlab, this ODE solver uses the explicit Runge-Kutta 45 formula. In Figure 4.2 we show the typical results.

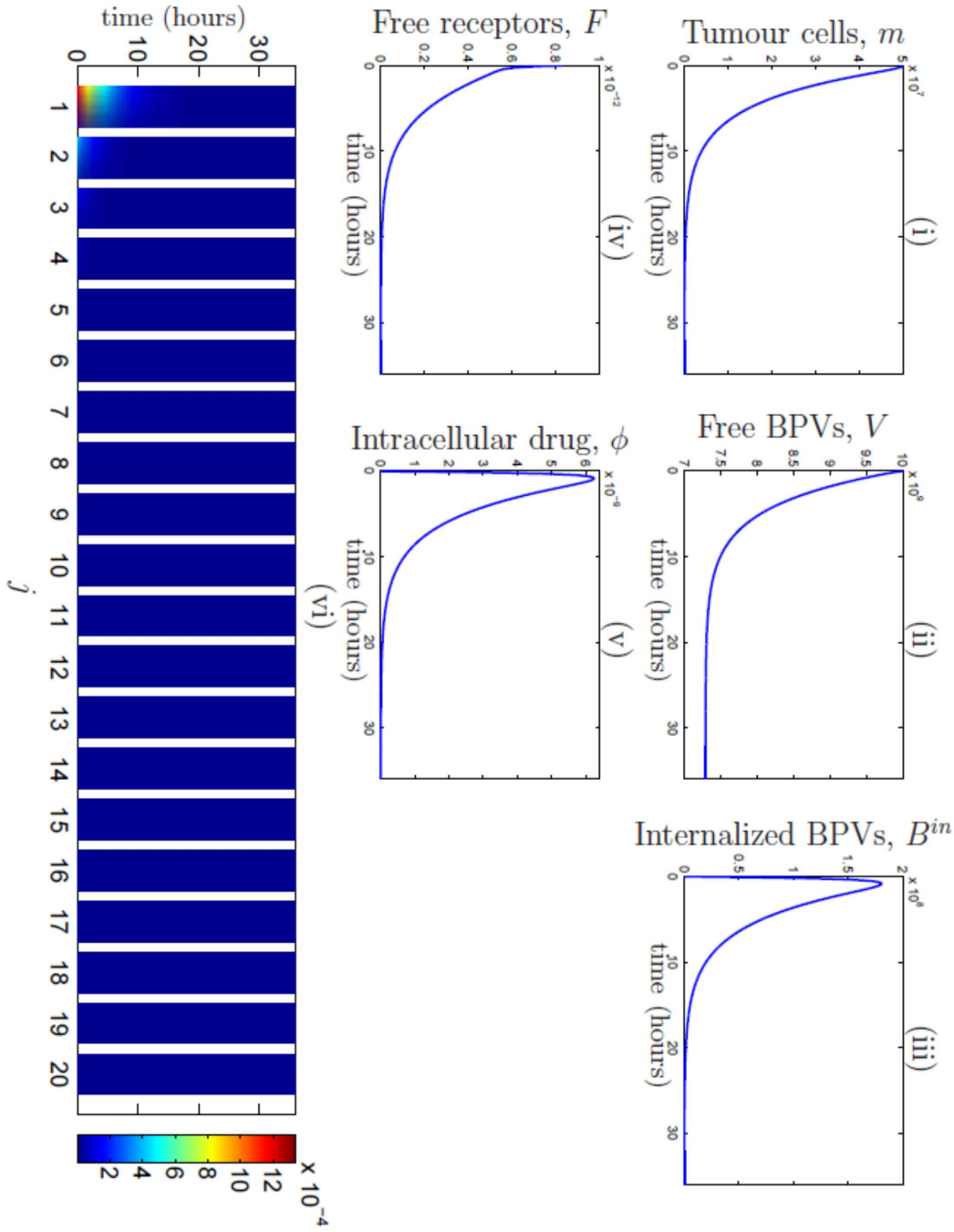

Figure 4.2: Shown are the solutions for (i) tumour cells, (ii) free BPVs, (iii) internalized BPVs, (iv) free receptors and (v) intracellular drug plotted over time. (vi) shows the density of BPVs bound with j complexes, as time increases (vertically). Solved with the initial conditions in (4.19) with $k_a = 2.212, k_d = 0.05, k_i = 72, l = 1200, d_f = 43.2, d_b = 72, d_p = 1.73 \times 10^{-3}, \nu = 4, \eta = 0.02, \mu = 1.73 \times 10^{-3}, c_1 = 0, c_2 = 43.2, c_3 = 0.5, d_m = 0.5$, and $\rho_l = \rho_f = \dfrac{1}{2}$.

The dynamics of the system show that for a specific set of parameters the tumour cell population decreases to zero over time after BPVs are introduced. We notice some interesting dynamics in the free receptors, initially there is a quick decrease due to the fast initial binding with ligands on the BPV surfaces. A more gradual decline is then observed as the number of tumour cells, and hence, cell surface receptors decrease to zero. We notice that, with these parameters, the majority of BPVs are bound by only 1 complex and are then quickly internalized, with the maximum number of internalized BPVs occurring after around 1 hour. The solution for intracellular drug exhibits a similar behaviour as the internalized BPVs, as we would expect as the drug release assumed to be proportional to the rate of internalization of BPVs.

In Figure 4.2, although the assumed maximum number of complexes that can form is set to 20, the majority are bound with only 1 complex, with only a small number being bound by 2 complexes. A slight change in parameters $\rho_{l,f}$ show that BPVs can bind to a much larger number of receptors before being internalized. As shown in Figure 4.3.

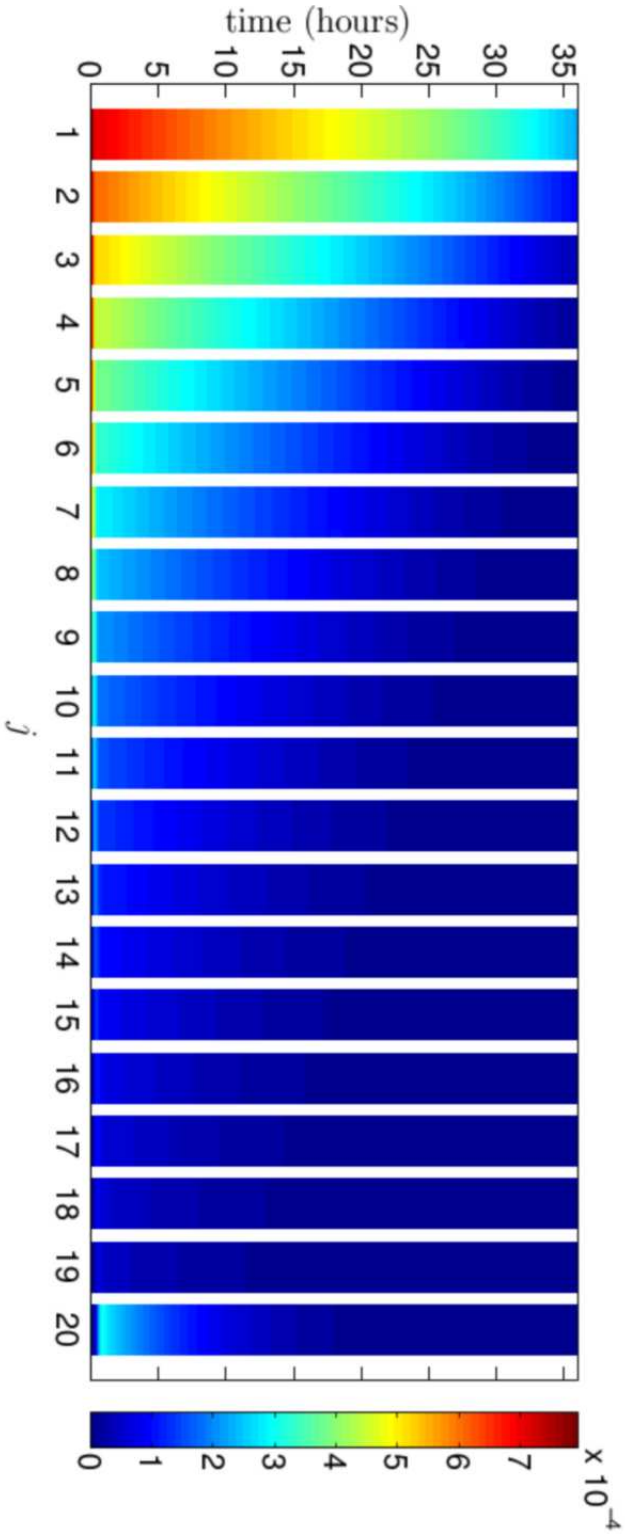

Figure 4.3: Shown are the densities of BPVs bound with j complexes as time increases, with $\rho_l = \rho_f = 1$ and $k_i = 881.9$, the remainder of the parameter values are as in Figure 4.2.

We notice when $j = 20$ that there is a slight accumulation of B^{20}, this is due to the truncation of the maximum number of complexes that can form, we have assumed at $n = 20$. We introduced this as there is very little or no binding occuring past this value in Figure 4.2. Hence even though there appears to be little binding events occuring after $j = 13$ there is still some binding occuring, due to the truncation of n at 20 we see the accumulation of B^{20} which are then internalized quickly.

We have seen that by increasing the proportion of receptors and ligands available for binding (ρ_f and ρ_l respectively) we see that BPVs are bound by an increasing number of complexes before either internalization or subsequent binding between receptors and ligands. Not shown in Figure 4.3 is that a longer time frame must be observed to see the tumour cell population decrease to zero as a result of the greater number of BPVs held on the cell surface and not being internalized. This simple result indicates that a small parameter change may result in a significant change in the system dynamics, hence in the next section we look to a parameter sensitivity analysis to examine this fully.

4.3.1 Parameter Sensitivity

As shown in Figure 4.3, only slightly varying some parameters results in significant changes within the system. In this section, we examine this further by carrying out a parameter sensitivity analysis.

We solve the system numerically in MATLAB again using an ODE solver, `ode45`. The first parameters we examine represent the proportion of ligands and receptors available for 2-D binding, ρ_l and ρ_f respectively. Recall that $\rho_l, \rho_f \in (0, 1]$. By varying ρ_l, we are either varying the tether length of the ligand or size of the

BPV. When varying ρ_f, we are mimicking the rate of clustering of receptors on the cell surface.

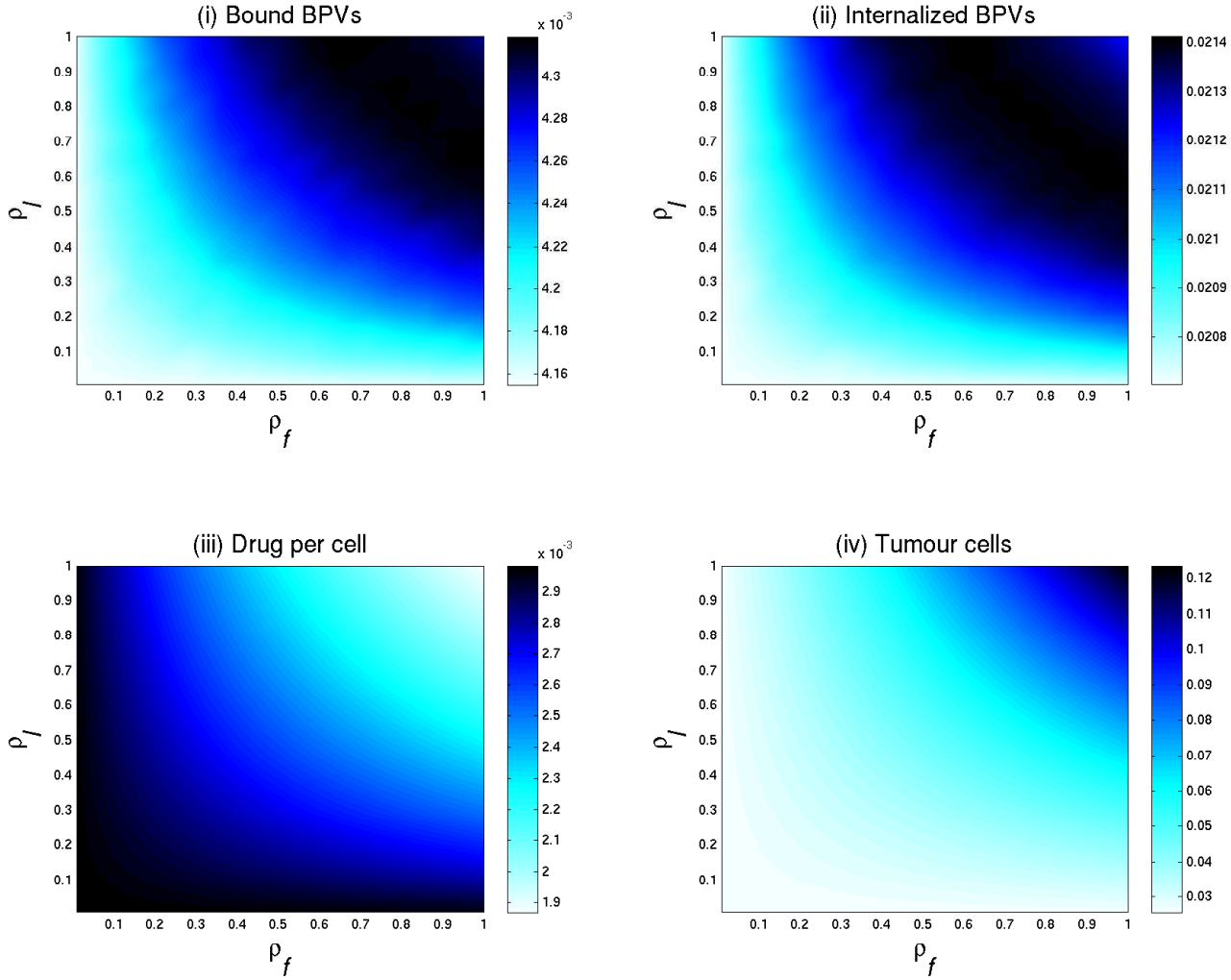

Figure 4.4: Shown are the non-dimensional densities of (i) bound BPVs, (ii) internalized BPVs, (iii) drug per cell and (iv) tumour cells when ρ_l and ρ_f are varied and $l = 1200$, at $t = 2$. Recall that $\rho_l, \rho_f \in (0, 1]$. The remaining parameters are as in Figure 4.2.

In Figure 4.4, we notice that if we have a high proportion of receptors and ligands available for binding the tumour cell density is at its highest. Recall, when varying ρ_f we are essentially varying receptor clustering on the cell surface (i.e. reducing ρ_f from 1 results in smaller receptor clusters), and by varying ρ_l we are implicitly modelling the size of the BPV and tether length of the ligand (tether length is the maximum length the ligands can extend to). For example, for a fixed BPV diameter, a high ρ_l would indicate a large tether length, or a low ρ_l would indicate a short tether length. When $\rho_f, \rho_l \approx 1$, we have high tumour density which is a result of the long tethers allowing many complexes to form. This extended binding slows the internalization rate of the BPVs and therefore less anti-cancer drug is released intracellularly.

We now vary the parameters ρ_l and l, the proportion of ligands available for binding and the (fixed) number of ligands per BPV, respectively. The results are shown in Figure 4.5. First, we notice that with a high number of ligands per BPV and large proportion of ligands available for binding ($\rho_l \approx 1$) the tumour cell population is relatively high. This is a similar result to that seen in Figure 4.4 whereby there is an increased number of complex formation which leads to slower internalization of the BPVs which then results in a higher density of tumour cells due to less drug being released intracellularly. This is a significant result which we would not have originally expected. Intuitively, we would expect that having a high number of ligands would account for more BPV binding, internalization and subsequently more cell death.

In Figure 4.6, we examine the behaviour of the system when we vary ρ_l and k_a, where k_a is the association rate of receptor-ligand binding.

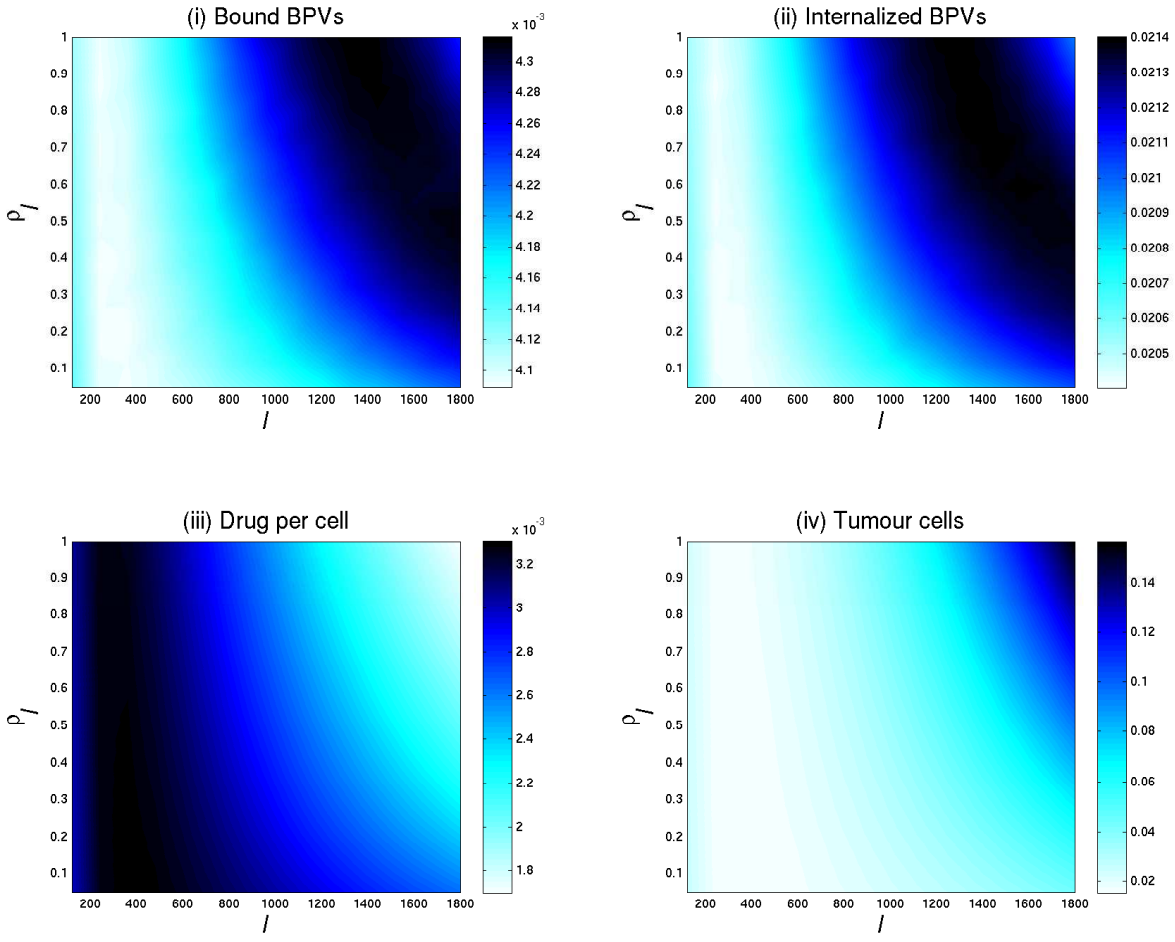

Figure 4.5: Shown are the non-dimensional densities of (i) bound BPVs, (ii) internalized BPVs, (iii) drug per cell and (iv) tumour cells when ρ_l and l are varied with $k_i = 72$ and $\rho_f = 0.5$, at $t = 2$. Recall that $\rho_l \in (0, 1]$. The remaining parameters are as in Figure 4.2.

When varying ρ_l and k_a together, we notice that if we increase the association rate, k_a, we see a decrease in tumour density with a greater decrease if the proportion of ligands, ρ_l, is low. The highest density of tumour cells occurs when k_a is low with a high proportion of ligands available for 2-D binding.

Having a higher association rate results in more BPVs being bound but a lower proportion of ligands results in less internalization inhibition that we have seen previously with high ρ_l (see Figures 4.4 and 4.5).

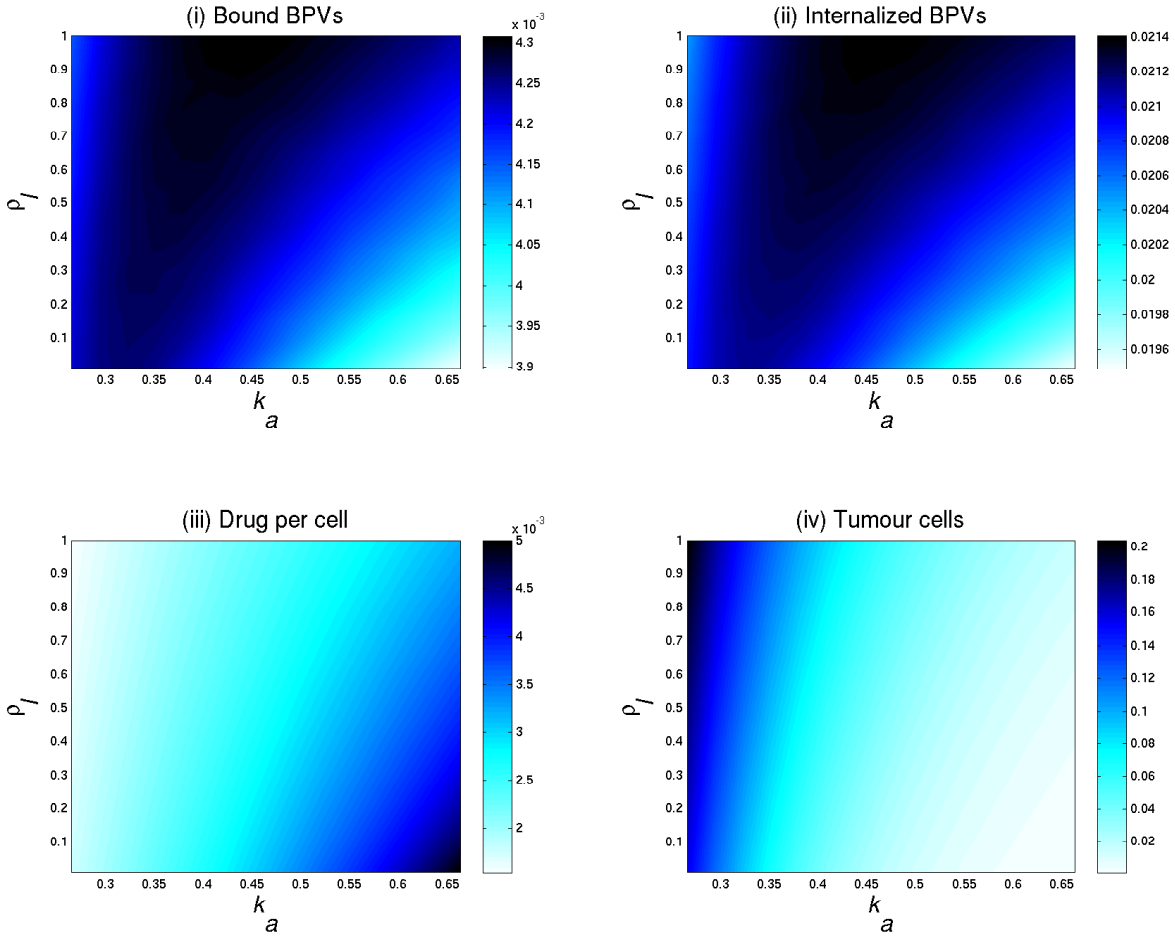

Figure 4.6: Shown are the non-dimensional densities of (i) bound BPVs, (ii) internalized BPVs, (iii) drug per cell and (iv) tumour cells when ρ_l and k_a are varied with $k_i = 72, l = 1200$ and $\rho_f = 0.5$, at $t = 2$. Recall that $\rho_l \in (0, 1]$. The remaining parameters are as in Figure 4.2.

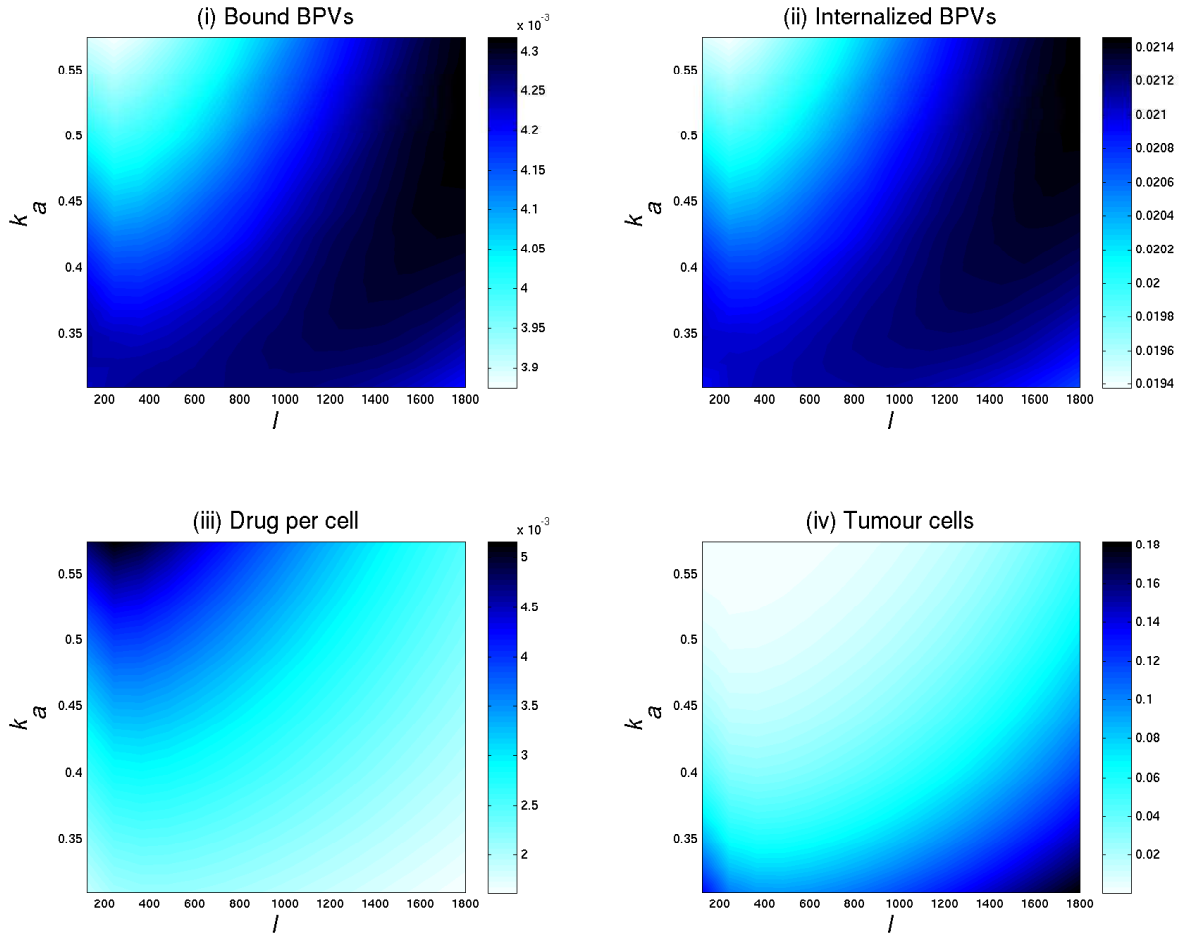

Figure 4.7: Shown are the non-dimensional densities of (i) bound BPVs, (ii) internalized BPVs, (iii) drug per cell and (iv) tumour cells when k_a and l are varied with $k_i = 72$ and $\rho_l, \rho_f = 0.5$, at $t = 2$. The remaining parameters are as in Figure 4.2.

We now vary the number of ligands available for binding and the binding association rate, l and k_a respectively (shown in Figure 4.7). This is a similar result to that of Figure 4.6, whereby a high association rate and low proportion of ligands results in a low density of tumour cells. The low number of ligands

reduces the internalization inhibition that is seen with high numbers of ligands, and hence more drug is released and tumour cell density decreases.

In Figure 4.8, we focus our attention on just the change of tumour cell density when varying k_i, l, k_d, ν and μ. In (i), we vary the internalization rate k_i and the number of ligands per BPV, l. We notice that there is little change in tumour density if we increase k_i. As we increase l, the tumour density increases to a slightly higher density when k_i is low. As we have seen before, a higher number of ligands inhibits the internalization process and by reducing the internalization rate further results in a higher tumour density.

In (ii) we vary the dissociation rate and number of ligands per BPV, k_d and l respectively. We notice that any change in k_d does not significantly affect the final densities of tumour cells and we only see variation by changing l. As we have seen previously increasing l, the number of ligands per BPV, results in an increased density of bound BPVs on tumour cells and an increased tumour cell density. Figure 4.8 (iii) shows the variation in tumour cell density when we vary μ and ν, where μ is the death rate associated with intracellular drug and ν is the proportion of drug that is released when a BPV ruptures. As expected, when increasing μ and ν, the tumour density decreases due to the higher volume and potency of drug delivered to the cells. The final parameters, in (iv), are μ and d_b, where d_b is the rate of BPV rupture once internalized. As μ is increased there is a decrease in tumour density (and bound BPVs), but this is independent of the value of the chosen range of d_b.

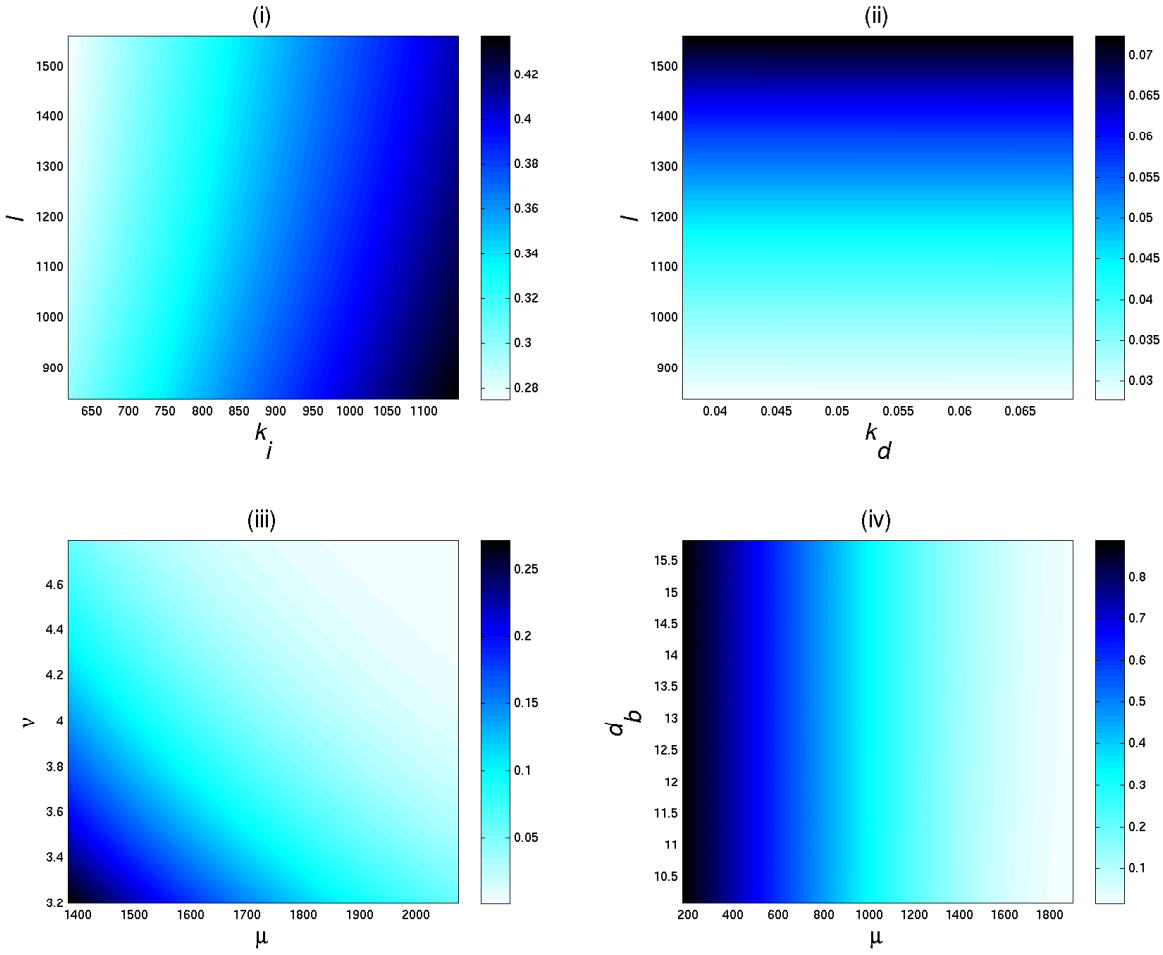

Figure 4.8: Shown are the non-dimensional density of tumour cells when parameters are varied, (i) varying l, k_i, (ii) varying l, k_d, (iii) varying μ, ν and finally in (iv) we vary μ and d_b. The tumour density is calculated at time, $t = 2$, all parameter values are given in Table 4.1

We have carried out an extensive parameter sensitivity analysis which has given insight into how specific parameters affect the dynamics of the multiple binding model framework. We now know that the dissociation rate, k_d, has little affect on the overall system dynamics, and there is an optimal number of ligands on

the BPV surface where exceeding this results in a slower internalization and hence a slower tumour cell death.

In the next section, we explore the fast transition that we observe in the receptor numbers near $t = 0$ (see, for example, Figure 4.2 (iv)).

4.4 Singular Perturbation Analysis

When solving the non-dimensional system, given by (4.11)-(4.18), numerically, we see that the solutions for $V(t)$, $F(t)$ and $B(t)$ change very quickly at early time due to the fast binding kinetics of the receptors and ligands (for example see Figure 4.2). To get an analytical handle on this we carry out a singular perturbation analysis.

For simplicity, we consider a single binding interaction, i.e. only one complex between ligand and receptor has to form for the drug-loaded BPV to be internalized. We do this by setting $\rho_l = l^{-1}$ and $\rho_f = 0$ so that $B^i(t) = 0$ for $2 \leq i \leq n$, and so the model is now given by:

$$\frac{dm}{dt} = m(1-m) - g(\phi)m, \tag{4.20}$$

$$\frac{dV}{dt} = -k_a VF + \frac{k_d}{l}B, \tag{4.21}$$

$$\frac{dF}{dt} = -\eta k_a lVF + \eta k_d B - d_f F + R(b)m, \tag{4.22}$$

$$\frac{dB}{dt} = k_a lVF - (k_d + k_i)B, \tag{4.23}$$

$$\frac{dB_{in}}{dt} = \frac{k_i}{l}B - d_b B_{in}, \tag{4.24}$$

$$\frac{dP}{dt} = \nu d_b B_{in} - d_p P, \tag{4.25}$$

where $B^1(t)$ has been replaced with $B(t)$ for notational convenience, with

$$R(b) = c_1 + \frac{c_2^\alpha b^\alpha}{c_3^\alpha + b^\alpha} \quad \text{and} \quad g(\phi) = d_m + \frac{\mu\phi^\beta}{1+\phi^\beta}, \tag{4.26}$$

where $P = \phi m$ and $B = bm$. We solve the system, (4.20)-(4.25), numerically and the results are shown in Figure 4.9. We notice the same very quick change in solutions as seen in the full model results.

For further simplification of the model we notice that, with the parameter values described in the previous section, we have $\frac{k_d}{l} \sim O(10^{-5})$, $k_d \sim O(10^{-3})$ and $\eta k_d \sim O(10^{-4})$. Also, knowing from the parameter sensitivity that having $k_d = 0$ does not significantly change the dynamics we set $k_d = 0$. To make the system as simple as possible we also look to simplify the saturating functions $R(b)$ and $g(\phi)$, given by (4.26), we make $g(\phi)$ linear. To simplify $R(b)$, we assume that c_3 is small, remember that c_3 is the threshold value for the half maxium value of $R(b)$. With c_3 small we can assume,

$$R(b) = c_1 + \frac{c_2^\alpha b^\alpha}{b^\alpha},$$

leading to $R(b) = c_2$. Note that $c_1 = 0$ as before. The numerical system dynamics do not change when using these simplifications.

The reduced system is then given by

$$\begin{aligned}
\frac{dm}{dt} &= m(1-m) - \mu\phi m, && (4.27)\\
\frac{dV}{dt} &= -k_a V F, && (4.28)\\
\frac{dF}{dt} &= -\eta k_a l V F - d_f F + c_2 m, && (4.29)\\
\frac{dB}{dt} &= k_a l V F - k_i B, && (4.30)\\
\frac{dB_{in}}{dt} &= \frac{k_i}{l} B - d_b B_{in}, && (4.31)\\
\frac{dP}{dt} &= \nu d_b B_{in} - d_p P. && (4.32)
\end{aligned}$$

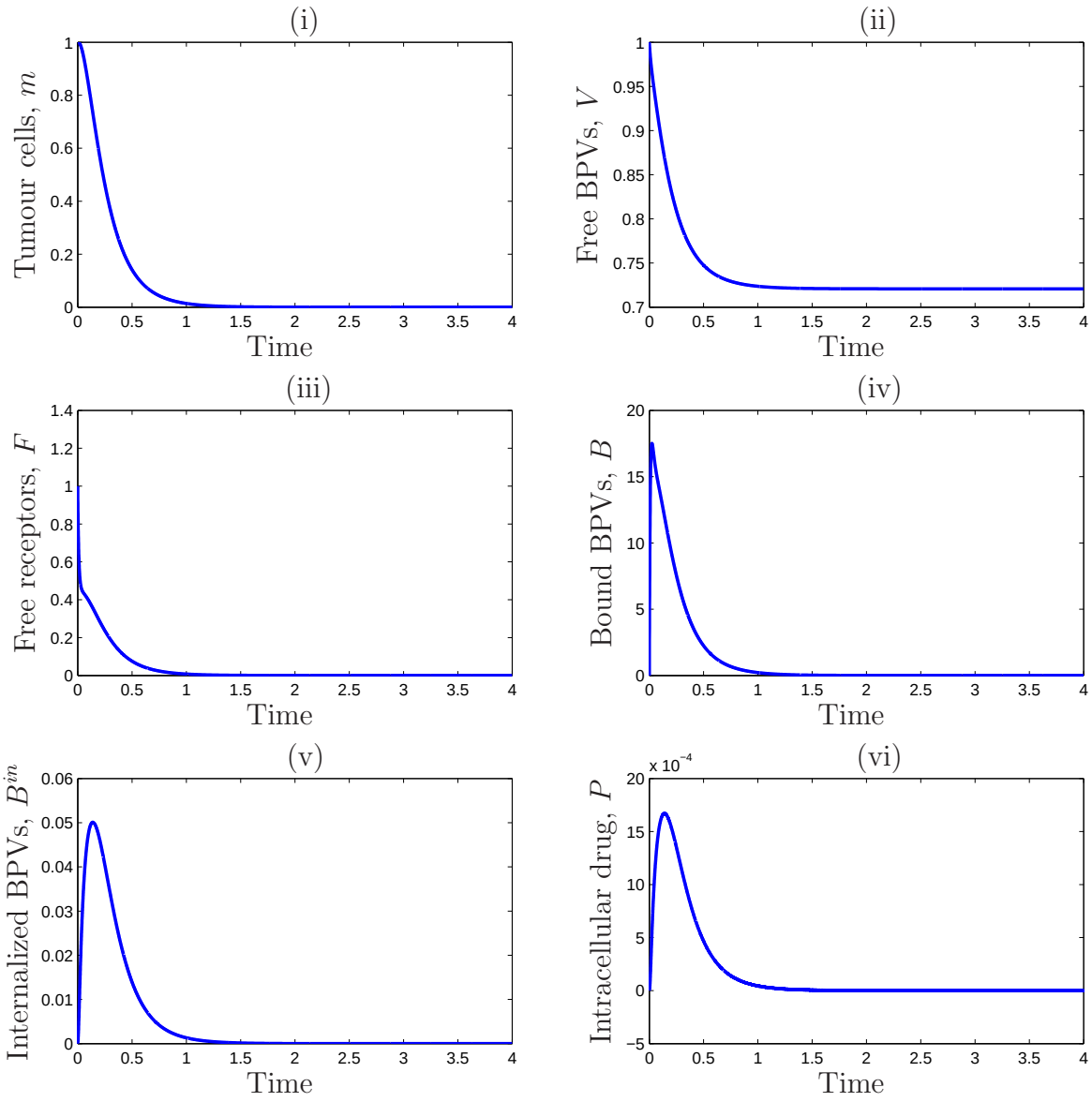

Figure 4.9: Numerical solution of the non dimensional single binding model (4.20)-(4.25) solved with initial conditions $m(0) = 1, V(0) = 1, F(0) = 1, B(0) = 0, B_{in}(0) = 0$ and $P(0) = 0$. The remaining parameters are the same as those in Figure 4.2.

Recall that $\phi = \dfrac{P}{m}$. Figure 4.10 shows the comparison between the numerical results produced from the full system, given by (4.20)-(4.25), and this reduced system, given by (4.27)-(4.32), where terms involving k_d are set to zero and the saturating functions describing receptor recycling and tumour cell death are replaced by linear functions. We notice that these changes do not significantly affect the dynamics of the system, and so we take the reduced system as an acceptable approximation to the full system for this analysis.

To carry out the perturbation analysis, we first look at the orders of magnitude of the parameter groupings involved in the kinetics of receptors and ligands. Recall that the parameter values are as follows: $k_a = 2.212$, $l = 1200$, $\eta = 0.002$ and $d_f = 43.2$. Hence we can write $\eta l = \dfrac{\widehat{\eta l}}{\varepsilon}$ and $d_f = \dfrac{\hat{d}_f}{\varepsilon}$ where $\varepsilon \ll 1$. We should note here that the values for c_2 and d_f are equal, hence we replace c_2 with d_f for notational convenience. After rescaling we want these terms to be of comparible order of magnitudes. These parameter rescalings only occur in the equation for free receptors, given by (4.29), hence we obtain

$$\varepsilon \frac{dF}{dt} = -k_a \widehat{\eta l} V F - \hat{d}_f F + \hat{d}_f m. \tag{4.33}$$

Further analysis will be carried out with the hats dropped for convenience.

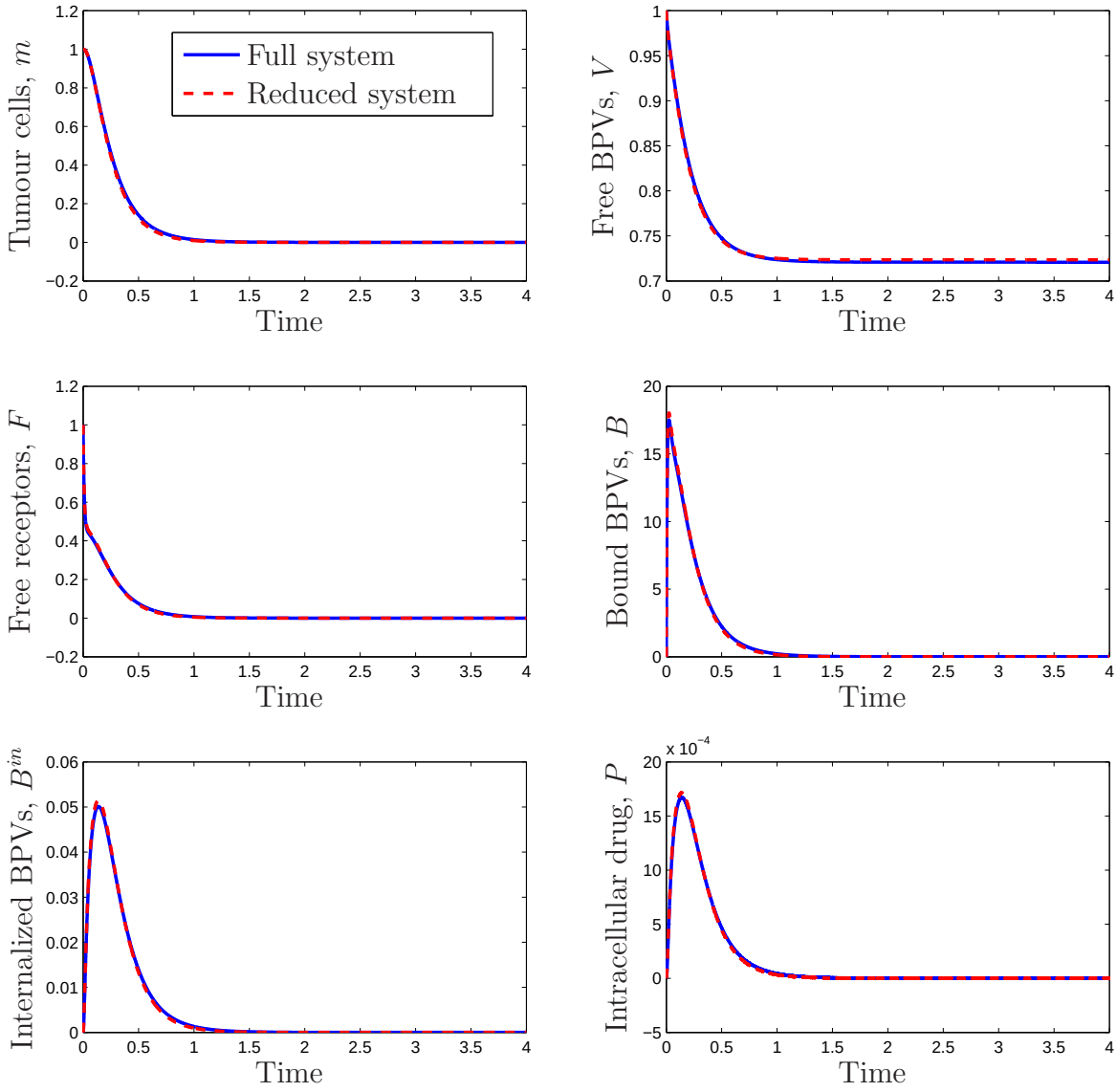

Figure 4.10: Numerical solution of the non-dimensional single binding model, solved with initial conditions: $m(0) = 1, V(0) = 1, F(0) = 1, B(0) = 0, B_{in}(0) = 0$ and $P(0) = 0$. The blue line represents the full system, (4.20)-(4.25), when solved with $R(b) = c_1 + \dfrac{c_2^{\alpha} b^{\alpha}}{c_3^{\alpha} + b^{\alpha}}$ and $g(\phi) = d_m + \dfrac{\mu \phi^{\beta}}{1 + \phi^{\beta}}$. The red dashed line represents the reduced system, (4.27)-(4.32), where $k_d = 0$ and solved with $R(b) = c_2 m$ and $g(\phi) = \mu\phi$. Note that in the full system $c_1 = d_m = 0$, and $c_2 = d_f$. The remaining parameters are the same as those in Figure 4.2.

We now look to find the inner solutions of the system by assuming $t = \tau\varepsilon$. Using this assumption the system then becomes

$$\begin{aligned}
\frac{dm}{d\tau} &= \varepsilon m(1-m) - \varepsilon\mu P, && (4.34)\\
\frac{dV}{d\tau} &= -\varepsilon k_a V F, && (4.35)\\
\frac{dF}{d\tau} &= -k_a\eta l V F - d_f F + d_f m, && (4.36)\\
\frac{dB}{d\tau} &= \varepsilon k_a l V F - \varepsilon k_i B, && (4.37)\\
\frac{dB_{in}}{d\tau} &= \varepsilon\frac{k_i}{l}B - \varepsilon d_b B_{in}, && (4.38)\\
\frac{dP}{d\tau} &= \varepsilon\nu d_b B_{in} - \varepsilon d_p P. && (4.39)
\end{aligned}$$

These parameter rescalings allow us to find the simple leading order solutions ($\varepsilon = 0$) in the inner region for m and P, given by $m = 1$ and $P = 0$, as given by the initial conditions. These solutions allow us to solve the more complicated leading order solution for free receptors, F. Note that the equations for bound BPVs (B) and internalized BPVs (B_{in}) decouple from the system. We shall return to these later.

Now, using the expansions, $V(\tau;\varepsilon) = \sum_{n=0}\varepsilon^n V^n$ and $F(\tau;\varepsilon) = \sum_{n=0}\varepsilon^n F^n$, we look for the inner solutions for free BPVs and free receptors.

To leading order, the equation for free BPVs, (4.35), is

$$\frac{dV^0}{d\tau} = 0. \tag{4.40}$$

Solving this with the intital condition $V(0) = V_0$, the leading order solution is then given simply by

$$V^0(\tau) = V_0. \tag{4.41}$$

Using this solution, we now look for the leading order solution for free receptors. Equation (4.36) becomes

$$\frac{dF^0}{d\tau} + (k_a\eta l V_0 + d_f)F^0(\tau) = d_f,$$

which is easily solved using the integration factor method with initial condition $F^0(0) = F_0$. The resulting solution then reads

$$F^0(\tau) = \frac{d_f}{\beta} + C_1 \exp(-\beta\tau), \tag{4.42}$$

where

$$\beta = k_a \eta l V_0 + d_f \quad \text{and} \quad C_1 = F_0 - \frac{d_f}{\beta}. \tag{4.43}$$

We know, by looking at the numerical solution for free BPVs (see Figure 4.10), that within this time range the $V(t)$ solution is not constant. Hence, we look to $O(\varepsilon)$ to find a more accurate solution for free BPVs, namely to $O(\varepsilon)$ we have

$$\frac{dV^1}{d\tau} = -k_a V^0(\tau) F^0(\tau).$$

Using (4.42) then leads to

$$\frac{dV^1}{d\tau} = -k_a V_0 \left(\frac{d_f}{\beta} + C_1 \exp(-\beta\tau) \right),$$

which can be easily solved by direct integration with respect to τ to give

$$V^1(\tau) = -k_a V_0 \left(\frac{d_f \tau - C_1 \exp(-\beta\tau)}{\beta} \right) + C_2. \tag{4.44}$$

With the initial condition, $V^1(0) = 0$, we then have

$$C_2 = -\frac{k_a V_0 C_1}{\beta}.$$

In Figure 4.11, we show the inner analytical solutions for free BPVs and free receptors, $V(t)$ and $F(t)$ respectively, compared to the corresponding numerical solutions. We see that the inner solutions are valid for early time producing a good match with the numerical solutions.

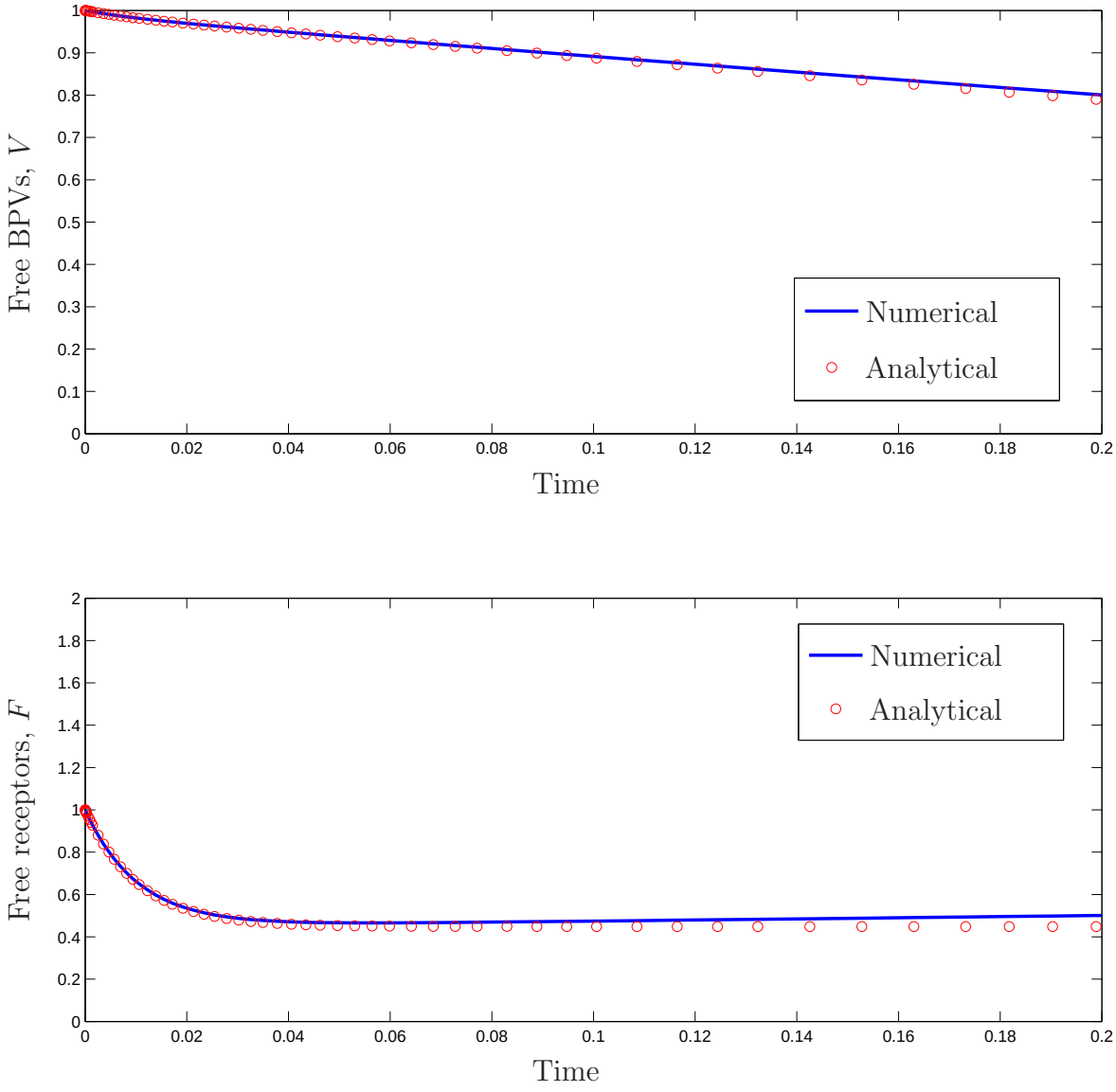

Figure 4.11: Showing the numerical and (inner) analytical solutions of free BPVs and free receptors from the non-dimensional single binding model, when solved with $m(0) = 1$, $P(0) = 0$, $V(0) = V_0$ and $F(0) = V_0$. The blue line represents the numerical solution and the red circles represent the inner analytical solution when using the assumptions $t = \tau\varepsilon$, $\widehat{\eta l} = \eta l\varepsilon$ and $\hat{d}_f = d_f\varepsilon$, where $\varepsilon = 0.1$. The remaining parameters are as in Figure 4.10.

We now use the leading order inner solutions for free BPVs, (4.41), and free receptors, (4.42), to find the solutions for the decoupled equations for bound BPVs and internalized BPVs, $B(t)$ and $B_{in}(t)$ respectively. Recall the equation for bound BPVs,

$$\frac{dB}{dt} = k_a l V(t) F(t) - k_i B(t),$$

where to leading order $V(t) = V_0$ and $F(t) = F^0(t)$. Therefore, we have

$$\frac{dB}{dt} = k_a l V_0 \left(\frac{d_f}{\beta} + C_1 \exp(-\beta t) \right) - k_i B(t),$$

where C_1 is defined in (4.43). Again we can solve for $B(t)$ using the integration factor method to give,

$$B(t) = k_a l V_0 \left(\frac{d_f}{\beta k_i} + \frac{C_1 \exp(-\beta t)}{k_i - \beta} \right) + C_3 \exp(-k_i t), \tag{4.45}$$

which, when solved with the intital condition $B(0) = 0$, gives

$$C_3 = -k_a l V_0 \left(\frac{d_f}{\beta k_i} + \frac{C_1}{k_i - \beta} \right).$$

We now use the solution for bound BPVs, (4.42), to solve for internalized BPVs. Recall the equation for $B_{in}(t)$ is given by

$$\frac{dB_{in}}{dt} = \frac{k_i}{l} B(t) - d_b B_{in}(t).$$

Which, by using (4.42), leads to

$$\frac{dB_{in}}{d\tau} + d_b B_{in}(t) = \frac{k_i k_a V_0}{l} \left(\frac{d_f}{\beta k_i} + \frac{C_1 \exp(-\beta t)}{k_i - \beta} \right) + C_3 \exp(-k_i t),$$

which can again be solved using the integration factor method. Note that we use the following parameter groupings for simplicity

$$\gamma_1 = \frac{k_a l V_0 d_f}{\beta k_i}, \;\; \gamma_2 = \frac{k_a l V_0 C_1}{k_i - \beta} \;\text{ and }\; \gamma_3 = \frac{k_i}{l}. \tag{4.46}$$

The solution for internalized BPVs can then be calculated as

$$B_{in}(t) = \frac{\gamma_1 \gamma_3}{d_b} + \frac{\gamma_2 \gamma_3}{d_b - \beta} \exp(-\beta t) + \frac{C_3 \gamma_3}{d_b - k_i} \exp(-k_i t) + C_4 \exp(-d_b t), \tag{4.47}$$

which, when solved with the initial condition $B_{in}(0) = 0$, we have

$$C_4 = -\frac{\gamma_1\gamma_3}{d_b} - \frac{\gamma_2\gamma_3}{d_b - \beta} - \frac{C_3\gamma_3}{d_b - k_i}.$$

In Figure 4.12, we show the comparison between numerical and analytical solutions for bound BPVs, $B(t)$, and internalized BPVs, $B_{in}(t)$, in the inner time region. We see a good match between the numerical and analytical solutions.

We observe from Figure 4.12 (upper panel) that the maximum number of bound BPVs occurs at a turning point (which occurs are around $t = 0.02$ in Figure 4.12. We now look for an approximated analytical value of this maximum. Recall the solution for bound BPVs, (4.45), is given by

$$B(t) = k_a l V_0 \left(\frac{d_f}{\beta k_i} + \frac{C_1 \exp(-\beta t)}{k_i - \beta} \right) + C_3 \exp(-k_i t),$$

where β, C_1 and C_3 are defined above. In the usual way, we can differentiate this with respect to t to find the maximum. The turning point then occurs when $\dfrac{dB}{dt} = 0$. This can be calculated to occur at $t = t^*$, where

$$t^* = \frac{1}{\beta - k_i} \ln \left(\frac{C_3 k_i (\beta - k_i)}{k_a l V_0 C_1 \beta} \right),$$

therefore the maximum of number bound BPVs is then given by

$$\begin{aligned} B^{max} \;=\; B(t^*) \;&=\; k_a l V_0 \left(\frac{d_f}{\beta k_i} + \frac{C_1}{k_i - \beta} \left(\frac{k_a l V_0 C_1 \beta}{C_3 k_i (\beta - k_i)} \right)^{\frac{\beta}{\beta - k_i}} \right) \\ &\quad + C_3 \left(\frac{k_a l V_0 C_1 \beta}{C_3 k_i (\beta - k_i)} \right)^{\frac{k_i}{\beta - k_i}}, \end{aligned} \tag{4.48}$$

where $\beta = k_a \eta l V_0 + df$.

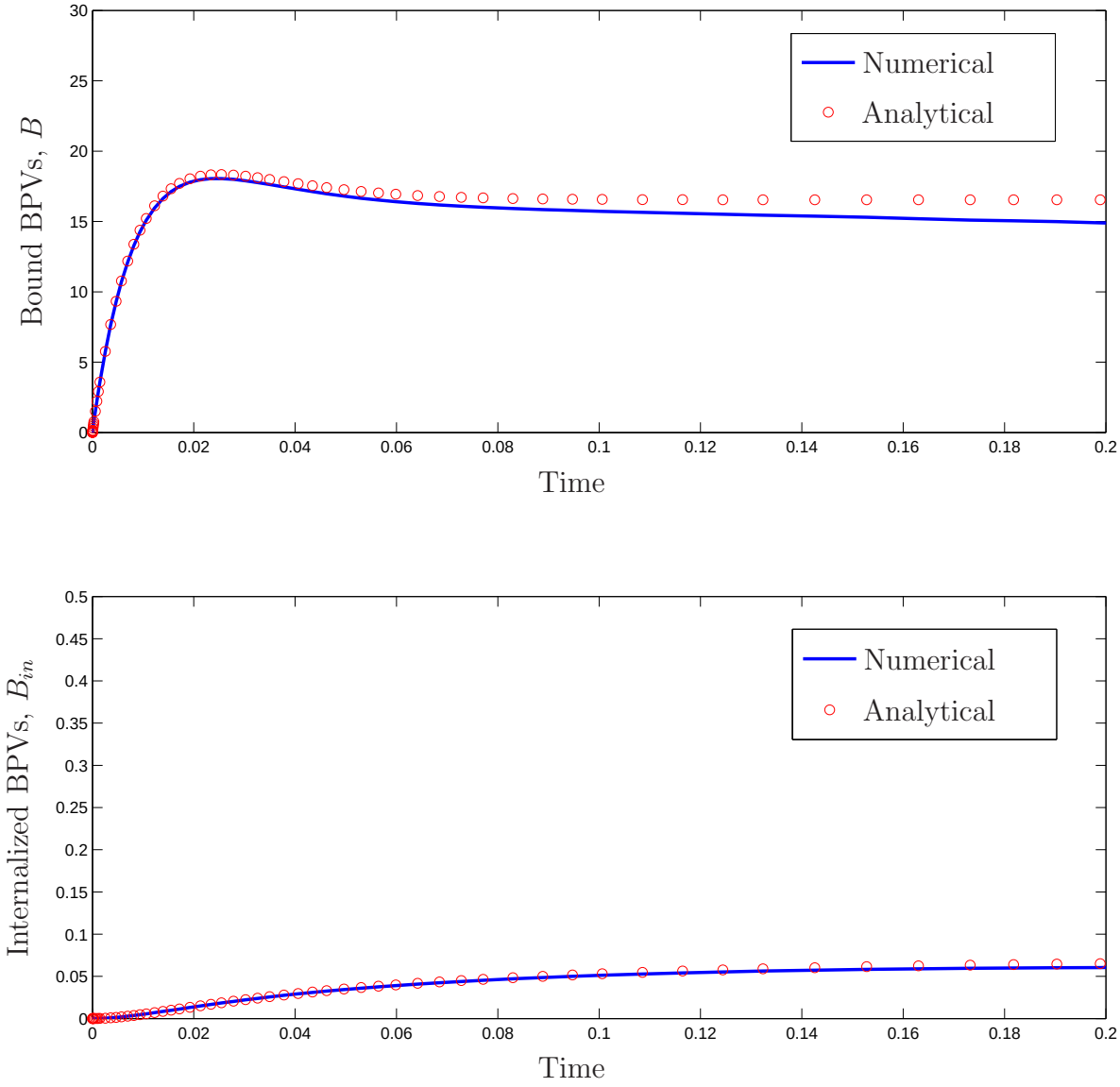

Figure 4.12: The numerical and analytical solutions of bound BPVs and internalized BPVs from the non-dimensional single binding model, when solved with $m(0) = 1$, $P(0) = 0$, $B(0) = 0$ and $B_{in}(0) = 0$. The blue line represents the numerical solution and the red circles represent the inner analytical solution. The remaining parameters are as in Figure 4.10.

Similarly, we can find the maximum of internalized BPVs. The analytical solution (4.47) tends to a constant value which, by observing the solutions in Figure 4.12, is the maximum value of the B_{in} numerical solution. Hence, the peak of internalized BPVs can be approximated using the analytical solution, (4.47), when $t \to \infty$, giving

$$B_{in} \to \frac{\gamma_1 \gamma_3}{d_b}, \quad \text{as} \quad t \to \infty.$$

Therefore the approximate maximum of internalized BPVs is given by

$$B_{in}^{max} = \frac{\gamma_1 \gamma_3}{d_b}, \tag{4.49}$$

where γ_1 and γ_3 are defined as in (4.46).

We now look to the behaviour of these quantities B^{max} and B_{in}^{max} when we vary key parameters. In Figure 4.13, we observe that B^{max} is an increasing saturating function of l, the fixed number of ligands per BPV. As we increase l, the maximum bound BPVs increases until it saturates. The internalized BPVs decreases exponentially as l increases, which indicates that, by having a large number of ligands, the internalization rate by tumour cells slows as we saw previously. As we would expect, B^{max} and B_{in}^{max} are both increasing saturating functions of k_a and exponentially decreasing functions of η as observed previously in the parameter sensitivity analysis.

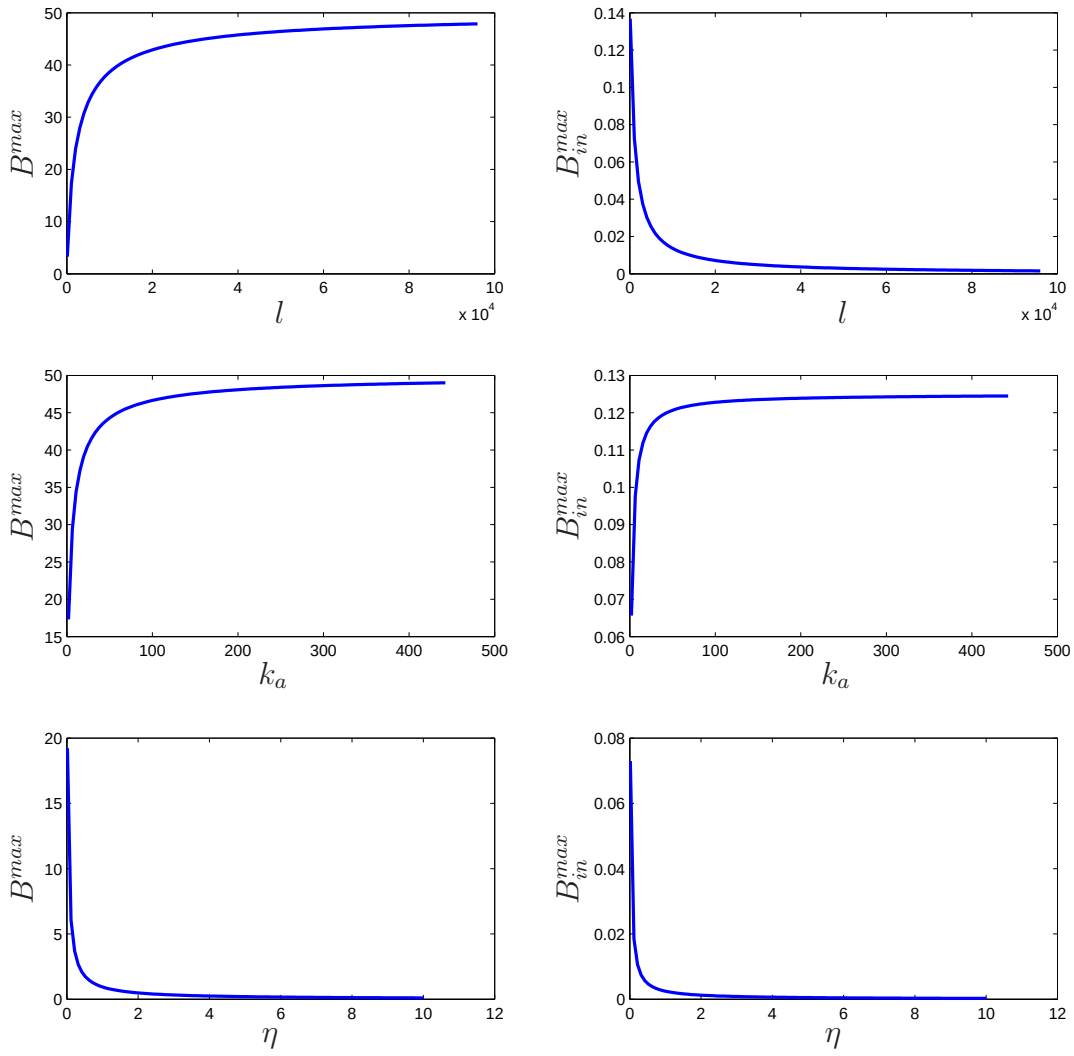

Figure 4.13: The analytical expression of the maximum bound BPVs and maximum internalized BPVs, given by B^{max} (first column) and B_{in}^{max} (second column). In the first row we vary l, the second row we vary k_a and in the third row we vary η. The remaining parameters are as in Figure 4.10.

4.5 Discussion

In this chapter, we present a mathematical model that describes the binding kinetics of synthetically produced biomimetic polymer vesicles (BPVs) to tumour cells. The system is described by ordinary differential equations. The model assumes that once a receptor-ligand complex forms, the BPV becomes bound to the tumour cell. We allow for multiple binding events to occur mimicking the behaviour of receptor-mediated endocytosis. Once bound to the cell, the BPV can be internalized, a process which we assume in this chapter is not dependant on the number of complexes present (we relax this assumption in the next chapter). Once internalized the BPV then ruptures, releasing the drug payload.

The model described is for a new cancer therapy, and as such it was very difficult to find parameter values specifically for this biological system. We looked to a similar model by Ghaghada *et al* [36] which describes liposomal targeting to tumour cells and we used this to find base parameter values for the binding kinetics of the BPVs (association, dissociation and internalization rates). Due to the uncertainty surrounding some of the parameters, we carry out a parameter sensitivity analysis which highlights how key parameters affect the model dynamics. The results from the parameter sensitivity facilitates a singular perturbation analysis, and also highlights that there is an optimal number of ligands per BPV to give maximum cell death.

In the singular perturbation analysis, we assume a single binding event which reduces the system. We further simplify the system by ignoring the BPV dissociation rate and linearising the functions that describe receptor recycling and cell death. We notice that these changes do not affect the observed early time system dynamics. By carrying out this analysis we can answer some important biological questions regarding the early kinetics of the BPV uptake. Using

the expression we obtained for the maximum number of bound BPVs, given by equation (4.45), we can show that the maximum number of bound BPVs is an increasing saturating function of l (number of ligands per BPV). This saturating nature shows that, after some given value of l, increasing l further has little effect. Indeed, we have seen that by having more than an optimal number of ligands, results in there being more bound BPVs, but this also results in a much slower internalization rate and a smaller peak of internalized BPVs and ultimately a reduced tumour cell death.

The findings from the perturbation analysis can be extremely useful for biologists working on this targeted therapy as the number to targeted ligands on BPVs (l in our model) is something specific to the BPV structure that can be modified during the manufacturing of the BPVs.

Chapter 5

BPV Infiltration into Tumour Spheroids

5.1 Introduction

The initiation of tumour growth begins with a mutated cell that can evade growth signals (for example, that signal apoptosis) from surrounding normal cells. As the mutated cell divides, a mass of cells will form that can develop into a tumour. The tumour mass can grow until it reaches a saturation size, roughly 2mm in diameter afterwhich the growth of the mass appears dormant [42]. *In vivo*, the tumour is referred to as an avascular tumour since it doesn't have a dedicated blood supply. A good *in vitro* representation of this is a tumour spheroid. The tumour acquires nutrients from the surrounding environment and so, once the tumour reaches this critical size, the inner regions of the tumour become deprived of nutrients, which then leads to a hypoxic region. As the inner cells are constantly not receiving nutrients they lyse creating an inner

necrotic core (of dead cells). So, the tumour spheroid typically has 3 regions, an inner necrotic core, a hypoxic region (where cells are quiescent) and an outer proliferating edge (which is a relatively thin layer of reproducing cells which has access to nutrients) [87] see Figure 5.1 for a sketch of this process.

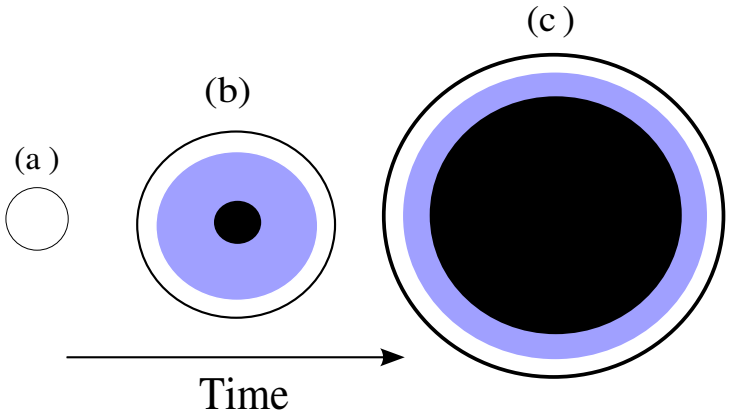

Figure 5.1: Sketch of the development of a tumour spheroid with increasing time. (a) The spheroid is at early development, where cells are proliferating exponentially. (b) The spheroid represents the linear growth stage, where the quiescent region forms and an inner necrotic (dead) core. (c) The tumour spheroid is at its saturated size, the white represents proliferating cells, blue region represents quiescent cells and the black region is the necrotic (dead) core.

In vivo, the cells within the hypoxic region typically release tumour angiogenic factors (TAFs) [53]. These TAFs, such as VEGF, encourage the blood epithelial cells to migrate towards the tumour, restoring the blood supply. Nutrients available to the tumour will then encourage growth, and the presence of a blood supply also allows for the spread of the malignant tumour as cells can then break away and create metastatic (secondary) tumours in other tissues, in the case of HNSCC this is often to the cervical lymph nodes [49, 84].

A new treatment idea is to treat the cancer using biomimetic polymer vesicles

(BPVs) loaded with anti-cancer drugs (see chapter 4 for full details) [2, 28]. These vesicles are designed to be cancer cell specific and so normal cells are affected minimally by the treatment, unlike conventional chemotherapy where any relatively fast reproducing cell is targeted (for example, stomach epithelial cells or hair follicle cells). The idea is to load the BPVs with a potent chemotherapy agent (such as doxorubicin, DOX) or DNA for gene therapy, which will then infiltrate and be released in the tumour. The tumour cells can endocytose the BPVs and, due to the pH sensitivity of the BPVs, the change from extracellular to endosomal pH (7.4 to 5-6) causes the BPVs to dissociate into its monomers [59]. Subsequently the endosome ruptures, which is thought be be due to the increase in osmotic pressure when the BPV dissociates. This sequence of events then results in the chemotherapy agent being released into the cytosol of the cancer cell.

In this chapter, we present a model for the BPV treatment on an avascular tumour spheroid. We assume that the avascular spheroid grows with a moving boundary on which growth is governed by the balance of proliferating and dying cells. In the model, we assume that tumour cells grow by utilising oxygen and cellular material (a by-product of lysing cells which is also found external to the spheroid *in vitro*). The tumour cells die by two mechanisms, the first is due to the lack of oxygen the second is due to the action of the therapeutic BPVs. We introduce free BPVs onto the spheroid boundary which are then free to permeate and diffuse through the spheroid. BPVs are internalized by the cells by the process of endocytosis, and we specifically look at the case for receptor-mediated endocytosis (as in Chapter 4). In the first half of the chapter, we examine a simple case, where only one binding event (one receptor-ligand complex can form between cell and BPV) is enough for the cell to internalize the BPV. The second half extends this assumption to include multiple binding events. The model is a system of parabolic PDEs with a coupled ODE that

describes the moving boundary. We look at the general dynamics of the system during a short period of treatment and also a large time analysis of continual treatment and aim to define parameter regions in which either linear growth of the spheroid occurs or growth saturates to an equilibrium state.

5.2 Model Derivation

In this section, we describe a radially symmetric model of avascular tumour growth with infiltrating BPVs. The model has two main phases, volume fraction of tumour cells per unit control volume $m(r,t)$ and volume fraction of cellular material per unit control volume $n(r,t)$. We assume that the cellular material is composed mainly of water, proteins and lipids, which is produced when the cells lyse and used when cells divide. The other model variables include oxygen concentration $c(r,t)$, free BPVs per cm^3 $V(r,t)$ (which we assume contributes negligible effect to the volume of the tumour spheroid due to their nanometre-size) and moles of bound BPVs per cm^3 $B(r,t)$. As in Chapter 4, we assume that a free BPV will become bound when a receptor-ligand complex forms between a ligand on a BPV and a receptor on the cells surface, and in this initial simplified case we assume that only one bond is required to form before the BPV can be internalized. We assume that the tumour spheroid occupies $0 \leq r \leq R(t)$ where $R(t)$ is the tumour boundary. We assume that this boundary moves with the velocity of the tumour cells at $r = R(t)$, resulting in a moving boundary problem.

We assume that each of the constitutive phases move with the same common advection velocity which is denoted by $\mathbf{v}(r,t)$. With which, we obtain the following system of partial differential equations

Tumour:

$$\frac{\partial m}{\partial t} = -\frac{1}{r^2}\frac{\partial}{\partial r}\left(r^2 J_m\right) + \overbrace{p_m(n,c)m}^{\text{proliferation}} - \overbrace{d_m(c)m - g(B)}^{\text{death}}, \tag{5.1}$$

Cellular material:

$$\frac{\partial n}{\partial t} = -\frac{1}{r^2}\frac{\partial}{\partial r}\left(r^2 J_n\right) - \overbrace{p_m(n,c)m}^{\text{utilised for growth}} + \overbrace{d_m(c)m + g(B)}^{\text{released from cell lysis}}, \tag{5.2}$$

Oxygen:

$$\frac{\partial c}{\partial t} = -\frac{1}{r^2}\frac{\partial}{\partial r}\left(r^2 J_c\right) - \overbrace{d_c(m,n,c)}^{\text{decay}}, \tag{5.3}$$

Free BPVs:

$$\frac{\partial V}{\partial t} = -\frac{1}{r^2}\frac{\partial}{\partial r}\left(r^2 J_v\right) - \overbrace{k_a V F}^{\substack{\text{association of}\\ \text{BPV to cell}}} + \overbrace{\frac{k_d}{l}B}^{\substack{\text{dissociation of}\\ \text{BPV from cell}}}, \tag{5.4}$$

Bound BPVs:

$$\frac{\partial B}{\partial t} = -\frac{1}{r^2}\frac{\partial}{\partial r}\left(r^2 \frac{B}{m} J_m\right) + \overbrace{k_a L F}^{\substack{\text{association of}\\ \text{free BPV}}} - \overbrace{k_d B}^{\substack{\text{dissociation of}\\ \text{bound BPV}}} - \overbrace{k_i B}^{\substack{\text{internalization by}\\ \text{cell}}}, \tag{5.5}$$

where

$$J_m = -D_m\frac{\partial m}{\partial r} + \mathbf{v}m, \qquad J_n = -D_n\frac{\partial n}{\partial r} + \mathbf{v}n,$$
$$J_c = -D_c\frac{\partial c}{\partial r} + \mathbf{v}c, \qquad J_v = -D_v\frac{\partial V}{\partial r} + \mathbf{v}V,$$

are the fluxes of tumour cells, cellular material, oxygen and BPVs respectively, where D_m and D_n are the random motility coefficients of the 2 phases for tumour cells and cellular material, and D_c and D_v are the diffusion coefficients of oxygen and BPVs, respectively. In equation (5.5) for the flux term we use $\frac{B}{m}J_m$, since bound BPVs do not actively move but are convected at the same velocity of the tumour cells on which they are bound.

The function $p_m(n,c)$ denotes tumour proliferation, which is an increasing saturating function of both on the cellular material and oxygen concentration. The

death rate due to apoptosis, $d_m(c)$, is a decreasing function of the oxygen concentration. The death rate due to the treatment, $g(B)$, is assumed to be linear and proportional to the number of BPVs internalized. In the oxygen equation, there is a decay of oxygen due to tumour cell consumption which increases with tumour cell density, and is given by $d_c(m, n, c)$. We use the following to describe these terms

$$p_m(n, c) = p_m^{max} S(c, c_p) \min\left(\frac{n}{n_0}, 1\right), \qquad d_m(n, c) = d_m^{max}\left(1 - S(c, c_c)\right),$$

$$d_c(m, n, c) = p_{cm}^{max} S(c, c_c)m + p_{cp}^{max} p_m(n, c)m, \qquad g(B) = \gamma k_i B,$$

where

$$S(c, c_p) = \frac{c^\alpha(c_p^\alpha + c_\infty^\alpha)}{c_\infty^\alpha(c_p^\alpha + c^\alpha)}.$$

$S(c, c_p)$ is a scaled Hill function with maximal value $S = 1$ when $c = c_\infty$ (which we assume is the maximum value of oxygen at the tumour boundary), with the steepness of the curve dependent on the value of $\alpha > 0$. The framework we are using here has been adapted from similar work which models the use of therapeutic macrophages [98].

For a free BPV to become bound, a receptor-ligand complex (requiring 1 ligand on the BPV surface and 1 receptor on the cell surface) must form. It does so at the association rate given by k_a. We assume that this reaction is reversible and we take the dissociation rate to be given by k_d. Once the BPVs become bound we assume that they are then internalized at the rate k_i. This internalization rate implicitly includes a measure of the size of the BPV; that is, a slower internalization rate will indicate a larger BPV.

In equation (5.4), F is the mole of receptors per volume, and in this spheroid model we make the simplifying assumption that there is a constant number of receptors per cell, f_0. The sum of free receptors and bound BPVs results in the

total number of receptors in the system per volume to be given by

$$F + B = f_0 m.$$

This assumption is similar to that adopted in Sherratt *et al* in [82]. We make this assumption as it allows us to neglect issues that arise from receptor recycling and it has the advantage of simplifying the problem by reducing the number of equations. In equation (5.5), L is the mole of free ligands per volume and as before we let $L = lV$ where l is the constant mole of ligands per BPV.

At this point we introduce a no void condition, where $m + n = N_0$, where N_0 is a constant representing the total amount of cellular material contained within a unit control volume. Using this no void condition and summing equations (5.1) and (5.2) we can obtain an expression for the advection velocity, $\mathbf{v}$:

$$\begin{aligned} \frac{\partial m}{\partial t} + \frac{\partial n}{\partial t} &= 0, \\ \therefore\ \mathbf{v} &= \frac{1}{N_0}\left(D_m \frac{\partial m}{\partial r} + D_n \frac{\partial n}{\partial r}\right). \end{aligned} \tag{5.6}$$

5.2.1 Initial and Boundary Conditions

Initially, we let the tumour grow without the therapeutic BPVs being present. That is

$$m(r,0) = m_0(r), \quad n(r,0) = N_0 - m_0(r), \quad c(r,0) = c_0(r), \tag{5.7}$$

$$V(r,0) = 0, \quad B(r,0) = 0 \quad \text{and} \quad R(0) = R_0. \tag{5.8}$$

We introduce the BPVs on the surface of the tumour spheroid at some time t^* by setting the surface concentration of BPVs, which we denote by V_∞, to some non-zero value (previously $V_\infty = 0$ when $0 < t < t^*$).

Assuming the tumour is symmetric about the origin, we have

$$\frac{\partial m}{\partial r} = \frac{\partial n}{\partial r} = \frac{\partial c}{\partial r} = \frac{\partial V}{\partial r} = \frac{\partial B}{\partial r} = 0 \qquad \text{on} \qquad r = 0. \tag{5.9}$$

On $r = R(t)$, we fix the nutrient concentration, $c = c_\infty$.

Let us denote n_∞ and V_∞ as the external concentrations of cellular material and free BPVs, respectively, with their flux across the tumour boundary proportional to $\big(n_\infty - n(R,t)\big)$ and $\big(V_\infty - V(R,t)\big)$, respectively. The tumour boundary moves with the velocity $\mathbf{v}_m$, hence the flux boundary conditions for cellular material and unbound BPVs on $r = R(t)$ are given by,

$$\begin{aligned} -n(\mathbf{v}_n - \mathbf{v}_m) &= h_n(n_\infty - n) \\ &\Rightarrow \quad D_n \frac{\partial n}{\partial r} - D_m \frac{n}{m}\frac{\partial m}{\partial r} = h_n(n_\infty - n)\,\big|_{r=R(t)}\,, \end{aligned} \tag{5.10}$$

and

$$\begin{aligned} -V(\mathbf{v}_v - \mathbf{v}_m) &= h_v(V_\infty - V) \\ &\Rightarrow \quad D_v \frac{\partial V}{\partial r} - D_m \frac{V}{m}\frac{\partial m}{\partial r} = h_v(V_\infty - V)\,\big|_{r=R(t)}\,, \end{aligned} \tag{5.11}$$

where h_n and h_v are the positive permeabilities of the cellular material and free BPVs, respectively, across the tumour boundary. The velocities of tumour cells, cellular material and free BPVs are given by

$$\mathbf{v}_m = \mathbf{v} - \frac{D_m}{m}\frac{\partial m}{\partial r}, \qquad \mathbf{v}_n = \mathbf{v} - \frac{D_n}{n}\frac{\partial n}{\partial r}, \qquad \mathbf{v}_v = \mathbf{v} - \frac{D_v}{V}\frac{\partial V}{\partial r}.$$

Using $n = N_0 - m$, (5.10) can be re-written as

$$-D_n \frac{\partial m}{\partial r} + D_m \frac{(N_0 - m)}{m}\frac{\partial m}{\partial r} = h_n(n_\infty - N_0 + m)\,\big|_{r=R(t)}. \tag{5.12}$$

The boundary conditions for B on $r = 0$ and $r = R(t)$ can be found by solving along the characteristics of the PDE at these points, namely

$$\frac{\partial B}{\partial t} = k_a l V(f_0 m - B) - (k_d + k_i)B. \tag{5.13}$$

The spheroid boundary moves with the tumour velocity $\mathbf{v}_m$,

$$\frac{dR}{dt} = \mathbf{v}_m|_{r=R(t)} = \left(\mathbf{v} - \frac{D_m}{m}\frac{\partial m}{\partial r}\right)\Big|_{r=R(t)}. \tag{5.14}$$

Using (5.6) we can re-write (5.14) as

$$\frac{dR}{dt} = \frac{1}{N_0}\left(D_m\left(1 - \frac{N_0}{m}\right)\frac{\partial m}{\partial r} + D_n\frac{\partial n}{\partial r}\right),$$

in other words

$$\frac{dR}{dt} = \frac{1}{N_0}h_n(n_\infty + m - N_0). \tag{5.15}$$

5.2.2 Non-Dimensionalization

In this section, we carry out a non-dimensionalization on the system (5.1)-(5.5) and the initial and boundary conditions described above. Note that we make the assumption that the oxygen concentration is at quasi-steady state. We do this due to the fast timescale of oxygen diffusion compared to the timescale of tumour growth. We use the following re-scalings to non-dimensionalize the system where the hats denote the non-dimensional variables

$$m = \hat{m}N_0, \quad n = \hat{n}N_0, \quad c = \hat{c}c_\infty, \quad V = \frac{\hat{V}N_0}{v_m}, \quad B = \frac{\hat{B}N_0}{v_m N_A}, \quad F = \frac{\hat{F}N_0}{v_m N_A},$$

$$r = \hat{r}R_m, \quad \mathbf{v} = \hat{\mathbf{v}}R_m p_m^{max}, \quad \hat{l} = lN_A, \quad \hat{t} = p_m^{max}t,$$

and on dropping the hats we obtain

$$\frac{\partial m}{\partial t} = -\frac{1}{r^2}\frac{\partial}{\partial r}\left(r^2\widetilde{J_m}\right) + \widetilde{p_m}(n,c)m - \widetilde{d_m}(c)m - \widetilde{g}(B), \tag{5.16}$$

$$0 = -\frac{1}{r^2}\frac{\partial}{\partial r}\left(r^2\widetilde{J_c}\right) - \widetilde{d_c}(m,n), \tag{5.17}$$

$$\frac{\partial V}{\partial t} = -\frac{1}{r^2}\frac{\partial}{\partial r}\left(r^2\widetilde{J_v}\right) - \widetilde{k_a}V(\widetilde{f_0} - b) + \frac{\widetilde{k_d}}{l}B, \tag{5.18}$$

$$\frac{\partial B}{\partial t} = -\frac{1}{r^2}\frac{\partial}{\partial r}\left(r^2\frac{B}{m}\widetilde{J_m}\right) + \widetilde{k_a}lV(\widetilde{f_0}m - B) - (\widetilde{k_d} + \widetilde{k_i})B, \tag{5.19}$$

where

$$\widetilde{p_m} = S(\hat{c}, \widetilde{c_p}) \min\left(\frac{n}{\widetilde{n_0}}, 1\right), \quad \widetilde{d_m} = \widetilde{d_m^{max}}\{1 - S(\hat{c}, \widetilde{c_c})\}, \quad \widetilde{d}_c(m,n) = \frac{d_c(m,n)}{D_c c_\infty},$$

$$\widetilde{g}(B) = \widetilde{\gamma}\widetilde{k_i}B, \quad S(\hat{c}, \widetilde{c_p}) = \frac{c^\alpha(\widetilde{c_p^\alpha} + 1)}{(\widetilde{c_p^\alpha} + c^\alpha)}.$$

With

$$\widetilde{J_m} = -\widetilde{D_m}\frac{\partial m}{\partial r} + \mathbf{v}m, \quad \widetilde{J_n} = -\widetilde{D_n}\frac{\partial n}{\partial r} + \mathbf{v}n,$$
$$\widetilde{J}_c = -\frac{\partial c}{\partial r}, \quad \widetilde{J}_v = -\widetilde{D_v}\frac{\partial V}{\partial r} + \mathbf{v}V.$$

Due to the no void condition, $m + n = 1$, we can neglect the cellular material equation and obtain its solution from the tumour solution. The non-dimensional advection velocity then is as follows

$$\mathbf{v} = \left(\widetilde{D_m} - \widetilde{D_n}\right)\frac{\partial m}{\partial r}. \tag{5.20}$$

The parameter re-scalings read as,

$$\widetilde{D_m} = \frac{D_m}{R_m^2 p_m^{max}}, \quad \widetilde{D_n} = \frac{D_n}{R_m^2 p_m^{max}}, \quad \widetilde{D_c} = \frac{D_c}{R_m^2 p_m^{max}}, \quad \widetilde{D_v} = \frac{D_v}{R_m^2 p_m^{max}},$$
$$\widetilde{k_i} = \frac{k_i}{p_m^{max}}, \quad \widetilde{k_d} = \frac{k_d}{p_m^{max}}, \quad \widetilde{k_a} = \frac{k_a N_0}{p_m^{max} v_m N_A}, \quad \widetilde{f_0} = f_0 N_A,$$
$$\widetilde{\gamma} = \frac{\gamma}{N_A}, \quad \widetilde{c_p} = \frac{c_p}{c_\infty}, \quad \widetilde{c_c} = \frac{c_c}{c_\infty}, \quad \widetilde{n_0} = \frac{n_0}{N_0},$$
$$\widetilde{d_m^{max}} = \frac{d_m^{max}}{p_m^{max}}.$$

For convenience in the remaining analysis we drop the tildes.

We further assume that equation (5.19) is at a quasi-steady state. We do so due to the fast binding, dissociation and internalization rates compared to the rate of tumour growth. We are then left with an algebraic equation for B given by,

$$0 = k_a l V(f_0 m - B) - (k_d + k_i)B.$$

From which, we can obtain an expression for bound BPVs per cell which is given by

$$B(r,t) = \frac{k_a l V f_0 m}{(k_a l V + k_d + k_i)}, \tag{5.21}$$

which we feed directly into the death term in the tumour cell equation, (5.16). With this expression for $B(r,t)$, we now solve the non-dimensionalized system (5.16)-(5.18) with the boundary conditions given by,

$$\frac{\partial m}{\partial r} = \frac{\partial c}{\partial r} = \frac{\partial V}{\partial r} = 0 \qquad \text{on} \qquad r = 0. \tag{5.22}$$

On the spheroid boundary, $r = R(t)$, the oxygen concentration is $c = 1$ and we have

$$-D_n \frac{\partial m}{\partial r} - D_m \frac{(1-m)}{m} \frac{\partial m}{\partial r} = h_n (n_\infty + m - 1) \Big|_{r=R(t)} , \tag{5.23}$$

$$D_v \frac{\partial V}{\partial r} - D_m \frac{V}{m} \frac{\partial m}{\partial r} = h_v (V_\infty - V) \Big|_{r=R(t)} . \tag{5.24}$$

The spheroid boundary ($r = R(t)$) now moves with the tumour velocity so that

$$\frac{dR}{dt} = h_n (n_\infty + m - 1). \tag{5.25}$$

5.3 Numerical Results

Using the non-dimensionalized system (5.16)-(5.18) and using the expression for bound BPVs per cell, (5.21), we solve the system numerically using the NAG routine D03PHF with the initial and boundary conditions described as in the previous section.

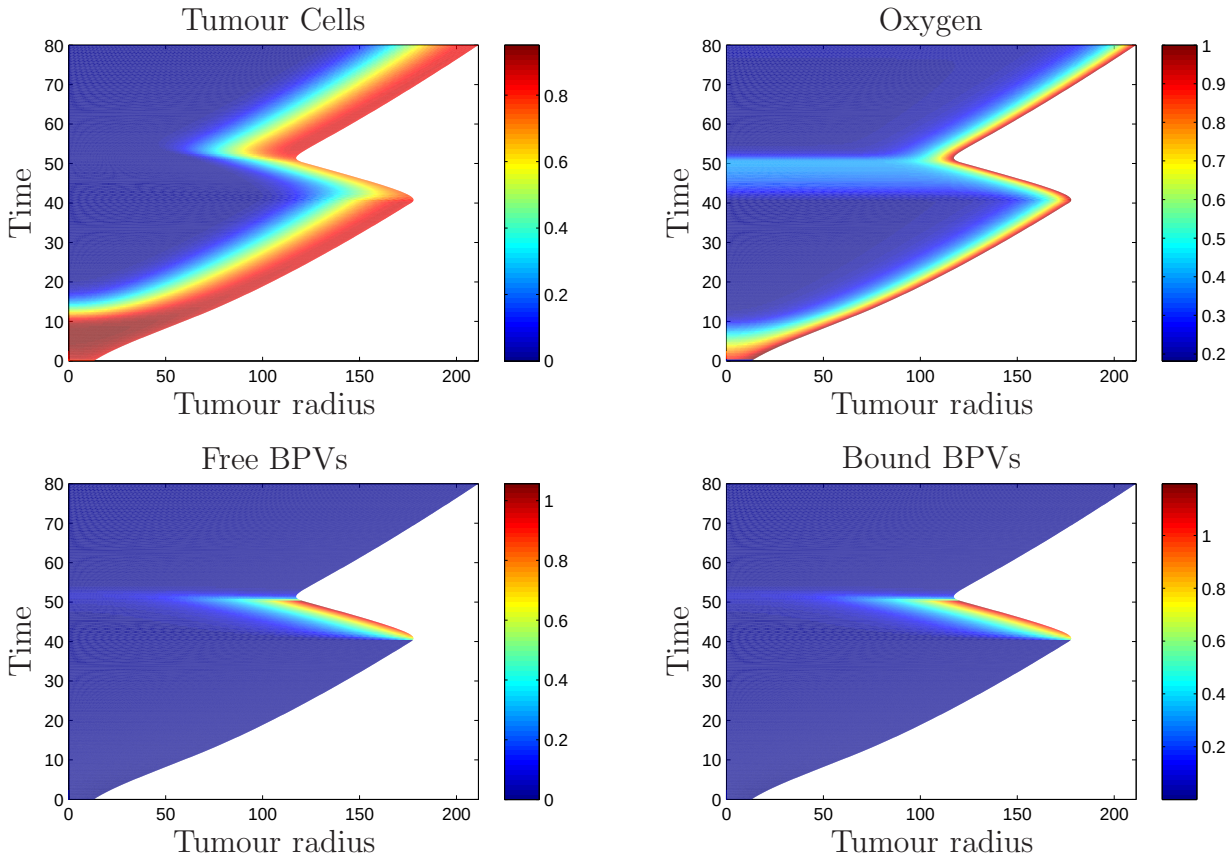

Figure 5.2: The tumour spheroid radius and composition changing with time. We plot the densities of tumour cells, oxygen concentration, free and bound BPVs. Initially growth occurs with no free BPVs on the tumour surface. Then we introduce BPVs by setting $V_\infty \neq 0$ when $40 \leq t \leq 50$. We notice that the tumour growth rate decreases for the period of time treatment is administered, but returns to linear growth afterwards. With $D_m = 10, D_n = 500, D_v = 500, k_a = 0.01, k_i = 880, k_d = 0.053, \gamma = 10^{-3}, d_m^{max} = 2, f_0 = 1000, n_\infty = 0.2, c_p = 0.6$ and $c_c = 0.2$.

In Figure 5.2, we show the density profiles of tumour cells, oxygen, free and bound BPVs in space as time increases. The highest density of tumour cells

occur at the spheroid boundary. The cells require oxygen for growth and the density of highest oxygen is found on the boundary due to the spheroid having no internal vasculature. The concentration of oxygen reduces as it diffuses into the tumour spheroid and is consumed by the outer proliferating cells. As time increases the reduction in nutrients creates a hypoxic region in which cells become quiescent and the inner core of the spheroid cells lyse due to the concentration of oxygen being too low for viability. We introduce the BPVs at some time $t > 0$ by setting the surface concentration, $V_\infty \neq 0$. We introduce the BPVs on the tumour surface when $t^* = 40$ and they are removed when $t = 50$. We can see that the highest concentration of free and bound BPVs occur at the spheroid boundary during this period. The free BPVs diffuse slightly into the spheroid but are quickly bound by cells at the periphery which slows the penetration into the spheroid. In the period of time the therapeutic BPVs are introduced, there was a notable decrease in tumour radius.

For a clear representation of the effect of BPV treatment, in Figure 5.3 we show the changes in tumour radius with time. At early time (when $V_\infty = 0$) the tumour grows linearly. When the BPVs are introduced, by setting $V_\infty \neq 0$ at time $t^* = 40$, the growth of the tumour decreases before the BPVs are removed at time $t = 50$. After this time of treatment the tumour recovers and returns to linear growth.

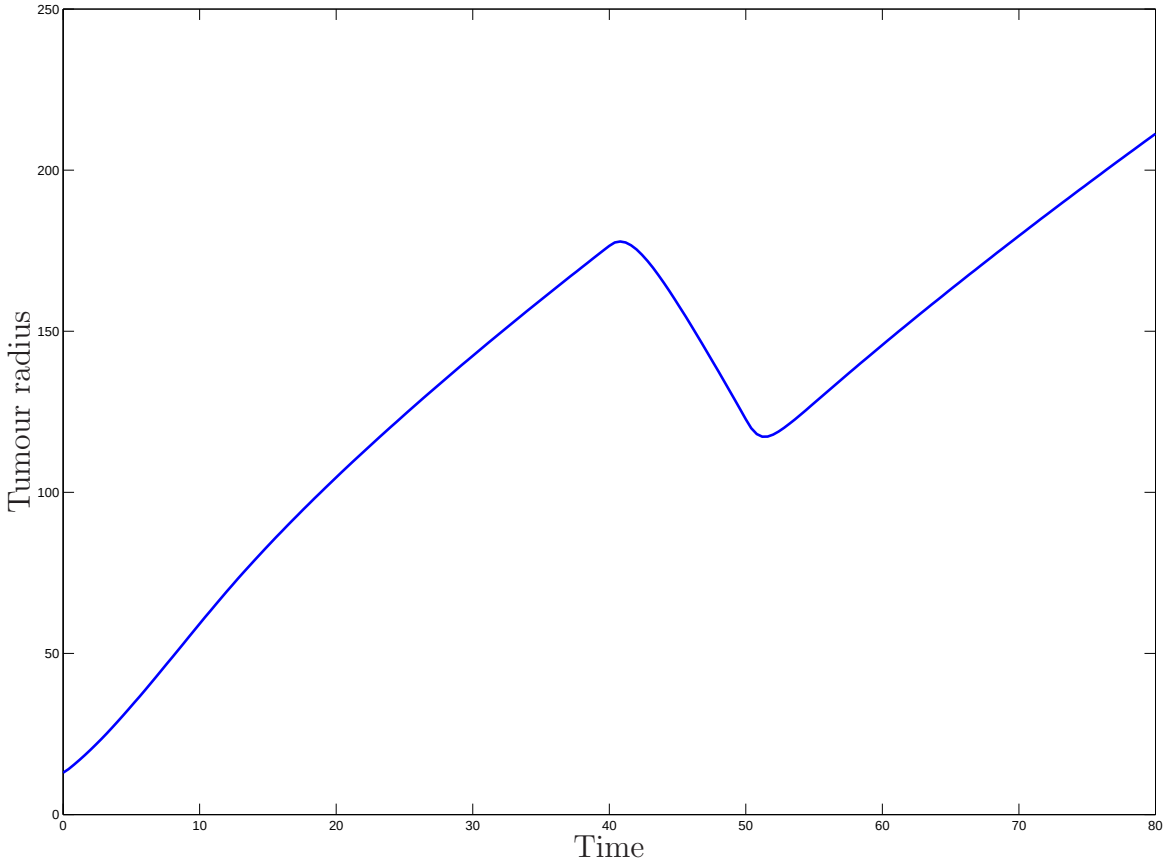

Figure 5.3: The tumour radius plotted against time. The BPVs are introduced on the surface of the spheroid by setting $V_\infty = 10$ at time $40 \leq t \leq 50$, for $t > 50$ we let $V_\infty = 0$ indicating the therapeutic BPVs have been removed from the spheroid surface. In the therapeutic time frame, there is a reduction in tumour radius. Before $t = 40$ and after $t = 50$, linear growth of the tumour is observed. The parameters are as in Figure 5.2.

From Figure 5.3 we observe that the spheroid radius growth is approximately linear in the absence of treatment which indicates that the solution may be settling down to that of a travelling wave. In this next section, we will carry

out a large-time travelling wave analysis on this problem and aim to find regions of parameter space in which we can determine if there will be travelling waves (linear growth) or steady state solutions (confined tumours).

5.3.1 Large Time Behaviour

From the numerical results presented in Figure 5.3, in the absence of BPVs the tumour spheroid appears to grow linearly. In order to get an analytical handle on this behaviour and the behaviour when we input BPVs, we now look to the asymptotic solutions of the system as $t \to \infty$ and hence we carry out a travelling wave analysis by assuming that the tumour grows at a constant speed, $u > 0$. The rate of change of the spheroid radius will then be

$$\frac{dR}{dt} = u.$$

So that $R \sim ut$ as $t \to \infty$. We redefine our system with the travelling wave coordinate, $z = r - ut$, and rewrite the equations (5.16)-(5.18) in terms of z. The prime denotes the derivative with respect to z:

$$\begin{aligned} -um' &= \frac{2}{r}\left(D_m m' - m\mathbf{v}\right) + \left(D_m m' - m\mathbf{v}\right)' + p_m(n,c)m \\ &\quad -d_m(c)m - g(B), \qquad (5.26) \\ c'' &= d_c(m,n), \qquad (5.27) \\ -uV' &= \frac{2}{r}\left(D_v V' - V\mathbf{v}\right) + \left(D_m V' - V\mathbf{v}\right)' - k_a V F \\ &\quad + \frac{k_d}{l}B. \qquad (5.28) \end{aligned}$$

We will use the quasi-steady expression for B as described in (5.19). Recall the advection velocity (5.20),

$$\mathbf{v} = \psi m' \quad \text{where} \quad \psi = D_m - D_n.$$

We now write this system as a system of 6 first order ODEs, given below

$$\begin{aligned} m' &= W, && (5.29)\\ c' &= P, && (5.30)\\ V' &= Q, && (5.31)\\ W' &= \frac{1}{\psi m - D_m}\left(uW - \psi W^2 + p_m(n,c)m - d_m(c)m - g(B)\right), && (5.32)\\ P' &= d_c(m,n), && (5.33)\\ Q' &= -\frac{1}{D_v}\left((u-\psi W)Q - \psi WV - k_a VF + \frac{k_d}{l}B\right), && (5.34) \end{aligned}$$

note that we have neglected the terms containing r^{-1} since they are $O(R^{-1})$ when $R \to \infty$.

We will solve this system of equations numerically using AUTO (a continuation and bifurcation software [29]). To facilitate the numerical solver we truncate the semi-finite domain $z \in (-\infty, 0]$ to $z \in [-R, 0]$, where $R > 0$ and taken to be sufficiently large, for AUTO to be able to solve the boundary value problem. We rescale z,

$$\hat{z} = \frac{z}{R} + 100 \quad \text{so that} \quad \hat{z} \in [0, 100].$$

The wavespeed u can be written using (5.25) as

$$u = h_n(n_\infty + m - 1)|_{\hat{z}=1}.$$

We use the following boundary conditions,

$$\begin{aligned} & m'(0) = c'(0) = V'(0) = 0, && (5.35)\\ & -D_n m' - D_m \frac{(1-m)}{m} m' = h_n(n_\infty + m - 1)\,|_{\hat{z}=1}\,, && (5.36)\\ & D_v V' - D_m \frac{V}{m} m' = h_v(V_\infty - V)\,|_{\hat{z}=1}\,, && (5.37) \end{aligned}$$

which follow from (5.22)-(5.24). We also fix the oxygen concentration $c = 1$ at $\hat{z} = 100$. We solve the system of 6 first order ODEs, (5.29)-(5.34), using AUTO.

Note that we have 7 boundary conditions which is overposed for our 6 ODE system. The additional boundary condition, namely $u = h_n(n_\infty + m - 1)$, is used to estimate the wavespeed u as the model parameters are varied.

Due to the long time frame being considered, we no longer use the initial condition for free BPVs, whereby BPV infiltration is not initially permitted i.e. $V_\infty = 0$ for $t < t^*$. Then at some time t^* we set $V_\infty \neq 0$ implying BPVs are administered on the tumour surface and then removed after a period of time. In contrast, for these large time solutions we allow $V_\infty \neq 0$ for all $t \geq 0$.

In Figure 5.4, we show the typical long-time solution profiles obtained from the AUTO calculation. We notice that the necrotic core of the tumour is present. The cells consume oxygen which lowers the concentration causing a hypoxic region which then causes the cells to lyse at the centre. When cells lyse they produce cellular material which living cells on the periphery of the tumour can then utilise as growth nutrients. The advection velocity is negative, which means that the BPVs will tend to be transported to the centre of the tumour if not first being bound by outer viable cells. The predicted wavespeed, u, for the advancement of the tumour in this case is $u = 0.72$.

Using the continuation and bifurcation software AUTO [29], we examine how changing model parameters affect the wavespeed of the moving boundary. In Figure 5.5(i), we plot the wavespeed u against γ which represents the lysis rate of the tumour cells due to the internalization of the BPV, and in (ii) we show u against V_∞, which represents the external concentration of the BPVs. We can see that by increasing the lysis rate (or in other words the potency of the BPVs), γ, the wavespeed decreases to zero, indicating a bifurcation from travelling waves (linear growth) to steady-states where tumour growth is confined. As V_∞ increases we observe similar dynamics, where the bifurcation between linear

and confined growth occurs at $V_\infty = 4.3$, i.e. a greater concentration of BPVs results in a more effective treatment.

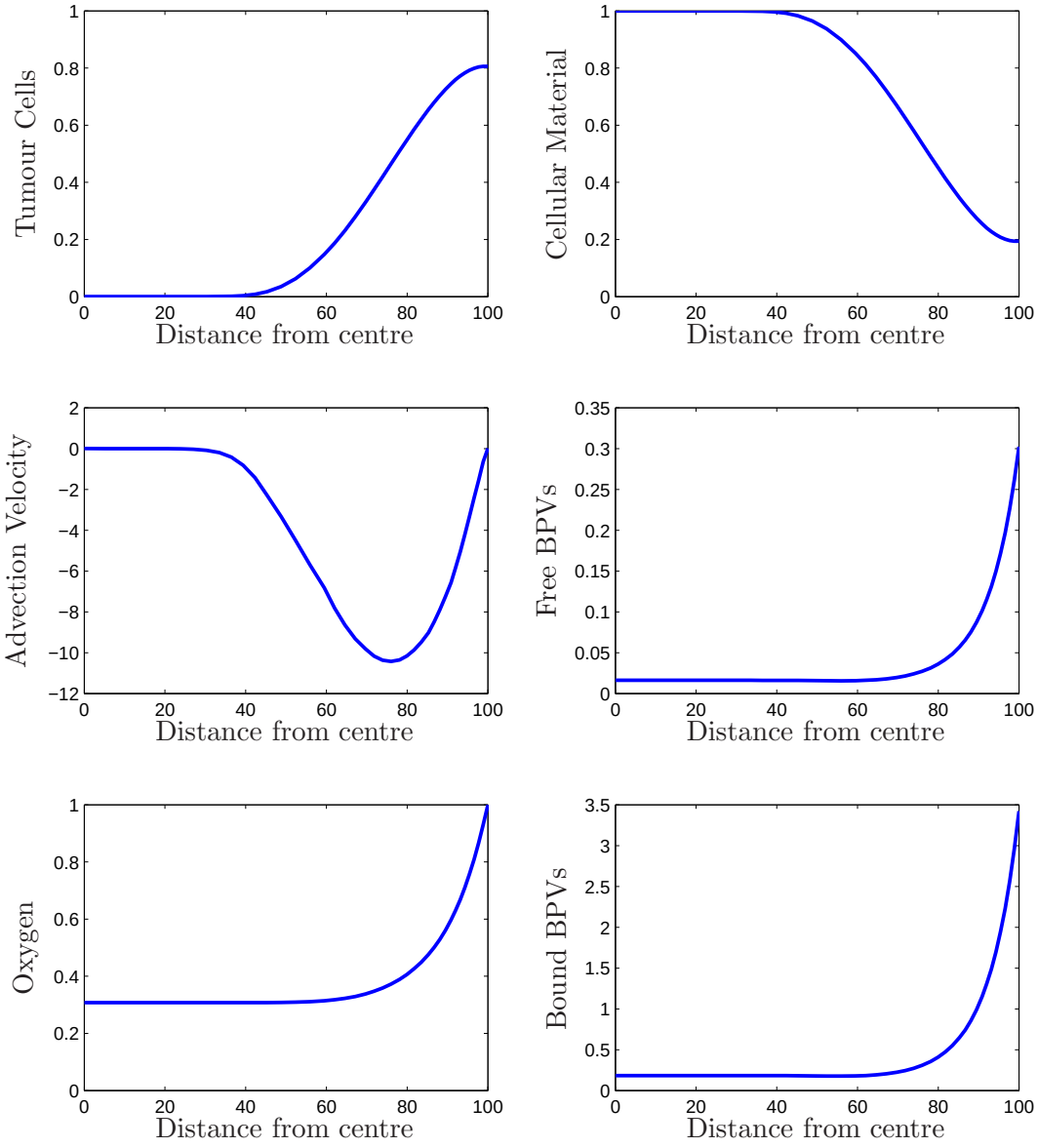

Figure 5.4: The leading edge profiles when solved using the AUTO bifurcation software [29]. $V_\infty = 10, k_a = 0.01, k_d = 0.053, k_i = 880, \gamma = 1 \times 10^{-5}, D_m = 10, D_n = 500$ and $D_v = 500$.

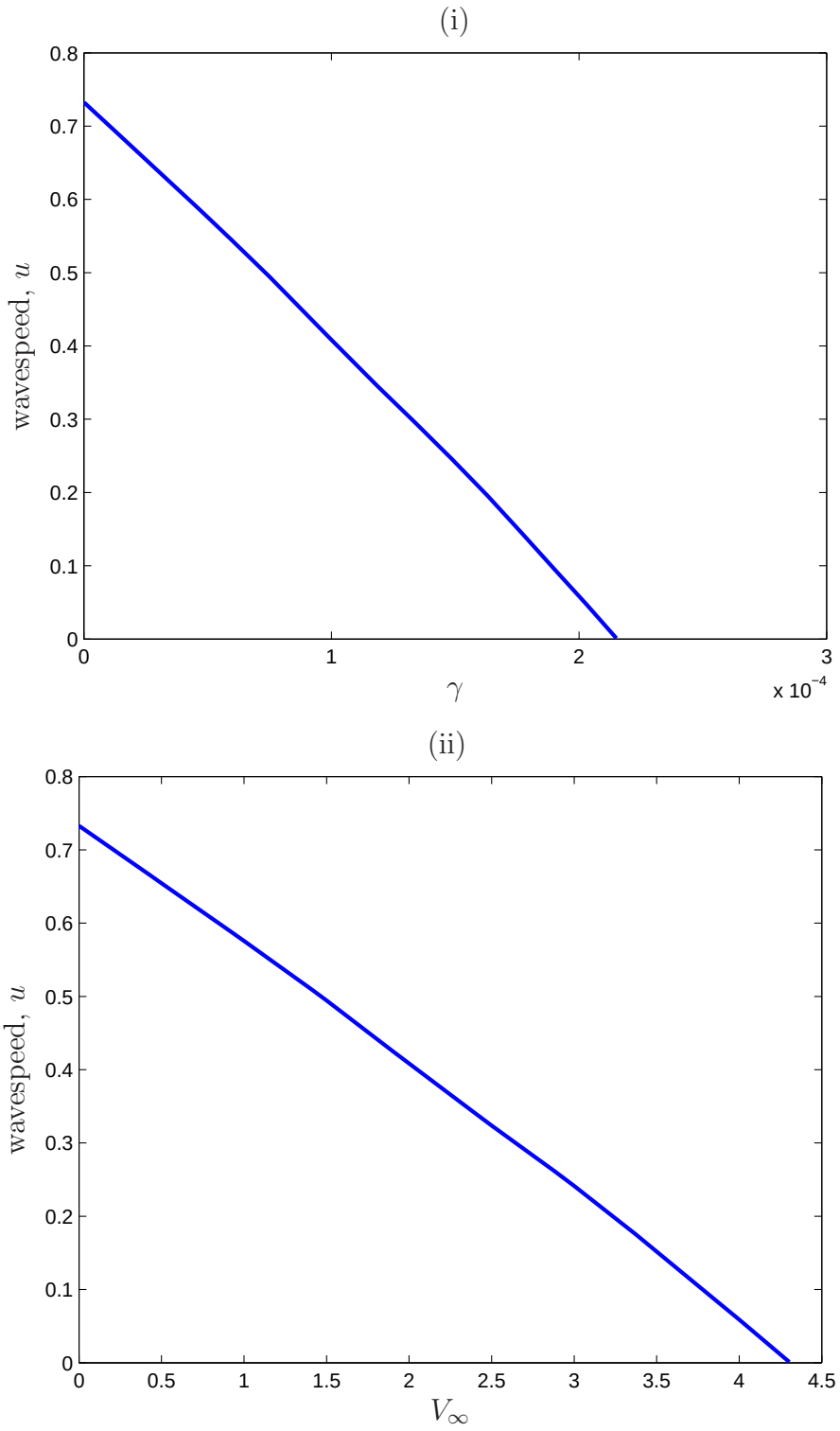

Figure 5.5: (i) The travelling wave velocity, u, with varying γ and fixed $V_\infty = 2$. As the death rate increases, the velocity increases. (ii) Travelling wave velocity with varying V_∞ and fixed $\gamma = 1 \times 10^{-4}$. A similar pattern can be seen as in (i). As V_∞ increases the velocity u deceases. The other parameters remain fixed, $k_a = 0.01, k_d = 0.053, k_i = 880, l = 1000, D_m = 10, D_v = 500$ and $D_n = 500$.

We now examine the different regions of parameter space that can predict linear growth of the spheroid (travelling wave solutions) or confined growth (corresponding to an equilibrium steady state). In Figure 5.6, we show the bifurcation of the two states (when the wavespeed $u = 0$) in the parameter space of (V_∞,γ). Recall V_∞ is the external BPV concentration and γ is the lysis rate associated with the BPV treatment. We can see that, with increasing concentration of applied BPVs, a lower death rate is required for steady state solutions. Or by increasing the potency of the BPVs, less BPVs are required to obtain an equilibrium state. The steady state solutions are to the right of the bifurcation curve whereas travelling waves occur to the left.

The bifurcation presented in Figure 5.6 is expected. We would expect that, by increasing the potency of the BPVs or by increasing their number, a reduction in tumour growth would be seen. Eventually, growth will be confined which corresponds to a steady state solution.

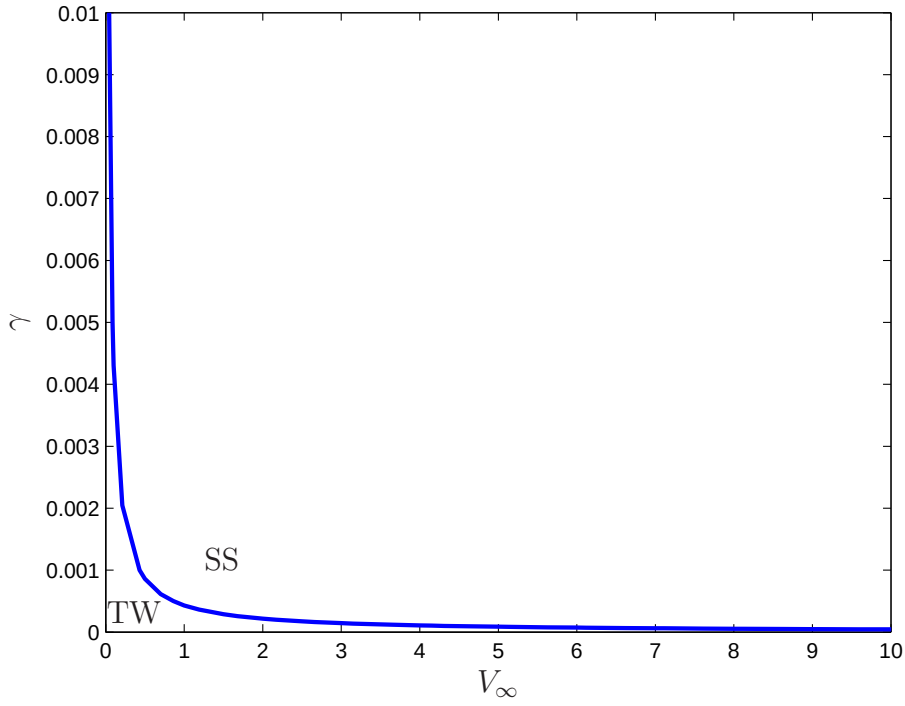

Figure 5.6: The travelling wave:steady-state bifurcation curve in (V_∞, γ) parameter space. Above the curve steady-state solutions (SS) occur, below there are travelling waves (TW). We use $k_a = 0.01, k_d = 0.053, k_i = 880, l = 1000, D_m = 10, D_n = 500$ and $D_v = 500$.

In Figure 5.7, we show again the travelling wave:steady-state bifurcation in (V_∞, γ) parameter space, but with varying n_∞. n_∞ is the parameter that describes the concentration of cellular material on the spheroid boundary. One can interpret n_∞ as the richness of the culture media conditions *in vitro* or the degree of oxidation of the tumout *in vivo*. We would expect that by increasing n_∞ the tumour growth would increase resulting in a larger parameter region for travelling waves. We have found that this is true but only to a certain threshold value of n_∞.

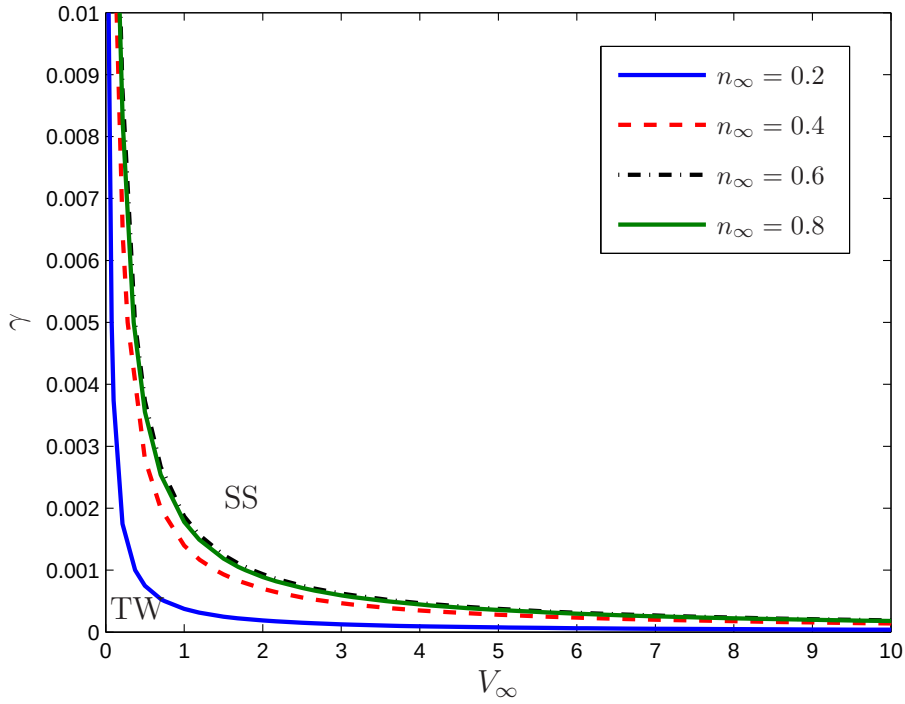

Figure 5.7: Travelling wave:steady-state bifurcation curves in (V_∞, γ) parameter space for different values of n_∞. Above the curve are the steady-state solutions (SS). Below are the travelling waves (TW). We use $k_a = 0.01, k_d = 0.053, k_i = 880, l = 1000, D_m = 10, D_n = 500$ and $D_v = 500$ with $n_\infty = 0.2, 0.4, 0.6$ and 0.8.

We notice that for a fixed V_∞, say, if we increase n_∞, an increasing potency of the BPVs (γ) is required for steady states to occur. That is, until a certain threshold of n_∞. Then the potency can be reduced whilst still achieving a decreased tumour growth. We examine this further by fixing V_∞ and following the travelling wave, steady state bifurcation in (n_∞, γ) parameter space (see Figure 5.8).

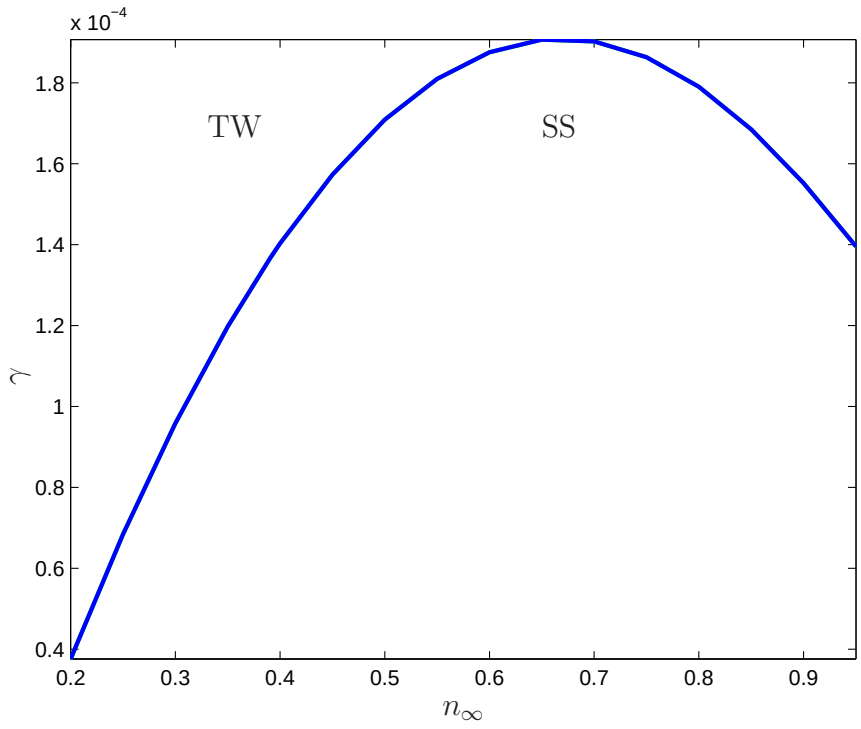

Figure 5.8: Travelling wave:steady-state bifurcation curve in (n_∞, γ) parameter space when $V_\infty = 5$. Under the curve are steady-state solutions. Above the curve are travelling waves. The remaining parameter values are the same as those in Figure 5.7.

In Figure 5.8, we see that when n_∞ is increased beyond a threshold value, the BPVs do not need to be as potent to achieve confined growth. In Figure 5.9, we examine the behaviour of the tumour cells and the internal velocity field within the tumour spheroid for these parameter values. Typically (for example, when $n_\infty = 0.2$ corresponding to the blue dotted line in Figure 5.9(iv)) the advection velocity within the spheroid is negative, which means that material is advected into the centre of the spheroid. However, when increasing n_∞ over a certain threshold, we see that the advection velocity becomes positive near the spheroid boundary (red dot-dashed line in Figure 5.9(iv)), this change in the direction of

the velocity results in the BPVs being kept at the tumour boundary where the tumour density is highest. As a consequence more viable cells are being targeted and subsequently a lower lysis rate (γ) is required to give the same reduction in tumour size.

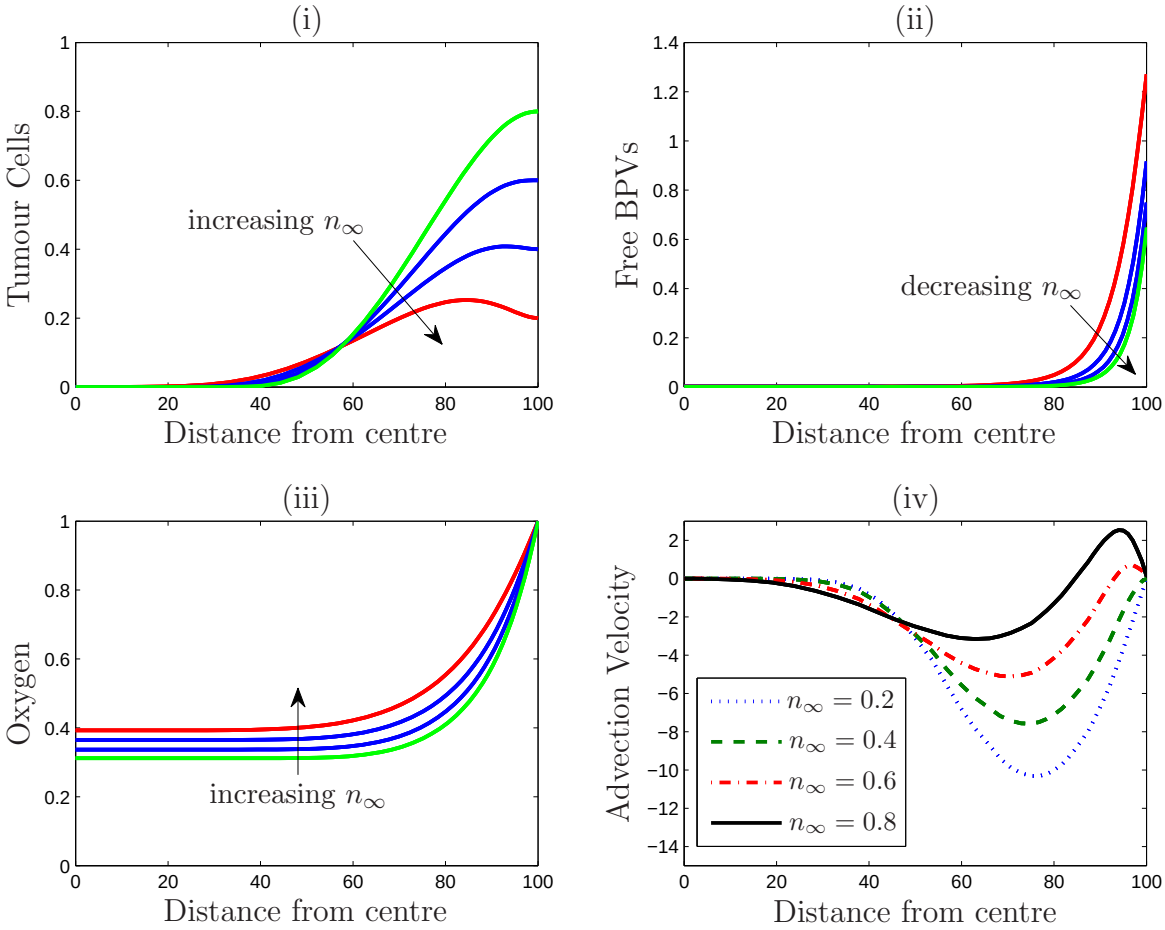

Figure 5.9: In (i), (ii) and (iii) are the solution profiles for tumour cells, free BPVs and oxygen, respectively, at varying values of n_∞; $n_\infty = 0.2$ (green),0.4,0.6,0.8 (red). (iv) Advection velocity with $n_\infty = 0.2, 0.4, 0.6, 0.8$. We see a positive velocity at the tumour boundary with larger values of n_∞. The remaining parameter values are the same as in Figure 5.7.

We now explore the travelling wave:steady-state bifurcation in (D_v, h_v) parameter space, where, as a reminder, D_v is the diffusion coefficient of the free BPVs and h_v is the permeability of the BPVs into the tumour spheroid, we observe an interesting result as shown in Figure 5.10.

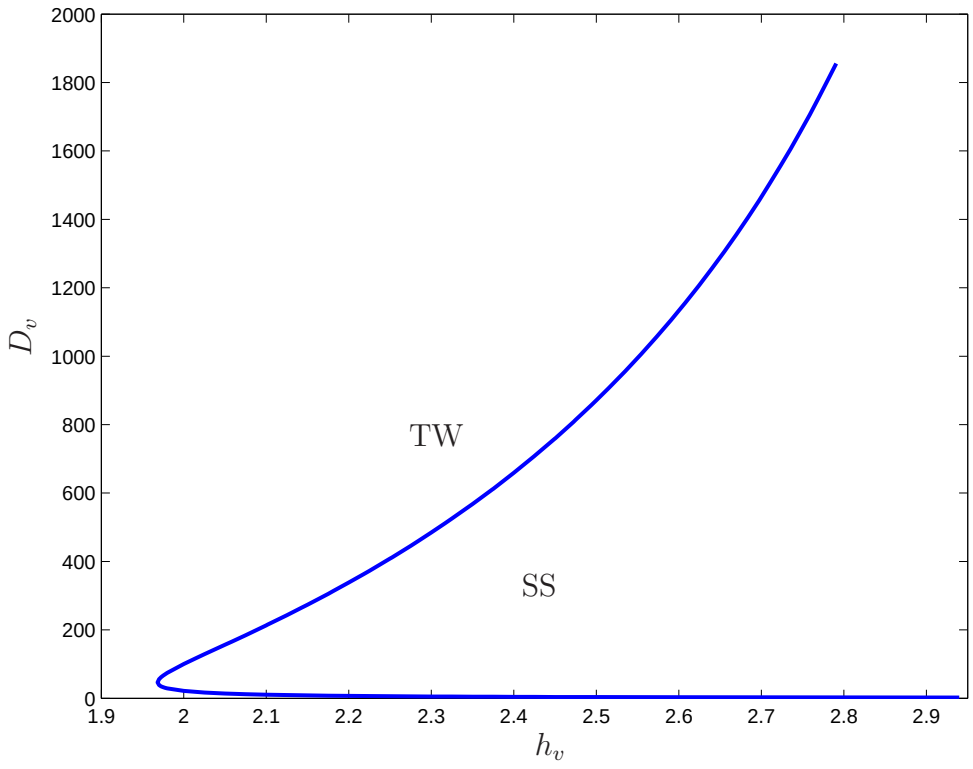

Figure 5.10: The travelling wave:steady-state bifurcation curve in (D_v, h_v) parameter space. To the right are the steady-state solutions (SS). To the left are the travelling waves (TW). The remaining parameter values are the same as in Figure 5.7.

We notice that for a fixed value of h_v (for example, if $h_v = 2.2$) the solutions can be either travelling waves for very small or very large values of D_v but steady state solutions occur for intermediate values of D_v. In simulations (not shown),

we see that when D_v is very small, the free BPVs are kept to the periphery and don't diffuse into the inner core of the spheroid, hence $V(R,t) \simeq V_\infty$ which slows infiltration of further therapeutic BPVs. The opposite occurs when the diffusion rate of free BPVs, D_v, is very large since the internal velocity will quickly move the BPVs into the core of the spheroid rendering the BPVs useless. We see that when the BPVs have an intermediate diffusion rate they are transported to the core of the spheroid slower than if D_v is very large, giving an opportunity for binding events and internalization to occur, and therefore slowing the growth of the spheroid. For $h_v \leq 1.96$, only travelling waves exist for any value of D_v. This is due to the permeability being too low to allow enough BPVs to penetrate the spheroid.

In Figure 5.11, we show the travelling wave:steady-state bifurcation in the (V_∞, k_a) parameter space, where V_∞ is the external BPV concentration and k_a is the association rate for a BPV to become bound to the tumour cell surface. Steady state solutions are to the right of the bifurcation curve and travelling wave solutions are to the left.

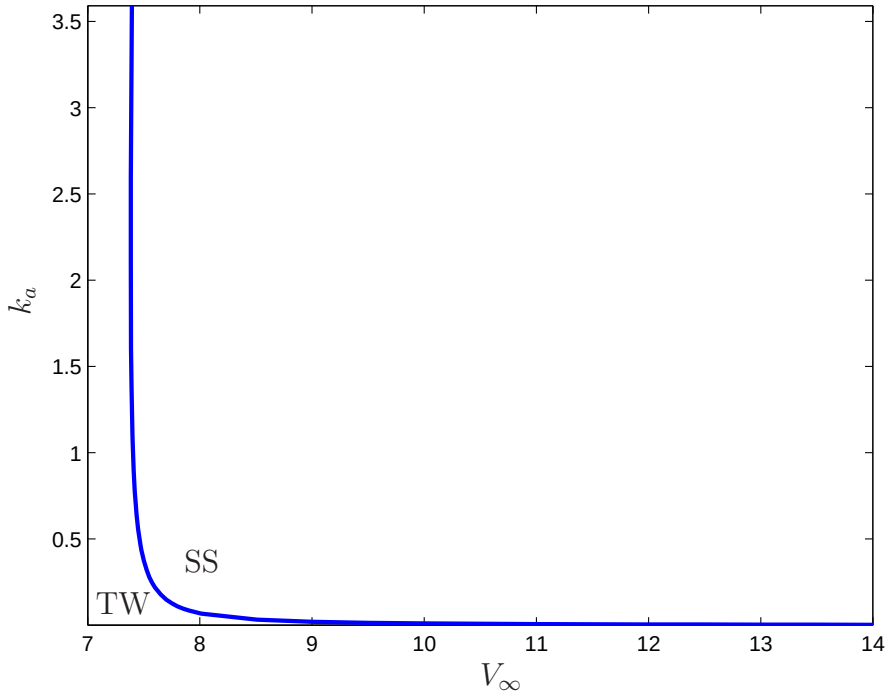

Figure 5.11: The travelling wave:steady-state bifurcation in the (V_∞, k_a) parameter space. Above the curve are steady-state solutions (SS), below are travelling waves (TW). With $\gamma = 10^{-4}$, $n_\infty = 0.2$ and the remaining parameter values are the same as in Figure 5.7.

Finally, we would expect that if we increase the concentration of BPVs infiltrating and also increase the binding association rate we will see a decreased tumour growth, and this is indeed what is observed (see, e.g. Figure 5.11).

5.4 Extension to Multiple Binding

In section 5.2, we assume that only one receptor-ligand complex is required for the tumour cells to internalize the BPVs. This is a simplistic assumption and

so, in this section, we extend the model to include multiple binding events, which represents the encapsulation of the BPV on the tumour surface through receptor-mediated endocytosis.

Receptor-mediated endocytosis occurs in a clathrin-coated pit (clathrin is found within the cell, and the pits form underneath the cell membrane) and is the process in which a ligand (external to the cell) binds to a receptor on the cell surface before it is internalized [21]. Once the complex between receptor and ligand have formed the cell membrane invaginates and then the membrane pinches off to create an internal clathrin-coated vesicle. The clathrin coat detaches in seconds and is recycled to the cell membrane. The uncoated vesicle will then fuse with an endosome where the ligand will be released, and the process of receptor recycling can begin [4]. The processes of membrane invagination, pinching off and vesicle transport are all carried out using the cell's cytoskeleton.

As in Section 5.2, we denote the volume fraction of tumour cells per unit control volume $m(r,t)$, the volume fraction of cellular material per unit control volume $n(r,t)$, oxygen concentration is given by $c(r,t)$ and BPVs per cm^3 $V(r,t)$. To convert the model to multiple binding we need to re-express the bound BPVs variable, i.e. we now assume that $B_k(r,t)$ is the mole of bound BPVs with k ligand-receptor complexes per cm^3, for $k = 1, ..., n$. We assume that the (constant) mole of free receptors per cm^3 is now given by

$$F = \underbrace{f_0 m}_{\substack{\text{total mol receptors} \\ \text{per cm}^3}} - \underbrace{\sum_{k=1}^{n} kB_k,}_{\substack{\text{mol ligand-receptor} \\ \text{complexes per cm}^3}} \tag{5.38}$$

which is similar to the single binding case. Although, here we take into account that a BPV may have more than one receptor-ligand complex.

To incorporate a more biologically realistic binding and internalization, we com-

pare two cases of internalization functions; (1) a constant internalization rate k_i fixed $\forall k$, where $k = 1, .., n$ is the number of receptor-ligand complexes, and (2) an internalization function that depends on the number of complexes formed, which we take to be given by

$$k_i(k) = k_i \left(\varepsilon_1 + H(k - j^*)\right). \tag{5.39}$$

We use ε_1 is a very small number, hence we assume that in this case there will always be a (small and constant) minimum internalization rate $k_i\varepsilon_1$ if the BPV bound number is less that j^*. The level of membrane deformation is represented by j^*, where $j^* \in \mathbb{N}, j^* \leq n$. With $j^* = 1$ being no deformation required and $j^* > 1$ represents that at least j^* receptor-ligand complexes are required for cell surface deformation and endocytosis. Note that, here, we choose an upper bound on j^* to be $j^* = 5$ due to the increasing complexity of the resulting algebraic equations (described later in more detail). The internalization function (5.39) describes the scenario where the BPVs will be internalized once bound with j^* compexes. This allows us to implicitly model the membrane deformation that occurs during receptor-mediated endocytosis.

To extend the model to include these multiple binding events we make the same assumptions for the ODE system we present in Chapter 4. In that, we assume a proportion of ligands and receptors will be available for 2-D binding, controlled by ρ_l and ρ_f respectively. We assume that B_j $(2 \leq j \leq n-1)$ leaves the system by either internalization at the rate $k_i(j)$, by the association (at rate k_a^d) of another ligand-receptor complex, becoming B_{j+1}, or when a ligand-receptor complex dissociates (at the rate k_d) becoming B_{j-1}. In the case when the receptor-ligand complex dissociates in the B_1 class, the BPV enters the free BPV class, V.

Recall that the bound BPVs per cell move with the same flux of the tumour

cells, $\frac{J_m}{m}$. Also, as previously described we use a no-void condition within the spheroid, hence $m + n = N_0$ where N_0 is a constant representing the amount of cellular material contained within the unit control volume. Using these assumptions, we extended the single binding model from Section 5.2 to include multiple binding events. We first show the full dimensional system for completeness and then employ the same rescalings as before. The system is given by,

Tumour:

$$\frac{\partial m}{\partial t} = -\frac{1}{r^2}\frac{\partial}{\partial r}\left(r^2 J_m\right) + p_m(n,c)m - d_m(c)m - g(B_k), \quad (5.40)$$

Material:

$$\frac{\partial n}{\partial t} = -\frac{1}{r^2}\frac{\partial}{\partial r}\left(r^2 J_n\right) - p_m(n,c)m + d_m(c)m + g(B_k), \quad (5.41)$$

Oxygen:

$$0 = -\frac{1}{r^2}\frac{\partial}{\partial r}\left(r^2 J_c\right) - d_c(m,n), \quad (5.42)$$

Free BPVs:

$$\frac{\partial V}{\partial t} = -\frac{1}{r^2}\frac{\partial}{\partial r}\left(r^2 J_v\right) - k_a V F + \frac{k_d}{l} B_1, \quad (5.43)$$

B_1's:

$$\frac{\partial B_1}{\partial t} = -\frac{1}{r^2}\frac{\partial}{\partial r}\left(r^2\frac{B_1}{m}J_m\right) + k_a l V F - (k_d + k_i(1))B_1 - k_a^d \rho_f \Big(\rho_l l N_A - 1\Big) F B_1 + 2k_d B_2, \tag{5.44}$$

B_j's:

$$\frac{\partial B_j}{\partial t} = -\frac{1}{r^2}\frac{\partial}{\partial r}\left(r^2\frac{B_j}{m}J_m\right) + k_a^d \rho_f \Big(\rho_l l N_A - (j-1)\Big) F B_{j-1} - (jk_d + k_i(j))B_j - k_a^d \rho_f \Big(\rho_l l N_A - (j-1)\Big) F B_j + (j+1)k_d B_{j+1}, \tag{5.45}$$

B_n's:

$$\frac{\partial B_n}{\partial t} = -\frac{1}{r^2}\frac{\partial}{\partial r}\left(r^2\frac{B_n}{m}J_m\right) + k_a^d \rho_f \Big(\rho_l l N_A - (n-1)\Big) F B_{n-1} - (nk_d + k_i(n))B_n, \tag{5.46}$$

where in (5.45) $j = 2, ..., n-1$ where n, as before, is the maximum number of ligand-receptor complexes that can form. J_m, J_n and J_v are the fluxes of tumour cells, cellular material and free BPVs, respectively, and are previously defined in Section 5.2. We assume, as before, that the death rate of tumour cells, $g(B_k)$, is proportional to the total number of internalized BPVs, i.e. $g(B_k) = \gamma \sum_{k=1}^{n} k_i(k) B_k$.

As before, using the no-void condition and by summing equation (5.40) and (5.40) we can deduce the following advection velocity,

$$\mathbf{v} = \frac{1}{N_0}\left((D_m - D_n)\frac{\partial m}{\partial r}\right). \tag{5.47}$$

As we have seen in the single binding case, the fast binding kinetics of the receptors and ligands compared to tumour cell growth allow us to take advantage

of a quasi-steady state assumption for bound BPVs. Hence (5.44)-(5.46) become

$$\begin{aligned} 0 &= k_a l V F - (k_d + k_i(1))B_1 \\ &\quad -k_a^d \rho_f \big(\rho_l l N_A - 1\big) F B_1 + 2k_d B_2, \qquad (5.48) \\ 0 &= k_a^d \rho_f \Big(\rho_l l N_A - (j-1)\Big) F B_{j-1} \\ &\quad -(jk_d + k_i(j))B_j - k_a^d \rho_f \Big(\rho_l l N_A - (j-1)\Big) F B_j \\ &\quad +(j+1)k_d B_{j+1}, \qquad \text{for} \qquad j = 2, ..., n-1 \qquad (5.49) \\ 0 &= k_a^d \rho_f \Big(\rho_l l N_A - (n-1)\Big) F B_{n-1} \\ &\quad -(nk_d + k_i(n))B_n, \qquad (5.50) \end{aligned}$$

where n is is maximum number of bonds that can form and F is defined in (5.38). We can solve (5.48)-(5.50) independently to give each B_k, (where $k = 1, ..., n$) in terms of the remaining model variables.

As described above, we non-dimensionalized the system using the same variable re-scalings as in Section 5.2.2, namely,

$$m = \hat{m}N_0, \quad n = \hat{n}N_0, \quad c = \hat{c}c_\infty, \quad V = \frac{\hat{V}N_0}{v_m}, \quad B = \frac{\hat{B}N_0}{v_m N_A}, \quad F = \frac{\hat{F}N_0}{v_m N_A}.$$

The full procedure and parameter re-scalings are given earlier in the chapter and so the process is not fully repeated here. Note that from this point onwards the variables are dimensionless with the hats dropped for simplicity.

5.5 Numerical Results

To solve the system numerically we must initially solve the system (5.48)-(5.50). First, we take $n = 2$. Equations (5.48)-(5.50) then give

$$\begin{aligned} 0 &= k_a lV(f_0 m - B_1 - B_2) - (k_d + k_i(1))B_1 \\ &\quad -k_a^d \rho_f(\rho_l l - 1)\left(f_0 m - B_1 - 2B_2\right) B_1 + 2k_d B_2, \qquad (5.51) \\ 0 &= k_a^d \rho_f(\rho_l l - 1)(f_0 m - B_1 - 2B_2)B_1 \\ &\quad -(2k_d + k_i(2))B_2. \qquad (5.52) \end{aligned}$$

Using appropriate parameter groupings for simplicity we can express the solution for B_1 and B_2 explicitly in terms of m and V, namely,

$$\begin{aligned} B_1(r,t) &= \frac{1}{2\gamma_1(2\mu_1 - \mu 2}\Big(- k_a lV\mu_2 - \gamma_1 k_i(2) f_0 m - \mu_1\mu_2 \\ &\quad + \Big(\gamma_1^2 ki(2)^2 f_0^2 m^2 + 2\gamma_1\mu_2 f_0 m\big(4k_a lV\mu_1 \\ &\quad - k_a lV k_i(2)\big) + \mu_2^2\big(k_a lV + \mu_1\big)^2\Big)^{\frac{1}{2}}\Big) \qquad (5.53) \\ B_2(r,t) &= \frac{\gamma_1(B_1 + f_0 m)B_1}{2\gamma_1 B_1 + \mu_2}, \qquad (5.54) \end{aligned}$$

where

$$\gamma_1 = k_a^d \rho_f(\rho_l l - 1), \quad \mu_1 = k_d + k_i(1) \quad \text{and} \quad \mu_2 = 2k_d + k_i(2). \qquad (5.55)$$

Note that we have attempted to solve the algebraic system (5.48)-(5.50) with $n = 3$ but the solutions have turned out to be analytically intractable with the equations in their current form, we therefore make a simplifying assumption to allow progress. We introduce an approximation to F. Recall from (5.38) that

$$F = f_0 m - \sum_{k=1}^{n} kB_k.$$

We now assume that there are much more free receptors than bound, i.e. $F \gg \sum_{k=1}^{n} kB_k$, so that we can therefore make the leading order approximation

$$F = f_0 m. \qquad (5.56)$$

First, we check if this approximation to F is acceptable. We first test this on the simplest case; the single binding model. Recall that we have an expression for bound BPVs per cell, (5.21). With this new approximation for free receptors per cm^3 (5.56) we now have the expression,

$$B(r,t) = \frac{k_a l V f_0 m}{(k_d + k_i)}, \tag{5.57}$$

Now, for the $n = 2$ case, we can get an expression for B_1 and B_2 explicitly in terms of m and V, and using (5.56) we get

$$B_1(r,t) = \frac{k_a l V f_0 m \mu_2}{\mu_1\mu_2 + f_0 m \gamma_1 k_i(2)}, \tag{5.58}$$

$$B_2(r,t) = \frac{\gamma_1 f_0 m B_1}{\mu_2}, \tag{5.59}$$

where γ_1, μ_1 and μ_2 are defined as in (5.55).

In Figure 5.12, we show the difference in the radius of the tumour over time when single binding ($n = 1$) and multiple binding (when $n = 2$) are compared. For simplicity we keep the internalization rate constant for this comparison. The BPVs are introduced to the tumour surface at time $t = 40$ and removed at time $t = 50$. We notice that when we extend the model to include multiple binding events (when $n = 2$) there is a slightly lower decrease in tumour volume compared to when $n = 1$. Importantly, we notice that when the free receptors are approximated by $F = f_0 m$ we have a very good match compared to the full system in both single ($n = 1$) and multiple binding cases ($n = 2$). Since the system is algebraically is intractable when using $F = f_0 m - \sum_{k=1}^{n} k B_k$ (if $n \geq 3$) we assume that the $F \approx f_0 m$ approximation holds for all cases when $n \geq 3$.

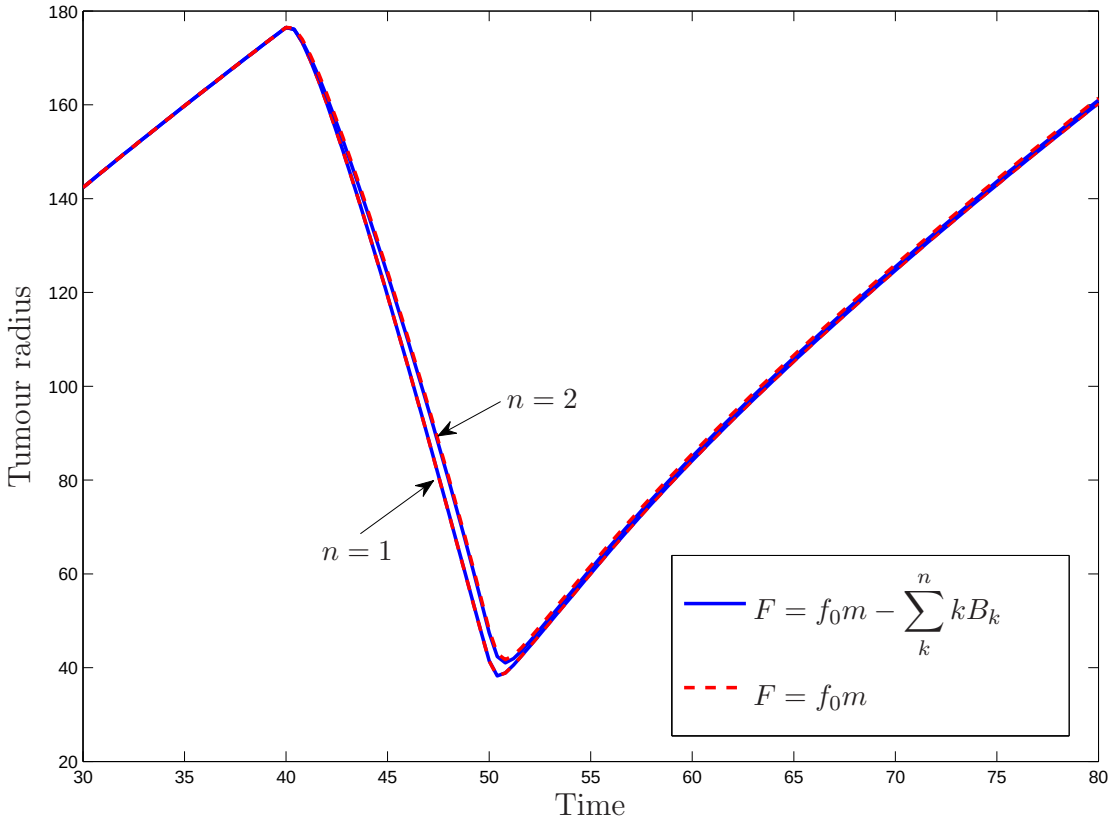

Figure 5.12: Shown are the tumour radii plotted against time when $n = 1$ and $n = 2$ using a direct comparison between the assumption when $F = f_0 m$ (red dashed lines) and the full expression when $F = f_0 m - \sum_k^n kB_k$ (blue solid lines). In the interval $t = 30, ..., 80$, we introduce the BPVs by letting $V_\infty = 10$ for $40 \leq t \leq 50$. We take $V_\infty = 0$ otherwise. With $D_m = 10, D_n = 500, D_v = 500, k_a = 0.01, k_i = 880, k_d = 0.053, \gamma = 10^{-3}, d_m^{max} = 2, f_0 = 1000, n_\infty = 0.2, c_p = 0.6$ and $c_c = 0.2$.

We now study the effects of taking $n = 4$ and $n = 5$, using a contant internalization rate. In Figure 5.13, we see that there is very little difference in the final tumour radii as we increase n. We saw a similar result in Chapter 4 where,

even though BPVs can bind to multiple receptors, with this parameter set, most BPVs were bound with one complex and internalized quickly.

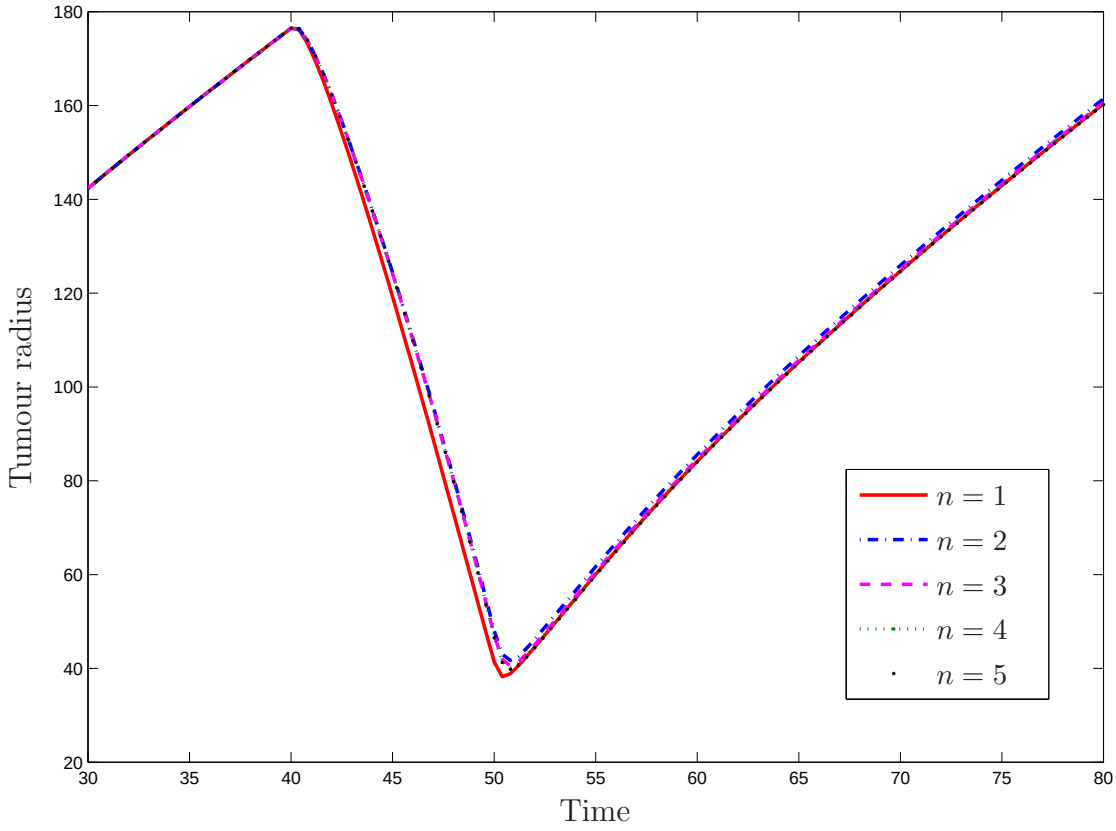

Figure 5.13: The tumour radii when we increase the maximum number of bonds available, n for $n = 1, ..., 5$. The parameter values are the same as in Figure 5.12.

We solve the non-dimensionalized system (5.40)-(5.43), using $n = 5$, together with the analytical solutions for bound BPVs, B_k where $k = 1, ..., 5$. The typical profiles are given in Figure 5.14, which show the spheroid radius versus time with the associated density of tumour cells, oxygen, free BPVs and bound BPVs within the tumour boundary. Here, we assume the BPVs are internalized at a

constant rate. For $0 \leq t < 40$ there are no BPVs present and we observe linear growth of the spheroid radius. As time increases, the tumour cells continue to proliferate which increases the size of the spheroid. Due to the limitation of oxygen diffusion there is a concentration gradient of oxygen with the highest concentration at the spheroid boundary. This gradient results in a region of lower density of tumour cells behind the proliferating edge. At the centre of the spheroid there is a very low concentration of oxygen which results in a necrotic core of dead cells. During this initial growth there are no BPVs present. At time $40 \leq t < 50$, BPVs are introduced to the surface of the spheroid and these infiltrate into the tumour. We see that the highest concentration of free BPVs occurs at the boundary but we do now see infiltration into the centre of the spheroid by $t = 50$. However, the highest concentration of bound BPVs are still found at the proliferating edge of the tumour since where the viable tumour cell density is highest. During the period of BPV application, we observe a noticeable decrease in spheroid radius. The BPVs are removed at $t = 50$. The spheroid then becomes re-oxygenated due to the smaller radius allowing for effective diffusion. This then provides a good environment for growth, hence the spheroid re-grows linearly for $t > 50$.

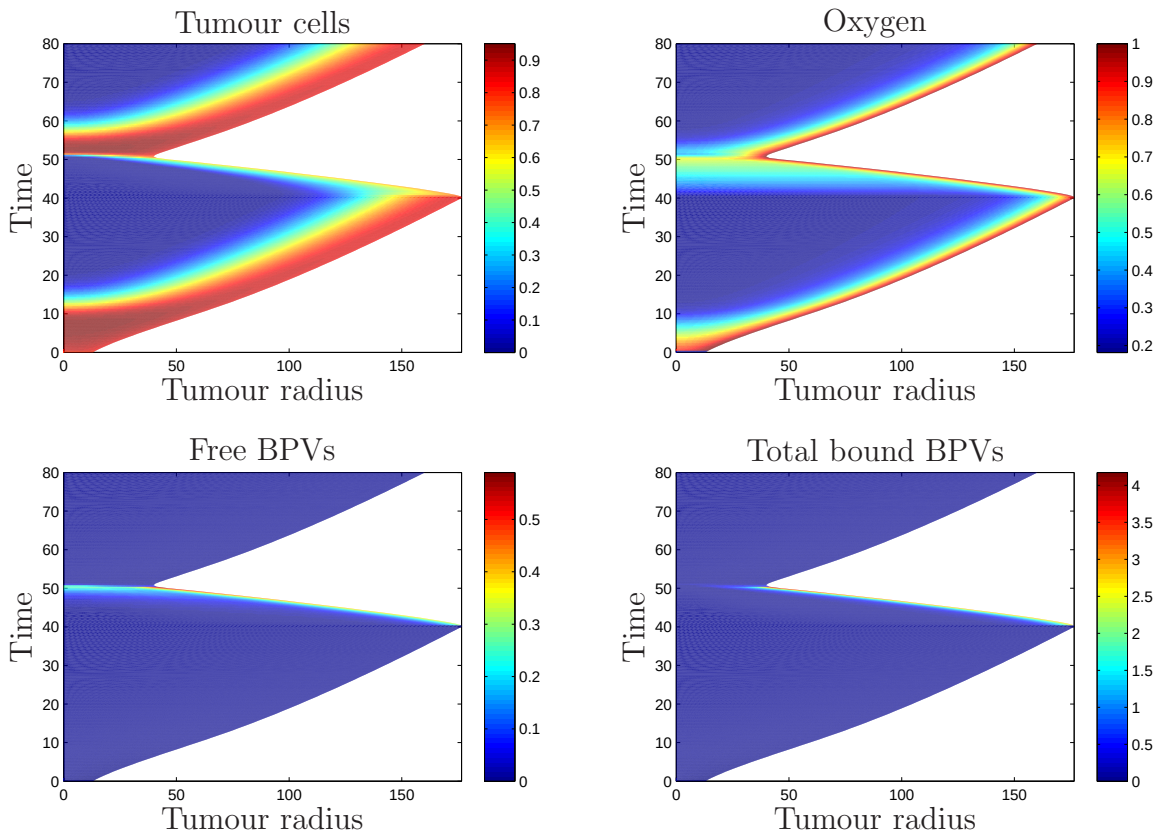

Figure 5.14: The tumour spheroid changing with time. We plot the densities of tumour cells, oxygen concentration, free and total bound BPVs. Initially growth occurs with no free BPVs on the tumour surface, then we introduce BPVs by setting $V_\infty = 10$ when $40 \leq t \leq 50$. We notice that the tumour growth rate decreases for the period of time when treatment is administered, but returns to linear growth (indicating travelling wave solutions) after. The parameters are the same as those in Figure 5.12.

5.5.1 Large Time Behaviour

As we see in Figure 5.14, travelling waves are still present in the multiple binding case and so, in this section, we look for travelling wave solutions in the multiple binding model. We also include the two internalization functions (5.39); one describing constant internalization independent on the number of receptor-ligand complexes formed and the other dependent on the number of complexes formed. We carry out this analysis with the intention to find out if, in the long term, the differing internalization functions can affect treatment efficacy.

As before we assume that tumour growth is at a constant speed, $u > 0$, so that $R \sim ut$ as $t \to \infty$. We redefine our system with the travelling wave coordinate, $z = r - ut$, and rewrite the equations (5.40)-(5.43) in terms of z, in the usual way. This system of three 2nd order ODEs is then converted to a system of six first order ODEs.

We have carried out the domain truncation in the same way as before, see Section 5.3.1 for details. The final system for the travelling wave analysis is then given by

$$
\begin{aligned}
m' &= W, && (5.60)\\
c' &= P, && (5.61)\\
V' &= Q, && (5.62)\\
W' &= \frac{1}{\psi m - D_m}\left(uW - \psi W^2 + p_m(n,c)m - d_m(c)m - g(B_k)\right), && (5.63)\\
P' &= d_c(m,n), && (5.64)\\
Q' &= -\frac{1}{D_v}\left((u-\psi W)Q - \psi W V - k_a V F + \frac{k_d}{l}B_1\right), && (5.65)
\end{aligned}
$$

for $k = 1, ..., n$, subject to the following boundary conditions on the truncated

domain $\hat{z} \in [0, 100]$: at $\hat{z} = 0$

$$m'(0) = c'(0) = V'(0) = 0; \tag{5.66}$$

at $\hat{z} = 100$,

$$-D_n m' - D_m \frac{(1-m)}{m} m' = h_n(n_\infty + m - 1)\,|_{\hat{z}=1}\ , \tag{5.67}$$

$$D_v V' - D_m \frac{V}{m} m' = h_v(V_\infty - V)\,|_{\hat{z}=1}\ , \tag{5.68}$$

As before, we also fix the oxygen concentration $c = 1$ at $\hat{z} = 100$. We have 6 boundary conditions as before see (5.66)-(5.68). We impose an additional boundary condition which fixes the wavespeed u at $\hat{z} = 100$ and this is given by $u = h_n(n_\infty + m - 1)$. This extra boundary condition allows us to use the bifurcation and continuation AUTO to solve (5.60)-(5.65) to calculate the wavespeed, u.

First, we explore the long term effects of the internalization function, $k_i(k)$ (5.39), on the long time solution profiles. In Figure 5.15, we show the densities of tumour cells, oxygen and free BPVs subject to the two different internalization functions. We can see no difference in the solutions for tumour cells, oxygen or free BPVs when using either internalization function.

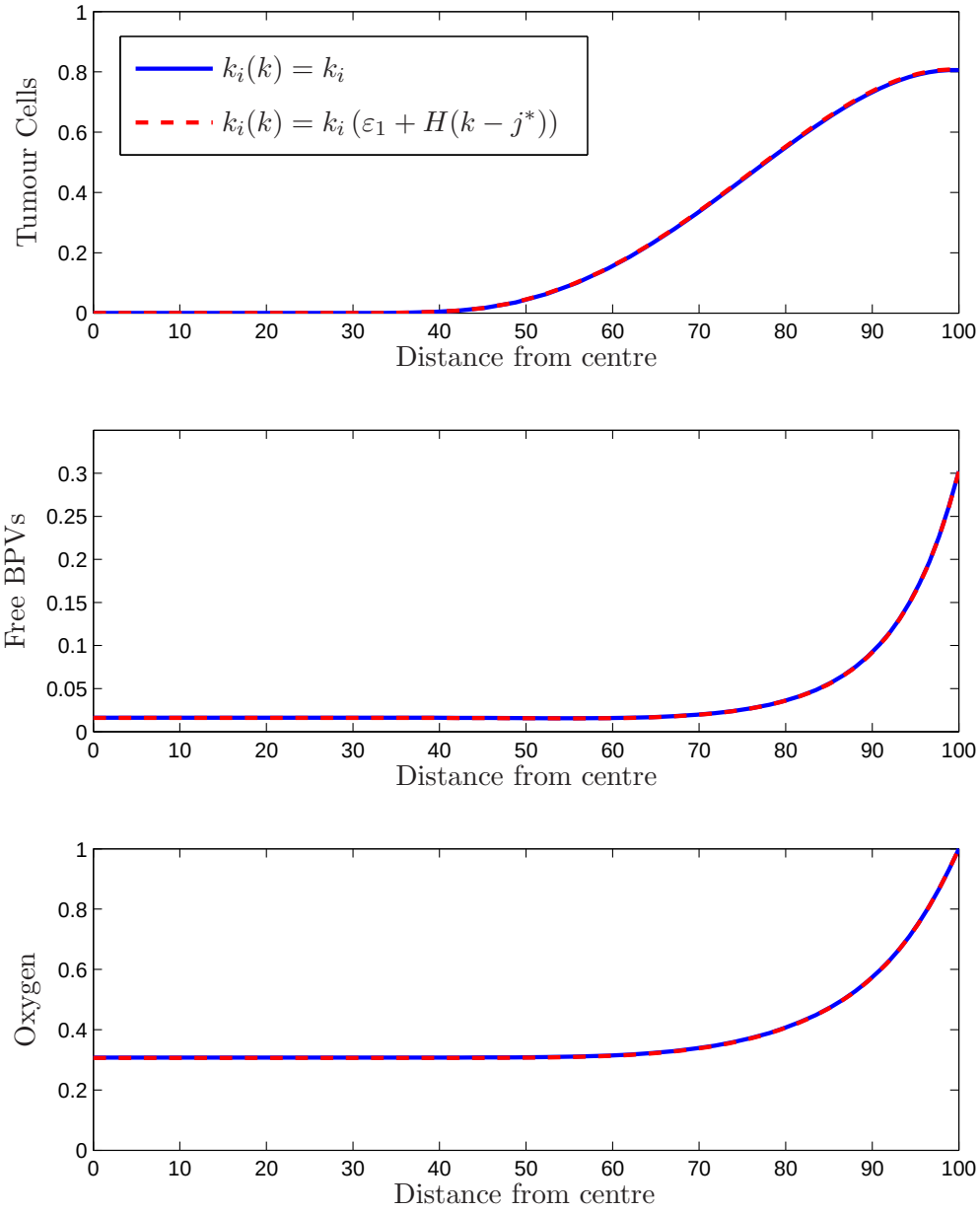

Figure 5.15: The profiles for tumour cells, free BPVs and oxygen, when solved with the two different internalization functions described in (5.39). The blue line represents the constant internalization rate k_i and the red dashed line represents the internalization when dependent on j^*. We observe no noticeable difference between the two solutions. The parameters are the same as in Figure 5.12, where $j^* = 5$ and $\gamma = 1 \times 10^{-5}$.

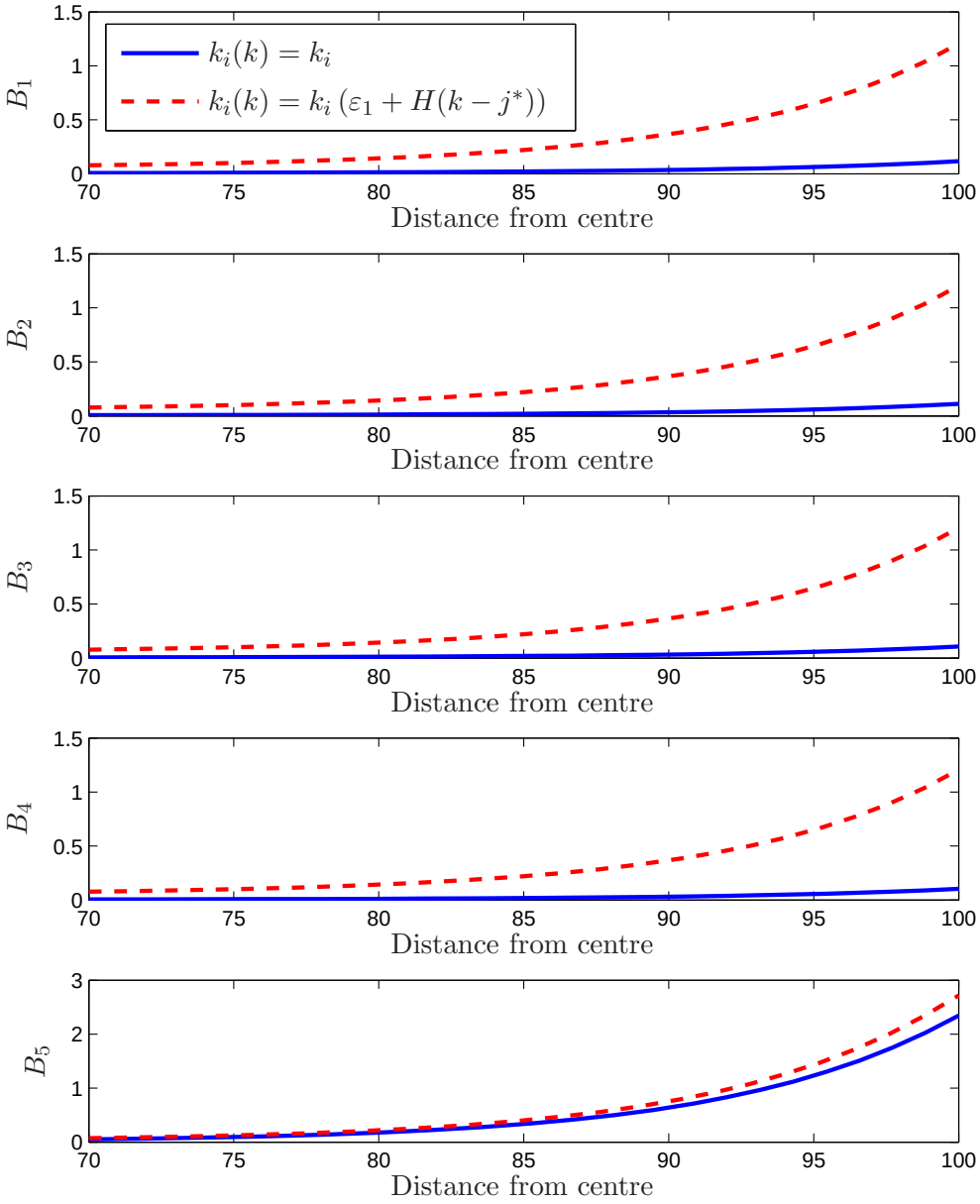

Figure 5.16: The numerical solutions for BPVs bound with k complexes, where $k = 1, ..., 5$, when solved with the two internalization functions described in (5.39). Here, we take $j^* = 5$ and $\gamma = 1 \times 10^{-5}$. The blue line represents the constant internalization rate k_i for all k and the red dashed line represents the internalization when bound by j^* complexes. We can see an accumulation of B_k's on the surface of the tumour when $k_i(k) = k_i\,(\varepsilon_1 + H(k - j^*))$ since they are only likely to be internalized when in the B_5 state. The parameters are the same as in Figure 5.12.

In Figure 5.16, we show the profiles of the bound BPVs by $k = 1, ..., 5$ complexes subject to the two internalization cases. In the function case, we take $j^* = 5$. In contrast to Figure 5.15, we do observe a change in bound BPVs with k bonds between the two internalization functions. We notice that there are a greater number of BPVs bound when the internalization is dependent on the number of complexes, i.e. when

$$k_i(k) = k_i \left(\varepsilon_1 + H(k - j^*)\right), \quad \text{where} \quad j^* = 5.$$

The increase in the number of BPVs bound is due to the restriction on internalization when $j \leq 4$. Instead of the BPVs with 1,2,3, or 4 complexes being internalized, they stay bound to the tumour cell until more complexes can form. In contrast, when

$$k_i(k) = k_i = \text{ constant}$$

we see a greater number of BPVs internalized as they are not restricted to additional bonds being formed.

In an attempt to explain why we do not see a significant difference in the long time solution profiles for the two different internalization functions, we examine the tumour death term $g(B_k)$. Figure 5.17 shows the death term $g(B_k)$ over the spheroid interior for both internalization functions. The two curves in Figure 5.17 are very similar with a very small difference between the two internalization cases. Although, from Figure 5.16, we see a difference in the number of bound BPVs from these two internalization cases, the number internalized in the long time are very similar.

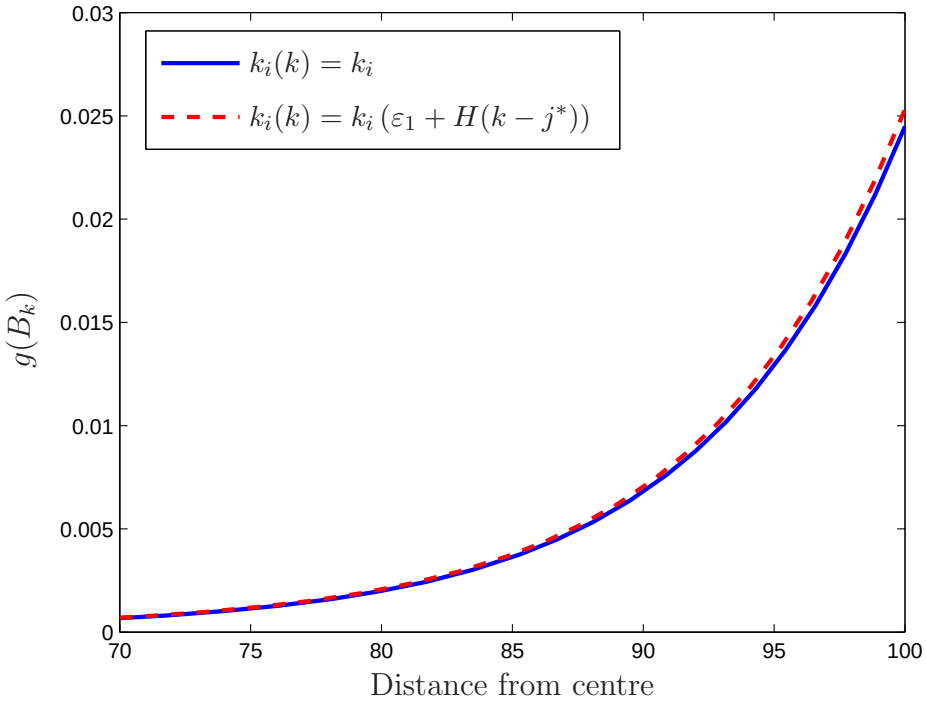

Figure 5.17: The blue line represents the constant internalization rate k_i for all k and the red dashed line represents the internalization when bound by j^* complexes (we take $j^* = 5$). There is no significant difference in the final death function $g(B_k)$ when using either of the internalization functions, which is reflected in the previous profile solutions where we also do not see a difference in the final tumour profile. The remaining parameters are the same as Figure 5.12 with $\gamma = 1 \times 10^{-5}$.

We now examine the effect of the internalization functions on the wavespeed, u, whilst also varying the tumour cell sensitivity to BPVs (γ). In Figure 5.18, we notice that there is an increasingly large difference between the values γ may take to decrease the wavespeed to zero.

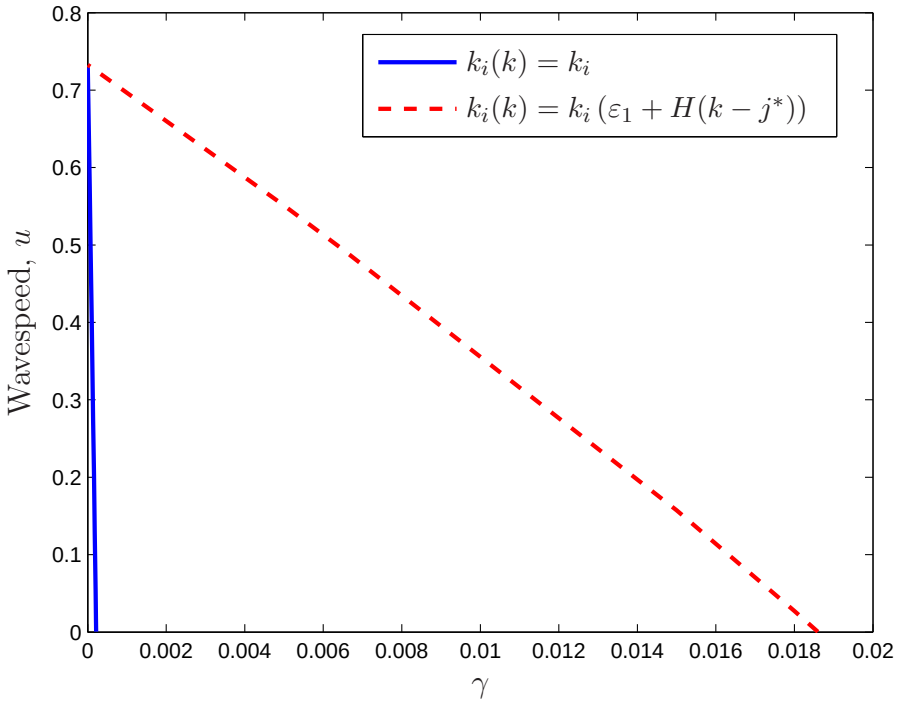

Figure 5.18: The wavespeed, u, versus γ with the two internalization functions of $k_i(k)$. Showing that if we assume $k_i(k) = k_i\,(\varepsilon_1 + H(k - j^*))$, where $j^* = 5$, we then require a larger death rate (γ) to confine growth (steady states). Here $V_\infty = 2$ in both cases, the remaining parameters are the same as in Figure 5.12.

When we take the Hill function internalization, we know (from Figure 5.16) that there are more BPVs attached to the tumour surface which don't appear to be internalized. Hence the tumour cells must be more sensitive to the BPVs that are internalized for a comparable decrease in wavespeed to be seen, thus, requiring a larger death rate, γ. In Figures 5.19-5.20, we vary with the effect of increasing the potency of the BPV and increasing the external concentration of BPVs to the tumour surface on a short-timescale of treatment to see if there is

any change in the spheroid radius when $j^* = 5$.

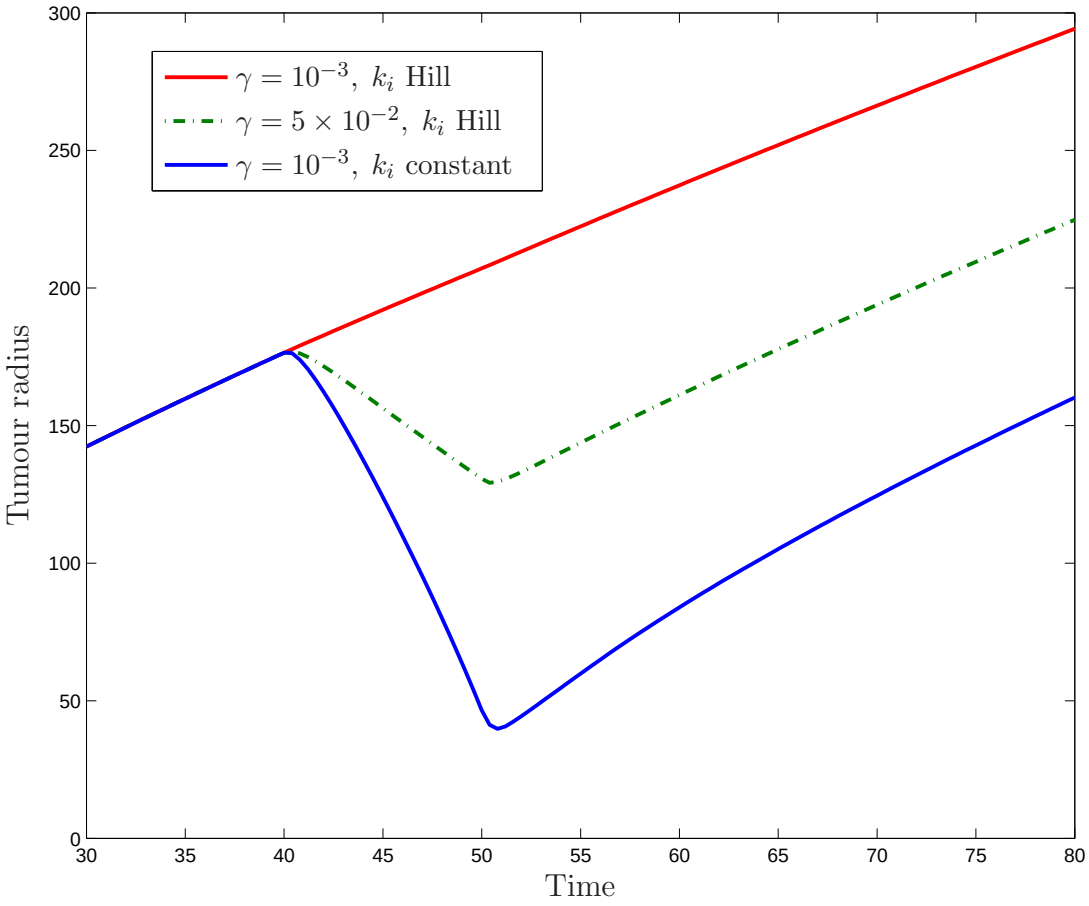

Figure 5.19: The spheroid radius when solved with the two internalization functions at different values of γ. By increasing γ, we are increasing the potency of the BPVs, by doing so we can produce a similar tumour radius profile to that of constant internalization (blue line). The red line and green dash-dotted line show the spheroid radius when solved with $k_i(k) = k_i\left(\varepsilon_1 + H(k - j^*)\right)$ when $j^* = 5$. The default value taken for γ is 10^{-3}, and this is increased 50-fold, with $V_\infty = 10$ when $40 \leq t \leq 50$. The remaining parameters are the same as Figure 5.12.

We notice that there is a difference in the spheroid radius (when $\gamma = 10^{-3}$) when solving with the two internalization cases. If k_i is not dependent on the number of complexes, we see a reduced radius during the period of treatment. However, if k_i is dependent on the number of complexes (when in this case $j^* = 5$), we do not see any decrease in spheroid radius during this short time period, due to the BPVs being held on the cell surface as they require additional bond formation before internalization. When the death rate γ is increased, however, we then observe a decrease in spheroid radius during the period of treatment. From Figure 5.20, we see that also there must be a considerable increase in V_∞ to see a decrease in tumour radius when the internalization is complex dependent. Therefore, a greater number of BPVs are required to be present when complex number dependent internalization is assumed.

When internalization is dependent on the number of complexes, BPVs remain on the cell surface instead of being internalized readily. This could suggest that although eventually they will be internalized, the low rate of internalization of BPVs in a short time frame means that we do not see the impact of the therapy. If the amount of BPV applied is the same in both internalization cases, due to low internalization rate when it is complex dependent, the tumour cells may recover and grow. In the case of constant internalization, BPVs are more readily internalized and the treatment has a much stronger impact.

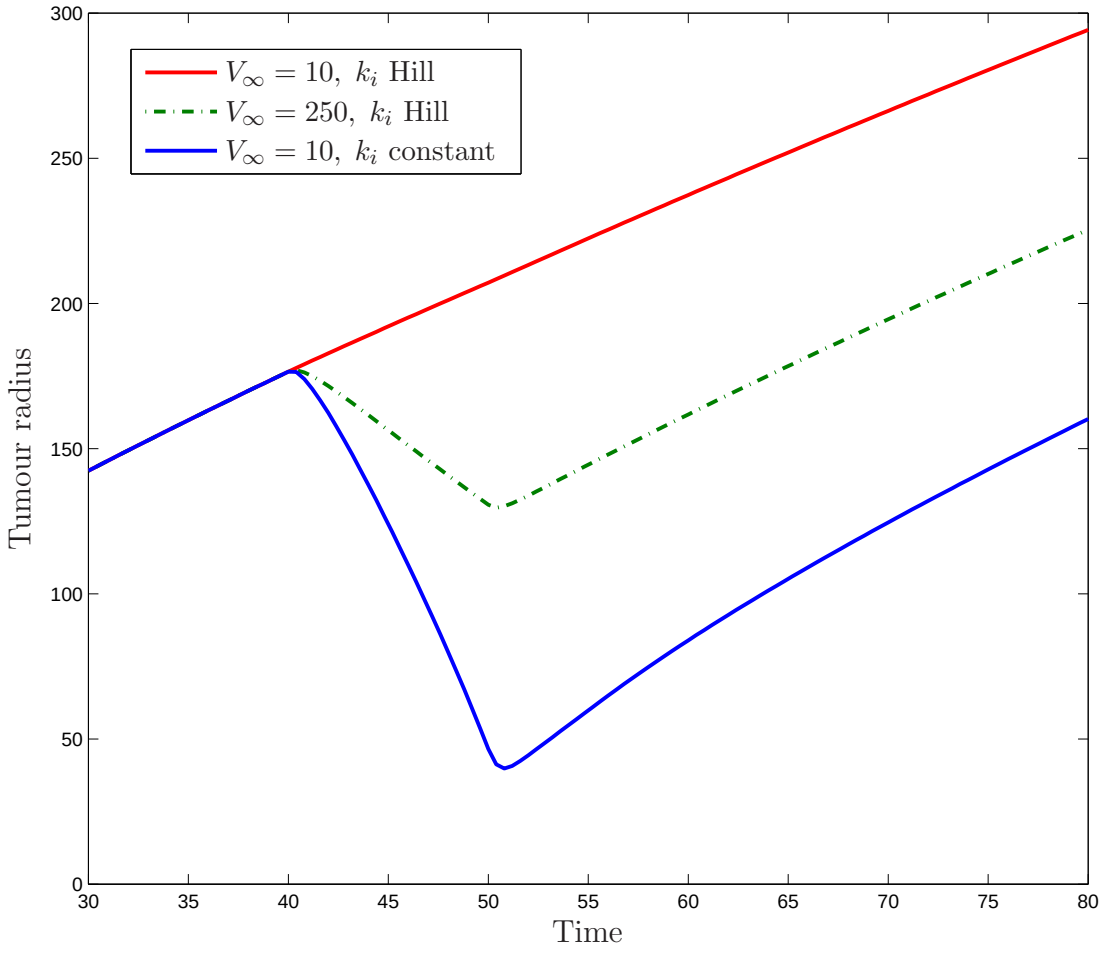

Figure 5.20: The spheroid radius versus time when solved with the two internalization functions at different values of V_∞ ($\gamma = 10^{-3}$ fixed). We vary the concentration of BPVs on the tumour surface during $40 \leq t \leq 50$. The red line and green dash-dotted line show the spheroid radius when solved with $k_i(k) = k_i\left(\varepsilon_1 + H(k - j^*)\right)$ where $j^* = 5$. The blue line represents when $V_\infty = 10$. A significant increase in V_∞ is required to get a similar radius profile to that of constant internalization. The remaining parameters are the same as Figure 5.12.

We have seen the difference between the 2 different cases of internalization when in the Hill function case, the threshold, j^*, is set to 5. We now relax the strictness of internalization function to see the effect when an intermediate j^* is chosen. Figure 5.21 shows the spheroid radii when $j^* = 1, .., 5$.

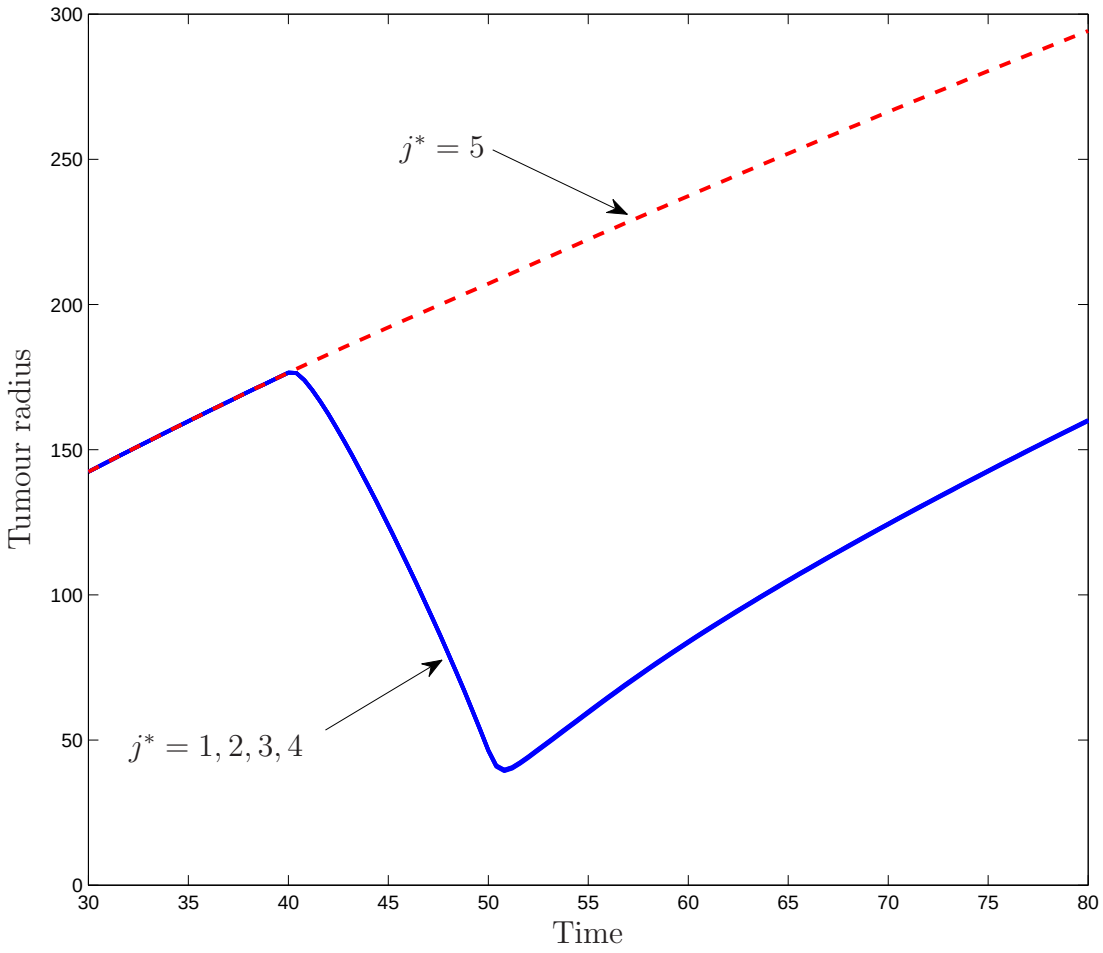

Figure 5.21: The change in tumour radius over time with the internalization function given by $k_i(k) = k_i\,(\varepsilon_1 + H(k - j^*))$, with various j^*. The growth rate is linear for $j^* = 5$, but when $1 \leq j^* \leq 4$, a decrease in tumour size is seen during the period of treatment. We have $\gamma = 10^{-3}$ and $V_\infty = 10$ when $40 \leq t \leq 50$. The remaining parameters are the same as Figure 5.12.

We notice from Figure 5.21 that when $j^* \leq 4$ there is a decrease in spheroid radius during the period of treatment comparable to that of constant internalisation, but if $j^* > 4$ there is no reduction in spheroid growth during the treatment time. Therefore, with this set of parameters $j^* = 5$ appears to be a threshold. That is, by forcing the BPV to bind to at least 5 complexes before internalization we slow down the internalization of the BPV sufficiently so that treatment is then not effective within this time frame.

We now compare the large-time solutions when $j^* = 3$ and $j^* = 5$. Previously in Figure 5.21 we saw that when $j^* > 4$ there is little effect on spheroid radius during the period of treatment with BPVs. In contrast, if $j^* < 5$ there is a decrease in radius. In Figure 5.22, we examine whether this is a transient or long term effect.

We observe in Figure 5.22, that the spheroid radius tends to a limit which is not dependent on j^*. In early time, when $j^* = 5$, we see a decrease in spheroid radius only if the potency or volume of BPVs are increased. When $j^* < 5$ no increase in potency is required for the transient decrease in spheroid growth to be seen.

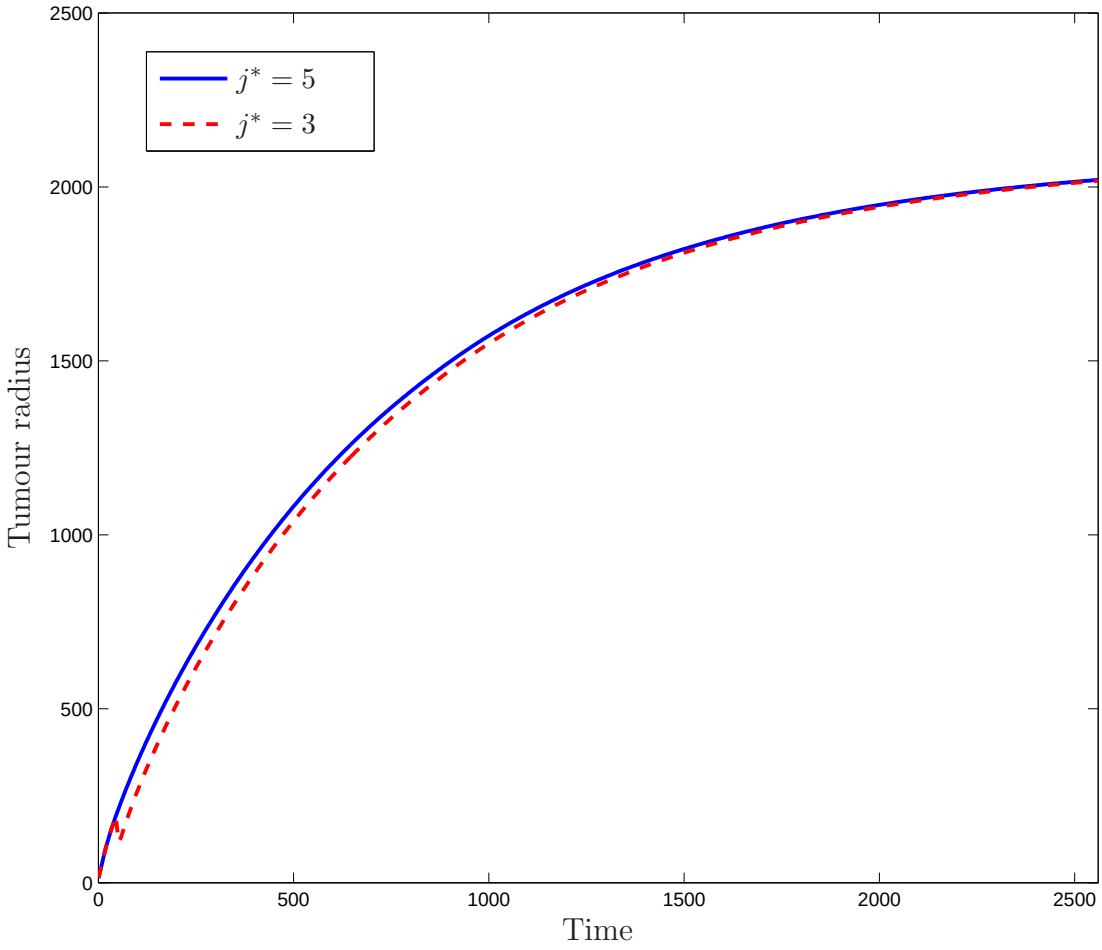

Figure 5.22: The spheroid radius changing with time when $k_i(k) = k_i\left(\varepsilon_1 + H(k - j^*)\right)$ where $j^* = 3, 5$. The treatment is applied for $t \in [40, 50]$ but we run the simulation for large-time to see if the differences between $j^* = 3$ and 5 are transient or long term. We notice transient spheroid radius decrease when $j^* = 3$ (not present when $j^* = 5$) but in large time both solutions tend to the same final spheroid radius. The parameters are the same as in Figure 5.12.

5.6 Discussion

In this chapter, we have presented a model of a novel targeted cancer therapy, where BPVs infiltrate avascular tumour spheroids. The model represents the growth of a tumour spheroid. In general the growth of the spheroid is dependent on the balance between proliferating and dying tumour cells, which is controlled by the nutrient (namely oxygen) availability. We include BPV infiltration into the model by assigning a fixed concentration of BPVs on the tumour spheroid boundary which are then free to permeate the boundary and diffuse throughout the spheroid. BPVs are internalized by cells by the process of endocytosis. We make the modelling assumption that the BPVs are only internalized by receptor-mediated endocytosis. We also assume a death rate which is proportional to the internalization of the BPVs.

In Section 5.2, we describe the simple case whereby we assume only one binding event (where one receptor-ligand complex is formed) is required for the BPV to become bound to a tumour cell and subsequently internalized. Whereas, in Section 5.4, we extend this assumption to include multiple binding events. We use numerical simulations and large time asymptotics to analyse the behaviour of these two systems.

The numerical simulations show that for appropriate parameter values the spheroid grows linearly when there is insufficient infiltration of the BPVs. When BPVs infiltrate the spheroid there is a noticeable decrease in spheroid radius in the single binding case which is dependent on the values of the therapeutic parameters. We carry out a bifurcation analysis which highlights the regions of parameter space where linear growth of the spheroid or saturation at an equilibrium state occurs. The parameter regions with unexpected results include γ and n_∞, the death rate due to BPV internalization and the external concentration of cellular

material, respectively. We assume that with an increase in n_∞ there would be an increase in growth and so require more potent BPVs to attain saturated growth. This was indeed observed until a threshold of n_∞, after which the model predicts that we are more likely to see saturation of growth when using less potent BPVs i.e. lower γ. In this case, the internal velocity within the spheroid came into play. By increasing n_∞ past the threshold, the gradient of cellular material switched direction, creating an opposite internal velocity. Hence, instead of the BPVs accumulating in the centre of the spheroid, they mainly lie at the proliferating edge of the spheroid where treatment will be most successful.

We see another interesting result when examining the h_v, D_v parameter space, where h_v the permeability of BPVs over the spheroid boundary and D_v the diffusion coefficient of free BPVs, respectively. We see that for a certain value of h_v, there can be either growth of the spheroid or saturation. For very small or very large values of D_v, we see travelling waves whereas intermediate values results in growth saturation.

When extending the model to include multiple binding events we also include a more biologically realistic internalization function, in which a BPV must be bound by a given number of complexes before internalization can occur mimicking the membrane deformation that occurs during receptor-mediated endocytosis. We introduce an approximation to the free receptors concentration as the multiple binding framework becomes algebraically intractable to solve when $n > 2$ (where n is the maximum number of complexes that can form).

Numerical simulations indicate no change in the long-time tumour cell density when using constant internalization or the complex dependent internalization, although there is a difference seen in the numbers of BPVs bound to the tumour cells. As expected more BPVs are bound on the tumour surface instead

of being internalized when the more complex dependent internalization function is assumed. There is also no change in long time tumour density due to the total death rate being almost identical in both cases. What we do observe, however, is that the multiple binding dynamics produce only transient differences. The radius of the spheroid tends to the same size, as $t \to \infty$, independent of internalization function used.

Chapter 6

Conclusions and Future work

6.1 *S. coelicolor* Growth and Metabolite Production

In Chapter 2 and 3 of this thesis we look at the growth and metabolite production of *S. coelicolor*, which are very important bacteria in the world's production of antibiotics. We derive a mixed system of hyperbolic-parabolic partial differential equations to describe the growth of a *S. coelicolor* pellet in 1-D radially symmetric space. We assume that growth of the pellet is driven by the hyphal tip flux, and used tip and trail expressions for the formation of hyphal biomass. In Chapter 2, we parameterize the model using experimental data provided by Dr P. Hoskisson and values from the literature. After rescaling the system we solve the system using NAG routine D03PHF and produce numerical simulations which correspond well to the real biological system. We carry out a parameter sensitivity analysis which gives us insight into how specific parameters may influence pellet growth. We find that by increasing the hyphal growth due to tip

extension the pellet decreases in hyphal density but produces more metabolites.

The model contains Heaviside functions which describe the switching between hyphal biomass production (by controlling the tip flux and death rates of the hyphae and hyphal tips) and antibiotic production. This switch is dependent on the concentrations of substrate (glucose) and oxygen. We use the properties of the Heaviside function to seek analytical solutions of the system in specified regions of substrate and oxygen. For a small pellet, where the substrate and oxygen concentrations are high and constant, i.e. at early time, we find that the solution of the hyphal tips was given by

$$p(r,t) = E\sum_{k=1}^{\infty} \frac{\exp(-ct)\sin(kr)}{kr},$$

where $E = AB'$ is constant, c is the separation constant and $k = \sqrt{\dfrac{c - d_p + b}{D_p}}$. In the case where there is low substrate but high oxygen we find that the tips and hyphae decay at an exponential rate which matches the numerical solutions very well.

Due to the shape of the numerical solutions we carry out a travelling wave analysis on a reduced growth model. The reduced system is simplified by setting $d_s^{cm} = 0$ which describes the consumption rate of substrate by hyphae, which decoupled the hyphae and antibiotic equation, and for this set of parameter values $c(r,t) > \hat{c}$ (where $\hat{c}$ is the threshold for hyphal tip branching, below which branching stops) we can neglect the oxygen equation, which leaves only the hyphal tip and substrate equations. We obtain the minimum wavespeed from the travelling wave analysis, an increasing function of tip diffusion and branching and a decreasing function of the tip decay rate. We find that the numerical wavespeed that we observe is indeed always greater than this analytical minimum wavespeed.

We observe oscillations in the numerical solutions for the tip equation, which result in the solutions becoming negative near the origin. We address this in Chapter 3 by solving a reduced system using a finite element method. Initially we solve a simplified problem to test the numerical scheme we develop. The problem contains the important aspects of the *S. coelicolor* reduced model including the nonlinearity and transport. We use a θ-method to discretize time in the simplified problem. We experiment with different values of $\frac{1}{2} \leq \theta \leq 1$, a clear difference in solutions is shown due to the diffusivity added to the system when $\theta = 1$. When solved with $\theta = \frac{1}{2}$ and $\theta = 1$, a timestep 10 times smaller is required when $\theta = 1$ for convergence of the solutions. Hence this leads us to using Crank-Nicolson ($\theta = \frac{1}{2}$) when solving the reduced *S. coelicolor* growth model. We use finite elements to discretize space in the reduced *S. coelicolor* growth model. We approximate the Jacobian and solve the problem in Matlab using a quasi-Newton algorithm. The results we obtain have no oscillations.

In this thesis, we aim to use mathematical models in order to get insight into the biological system. In particular, we have found that a less dense pellet produces more antibiotics, which could be implemented during experiments by introducing a force which periodically breaks up the pellets to keep the density low. We have also shown that by using our finite element code we can produce non-oscillatory solutions that appear non-negative for this problem, unlike NAG routine D03PHF.

Future work

The main focus of the work we present in Chapters 2 and 3 is on the growth dynamics of the streptomyces system. We included antibiotic production within the models but we assumed that it is merely a by-product of hyphal growth.

The next stage is to focus more on the modelling of *S. coelicolor* antibiotic production. There is a lack of knowledge surrounding this area. With a greater understanding of the biological system a more realistic model of antibiotic production can be produced. Due to the lack of practical data, some parameter values are obtained from literature. We would have liked more experimental data that was in the correct form for this model. The next stage of modelling this system is gaining more usable experimental data to parameterize the model fully.

We use simple numerical techniques to model a complex system. Future work carrying on from Chapter 3 would be to extend the model to 2-D finite elements, this would hopefully show the non-symmetrical nature in which pellets grow. With this, along with the extension into 2-D finite elements, an adaptive mesh would be advantageous for the regions such as the peak of the tips or the sharp gradient change of the substrate.

6.2 Targeted Cancer Therapy

In Chapters 4 and 5 we introduce mathematical models to describe a novel cancer therapy which involves the cancer cell-specific targeting by BPVs (bio-mimetic polymer vesicles). These BPVs can be loaded with either DNA for gene therapy or anti-cancer drugs.

We derive a deterministic model that describes the binding kinetics between cell receptors and ligands on the BPV surface using a system of ordinary differential equations. We parameterize the model using values obtained from a similar system that model liposomal targeting [36] which are specific to the folate receptors on C6 glioma cells. We carry out a parameter sensitivity analysis

which gives us insight into how key parameters affect the dynamics of the system. Due to the uncertainty of receptor-ligand interactions that are used when targeting HNSCC, the parameter sensitivity provides an insight into what may occur with HNSCC cells. We notice that, when the number of ligands per BPV is high this restricts entry into cells, hence the treatment is more effective with less ligands per BPV. Furthermore, by carrying out this analysis, we find that by varying the dissociation rate, k_d, there is little to no effect which allows us to make simplifications that facilitates the singular perturbation analysis of the early behaviours.

We explore the special case where $n = 1$, i.e. the single binding case. At early time the solutions for free receptors, free BPVs and bound BPVs change rapidly due to the fast binding kinetics of receptors and ligands compared to the slower growth rate of the tumour cells. Using the fact that k_d does not change system dynamics, we carry out a singular perturbation on a reduced version of the model with $k_d = 0$. At early time we assume that $m = 1$ and $P = 0$, then we rescaled parameter groupings by a small parameter ε, i.e. we let $\eta l = \dfrac{\widehat{\eta l}}{\varepsilon}$ and $d_f = \dfrac{\hat{d}_f}{\varepsilon}$ where $\varepsilon \ll 0.1$. Using these rescalings we find analytical solutions for free BPVs, free receptors, bound BPVs and internalized BPVs at very early time which match the numerical solutions. We find that the maximum value for internalized BPVs was an increasing saturating function of ligands per BPV, l. Hence this re-enforces the hypothesis that there is a optimal number of ligands per BPV. Ghaghada *et al* [36] also find that there should be an optimal number of ligands on the liposome surface and that over this value there is decreased uptake of the liposomes. due to the synthetic nature of the BPVs.

We extend the model in Chapter 5 to represent BPV infiltration into a tumour spheroid. The spheroid is composed of tumour cells and cellular material with

the growth dependent on the nutrients available which diffuse across the spheroid boundary. We include multiple binding kinetics between BPV ligands and cell receptors derived in Chapter 4.

Initially, we present numerical solutions for the single binding case where only one receptor-ligand complex is required before the BPV is internalized. We noticed that the growth of the spheroid radius is linear except when the BPVs are applied. This lead us to use large time asymptotics to analyse the behaviour of the system. Using AUTO [29], we conduct a bifurcation analysis which results in regions of parameter space where spheroid growth could either be saturated (steady states) or linear (travelling waves).

We then look at the multiple binding case and use a quasi-steady state assumption for bound BPVs. This allows us to solve the equations when the maximum number of allowed complexes is low $n < 3$. When it is large ($n \geq 3$), the solutions were intractable. Hence to solve for $n \geq 3$ we introduced the assumption that the number of free receptors far exceeds the number of bound complexes, i.e. $F \gg kB_k$, where $k \geq 3$. Using large time asymptotics we then investigate the internalization of the BPV in more detail. We used two functions to describe the internalization; the first was constant, (k_i previously used in Chapter 4), the second is dependent on the number of receptor-ligand complexes, $k_i(k)$ which would mimic the membrane deformation and encapsulation of the BPV. We find no difference in final tumour cell density, free receptors or free BPVs, but we see higher instances of BPVs with 1-5 complexes when $k_i(k)$ is used which is due to the BPVs being held on the tumour surface until a sufficient number of complexes have been reached.

The important aspect of this analysis is that the radius of the spheroid tends to the same size as $t \to \infty$, for both the constant internalization rate and the

rate dependent on number of bound complexes, independent on the value of the internalization terms used.

Future work

There are a few things that could continue from this work. The first improvement would be to get a fully parameterized model using data provided by Dr Craig Murdoch from Sheffield University. This would provide useful conclusions that are specific to the BPVs they synthesize. An experiment carried out by this research group involves using a monolayer of cells with BPVs placed over them. To mimic this mathematically we can solve the system on a 2-D lattice geometry and try to reproduce their experimental findings.

One issue we have with the PDE model described in Chapter 5 is the algebraic difficulties when assuming that multiple binding interactions can occur and this has restricted our analysis to a very low number of bonds. To carry this work forward, we should implement a method that can sustain many binding events which will allow for the improved modelling of membrane deformation and additional binding events that can occur through this cell internalization process.

Bibliography

[1] Breast cancer-survival statistics:Cancer Research UK, December 2009. URL `http://info.cancerresearchuk.org/cancerstats/types/breast/survival/`.

[2] F. Ahmed, R.I. Pakunlu, A. Brannan, F. Bates, T. Minko, and D.E. Discher. Biodegradable polymersomes loaded with both paclitaxel and doxorubicin permeate and shrink tumors, inducing apoptosis in proportion to accumulated drug. *J. Control Release*, 116:150–158, 2006.

[3] F. Ahmed, R.I. Pakunlu, G. Srinivas, A. Brannan, F. Bates, M.L. Klein, T. Minko, and D.E. Discher. Shrinkage of a Rapidly Growing Tumor by Drug-Loaded Polymersomes: pH-Triggered Release through Copolymer Degradation. *Mol. Pharmaceutics*, 3:340–350, 2006.

[4] B. Alberts, A. Johnson, J. Lewis, M. Raff, K. Roberts, and P. Walter. *Molecular Biology of the Cell*. Garland Science, New York, fourth edition, 2002.

[5] E.J. Allan and J.I. Prosser. Mycelial Growth and Branching of *Streptomyces coelicolor* A3(2) on Solid Medium. *J. Gen. Microbiol.*, 129:2029–2036, 1983.

[6] A.R.A Anderson and M.A.J. Chaplain. Continuous and discrete math-

ematical models of tumour-induced angiogenesis. *Bull. Math. Biol.*, 60: 857–899, 1998.

[7] J.W. Barton and R.M. Ford. Mathematical model for characterization of bacterial migration through sand cores. *Biotechnol. Bioeng.*, 53, 1996.

[8] G. Battaglia, A.J. Ryan, and S. Tomas. Polymeric Vesicle Permeability: A Facile Chemical Assay. *Langmuir*, 22:4910–4913, 2006.

[9] S.D. Bentley, K.F. Chater, A.-M. Cerdeño-Tárraga, G.L. Challis, N.R. Thomson, K.D. James, D.E. Harris, M.A. Quail, H. Kieser, D. Harper, A. Bateman, S. Browth, C.W. Chen, M. Collins, A. Cronin, A. Fraser, A. Goble, J. Hidalgo, T. Tornsby, S. Howarth, C.-H. Huang, T. Kieser, L. Larke, L. Murphy, K. Oliver, S. O'Neil, E. Rabbinowitsch, M.-A. Rajandream, K. Rutherford, S. Rutter, K. Seeger, D. Saunders, S. Sharp, R. Squares, S. Squares, K. Taylor, T. Warren, A. Wietzorrek, J. Woodward, B.G. Barrell, J. Parkhill, and D.A. Hopwood. Complete genome sequence of the model actinomycete *Streptomyces coelicolor* A3(2). *Nature*, 417:141–147, 2002.

[10] M.J. Bibb. Regulation of secondary metabolism in streptomycetes. *Curr. Opin Microbiol.*, 8:208–215, 2005.

[11] L. Bingle, Brown N.J., and C.E. Lewis. The role of tumour-associated macrophages in tumour progression: implications for new anticancer therapies. *J. Pathol.*, 196:254–265, 2002.

[12] G.P. Boswell, H. Jacobs, F.A. Davidson, G.M. Gadd, and K. Ritz. Functional consequences of nutrient translocation in mycleial fungi. *J. Theor. Biol.*, 217:459–477, 2002.

[13] G.P. Boswell, H. Jacobs, F.A. Davidson, G.M. Gadd, and K. Ritz. Growth

and function of fungal mycelia in heterogeneous environments. *Bull. Math. Biol.*, 65:447–477, 2003.

[14] G.P. Boswell, H. Jacobs, F.A. Davidson, G.M. Gadd, and K. Ritz. A positive numerical scheme for a mixed-type differential equation model for fungal growth. *Appl. Math. Comput.*, 138:321–340, 2003.

[15] J. Bourhis, M. Lapeyre, J. Tortochaux, M. Rives, M. Aghili, S. Bourdin, F. Lesaunier, T. Benassi, C. Lemanski, L. Geoffrois, A. Lusinchi, P. Verrelle, E. Bardet, M. Julieron, P. Wibault, M. Luboinski, and E. Benhamou. Phase III Randomized Trial of Very Accelerated Radiation Therapy Compared With Conventional Radiation Therapy in Squamous Cell Head and Neck Cancer: A GORTEC Trial. *J. Clin. Oncol.*, 24:2873–2878, 2006.

[16] R.G. Bristow and R.P. Hill. Hypoxia, DNA repair and genetic instability. *Nat. Rev. Cancer*, 8:180–192, 2006.

[17] H.M. Byrne and M.A.J. Chaplain. Growth of nonnectotic tumours in the presence and absence of inhibitors. *Math. Biosci.*, 130:151–181, 1995.

[18] G. Cassinelli, M. Ballabio, A. Grein, S. Merli, G. Rivola, F. Arcamone, B. Barbieri, and T. Bordoni. A new class of biosynthetic anthracyclines: Anthracyclinone glucuronides. *J. Antibiot.*, 40:1071–1074, 1987.

[19] M.A.J. Chaplain and A.M. Stuart. A model mechanism for the chemotactic response of endothelial cells to tumour angiogenesis factor. *IMA J. Math. Appl. Med.*, 10:149–168, 1993.

[20] I. Cheong, X. Huang, K. Thornton, L.A. Jr. Diaz, and S. Zhou. Targeting cancer with bugs and liposomes: Ready, aim, fire. *Cancer Res.*, 67:9605–9608, 2007.

[21] S.D. Conner and S.L. Schmid. Regulated portals of entry into the cell. *Nature*, 422:37–44, 2003.

[22] F.A. Davidson. Modelling the qualitative response of fungal mycelia to heterogeneous environments. *J. Theor. Biol.*, 195:281–292, 1998.

[23] T.A. Day, A. Chi, B. Neville, and J.R. Hebert. Prevention of head and neck cancer. *Curr. Oncol. Rep.*, 7:145–153, 2005.

[24] F. Dayyani, C.J. Etzel, M. Liu, C.-H. Ho, S.M. Lippman, and A.S. Tsao. Meta-analysis of the impact of human papillomavirus (HPV) on cancer risk and overall survival in head and neck squamous cell carcinomas (HNSCC). *Head Neck Oncol.*, 2:15, 2010.

[25] A. Daza, J.K. Matrín, A. Dominguez, and J.A. Gil. Sporulation of Several Species of *Streptomyces* in Submerged Cultures after Nutritional Downshift. *J. Gen. Microbiol.*, 135:2483–2491, 1989.

[26] A.M.B. De Paula, L.R. Souza, L.C. Farias, G.T.B Corrêa, C.A.C Fraga, N.B. Eleutério, A.C.O. Silveira, F.B.G Santos, D.S. Haikal, A.L.S. Guimarães, and R.S. Gomez. Analysis of 724 cases of primary head and neck squamous cell carcinoma (HNSCC) with a focus on young patients and p53 immunolocalization. *Oral Oncol.*, 45:777–782, 2009.

[27] D.E Discher and E. Adi. Polymer vesicles. *Science*, 297:967–973, 2002.

[28] D.E. Discher, V. Ortiz, G. Srinivas, M.L. Klein, Y. Kim, D. Christian, S. Cai, P. Photos, and A. Ahmed. Emerging applications of polymersomes in delivery: From molecular dynamics to shrinkage of tumors. *Prog. Polym. Sci.*, 32:838–857, 2007.

[29] E. Doedel, R. Paffenroth, A. Champneys, T. Fairgrieve, Y. A. Kuznetsov, B. Sandstede, and X. Wang. Continuation and bifurcation software for or-

dinary differential equations (with HomCont). *Technical Report, Caltech*, (2001).

[30] M. Elibol and F. Mavituna. A kinetic model for actinorhodin production by *Streptomyces coelicolor* A3(2). *Process Biochem.*, 34:625–631, 1999.

[31] M.A. Elliot and N.J. Talbot. Building filaments in the air: aerial morphogenesis in bacteria and fungi. *Curr. Opin. Microbiol.*, 7:594–601, 2004.

[32] M.A. Elliot, M.J. Buttner, and J.R. Nodwell. *Myxobacteria: Multicellularity and Differentiation*, chapter 24. ASM Press, 2008.

[33] S.C. Evans and G. Lozano. The Li-Fraumeni syndrome: an inherited susceptibility to cancer. *Mol. Med. Today*, 3:390–395, 1997.

[34] K. Flärdh and M.J. Buttner. *Streptomyces* morphogenetics: dissecting differentiation in a filamentous bacterium. *Nat. Rev. Microbiol.*, 7:36–49, 2009.

[35] R.A. Gatenby and E.T. Gawlinski. A Reaction-Diffusion Model of Cancer Invasion. *Cancer Res.*, 56:5745–5753, 1996.

[36] K.B. Ghaghada, J. Sauld, J.V. Natarajanb, R.V. Bellamkondad, and A.V. Annapragadaa. Folate targeting of drug carriers: A mathematical model. *J. Control Release*, 104:113–128, 2005.

[37] P.P. Ghoroghchian, P.R. Frail, K. Susumu, D. Blessington, A.K. Brannan, F.S. Bates, B. Chance, D.A. Hammer, and M.J. Therien. Near-infrared-emissive polymersomes: Self-assembled soft matter for in vivo optical imaging. *Proc. Natl. Acad. Sci. USA*, 102:2922–2927, 2005.

[38] M. Goerner, T.Y Seiwert, and H. Sudhoff. Molecular targeted therapies in head and neck cancer - An update of recent developements. *Head Neck Oncol.*, 2:8, 2010.

[39] D.I. Gray, G.W. Gooday, and J.I. Prosser. Apical hyphal extension in *Streptomyces coelicolor* A3(2). *J. Gen. Microbiol.*, 136:1077–1084, 1990.

[40] H.P. Greenspan. Models for the growth of a solid tumor by diffusion. *Stud. Appl. Math.*, 51:317–340, 1972.

[41] L. Griffiths, K. Binley, S. Iqball, O. Kan, P. Maxwell, P. Ratcliffe, C. Lewis, A. Harris, S. Kingsman, and S. Naylor. The macrophage a novel system to deliver gene therapy to pathological hypoxia. *Gene Ther.*, 7:255–262, 2000.

[42] M.A. Grimbone, S.B. Leapman, R.S. Cotran, and J. Folkman. Tumor dormancy *in vivo* by prevention of neovascularization. *J. Exp. Med.*, 136: 261–276, 1972.

[43] R.I. Haddad and D.M. Shin. Recent advances in head and neck cancer. *N. Engl. J. Med.*, 359:1143–1154, 2008.

[44] D. Hanahan and R.A. Weinberg. The hallmarks of cancer. *Cell*, 100:57–70, 2000.

[45] T.F Ho, C.J. Ma, C.H Lu, Y.T Tsai, Y.H. Wei, J.S Chang, J.K Lai, P.J Cheuh, C.T Yeh, P.C Tang, J.T. Chang, J.L Ko, F.S Liu, H.E. Yen, and C.C. Chang. Undecylprodigiosin selectively induces apoptosis in human breast carcinoma cells independent of p53. *Toxicol. Appl. Pharm.*, 225: 318–328, 2007.

[46] D.A. Hodgson. Primary Metabolism and its Control in Streptomycetes: A Most Unusual Group of Bacteria. *Adv. Microb. Physiol.*, 42:47–238, 2000.

[47] F.D. Hong and G.L. Clayman. Isolation of a Peptide for Targeted Drug Delivery into Human Head and Neck Solid Tumors. *Cancer Res.*, 60: 6551–6556, 2000.

[48] S.H. Jung, S.H. Jung, H. Seong, S.H. Cho, K.-S. Jeong, and B.C. Shin. Polyethylene glycol-complexed cationic liposome for enhanced cellular uptake and anticancer activity. *Int. J. Pharm.*, 382:254–261, 2009.

[49] S. Kang, S. Elf, K. Lythgoe, T. Hitosugi, J. Taunton, W. Zhou, L. Xiong, D. Wang, S. Muller, S. Fan, S. Sun, A.I. Marcus, and T. Gu. p90 ribosomal S6 kinase 2 promotes invasion and metastasis of human head and necksquamous cell carcinoma cells. *J. Clin. Invest.*, 120:1165–1177, 2010.

[50] S.G. Kang, W. Jin, M. Bibb, and K.J. Lee. Actinorhodin and undecylprodigiosin production in wild-type and *relA* mutant strains of *Streptomyces coelicolor* A3(2) grown in continuous culture. *FEMS Microbiol. Lett.*, 168:221–226, 1998.

[51] C.T. Kelley. *Solving Nonlinear Equations with Newton's Method*. SIAM, Philadelphia, 2003.

[52] T. Kieser, M.J. Bibb, M.J. Buttner, K.F. Chater, and D.A. Hopwood. *Practical Streptomyces Genetics*. John Innes Foundation, 2nd edition, 2000.

[53] K.J. Kim, B. Li, J. Winer, M. Armanini, N. Gillett, H.S. Phillips, and N. Ferrara. Inhibition of vascular endothelial growth factor-induced angiogenesis supresses tumour growth *in vivo*. *Nature*, 362:841–844, 1993.

[54] C. Ko and D. Citrin. Radiotherapy for the management of locally advanced squamous cell carcinoma of the head and neck. *Oral Dis.*, 15:121–132, 2009.

[55] P. Lassen. The role of Human papillomavirus in head and neck cancer and the impact on radiotherapy outcome. *Radiother. Oncol.*, 95:371–380, 2010.

[56] C.P. Leamon, S.R. Cooper, and G.E. Hardee. Folate-liposome-mediated antisense oligodeoxynucleotide targeting to cancer cells: Evaluation in Vitro and in Vivo. *Bioconjugate Chem.*, 14:738–747, 2003.

[57] D.A. Levine, P.P. Ghoroghchian, J. Freudenberg, G. Zhang, M.J. Therien, M.I. Greene, D.A. Hammer, and R. Murali. Polymersomes: A new multi-functional tool for cancer diagnosis and therapy. *Methods*, 46:25–32, 2008.

[58] C.E. Lewis and J.W. Pollard. Distinct role of macrophages in different tumour microenvironments. *Cancer Res.*, 66:605–612, 2006.

[59] H. Lomas, I. Canton, S. MacNeil, J. Du, S.P. Armes, A.J. Ryan, A.L. Lewis, and G. Battaglia. Biomimetic pH Sensitive Polymersomes for Efficient DNA Encapulation and Delivery. *Adv. Mater.*, 19:4238–4243, 2007.

[60] H. Lomas, M. Massignani, K.A. Abdullah, I. Canton, K.L. Presti, S. MacNeil, J. Du, A. Blanazs, J. Madsen, S.P. Armes, A.L. Lewis, and G. Battaglia. Non-cytotoxic polymer vesicles for rapid and efficient intracellular delivery. *Faraday Discuss.*, 139:143–159, 2008.

[61] H. Lomas, J. Du, I. Canton, J. Madsen, N. Warren, S.P. Armes, A.L. Lewis, and G. Battaglia. Efficient Encapsulation of Plasmid DNA in pH Sensitive PMPC-PDPA Polymersomes: Study of the Effect of PDPA Block Length on Copolymer-DNA Binding Affinity. *Macromol. Biosci.*, 10:513–530, 2010.

[62] B. Lucas, K. Remaut, N.N. Sanders, K. Braeckmans, S.E. De Smedt, and J. Demeester. Towards a better understanding of the dissociation behavior of liposome-oligonucleotide complexes in the cytosol of cells. *J. Control. Release*, 103:435–450, 2005.

[63] K.J.K. Luti and F. Mavituna. *Streptomyces coelicolor* increases the

production of undecylprodigiosin when interacted with *Bacillus subtilis*. *Biotechnol. Lett.*, 33:113–118, 2011.

[64] A. Manteca, R. Alvarez, N. Salazar, P. Yagüe, and J. Sanchez. Mycelium differentiation and antibiotic production in submerged cultures of *Streptomyces coelicolor*. *Appl. Environ. Microb.*, 74(12):3877–3886, 2008.

[65] J. Meyerhoff and K.H. Bellgardt. Two mathematical models for the development of a single microbial pellet. Part II: Simulation of the pellet growth of *Penicillium chrysogenum* by a fast method equivalent to a morphological detailed description. *Bioprocess Eng.*, 12:315–322, 1995.

[66] J. Meyerhoff, V. Tiller, and K.H. Bellgardt. Two mathematical models for the development of a single microbial pellet. Part I: Detailed morphological model based on the description of individual hyphae. *Bioprocess Eng.*, 12: 305–313, 1995.

[67] J.E. Moulder and S. Rockwell. Tumour hypoxia: its impact on cancer therapy. *Cancer Metast. Rev.*, 5:313–341, 1984.

[68] K.J. Murdoch, C. andReeves, V. Hearnden, H. Colley, M. Massignani, I. Canton, J. Madsen, A. Blanazs, S.P. Armes, A.L. Lewis, S. MacNeil, N.J. Brown, M.H. Thornhill, and Battaglia G. Internalization and biodistribution of polymersomes into oral squamous cell carcinoma cells *invitro* and*invivo*. *Nanomedicine-UK*, 5:1025–1036, 2010.

[69] M. Nordsmark, M. Overgaard, and J. Overgaard. Concurrent Paclitaxel and Radiation in the Treatment of Locally Advanced Head and Neck Cancer. *Radiother. Oncol.*, 41:31–39, 1996.

[70] J. Oostra, E.P. le Comte, J.C. van den Heuvel, J. Tramper, and A. Rinzema. Intra-Particle Oxygen Diffusion Limitation in Solid-State Fermentation. *Biotechnol. Bioeng.*, 75:13–24, 2001.

[71] M.E. Orme and M.A.J. Chaplain. A mathematical model of vascular tumour growth and invasion. *Math. Comp. Modelling*, 23:43–60, 1996.

[72] M.E. Orme and M.A.J. Chaplain. A mathematical model of the first steps of tumour-related angiogenesis: Capillary sprout and secondary branching. *IMA J. Math. Appl. Med.*, 13:73–98, 1997.

[73] M.R. Owen, H.M. Byrne, and C.E. Lewis. Mathematical modelling of the use of macrophages as vehicles for drug delivery to hypoxic tumour sites. *J. Theor. Biol.*, 226:377–391, 2004.

[74] K. Ozergin-Ulgen and F. Mavituna. Oxygen transfer and uptake in *Streptomyces coelicolor* A3(2) culture in a catch bioreactor. *J. Chem. Technol. Biotechnol.*, 73:243–250, 1998.

[75] J. Panovska, H.M. Byrne, and P.K. Maini. A theoretical study of the response of vascualr tumours to different types of chemotherapy. *Math. Comput. Model.*, 47:560–579, 2008.

[76] N. Parker, M.J. Turk, E. Westrick, J.D. Lewis, P.S. Low, and C.P. Leamon. Folate receptor expression in carcinomas and normal tissues determined by a quantitative radioligand binding assay. *Anal. Biochem.*, 338:284–293, 2005.

[77] A. Quarteroni and A. Valli. *Numerical Approximation of Partial Differential Equations*. Springer-Verlag, Heidelberg, 1994.

[78] J.A. Reddy and P.S. Low. Enhanced folate receptor mediated gene therapy using a novel pH-sensitive lipid formulation. *J. Control. Release*, 64:27–37, 2000.

[79] K. Remaut, Lucas B., K. Braeckmans, N.N. Sanders, J. Demeester, and S.E. De Smedt. Delivery of Phosphodiester Oligonucleotides: Can

DOTAP/DOPE Liposomes Do the Trick? *Biochemistry*, 45:1755–1764, 2006.

[80] Y. Remvikos, P. Beuzeboc, A. Zajdela, N. Voillemot, H. Magdelénat, and P. Pouillart. Correlation of pretreatment proliferative activity of breast cancer with the response to cytotoxic chemotherapy. *J. Natl Cancer I.*, 81:1382–1387, 1989.

[81] S.J.M. Russell and P. MacArthur. Tuberculous meningitis treated with streptomycin. *Brit. Med. J.*, 1:192–194, 1953.

[82] J.A. Sherratt, E.H. Sage, and J.D. Murray. Chemical Control of Eukaryotic Cell Movement: A New Model. *J. Theor. Biol.*, 162:23–40, 1993.

[83] A. Sigal and V. Rotter. Oncogeneic Mutations of the p53 Tumour Supressor: The demons of the Guardian of the Genome. *Cancer Res.*, 60: 6788–6793, 2000.

[84] D.J. Smiraglia, L.T. Smith, J.C Lang, L.J. Rush, Z. Dai, D.E. Schuller, and C. Plass. Differential targets of CpG island hypermethylation in primary and metastatic head and neck squamous cell carcinoma (HNSCC). *J. Med. Genet.*, 40:25–33, 2003.

[85] S.M. Stocks. Mechanism and Use of the Commercially Available Viability Stain, BacLight. *Cytom. Part A*, 61A:189–195, 2004.

[86] J.B. Sunwoo, L.L. Herscher, G.S. Kroog, G.R. Thomas, F.G. Ondrey, D.C. Duffey, B.I. Solomon, C. Boss, P.S. Albert, L. McCullugh, S. Rudy, C. Muir, S. Zhai, W.D. Figg, J.A. Cook, J.B. Mitchell, and C. Van Waes. Concurrent Paclitaxel and Radiation in the Treatment of Locally Advanced Head and Neck Cancer. *J. Clin. Oncol.*, 19:800–811, 2001.

[87] R.M. Sutherland. Cell and Environment Interactions in Tumor Microregions: The Multicell Spheroid Model. *Science*, 240:177–184, 1988.

[88] J.A. Swanson and C. Watts. Macropinocytosis. *Trends Cell Biol.*, 5:424–427, 2005.

[89] S. Syrjänen. The role of human papillomavirus infection in head and neck cancers. *Ann. Oncol.*, 21, 2010.

[90] R.H. Thomlinson and L.H. Gray. The histological stucture of some human lung cancers and the possible implications for radiotherapy. *Brit. J. Cancer*, 9:539–549, 1955.

[91] A.J. Tought and J.I. Prosser. Experimental verification of a mathematical model for pelleted growth of *Streptomyces coelicolor* A3(2) in submerged batch culture. *Microbiology*, 142:639–648, 1996.

[92] R.M. Trüeb. Chemotherapy-induced alopecia. *Semin. Cutan. Med. Surg.*, 12:11–14, 2009.

[93] S.A. Waksman, H.C. Reilly, and D.B. Johnstone. Isolation of streptomycin-producing strains of *Streptomyces griseus*. *J. Bacteriol.*, 52: 393–397, 1946.

[94] F.M. Waleed, A. Kotba, C. Blind, K. Friedrich, C. Schewe, Z.G. Zhang, J.M. Zheng, N. Deutschman, M. Pacyna-Gengelbach, M. Dietel, and I. Petersen. Core classification of head and neck squamous cell carcinomas: Correlations between morphology, DNA ploidy and HPV infection. *Pathol. Res. Pract.*, 206:768–771, 2010.

[95] J.P. Ward and J.R. King. Mathematical modelling of avascular-tumour growth. *IMA J. Math. Appl. Med.*, 14:39–69, 1997.

[96] J.P. Ward and J.R. King. Mathematical modelling of avascular-tumour growth II: Modelling growth saturation. *IMA J. Math. Appl. Med.*, 16: 171–211, 1999.

[97] S.D. Webb and M.R. Owen. Oscillations and patterns in spatially discrete models for developmental intercellular signalling. *J. Math. Biol.*, 48:444–476, 2004.

[98] S.D. Webb, M.R. Owen, H.M. Byrne, C. Murdoch, and C.E. Lewis. Macrophage-Bases Anti-Cancer Therapy: Modelling Different Modes of Tumour Targeting. *B. Math. Biol.*, 69:1747–1776, 2007.

[99] J.M. Willey, A. Willems, S. Kodani, and J.R. Nodwell. Morphological surfacetant and their role in the formation of aerial hyphae in *Streptomyces coelicolor*. *Mol. Microbiol.*, 59:731–742, 2006.

[100] L.F. Wright and D.A. Hopwood. Identification of the Antibiotic Determined by the SCP1 Plasmid of *Streptomyces coelicolor* A3(2). *J. Gen. Microbiol.*, 95:96–106, 1976.

[101] H. Yang, R. King, U. Reichl, and E.D. Gillies. Mathematical model for apical growth, septation, and branching in mycelial microorganisms. *Biotechnol. Bioeng.*, 39:49–58, 1992.

[102] H. Yang, U. Reichl, R. King, and E.D. Gillies. Measurement and simulation of morphological development of filamentous microorganisms. *Biotechnol. Bioeng.*, 39:44–48, 1992.